

# Transactions of the ASME

FLUIDS ENGINEERING DIVISION  
Technical Editor  
FRANK M. WHITE (1989)  
Executive Secretary  
L. T. NELSON (1989)  
Calendar Editor  
M. F. ACKERSON

Associate Editors  
Fluid Machinery  
WIDEN TABAKOFF (1988)  
RICHARD F. SALANT (1987)  
Fluid Measurements  
ALEXANDER DYBBS (1987)  
Fluid Mechanics  
J. A. MILLER (1987)  
HUGH W. COLEMAN (1987)  
STANLEY F. BIRCH (1988)  
WILLIAM W. DURGIN (1986)  
Fluid Transients  
FREDERICK J. MOODY (1986)  
Numerical Methods  
PATRICK J. ROACHE (1988)  
Multiphase Flow  
M. C. ROCO (1988)  
GEORGES L. CHAHINE (1986)  
Review Articles  
K. N. GHIA (1986)

BOARD ON COMMUNICATIONS  
Chairman and Vice President  
K. N. REID, Jr.

Members-at-Large  
W. BEGELL  
J. T. COKONIS  
M. FRANKE  
W. G. GOTTENBERG  
M. KUTZ  
F. LANDIS  
J. R. LLOYD  
T. C. MIN  
R. E. NICKELL  
R. E. REDER  
F. W. SCHMIDT

President, N. D. FITZROY  
Executive Director  
PAUL ALLMENDINGER  
Treasurer,  
ROBERT A. BENNETT

PUBLISHING STAFF  
Mng. Dir. Publ., J. J. FREY  
Dep. Mng. Dir. Publ.,  
JOS. SANSONE  
Managing Editor,  
CORNELIA MONAHAN  
Editorial Production Assistant,  
MARISOL ANDINO

Transactions of the ASME, The Journal of Fluids Engineering (ISSN 0098-2202) is published quarterly (Mar., June, Sept., Dec.) for \$105 per year by The American Society of Mechanical Engineers, 345 East 47th Street, New York, NY 10017. Second class postage paid at New York, NY and additional mailing offices. POSTMASTER: Send address changes to The Journal of Fluids Engineering, c/o THE AMERICAN SOCIETY OF MECHANICAL ENGINEERS, 22 Law Drive, Box 2300, Fairfield, NJ 07007-2300.

CHANGES OF ADDRESS must be received at Society headquarters seven weeks before they are to be effective. Please send old label and new address.

PRICES: To members, \$24.00, annually; to nonmembers, \$100. Add \$6.00 for postage to countries outside the United States and Canada.

STATEMENT from By-Laws:  
The Society shall not be responsible for statements or opinions advanced in papers or . . . printed in its publications (B7.1, Par. 3).

COPYRIGHT © 1986 by The American Society of Mechanical Engineers. Reprints from this publication may be made on condition that full credit be given to THE TRANSACTIONS OF THE ASME, JOURNAL OF FLUIDS ENGINEERING and the author, and date of publication be stated.

INDEXED by Engineering Information

# Journal of Fluids Engineering

Published Quarterly by The American Society of Mechanical Engineers

VOLUME 108 • NUMBER 4 • DECEMBER 1986

- 390 Fluids Engineering Calendar
- 392 Transient Characteristics of a Centrifugal Pump During Stopping Period (86-WA/FE-1)  
H. Tsukamoto, S. Matsunaga, H. Yoneda, and S. Hata
- 400 A Simplified Wake Method for Horizontal-Axis Wind Turbine Performance Prediction (87-FE-1)  
A. A. Afjeh and T. G. Keith, Jr.
- 407 Measurements of Apparent Mass Torque Coefficients of Two-Dimensional Centrifugal Impellers (86-WA/FE-2)  
Y. Tsujimoto, K. Imaichi, T. Moritani, and K. Kim
- 414 Optimal Supersonic Ejector Designs (86-WA/FE-3)  
J. C. Dutton and B. F. Carroll
- 421 Cavitation Inception on a Circular Cylinder at Critical and Supercritical Flow Range  
A. Ihara and H. Murai
- 428 Critical Conditions of Cavitation Occurrence in Various Liquids  
S. Kamiyama and T. Yamasaki
- 433 Contribution of Homogeneous Condensation Inside Cavitation Nuclei to Cavitation Inception  
Y. Matsumoto
- 438 Stochastic Behavior (Randomness) of Desinent Cavitation  
R. Oba, T. Ikohagi, Y. Ito, H. Miyakura, and K. Sato
- 444 Bubble Dynamics and Cavitation Inception in Cavitation Susceptibility Meters  
G. L. Chahine and Y. T. Shen
- 453 Casing Headloss in Centrifugal Slurry Pumps  
M. C. Roco, P. Nair, and G. R. Addie
- 465 Automatic Remeshing Scheme for Modeling Hot Forming Process  
H. P. Wang and R. T. McLay
- 470 Calculation of Boundary Layers With Sudden Transverse Strain  
M. M. Gibson and B. A. Younis
- 476 Integral Skin Friction Prediction for Turbulent Separated Flows  
D. K. Das and F. M. White

## Technical Briefs

- 483 Some Remarks on the Helical-Cartesian Coordinate System and Its Applications  
Zhong-Guang Xu and Dah-Nien Fan
- 486 Modeling of Wall Friction for Multispecies Solid-Gas Flows  
E. D. Doss and M. G. Srinivasan
- 489 Discussion on a Previously Published Paper

## Announcements and Special Notices

- 389 New ASME Prior Publication Policy
- 389 Submission of Papers
- 389 Statement of Experimental Uncertainty
- 399 Call for Papers – Third International ASME Symposium on Laser Anemometry
- 427 Titles of Recent and Forthcoming Articles in Applied Mechanics Reviews
- 443 Transactions Change of Address Form
- 452 Announcement—ASME Freeman Scholar Program
- 490 Call for Papers – First National Fluid Dynamics Conference

**H. Tsukamoto**

Associate Professor.

**S. Matsunaga**

Professor.

**H. Yoneda**

Graduate Student.

Department of Mechanical Engineering,  
Kyushu Institute of Technology,  
Kitakyushu, Japan

**S. Hata**

Engineer,  
Hiroshima Shipbuilding Yard,  
Mitsubishi Heavy Industries, Ltd.,  
Hiroshima, Japan

# Transient Characteristics of a Centrifugal Pump During Stopping Period

*A theoretical and experimental study has been made on the transient characteristics of a centrifugal pump during its rapid deceleration from initial speed to zero. Instantaneous rotational speed, flow-rate, and total pressure rise are measured for various stopping schemes. Theoretical calculations for the prediction of transient characteristics are developed and compared with the corresponding experimental results. As a result of this study, it becomes clear that impulsive pressure and the lag in circulation formation around impeller vanes play predominant roles for the difference between dynamic and quasi-steady characteristics of turbopumps. Moreover, a criterion for the assumption of quasi-steady change is presented.*

## Introduction

The characteristics of a pump under unsteady operational conditions have usually been thought to follow along its steady-state characteristic curves [1]. This assumption, called hereafter quasi-steady change, is obviously acceptable in the case of slow change in operational condition. When the rate of change of the operating point exceeds a certain limit, however, the pump cannot respond quickly enough to traverse its steady-state characteristic curves, thus resulting in a considerable change of the actual characteristic curves. There has been, therefore, a need for understanding the dynamics of the pump characteristics.

Dynamic performance of a pump has been investigated intensively for the case in which the flow-rate oscillates periodically about a mean operating point with a small amplitude. In this case the pump dynamic performance can be described by a transfer matrix representation to relate the quantities at the inlet and exit of the pump. Ohashi [2], Anderson et al. [3], and Brennen and Acosta [4] have contributed to such a description.

Another aspect of unsteady characteristics involves the transient ones with a large shift of the operating point in cases such as starting or stopping, and the quick closure or opening of the discharge valve. From the viewpoint of the theoretical treatment, these cases offer far more difficulties than the previous ones, because the linearization of the problem is fundamentally impossible. Pressure response during quick opening or closure of the discharge valve was studied by Kaneko and Ohashi [5]; while transient characteristics during quick start-

up were reported by Tsukamoto and Ohashi [6], and Saito [7]. However, studies on the transient characteristics during the stopping period have not been reported to date, and thus we have no knowledge of how the dynamic characteristics deviate from the quasi-steady ones as the rotational speed decreases.

The aim of this study is to try to explain the nature of pumping action during stopping transients. In order to find a critical deceleration rate beyond which the assumption of the quasi-steady change becomes unacceptable, tests were conducted up to a very rapid deceleration rate, which hardly occurs in practice. Such extreme test conditions result in a clear difference between dynamic and quasi-steady change, and help in understanding the mechanism of transient phenomena. Another aim is to establish the method by which the transient characteristics of a centrifugal pump during the stopping period can be predicted theoretically.

The present study is done for incompressible and cavitation-free flow so that the knowledge of basic phenomena may be obtained.

## Experiment

**Test Equipment and Method.** A single-stage, volute type centrifugal pump is used for the experiment, and its principal specifications are summarized in Table 1. The arrangement of the test setup and instrumentation system is illustrated schematically in Fig. 1, most parts of which are similar to the one in reference [6] except for the data recording and torque measuring system.

In order to realize an extremely high deceleration rate of rotational speed, the electro-magnetic brake is used, which connects the rotating pump shaft with the stationary brake disk after disconnecting the shaft from the rotating motor

Contributed by the Fluids Engineering Division and presented at the Winter Annual Meeting, Anaheim, Calif., December 7-12, 1986 of THE AMERICAN SOCIETY OF MECHANICAL ENGINEERS. Manuscript received by the Fluids Engineering Division, February 26, 1985. Paper No. 86-WA/FE-1.

**Table 1 Specifications of test pump**

Suction diameter	65 ± 0.7 mm
Discharge diameter	50 ± 0.5 mm
Impeller: Outer diameter	137 ± 1.0 mm
Outer passage width	9.3 ± 0.1 mm
Outlet vane angle	20 ± 0.5 °
Number of vanes	7
Rating: Rotational speed	3455 rpm
Flow-rate	0.25 m <sup>3</sup> /min
Total head rise	31.5 m

**Table 2 List of test conditions**

Case No.	$N_0$ [rpm]	$T_{nd}$ [sec]	$\phi_0/\phi_r$
1	2500 ± 5	0.112 ± 0.001	1.00 ± 0.03
2	3455 ± 5	0.217 ± 0.001	1.00 ± 0.03

shaft. For slower deceleration rates two different methods are adopted; i.e., the usual switch-off stop of the motor, and the disconnection of the pump shaft from the clutch disk without the activation of the brake.

The pulse signal from the relay circuit is gated to insure the start of the deceleration, i.e., to control the electro-magnetic clutch/brake and motor. Because of the difficulty in finding out the exact moment when the pump begins to decelerate, this signal is used as the time origin  $t = 0$ .

The instantaneous rotational speed  $N_i$ , flow-rate  $Q_i$ , suction and discharge pressure,  $p_s$  and  $p_d$ , are measured in the manner similar to reference [6]. In addition, the shaft torque  $T_i$  is also measured for reference. The above five analogue signals as well as the pulse signal for the time origin are transmitted to an A/D converter, and then recorded on the data file in the computer. From the data on the data file, instantaneous rotational speed  $N_i(t)$ , flow-rate  $Q_i(t)$ , total pressure difference between discharge and suction port,  $P_i(t)$ , and shaft torque  $T_i(t)$  are read out as a function of time  $t$  after initiation of the stop operation.

**Presentation of Data.** In order to generalize the experimental results, first we will define a deceleration rate of the rotational speed. Deceleration rate  $dN_i/dt$  is not constant for the entire stopping period. It is, therefore, difficult to express this complicated deceleration history by a simple parameter. In this study, we introduce a nominal deceleration time  $T_{nd}$ , which is defined as the deceleration time of the pump shaft from the initial value to 36.8 percent of its initial rotational speed  $N_0$ .

Next, we will consider the meaning of the total pressure rise of the pump during the stopping period. In the case of unsteady flow-rate, it is necessary to differentiate the total pressure rise of the pump,  $P(t)$  from the indicated total pressure difference between the suction port and the discharge of the pump,  $P_i(t)$ . The total pressure difference is, of course, generated mainly by the pumping action itself. However, it is also affected by the inertia of the water contained in the pump casing. In the present study where we are interested only in the dynamic behavior of the pumping action, therefore, the true total pressure rise containing no inertial effect of the water should be compared with a quasi-steady value in order to discuss the deviation of the dynamic performance from a quasi-steady one.

The true total pressure rise  $P(t)$  is obtained by subtracting the apparent static pressure difference  $p_c(t)$  due to the inertia from the indicated total pressure difference  $P_i(t)$ , as the following equation shows [8]:

$$P(t) = P_i(t) - p_c(t) = P_i(t) + (\rho L_{eq}/A_0) \{dQ_i(t)/dt\} \quad (1)$$

where the pump is represented by a straight pipe with cross

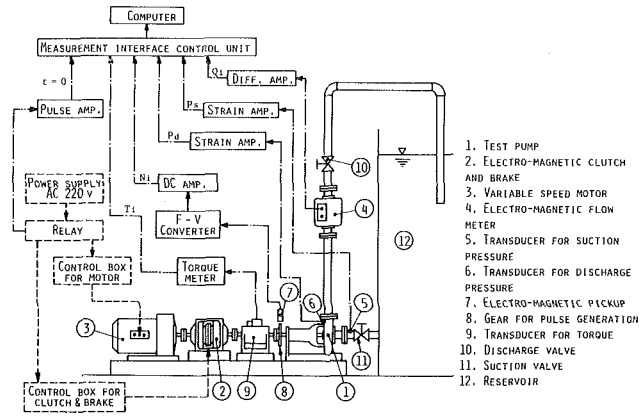


**Fig. 1 Schematic view of test setup and instrumentation system**

sectional area  $A_0$  and length  $L_{eq}$ . The equivalent pipe length  $L_{eq}$  of the pump is calculated by the equation

$$L_{eq} = \int_{s=0}^L \{A_0/A(s)\} ds \quad (2)$$

where  $s$  is the distance measured from the suction port, and  $L$  is the total path length.

The instantaneous flow coefficient  $\phi_i$  and the instantaneous total pressure rise coefficient  $\psi_i$  are defined as follows:

$$\phi_i(t) = Q_i(t) / \{\pi d_2 b_2 u_2(t)\} \quad (3)$$

$$\psi_i(t) = P(t) / \{\rho u_2(t)^2 / 2\}$$

where  $d_2$  and  $b_2$  are the outer diameter and passage width of the impeller, respectively, and  $u_2(t) = \pi d_2 N_i(t)$  is the instantaneous peripheral speed of the impeller.

In order to derive the nondimensional parameters which regulate the transient characteristics, let us compare the transient phenomena in the pumping system with geometrically similar pump and piping. Once we fix the following seven parameters, i.e., the representative length of the pump,  $r_m$ , total length of the piping,  $l_{eq}$ , density and viscosity coefficient  $\rho$  and  $\mu$ , initial rotational speed  $N_0$ , initial flow-rate  $Q_0$ , and nominal deceleration time  $T_{nd}$ ; a unique experimental condition can be established, under which a specific transient phenomenon takes place. According to the theory of dimensional analysis, the above seven physical quantities can be reduced to four independent nondimensional parameters, i.e., normalized piping length  $l_{eq}/r_m$ , Reynolds number  $N_0 r_m^2 / (\mu/\rho)$ , normalized flow-rate  $Q_0 / (N_0 r_m^3) \propto \phi_0/\phi_r$ , and newly introduced dimensionless number  $N_0 T_{nd}$ . Here  $\phi_0$  and  $\phi_r$  are initial and rated flow coefficient, respectively.

The latter two parameters can be controlled in the experiment by adjusting the opening of the delivery valve, and the deceleration rate and initial rotational speed. The influence of Reynolds number on transient characteristics is omitted from the present study.

**Test Results.** Experimental results will be shown for the two representative cases listed in Table 2. Presented data are for the case in which the pump is stopped by the activation of the magnetic brake, and thus the dynamic characteristics result in a clear deviation from the quasi-steady ones. In Case 1, in which the pump is stopped with the highest deceleration rate, the total number of rotations from  $t = 0$  to  $T_{nd}$  is about 3 revolutions. On the other hand, Case 2 is the one in which the total number of rotations from  $t = 0$  to  $T_{nd}$  is about 6.2 revolutions and is thus a relatively slower deceleration case.

Figure 2 shows a sample of the time histories of the rotational speed  $N_i$ , flow-rate  $Q_i$ , shaft torque  $T_i$ , indicated and true total head rise,  $H_i = P_i/(\rho g)$  and  $H_p = P/(\rho g)$ , during stopping transient for Case 1. As can be seen from this figure, the flow-rate as well as the total head rise decreases as the rota-

tional speed decreases. The flow-rate does not reach zero immediately after the rotational speed reaches zero. This is due to the inertia effect of the water contained in the piping of the test loop.

There is a period in which the true total head rise falls into negative values when the rotational speed approaches zero. In this region, the reliability of the measured values is poor because of the difficulties in the precise estimation of the equivalent pipe length of the pump as well as the increase in the relative errors of measured values. However, judging from the tendency of the flow coefficient change shown later, which indicates higher negative incidence angle in this region,

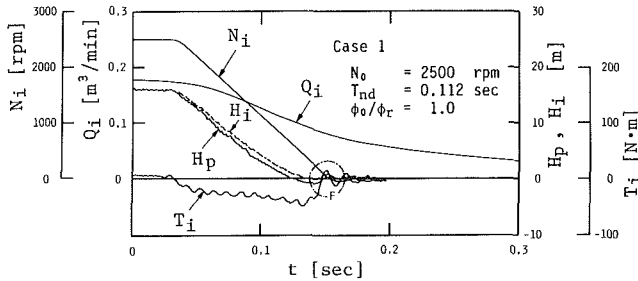


Fig. 2 Time histories of  $N_i$ ,  $Q_i$ ,  $T_i$ ,  $H_i$ , and  $H_p$  for Case 1. Uncertainty:  $N_i/N_0 \pm 3.5$  percent,  $Q_i/Q_0 \pm 3.5$  percent,  $T_i/T_i(0) \pm 3.5$  percent,  $H_i/H_i(0) \pm 3.5$  percent,  $H_p/H_p(0) \pm 3.5$  percent (20:1 odds).

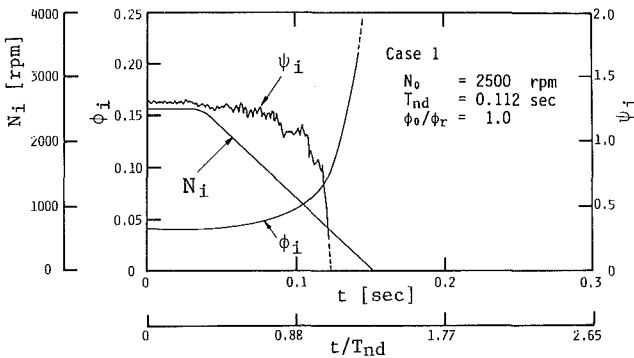


Fig. 3 Time histories of  $N_i$ ,  $\phi_i$ , and  $\psi_i$  for Case 1. Uncertainty:  $N_i/N_0 \pm 3.5$  percent,  $\phi_i/\phi_0 \pm 5.5$  percent,  $\psi_i/\psi_0 \pm 5.5$  percent (20:1 odds).

negative total head rise, in other words turbine action by the pump, is possible.

Time history of  $T_i$  shows stick-slip oscillation [9] because of the torque transmission characteristics of the friction plate in the pump shaft/magnetic brake system. At the first stage of the stopping after the initiation of the magnetic brake activation, the brake disk slips relative to the pump shaft. This causes slip-type oscillation which continues during the most period of the stopping, and the impeller is subjected to a negative torque, i.e., that acts in a direction opposite to the pump rotation. However, this slip-type oscillation does not have a marked effect on the change in the total head rise because of the large inertia of the pump impeller. Near the instant when the pump stops, the torque oscillation changes to stick-type oscillation in which the connection between the brake disk and the pump shaft is rigid. This causes slow fluctuation of the total head rise, which is designated as  $F$  in the figure, and which is nearly in phase with the one in the shaft torque.

Time histories of  $N_i$ ,  $\phi_i$ , and  $\psi_i$  are shown in Fig. 3. Flow coefficient  $\phi_i$  starts from its initial value and then increases with time, while  $\psi_i$  decreases with time.

Figures 4(a) and (b) indicate the locus along which the coordinates of  $\phi_i$  and  $\psi_i$  move during the stopping transient for Case 1 and 2, respectively. The time sequence is written on the locus as a parameter and the point corresponding to the nominal deceleration time  $T_{nd}$  is marked by a large circle. These loci represent the characteristic curves during the stopping transient and should be compared with the steady-state characteristic curves drawn by dash line. As can be seen clearly from these figures, the deviation of transient characteristics from quasi-steady ones is evident.

Here we classify these stopping transients into two stages, i.e., A and B as indicated in Fig. 4(a). At the very beginning of the stopping period, stage A, the total pressure rise coefficient  $\psi_i$  is greater than the quasi-steady one  $\psi_s$  at the same instantaneous flow coefficient  $\phi_i$ . This reason might be attributed largely to the lag in circulation formation around the impeller vanes. As presented later this lag can be fundamentally calculated by the potential flow theory.

In the last deceleration stage B,  $\psi_i$  is smaller than  $\psi_s$ , and the difference between  $\psi_i$  and  $\psi_s$  becomes larger with time. This tendency is mainly caused by the effect of the impulsive pressure difference between inlet and exit port of the impeller as supported by the numerical calculations described in the analysis.

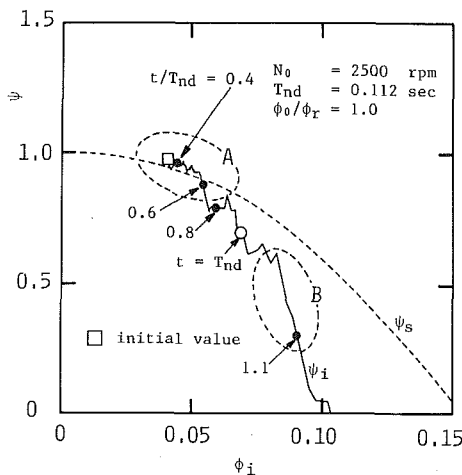


Fig. 4(a) Case 1

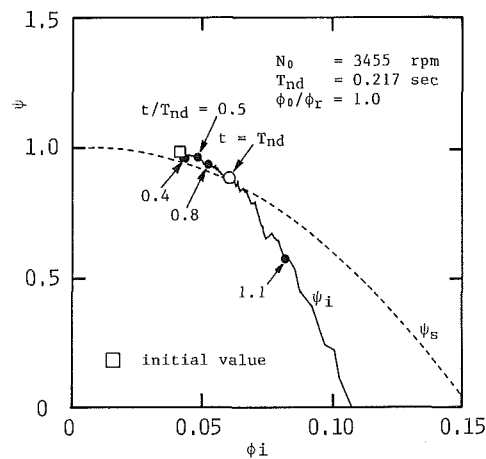


Fig. 4(b) Case 2

Fig. 4 Dynamic characteristic curves during stopping period. Uncertainty:  $\phi_i/\phi_0 \pm 5.5$  percent,  $\psi_i/\psi_0 \pm 5.5$  percent (20:1 odds).



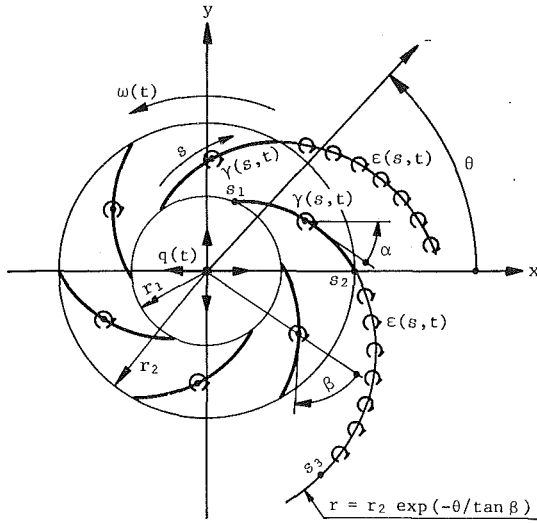
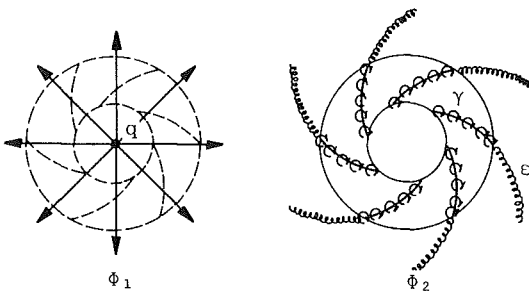


Fig. 5 Model of an airfoil cascade



Through Flow Induced Flow

Fig. 6 Construction of flow field expressed by  $\Phi$

## Analysis

**Modeling of Flow.** The aim of this analysis is to develop a calculation method for the time histories of the flow-rate and total pressure rise when the decrease in the rotational speed is given as a function of time. Among many assumptions necessary for the analysis, it is first assumed that the transient characteristics of a pump can be determined by solving the unsteady flow on a representative stream surface, i.e., mean stream surface.

In a centrifugal impeller, which is our main concern, the impeller blades on the stream surface constitute a rotating circular cascade. Unsteady flow analysis is, therefore, made for a two-dimensional circular cascade under the assumption similar to reference [10].

A guide vane or a diffuser which follows the impeller may also produce an unsteady flow effect on the transient characteristics of the pump. However, the basic mechanism of the dynamic performance of the pump might be thought to be explained by the unsteady flow effect of the impeller, since the total pressure rise of the pump is generated mainly by the pumping action of the impeller. The pressure rise across the guide vane or diffuser is, therefore, assumed simply to be quasi-steady. Then, the total pressure rise per stage of a pump can be determined as the sum of the increase in both static and dynamic pressure at the outlet edge of the impeller.

It is assumed also that flow is incompressible, cavitation-free and inviscid, and that inlet flow to the impeller has no prerotation and is axisymmetric.

**Vorticity Distribution.** The configuration of the cascade used in the present analysis is shown in Fig. 5. It is a rotating

circular cascade of thin blades with a rotational speed  $\omega(t)$ , flow-rate per unit passage width  $q(t)$ , and number of vanes  $N$ . The blade shape chosen herein for analysis is a logarithmic spiral, i.e., a vane of constant angle, and each blade is represented by an identical bound vortex sheet  $\gamma(s, t)$ . According to the change in circulation, each blade sheds vorticity downstream forming a vortex sheet of strength  $\epsilon(s, t)$ . This vortex sheet is assumed to be convected along the logarithmic spiral extended from the trailing edge with the radial velocity component  $q(t)/(2\pi r)$ . The shed vortex sheet from the first blade extends on the logarithmic spiral from  $s_2$  ( $r = r_2$ ) to  $s_3$  ( $r_3 = \{r_2^2 + \int_0^t q(\tau)/\pi \cdot d\tau\}^{1/2}$ ). All other vortex sheets have the same extension.

The absolute velocity at the point  $z' = Re^{i\theta}$  on the blade can be expressed by

$$u - i \cdot v = \frac{q(t)}{2\pi z'} + \frac{i}{2\pi} \int_{s_1}^{s_2} \gamma(s, t) G(z, z') ds + \frac{i}{2\pi} \int_{s_2}^{s_3} \epsilon(s, t) G(z, z') ds \quad (4)$$

where,  $G(z, z') = Nz'^{N-1} / \{z'^N - z(s)^N\}$ ,  $z = re^{i\theta}$ ,  $s$ : coordinate along the logarithmic spiral,  $u$  and  $v$ :  $x$  and  $y$  components of the absolute velocity.

The boundary condition on the blade requires that there is no flow through the surface in the relative system. This condition is fulfilled for a rotating blade if

$$\text{Im}[e^{i\alpha} \{u - i \cdot v + i \cdot \omega(t) z'\}] = 0 \quad (5)$$

where,  $\alpha = \theta - \beta$ .

Substitution of equation (4) into equation (5) then gives the following integral equation for unknown vorticity  $\gamma(s, t)$ , in which the velocity induced by shed vortices is rewritten in the manner similar to reference [6]:

$$\text{Im} \left[ e^{i\alpha} \left\{ \frac{q(t)}{2\pi z'} + \frac{i}{2\pi} \int_{s_1}^{s_2} \gamma(s, t) G(z, z') ds \right\} + \frac{ie^{i\alpha}}{2\pi} \left\{ \Gamma_0 F(z', 0) - F(z', t) \int_{s_1}^{s_2} \gamma(s, t) ds \right\} + \frac{ie^{i\alpha}}{2i} \sum_{i=0}^{M-1} (\Gamma_i + \Gamma_{i+1}) \{ F(z', t_{i+1}) - F(z', t_i) \} + ie^{i\alpha} \omega(t) z' \right] = 0 \quad (6)$$

where,

$$F(z', t_i) = Nz'^{N-1} / \{z'^N - z(t_i)^N\}, \quad z(t_i) = r_w e^{i\theta_w},$$

$$r_w = \left\{ r_2^2 + \int_{t_i}^t q(\tau) d\tau / \pi \right\}^{1/2}, \quad \theta_w = -\tan\beta \cdot \ln(r_w/r_2),$$

$$\Gamma_i = \int_{s_1}^{s_2} \gamma(s, t_i) ds, \quad 0 = t_0 < t_1 < \dots < t_M = t,$$

and  $\Gamma_i$  is known except for  $\Gamma_M = \Gamma(t)$ .

For the numerical calculation by use of the trapezoidal rule, a transformation is made from  $r$  and  $R$  to new independent variables  $\lambda$  and  $\Lambda$ :

$$r = r_1 + r_2(1 - r_1/r_2)(1 - \cos\lambda)/2 \quad (0 \leq \lambda \leq \pi)$$

$$R = r_1 + r_2(1 - r_1/r_2)(1 - \cos\Lambda)/2 \quad (0 \leq \Lambda \leq \pi)$$

The bound vortices can be specified at  $(n + 1)$  points

$$\lambda = (k - 1)\pi/n \quad (k = 1, 2, \dots, n + 1)$$

The values of  $\gamma$  for  $k = n + 1$ , that is at the trailing edge, is unnecessary since in the integration it is always multiplied by  $\sin \lambda = 0$ . The  $n$  values of  $\gamma$  can be determined so as to satisfy equation (6) at  $n$  points only, and these points are chosen so as to be allocated midway between the points at which bound vortices are specified.

$$\Lambda = (2k - 1)\pi/(2n) \quad (k = 1, 2, \dots, n)$$

**Table 3 Input data for the numerical calculations**

Impeller:	
Number of impeller vanes	$N$
Complement of vane angle	$\beta$
Ratio of inlet to outlet radius	$r_1/r_2$
Pipe-line:	
Nondimensional equivalent pipe length	$l_{eq}^*(=l_{eq}/r_2)$
Pump stopping condition:	
Initial flow coefficient	$\phi_0$
Initial total pressure rise coefficient	$\psi_0$
Initial rotational speed	$N_0$
Nominal deceleration time	$T_{nd}$

In this manner, equation (6) yields  $n$  simultaneous equation for the  $n$  unknowns,  $\gamma(s, t)$ .

**Pressure Rise.** For a given rotational speed of the impeller,  $\omega$ , the static pressure difference between inlet and outlet of the impeller can be calculated by the unsteady Bernoulli's equation with respect to the moving relative system [11]. To calculate the impulsive pressure term  $\rho(\partial\Phi/\partial t)$  in the unsteady Bernoulli's equation, the flow field represented by the velocity potential of absolute velocity,  $\Phi$ , is here resolved into two basic parts,  $\Phi_1$  and  $\Phi_2$ , as shown in Fig. 6. The  $\Phi_1$  represents the through flow due to a source placed at the origin, and the  $\Phi_2$  the flow induced by vortices on blades as well as in wakes. As can be seen easily, the flow represented by  $\Phi_1$  is not related to the change in circulation around blades. The contribution of  $\Phi_1$  to the impulsive pressure term can be omitted from our interest.

The effect of  $\Phi_2$  on the impulsive pressure term is calculated using the control surface shown in Fig. 7, where the line integral of the complex function ( $\Phi_2/z$ ) along a closed curve  $C$  becomes

$$2\pi i(\bar{\Phi}_{22} - \bar{\Phi}_{21}) + N \left\{ \Gamma(t) \ln Z_2 - \int_{s_1}^{s_2} \gamma(s, t) \ln Z ds \right\} = 0$$

where,  $Z_2 = r_2 e^{i\theta_2}$ : complex variable which expresses the blade trailing edge, and  $\bar{\Phi}_2$  is the velocity potential defined by

$$\bar{\Phi}_2 = \int_0^{2\pi} \Phi_2 d\theta / (2\pi)$$

The consideration of the imaginary part in the above equation gives the following impulsive pressure difference between inlet and outlet of the impeller:

$$\rho \{ (\partial\Phi/\partial t)_1 - (\partial\Phi/\partial t)_2 \} = \frac{\rho N}{2\pi} \left\{ \theta_2 \frac{d}{dt} \Gamma(t) - \frac{d}{dt} \int_{s_1}^{s_2} \gamma(s, t) \theta(s) ds \right\}$$

Substituting the above expression into the unsteady Bernoulli equation, we obtain the increase in static pressure at the outlet of the impeller as follows:

$$p_2 - p_1 = \frac{\rho N}{2\pi} \left\{ \theta_2 \frac{d}{dt} \Gamma(t) - \frac{d}{dt} \int_{s_1}^{s_2} \gamma(s, t) \theta(s) ds \right\} + \frac{\rho}{2} \left[ \left\{ \frac{q(t)}{2\pi r_1} \right\}^2 - \left\{ \frac{q(t)}{2\pi r_2} \right\}^2 - \frac{N\omega(t)\Gamma(t)}{\pi} - \left\{ \frac{N\Gamma(t)}{2\pi r_2} \right\}^2 \right] \quad (7)$$

Since our analysis is limited to the case in which inlet flow to impeller has no prerotation, the increase in dynamic pressure at the outlet of the impeller is given by

$$\Delta p_d = \frac{\rho}{2} \left[ \left\{ \frac{q(t)}{2\pi r_2} \right\}^2 + \left\{ \frac{N\Gamma(t)}{2\pi r_2} \right\}^2 - \left\{ \frac{q(t)}{2\pi r_1} \right\}^2 \right] \quad (8)$$

Thus, total pressure rise per a stage of a pump,  $P(t)$ , is given as the sum of equation (7) and equation (8), and then becomes

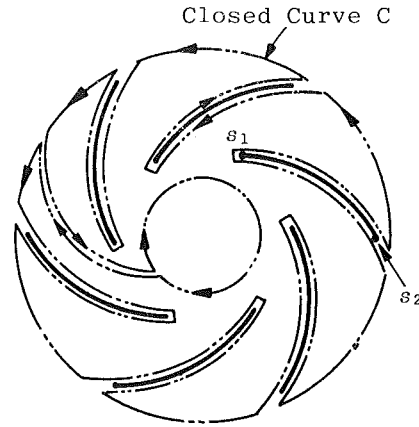


**Fig. 7 Control surface for considering pressure rise through cascade**

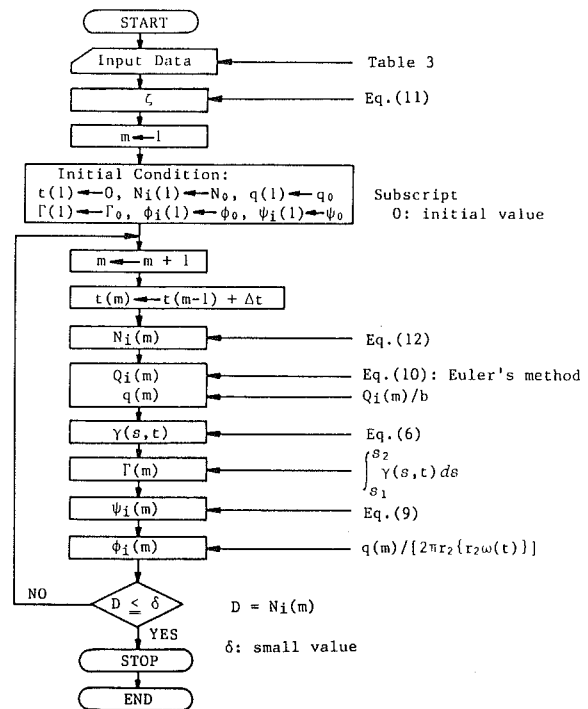


**Fig. 8 Calculating procedure**

$$\begin{aligned} \psi_i(t) &= P(t) / [\rho \{ r_2 \omega(t) \}^2 / 2] \\ &= N \left\{ \theta_2 \frac{d}{dt} \Gamma(t) - \frac{d}{dt} \int_{s_1}^{s_2} \gamma(s, t) \theta(s) ds \right\} \\ &\quad / \left[ \pi \{ r_2 \omega(t) \}^2 - N\Gamma(t) / \{ \pi r_2^2 \omega(t) \} \right] \quad (9) \end{aligned}$$

**Numerical Calculation.** Before going into the numerical calculations, the equation for determining the instantaneous flow-rate  $Q_i(t)$  should be derived. Assuming that the pump delivers no elevation head, the total pressure rise generated by pumping,  $P(t)$ , balances the pressure loss in the piping system,  $p_l(t)$ , and apparent pressure difference  $p_c(t)$  caused by the inertia of the water contained in the piping:

$$P(t) - p_l(t) + p_c(t) = 0$$

that is,

$$(\rho l_{eq} / A_0) \{ dQ_i(t) / dt \} + (\rho \zeta / 2) \{ Q_i(t) / A_0 \}^2 = P(t) \quad (10)$$

where,  $A_0$ : nominal flow area,  $l_{eq}$ : equivalent pipe length referred to area  $A_0$ , and  $\zeta$ : pressure loss coefficient which is

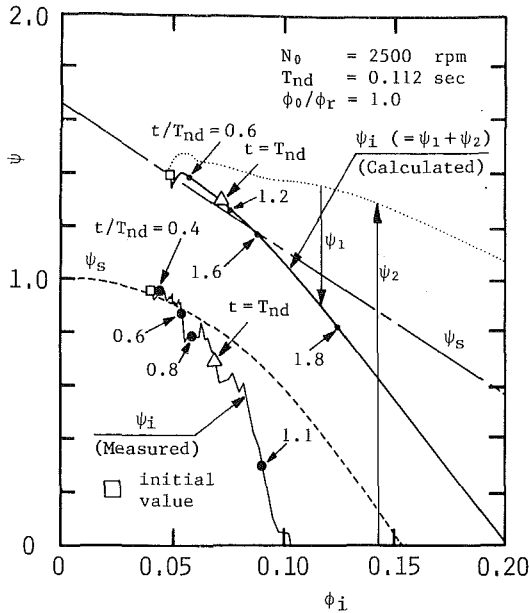


Fig. 9(a) Case 1

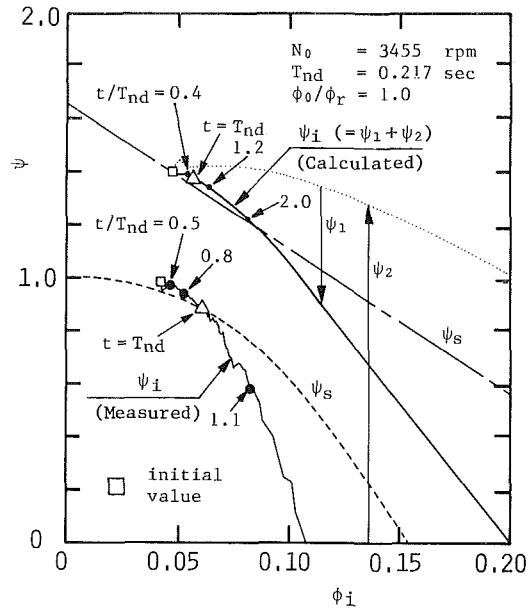


Fig. 9(b) Case 2

Fig. 9 Comparison between experimental and calculated dynamic characteristic curves during stopping period. Experimental uncertainty:  $\phi_i/\phi_0 \pm 5.5$  percent,  $\psi_i/\psi_0 \pm 5.5$  percent (20:1 odds).

determined by using equation (10) at the initial operating condition.

$$\zeta = \psi_0/\phi_0^2 \quad (11)$$

Table 3 shows the input data in the calculation of transient characteristics. As a stopping condition, the instantaneous rotational speed  $N_i(t)$  is assumed to follow

$$N_i(t) = N_0 \exp(-t/T_{nd}) \quad (12)$$

where initial rotational speed  $N_0$  and nominal deceleration time  $T_{nd}$  are the given parameters.

The numerical procedure is presented in Fig. 8. Starting from  $t=0$ , equation (10) is computed to obtain  $Q_i(t)$  as a function of time  $t$  by application of Euler's method [12], which is explicit and requires no additional starting values. Under the unsteady boundary condition expressed in equation (6) the circulation  $\Gamma$  is subsequently computed by the method mentioned previously. Finally total pressure rise by pumping is determined by equation (9). This procedure is repeated step by step in time till the rotational speed reaches zero.

## Discussion

**Comparison Between Theory and Experiment.** Figure 9 indicates the calculated and measured loci, along which the coordinates of  $\phi_i$  and  $\psi_i$  move during the stopping transient for Case 1 and 2. Time sequences as well as the point corresponding to nominal deceleration time  $T_{nd}$  are written in these figures in the same manner as in Fig. 4. The measured steady-state characteristic curve and the calculated one are indicated by a dash-line and a dot-dash-line, respectively.

Calculated total pressure rise coefficient  $\psi_i$  is here split into two parts; i.e.,  $\psi_1$  and  $\psi_2$ , as shown in Fig. 9. The  $\psi_1$  is the part contributed by the impulsive pressure difference between inlet and exit of an impeller, which is expressed by the first term in the right side of equation (9). This part of the pressure rise starts at zero, and then its absolute value increases with time.

The pressure rise designated as  $\psi_2$  is the part contributed by the relative and absolute velocity difference between inlet and

exit of an impeller, which is expressed by the second term in the right side of equation (9). This part of the pressure rise starts from the initial value  $\psi_0$ , and then the difference ( $\psi_2 - \psi_s$ ) increases with time. This is due to the fact that the circulation around impeller vanes cannot respond quickly to the rapid change in the circumferential condition, i.e., the lag in the circulation formation.

As seen clearly from these figures, the dynamic relationship between  $\phi_i$  and  $\psi_i$  is determined by the above two unsteady effects, i.e., the lag in circulation formation and the impulsive pressure difference. They have, however, an inverse tendency of deviation from a quasi-steady change.

At the very beginning of the stop, stage A in Fig. 4(a),  $\psi_i$  is greater than  $\psi_s$  since the lag in circulation formation is greater than the impulsive pressure difference, as seen clearly in these figures. Conversely, the impulsive pressure difference plays a predominant role in stage B where  $\psi_i$  is smaller than  $\psi_s$ .

From the comparison between Figs. 9(a) and (b), it is also found that  $|\psi_i|$  as well as  $(\psi_2 - \psi_s)$  at  $t = T_{nd}$  is greater in the quicker deceleration case than in the slower case. Therefore, the effect of unsteadiness on the pump characteristics increases with decreased  $N_0 T_{nd}$  so that the period on the quasi-steady characteristic curves becomes shorter.

Since the analysis was conducted on the basis of inviscid flow, i.e., 100 percent efficiency, the quantitative agreement between theory and experiment is poor. However, the calculated results agree qualitatively with the measured ones and offer a basis of explaining transient characteristics during the stopping period.

**Criterion for Quasi-Steady Change.** To get a critical deceleration rate beyond which the assumption of quasi-steady change becomes unacceptable, the following variable is introduced.

$$\Delta\psi = \int_{t=0}^{T_{nd}} |\psi_i - \psi_s| d\phi_i / \int_{t=0}^{T_{nd}} \psi_s d\phi_i \quad (13)$$

The above variable expresses the ratio of the deviation of water power from the quasi-steady one, to the quasi-steady

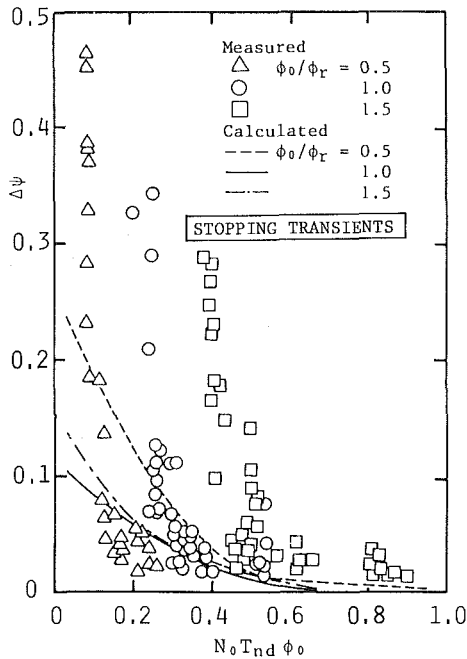


Fig. 10 Deviation of dynamic characteristics from quasi-steady ones during stopping period. Experimental uncertainty:  $\Delta\psi \pm 10.0$  percent.

one, and thus the smaller  $\Delta\psi$  implies the smaller deviation from the quasi-steady change.

After examining the relationship of  $\Delta\psi$  to  $N_0T_{nd}$  and  $\phi_0/\phi_r$ , it was found that the increase in  $N_0T_{nd}$  as well as  $\phi_0/\phi_r$  results in the decrease in  $\Delta\psi$ . Therefore, the relationships of  $\Delta\psi$  to  $N_0T_{nd}$  and  $\phi_0/\phi_r$  are rearranged as shown in Fig. 10. As can be seen in this figure, the greater  $N_0T_{nd}\phi_0$  results in the smaller  $\Delta\psi$ , i.e., smaller deviation from the quasi-steady. And it can be seen that the assumption of the quasi-steady change may be acceptable within the range of  $N_0T_{nd}\phi_0 > 0.6$  as far as the present test pump is concerned. A similar result is obtained for the starting problem as shown in the Appendix.

To check the validity of the above result, let us compare this with the ramp response of pressure rise to the changing flow-rate under a constant rotational speed  $n$ . According to a linearized dynamic model for turbopumps [2], dynamic variations in pressure rise across the pump,  $\Delta P$ , to the corresponding variations in instantaneous flow-rate  $\Delta Q$  may be formulated by the following equation written in Laplace transform notation

$$\Delta P/\Delta Q = R_p/(1 + Ts)$$

where,  $R_p = (\partial P/\partial Q)_{qs} \cong (\Delta P/\Delta Q)_{qs}$ : pump resistance,  $T = 1/\{0.2\pi(N\phi/\cos\lambda_R)n\}$ : pump time constant,  $\lambda_R$ : equivalent stagger angle of impeller cascade. When the flow-rate changes with  $dQ_i/dt = \Delta Q/\Delta T$ , the time lag in pressure response is  $T$ , and the deviation from the quasi-steady one becomes

$$D = (P - P_{qs})/(\Delta P)_{qs} = T/\Delta T$$

If  $D < 0.1$  is accepted as the dividing line between quasi-steady and dynamic pump operation, then the corresponding critical speed changing rate for the present test pump is given by

$$n\Delta T\phi > 0.78$$

The parameter  $n\Delta T\phi$  corresponds to the  $N_0T_{nd}\phi_0$  in the case of stopping, and the above parameter value is the same order as the one for the stopping transient.

Therefore, the parameter  $N_0T_{nd}\phi_0$  expresses the strength of unsteadiness at stopping, and the smaller its value, the greater the shift from a quasi-steady change.

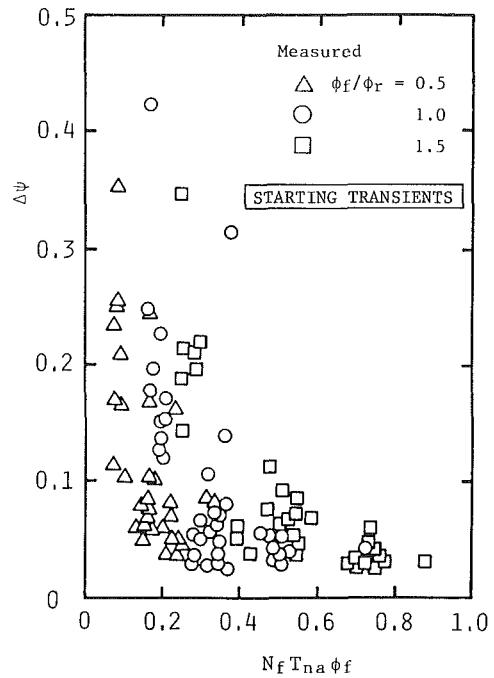


Fig. 11 Deviation of dynamic characteristics from quasi-steady ones during starting period. Experimental uncertainty:  $\Delta\psi \pm 10.0$  percent.

## Conclusion

The performance of a centrifugal pump during rapid deceleration of the rotational speed was studied experimentally and theoretically. When the pump is stopped quickly, the dynamic relationship between flow coefficient and total pressure rise coefficient does not coincide with the one obtained for steady-state operation.

The results of the numerical calculations were compared with the experiments, and then the following conclusions were found:

(1) At the very beginning of the stopping transient, the total pressure rise coefficient tends to become larger than the quasi-steady value. This is due to the lag in circulation formation around the impeller vanes.

(2) In the last half of the deceleration, the total pressure rise coefficient tends to be smaller than the quasi-steady value. The impulsive pressure difference is the primary reason of this tendency.

In addition to the above results, the nondimensional parameter  $N_0T_{nd}\phi_0$  was introduced as the parameter which determines the transient characteristics of a pump during the stopping period. A decrease in the above parameter results in a greater shift from a quasi-steady change. And the assumption of quasi-steady change may be acceptable within the range of  $N_0T_{nd}\phi_0 > 0.6$ .

## Acknowledgment

This study was supported by a Grant-in-Aid for Scientific Research by the Ministry of Education and the Harada Memorial Scholarship Foundation. The authors appreciate the dedicated assistance in the experimental work by Messrs. K. Takai, M. Nakamura, and K. Nagano.

## References

- Knapp, R. T., "Complete Characteristics of Centrifugal Pumps and Their Use in the Prediction of Transient Behavior," *TRANS. ASME*, Vol. 59, Nov. 1937, pp. 683-689.
- Ohashi, H., "Analytical and Experimental Study of Dynamic Characteristics of Turbopumps," NASA TN D-4298, Apr. 1968.
- Anderson, D. A., Blade, R. J., and Stevans, W., "Response of a Radial-



Bladed Centrifugal Pump to Sinusoidal Disturbances for Noncavitating Flow," NASA TN D-6556, Dec. 1971.

4 Brennen, C., and Acosta, A. J., "The Dynamic Transfer Function for a Cavitating Inducer," ASME JOURNAL OF FLUIDS ENGINEERING, Vol. 98, No. 2, June 1976, pp. 182-191.

5 Kaneko, M., and Ohashi, H., "Transient Characteristics of a Centrifugal Pump During Quick Change of Flow Rate," *Trans. JSME*, Ser. B, Vol. 48, No. 426, Feb. 1982, pp. 229-237 (in Japanese).

6 Tsukamoto, H., and Ohashi, H., "Transient Characteristics of a Centrifugal Pump During Starting Period," ASME JOURNAL OF FLUIDS ENGINEERING, Vol. 104, No. 1, Mar. 1982, pp. 6-14.

7 Saito, S., "The Transient Characteristics of a Pump During Start Up," *Bulletin of JSME*, Vol. 25, No. 201, Mar. 1983, pp. 372-379.

8 Ohashi, H., Tsukamoto, H., Kaneko, M., and Shoji, H., "Dynamic Performance and Impeller Force of Turbopumps in Unsteady Operation," *Proceedings of China-Japan Joint Conference on Hydraulic Machine and Equipment*, Hangzhou, Oct. 1984, pp. 307-318.

9 Tobias, S. A., *Machine-Tool Vibration*, Blackie, 1965, pp. 39-44.

10 Imaichi, K., Tsujimoto, Y., and Yoshida, Y., "An Analysis of Unsteady Torque on a Two-Dimensional Radial Impeller," ASME JOURNAL OF FLUIDS ENGINEERING, Vol. 104, No. 2, June 1982, pp. 228-234.

11 Milne-Thomson, L. M., *Theoretical Hydrodynamics*, 5th ed., Macmillan, 1968, p. 89.

12 Lambert, J. D., *Computational Methods in Ordinary Differential Equations*, Wiley, 1973, pp. 114-116.

## APPENDIX

Dynamic characteristics during starting period are compared with the quasi-steady ones in the manner similar to Fig. 10. The deviation of dynamic from quasi-steady performance is related to the parameter  $N_f T_{na} \phi_f$  as shown in Fig. 11. Here,  $N_f$  is final rotational speed,  $T_{na}$  is nominal acceleration time [6],  $\phi_f$  is final flow coefficient, and  $\Delta\psi$  is defined by

$$\Delta\psi = \int_{t=T_{na}/2}^{T_{na}} |\psi_i - \psi_s| d\phi_i / \int_{t=T_{na}/2}^{T_{na}} \psi_s d\phi_i$$

The parameter  $N_f T_{na} \phi_f$  expresses the strength of unsteadiness at start up, and its smaller value leads to a bigger shift of dynamic performance from the quasi-steady one. As can be seen from this figure, the assumption of the quasi-steady change may be acceptable within the range of  $N_f T_{na} \phi_f > 0.6$  as far as the present test pump is concerned.

# A Simplified Free Wake Method for Horizontal-Axis Wind Turbine Performance Prediction

A. A. Afjeh  
Assistant Professor.

T. G. Keith Jr.  
Professor.

Department of Mechanical Engineering,  
University of Toledo,  
Toledo, Ohio

*Based on the assumption that wake geometry of a horizontal-axis wind turbine closely resembles that of a hovering helicopter, a method is presented for predicting the performance of a horizontal-axis wind turbine. A vortex method is used in which the wake is composed of an intense tip-vortex and a diffused inboard wake. Performance parameters are calculated by application of the Biot-Savart law along with the Kutta-Joukowski theorem. Predictions are shown to compare favorably with values from a more complicated full free wake analysis and with existing experimental data, but require more computational effort than an existing fast free wake method.*

## Introduction

Because of the complex nature of the flowfield in which horizontal-axis wind turbines must function, determination of the aerodynamic performance can be quite difficult. Development of a method for predicting machine performance over the complete range of wind speeds without recourse to certain simplifying assumptions is doubtful. Clearly, accuracy of the performance estimates depends largely on the validity of the assumptions employed and on the rigor of the method of analysis adopted.

Methods concerned with the prediction of aerodynamic loading and performance of wind turbines have been reviewed in a number of places, e.g., see DeVries [1] and [2]. In general these methods have been developed by modifying conventional propeller and/or helicopter theories. Classification of the methods is based on the manner in which the induced velocity at a blade section is evaluated.

Simple blade element-momentum/theories (strip theories) replace the rotor with an actuator disk having an infinite number of blades. The induced velocity at a blade section is evaluated from streamtube momentum considerations assuming the flow to be planar or without swirl. All blade sections are assumed to operate independently of each other. Strip theory methods, e.g., that of Wilson and Walker [3], are simple to use, require little computer time and provide accurate results. Hence, these methods are quite popular. However, it has been found that an empirical correction to the methods is required for computations when the wind turbine operation is in the vortex ring state.

Vortex theories are more involved as the induced velocity is determined from an analysis of the flowfield created by the vortex system in the rotor wake, refer to Jeng et al. [4]. Vortex methods can account for a finite number of blades and can ac-

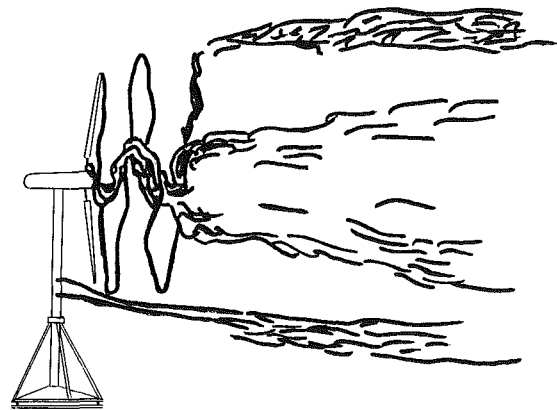


Fig. 1 Sketch of flow pattern of a full scale wind turbine operating under low power generation conditions, Savino and Nyland, [9]

count for blade span effects (lifting line theories) or for blade chord effects (lifting surface theories).

Analysis, by either blade-element/momentum theory or by vortex theory, reveals that the induced velocity far downstream of the rotor differs from that at the rotor disk. Consequently, the blade wake size must change: expand or contract depending on the sign of the induced velocity. On the other hand, if the freestream velocity, which is the primary factor in establishing the mass flow rate into the wake, is high, wake deformation effects are negligible. The freestream velocity also transports the tip-vortex away from the plane of the rotor so that for high wind speeds, relative to the tangential velocities of rotation at the rotor tip, it is far removed from the tip-vortex of the following blade. Thus, interaction effects are minimized.

The method of analysis for an unconstrained wake of a rotor is referred to as a free wake method (FWM). Landgrebe [5, 6] and Gray [7] developed free wake models of a hovering helicopter. Gohard [8] developed a FWM for horizontal-axis wind turbines. Unfortunately, the latter analysis requires large amounts of computer time making it somewhat impractical as

Contributed by the Fluids Engineering Division for presentation at the Applied Mechanics, Biomechanics, and Fluids Engineering Conference, Cincinnati, Ohio, June 21-24 of THE AMERICAN SOCIETY OF MECHANICAL ENGINEERS. Manuscript received by the Fluids Engineering Division April 26, 1985. Paper No. 87-FE-1.

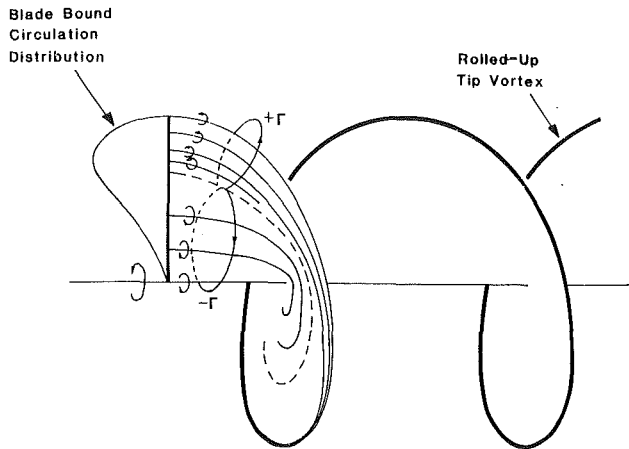


Fig. 2 Physical model of the flowfield

a design tool. To remedy the problem, a rigid wake is often assumed to replace the actual wake. But such wake models are generally limited to relatively low values of tip-speed ratio (tangential over freestream velocity) where wake deformation effects are negligible.

Although a detailed experimental study of the wake of a wind turbine has yet to be undertaken, a qualitative study of the flowfield of a full-scale wind turbine was performed by Savino and Nyland, [9]. The study included smoke flow visualization of the wake of a wind turbine at zero and low power generating conditions. In the experiment, four smoke grenades, two for tip and root vortices and two for the freestream flow, were used. The grenades in the freestream were located on a cable upstream of the rotor. Photographs of the smoke traces were recorded with two movie cameras as well as a still camera. Figure 1 is a sketch of the flow pattern for low power generating conditions.

In light of the preceding discussion, it was felt that a simple method capable of accounting for the wake deformation and wake expansion behind the wind turbine would be of value. The method that evolved is based on vortex theory and attempts to model the physics of the flow to the extent possible. Even though the flow visualization studies of [9] have clearly shown the existence of a tip-vortex and an expanding inboard wake, detailed data on the structure of the wake of a wind turbine is still lacking. For this reason, the model developed was

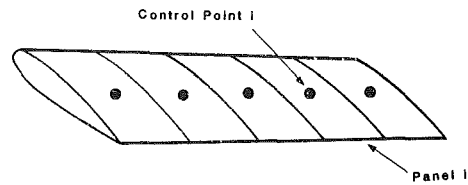


Fig. 3 Blade panel and control point arrangement

made consistent with the experimentally observed wake of hovering helicopters. The approach was termed a simplified free wake method (SFWM).

The concept of developing a performance prediction method based on a model of the rotor wake is not new. In fact, a few other rotor wake approximation techniques have been described in the literature. Most notable among these is the fast free wake method (FFWM) of Miller. The FFWM and its variants have been described in a substantial series of papers and reports, viz., Miller [10-14]. The SFWM and FFWM differ in the modeling approach used. Some of these differences will emerge when the two methods are used to compute the performance of a wind turbine later in the paper.

## Analysis

**Physics of the Flow and Model Development.** The local air velocity relative to a rotor blade consists of the free-stream velocity, that due to the blade motion and the wake induced velocities. In order to predict the inflow at the blades, it is necessary to describe the blade surfaces and the wake. The blades are simply lifting surfaces of finite span. The wake consists of trailing streamwise vorticity which results from spanwise variation in loading. These trailing vortex filaments lie in a generally helical contour due to the rotor rotation, and distort under their own self-induced effects as well as the influence of other filaments. The resulting wake may be broadly viewed as composed of two regions: an intense tip-vortex outer region and a weak diffused vortex sheet inner region. Vortex filaments that emanate from radial locations beyond the point of maximum bound circulation outward to the blade tip are assumed to unite to form a strong tip-vortex. Trailing vortices from the point of maximum bound circulation inward to the blade hub are assumed to form a diffused vortex sheet. This wake arrangement is shown in Fig. 2.

The complexity of the flowfield precludes any hope of a closed form solution; hence a numerical method employing a

## Nomenclature

$c$ = blade chord	$r$ = distance along the blade	
$C_D$ = drag coefficient	$\mathbf{r}$ = position vector	
$C_F$ = axial force (thrust) coefficient	$r_1, r_2$ = magnitude of vectors $\mathbf{r}_1, \mathbf{r}_2$ defined in Fig. 5	$\alpha$ = angle of attack
$C_L$ = lift coefficient	$R$ = radius of blade	$\alpha_e$ = effective angle of attack
$C_p$ = power coefficient	$s$ = vortex filament position vector	$\alpha_s$ = stall angle of attack
$F$ = axial force on wind turbine	$s$ = length of vortex filament	$\Gamma$ = circulation
$\hat{i}, \hat{j}, \hat{k}$ = unit vectors in $x, y$ and $z$ directions	$V_0$ = wind velocity	$\epsilon$ = viscous core radius
$L$ = magnitude of position vector $\mathbf{L}$ defined in Fig. 5	$\mathbf{w}_i$ = induced velocity vector	$\theta$ = azimuthal angle
$N$ = number of blades	$w_{ix}, w_{iy}, w_{iz}$ = $x, y, z$ components of $\mathbf{w}_i$	$\phi$ = flow angle
$P$ = power	$W$ = resultant velocity	$\rho$ = density
$\mathbf{q}_i$ = localized induced velocity	$x, y, z$ = rectangular coordinates of a point, refer to Fig. 4	$\psi$ = coning angle
$q_{ix}, q_{iy}, q_{iz}$ = $x, y, z$ components of $\mathbf{q}_i$		$\Omega$ = rotational speed
$Q$ = torque		

## Abbreviations

FFWM = fast free wake method
FWM = free wake method
SFWM = simplified free wake method

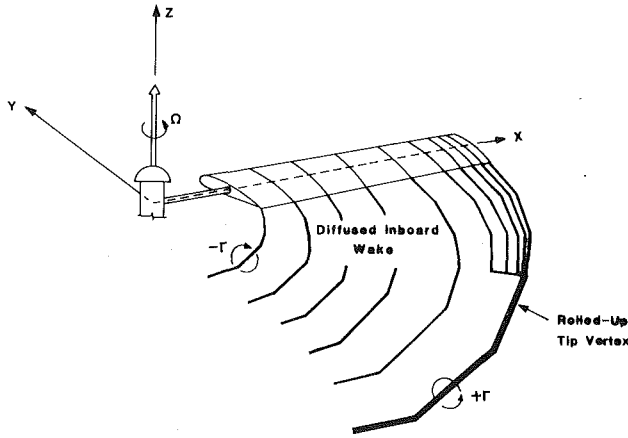


Fig. 4 Approximate representation of the rotor wake

vortex panel technique is used. The numerical model for the blade consists of radially distributed panels, each of which is considered as having a constant vortex strength. Each resulting panel contains a control point located on the local chord at  $x + \Delta x/2$  for the segment between  $x$  and  $x + \Delta x$ . The arrangements of panels and control points are depicted in Fig. 3. The panel is spanned by a straight-line vortex segment located  $1/4$  chord back from the leading edge. One requirement of this piece-wise constant representation is that the spanwise segments be small enough so that any chord variation or blade twist is adequately represented by straight-line segments between  $x$  and  $x + \Delta x$ . Typical wind turbine rotors will fulfill this requirement adequately except perhaps at the blade-tips.

The wake consists of a system of trailing vortices, the strength of which reflects any spanwise variation in loading. The strength of each vortex in the wake is assumed to be constant, equal in value to the difference in bound vortex strength on either side of it. The wake contains a finite number of points whose motion describes vortex end-point deformation. These points are taken to be connected by straight-line vortex segments which represented the disturbance. No deformation of these segments from a straight line is permitted. The induced velocity at the end points is computed by application of the Biot-Savart law.

In this simplified vortex analysis, the wake is divided axially into two parts: a near wake and a far wake. The near wake consists of the first  $\pi$  radians of azimuthal displacement. No deformation of this wake vortex is allowed. The vortex filaments trailing from outboard blade sections, i.e., from the point of maximum circulation to the blade tip, are assumed to roll-up to form a strong tip-vortex. In the present analysis, it is assumed that this roll-up occurs almost immediately. Consequently, the far wake will consist of an inboard wake in which trailing vortex filaments follow a helical path and a rolled-up strong tip-vortex which is permitted to deform. The inboard wake vortices are assumed to move with local azimuthally averaged velocities at the rotor plane. The vortex wake is truncated after a few revolutions. A sketch of the flow model of the wake used in the computations is provided in Fig. 4.

As mentioned, the blade surfaces are replaced by a number of spanwise panels, each spanning a straight line vortex of constant strength. The trailing vortices are laid down in a finite number of straight-line segments which describe the wake motion. Hence, at a point in space and time, the disturbance flowfield is that due to a number of straight-line vortex segments.

**Formulation of Governing Equations.** According to the

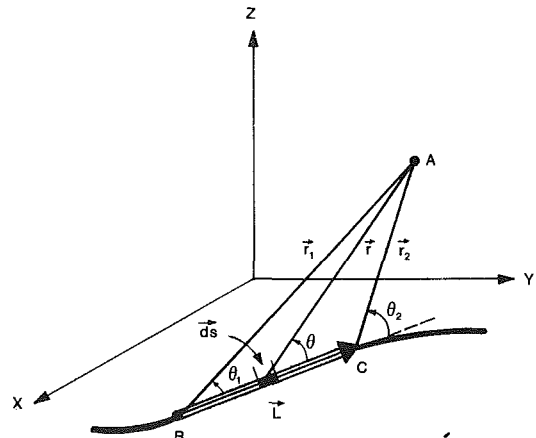


Fig. 5 Nomenclature used in the induced velocity calculation at a point due to a straight line vortex filament

Biot-Savart law, the increment of induced velocity at point A in Fig. 5 due to a vortex of differential length is

$$dw_i = \frac{\Gamma}{4\pi} \frac{ds \times \mathbf{r}}{r^3} \quad (1)$$

where  $ds$  is an element of the vortex of strength  $\Gamma$  and  $\mathbf{r}$  is the position vector from point A to the element  $ds$ . Hence, the induced velocity due to a straight line vortex with end points at B and C, see Fig. 5, is obtained by integrating equation (1) over the length of the vortex line. The components of this velocity are given in a Cartesian coordinate system by

$$w_{ix}(A) = \frac{\Gamma(r_1 + r_2)}{2\pi r_1 r_2 [(r_1 + r_2)^2 - L^2]} [(y_A - y_C)(z_C - z_B) - (z_A - z_C)(y_C - y_B)] \quad (2)$$

$$w_{iy}(A) = \frac{\Gamma(r_1 + r_2)}{2\pi r_1 r_2 [(r_1 + r_2)^2 - L^2]} [(z_A - z_C)(x_C - x_B) - (x_A - x_C)(z_C - z_B)] \quad (3)$$

$$w_{iz}(A) = \frac{\Gamma(r_1 + r_2)}{2\pi r_1 r_2 [(r_1 + r_2)^2 - L^2]} [(x_A - x_C)(y_C - y_B) - (y_A - y_C)(x_C - x_B)] \quad (4)$$

where

$$r_1 = [(x_A - x_B)^2 + (y_A - y_B)^2 + (z_A - z_B)^2]^{1/2}$$

$$r_2 = [(x_A - x_C)^2 + (y_A - y_C)^2 + (z_A - z_C)^2]^{1/2}$$

$$L = [(x_C - x_B)^2 + (y_C - y_B)^2 + (z_C - z_B)^2]^{1/2}$$

Superposition of the results of equations (2), (3), and (4) for all the elements of the vortex representing the blade and wake give the components of disturbance velocity at any point in the field.

The self-induced velocity has been found to be, e.g., see Hama [15] or Arms and Hama [16],

$$\mathbf{q}_i = - \frac{\Gamma \left( \frac{\partial \mathbf{r}}{\partial s} \right) \times \left( \frac{\partial^2 \mathbf{r}}{\partial s^2} \right)}{4\pi \left| \frac{\partial \mathbf{r}}{\partial s} \right|^3} \ln \epsilon \quad (5)$$

where  $\mathbf{r}$  = the position vector of a point on the vortex filament  $ds$ , and  $\epsilon$  = effective core radius.



**Table 1 Blade geometry and operating conditions for numerical comparisons**

Case	Solidity	Speed ratio	Pitch angle degrees	Chord distribution
	$\frac{Nc}{\pi R}$	$\frac{V_0}{R\Omega}$		
1	0.106	0.105	2	constant
2	0.106	0.154	0	constant
3	0.106	0.154	2	constant
4	0.106	0.154	4	constant

For a continuous vortex filament, both  $\partial \mathbf{r} / \partial s$  and  $\partial^2 \mathbf{r} / \partial s^2$  can be readily determined. For the numerical problem, with the vortex filaments being approximated by a finite number of points, these derivatives can be written at a field point in terms of the coordinates of the field point and the coordinates of adjacent field points. If  $\mathbf{r}$  is the position vector of the vortex filament, and if  $\mathbf{r}_A$ ,  $\mathbf{r}_B$ , and  $\mathbf{r}_C$  are the locations of three adjacent points in the positive direction of the filament  $ds$ , then a Taylor series expansion about point B can be used to represent  $r_A$  and  $r_C$

$$\mathbf{r}_{A,C} = \mathbf{r}_B \pm \left. \frac{\partial \mathbf{r}}{\partial s} \right|_{\mathbf{r}_B} \Delta s_{1,2} + \left. \frac{\partial^2 \mathbf{r}}{\partial s^2} \right|_{\mathbf{r}_B} \frac{(\Delta s_{1,2})^2}{2} \quad (6)$$

where  $\Delta s_1 = |\mathbf{r}_A - \mathbf{r}_B|$ ,  $\Delta s_2 = |\mathbf{r}_C - \mathbf{r}_B|$  and the + and - signs are associated with  $\mathbf{r}_C$  and  $\mathbf{r}_A$ , respectively ( $\mathbf{r}_C$  lies on the positive side of  $\mathbf{r}_B$ ,  $\mathbf{r}_A$  on the negative side). Eliminating one derivative at a time from the pair of equations produces the following which for numerical purposes is written in Cartesian coordinates

$$\begin{aligned} \frac{\partial^k \mathbf{r}}{\partial s^k} = & \frac{2^{k-1}}{(\Delta s_1 + \Delta s_2)} \left\{ \frac{\Delta s_1^{2-k}}{\Delta s_2} [(x_C - x_B)\hat{i} + (y_C - y_B)\hat{j} \right. \\ & \left. + (z_C - z_B)\hat{k}] \right\} \\ & + (-1)^k \frac{\Delta s_2^{2-k}}{\Delta s_1} \\ & \left\{ (x_A - x_B)\hat{i} + (y_A - y_B)\hat{j} + (z_A - z_B)\hat{k} \right\} \end{aligned} \quad (7)$$

where  $k=1$  or  $2$ .

These results can now be employed in equation (5) to obtain the self-induced velocity at point B. The  $x$  component of this velocity is

$$\begin{aligned} q_{ix} = & \frac{-\Gamma(\Delta s_1 + \Delta s_2)^2 \ln e}{2\pi \Delta s_1 \Delta s_2} \{ (\Delta s_1)^2 + (\Delta s_2)^2 \\ & - 2[(x_C - x_B)(x_A - x_B) + (y_C - y_B)(y_A - y_B) \\ & + (z_C - z_B)(z_A - z_B)] \}^{-3/2} [(y_C - y_B)(z_A - z_B) \\ & - (y_A - y_B)(z_C - z_B)] \end{aligned} \quad (8)$$

Similar equations can be developed for  $q_{iy}$  and  $q_{iz}$ .

**Numerical Procedure.** The numerical procedure for the SFWM begins with an assumed undeformed wake geometry and circulation distribution. A starting value is generated using spanwise momentum theory, refer to McCormick [17]. A second value is then obtained using a non-expanding wake analysis. The wake is assumed to consist of helical vortices trailing from the blade. The helical path of a trailing vortex filament is approximated by a series of points connected by straight lines. Pitch of the helix and convective velocity of the wake are assumed to be the local values of corresponding parameters at the trailing edge of the blade. Radial flow is

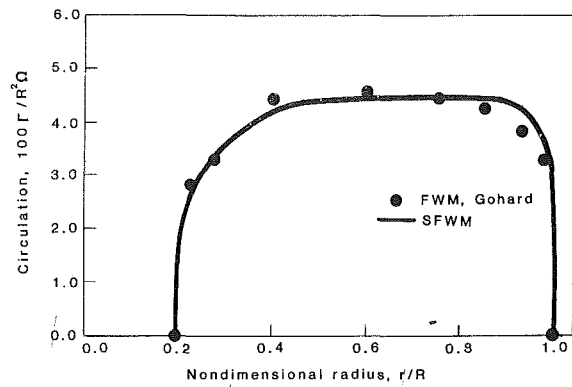


**Fig. 6 Computed nondimensional circulation distribution along the blade for case 2 conditions, Table 1**

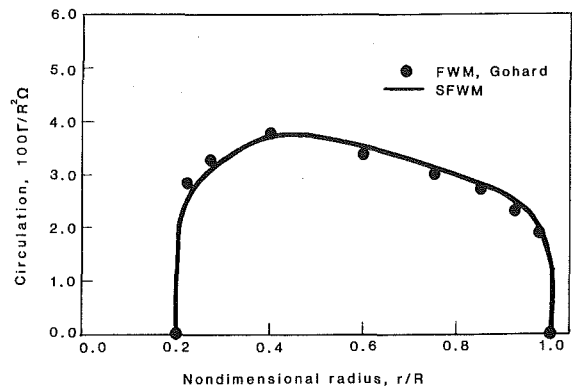


**Fig. 7 Computed nondimensional circulation distribution along the blade for case 4 conditions, Table 1**

neglected, however, the distribution of axial component of disturbance velocity is found using an iterative method. Results of this analysis form the initial value of parameters for the loop on wake deformation and distortion.

The actual deformed wake geometry is computed employing an iterative method. The initial values of wake displacement are calculated using the non-rigid wake induced flowfield. A new wake geometry and its corresponding induced flowfield are then calculated. The wake geometry is updated and calculations are repeated until a consistent wake geometry-induced flow is established.

The last phase of the computations consists of calculations of blade forces and performance. This procedure is rather straightforward. The necessary equations are given as follows

$$F = \int_{r_{\text{hub}}}^{r_{\text{tip}}} 1/2\rho Nc W^2 (C_L \cos\phi + C_D \sin\phi) dr \quad (9)$$

$$Q = \int_{r_{\text{hub}}}^{r_{\text{tip}}} 1/2\rho Nc W^2 (C_L \sin\phi - C_D \cos\phi) r dr \quad (10)$$

$$P = \int_{r_{\text{hub}}}^{r_{\text{tip}}} 1/2\rho Nc W^2 (C_L \sin\phi - C_D \cos\phi) r \Omega dr \quad (11)$$

where  $\phi$  is the flow angle. The effect of blade coning can be included by replacing  $r$  in the above equations with  $r \cos\psi$ , where  $\psi$  is the coning angle.

## Results and Discussions

**Comparison With Existing Numerical Data.** The theoretical aerodynamic loadings and performance of a number of rotor configurations were computed using the numerical procedure. The blade geometries and operating

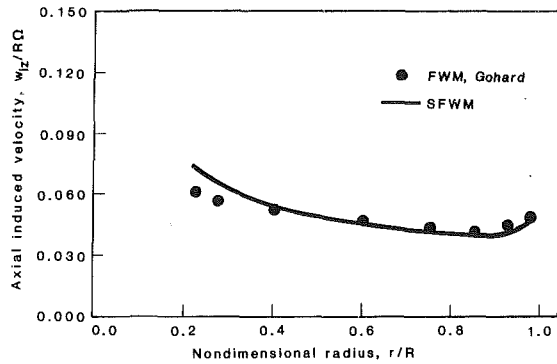


Fig. 8 Computed spanwise axial induced velocity distribution along the blade for case 2 conditions, Table 1

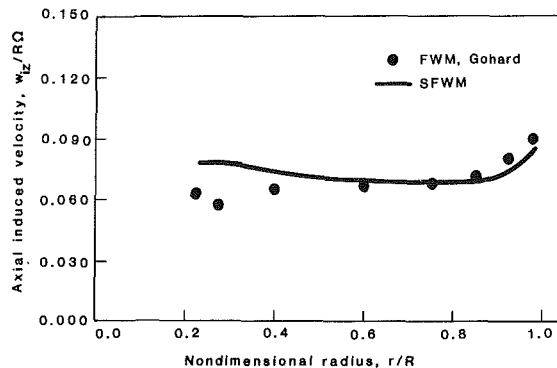


Fig. 9 Computed spanwise axial induced velocity distribution along the blade for case 4 conditions, Table 1

conditions are presented in Table 1. The airfoil data used in the calculations are given in equation form as:

if  $\alpha < \alpha_s = 0.2 \text{ rad} (11.45^\circ)$

$$C_L = 2\pi\alpha, \quad C_D = 0.01 + 0.5\alpha^2 \quad (12)$$

if  $\alpha \geq \alpha_s$

$$C_L = 2\pi\alpha_s, \quad C_D = 0.01 + 0.5\alpha_s^2 \quad (13)$$

This particular set of rotor configurations and airfoil data were used in order to make possible direct comparisons with the FWM results of Gohard, [8]. Results for only three aerodynamic quantities, namely, the circulation distribution, the axial induced velocity distribution and the effective angle of attack distribution are presented for these numerical comparisons. Only results for cases 2 and 4 will be given herein. Results for the other two cases are comparable to those shown and can be found in Afjeh [18]. The nondimensional circulation distributions,  $(\Gamma/\Omega R^2)$  along the blade for the operating conditions for cases 2 and 4 are compared with those of Gohard in Figs. 6 to 7, respectively. It is seen that the computed results agree favorably with those of Gohard's FWM. The differences are attributed to the different modeling of the outboard trailing vortices. It should be borne in mind that the continuous vorticity of the vortex sheet is approximated by vortex filaments that have concentrated vorticity. Moreover, since the wake geometry calculations take an appreciably long time, only a low number of trailing vortex filaments were considered. If the number of the filaments is increased the intensity and the location of the circulation peaks may be altered. This is believed to improve the results of the present model.

The spanwise axial induced velocity distributions for the two cases considered are shown in Figs. 8 and 9. It is seen that the SFWM results are slightly lower than those of Gohard. These results are consistent with the results obtained for the circulation distribution.

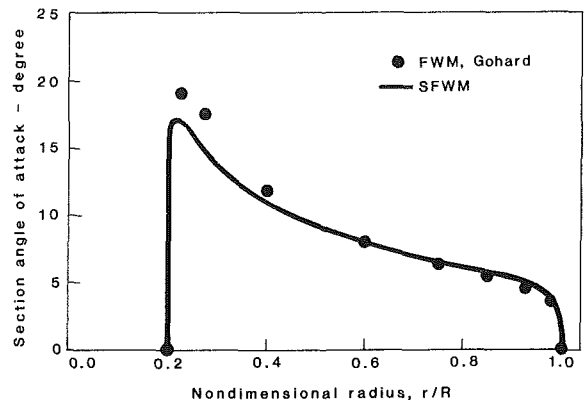


Fig. 10 Computed effective angle of attack distribution along the blade for case 2 conditions, Table 1

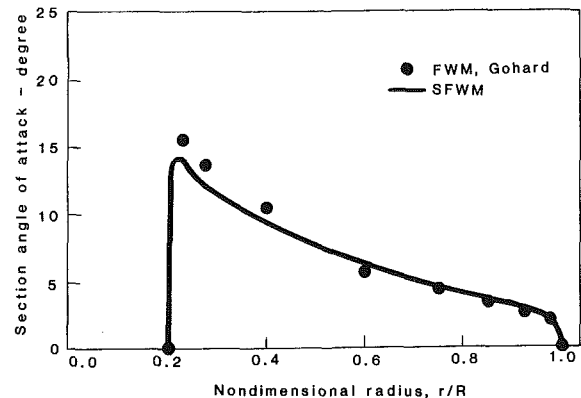


Fig. 11 Computed effective angle of attack distribution along the blade for case 4 conditions, Table 1

Table 2 Comparison of power coefficients and axial force (thrust) coefficients

	Case	FWM Gohard [8]	SFWM
$C_P = \frac{P}{\frac{1}{2}\rho\pi R^2 V_0^3}$	1	0.3489	0.417
	2	0.4575	0.454
	3	0.4609	0.473
	4	0.4379	0.451
$C_F = \frac{F}{\frac{1}{2}\rho\pi R^2 V_0^2}$	1	1.0762	1.144
	2	1.1145	1.103
	3	0.9527	0.959
	4	0.7964	0.803

Plots of the effective angle of attack distribution for the two operating conditions are provided in Figs. 10 and 11. It should be recalled that below stall the effective angle of attack distribution along the blade is proportional to the circulation distribution. The degree of dissimilarity between the distribution of the effective angle of attack,  $\alpha_e$ , and the distribution of circulation,  $\Gamma$ , is due to the variation of lift coefficient against the effective angle of attack (since there is no variation of chord along the span). The drastic changes in the plot of the  $\alpha_e$  distribution are due to the discontinuity of the slope of the lift curve at the stall angle,  $\alpha_s$ .

The total integrated power and thrust coefficients calculated by different methods of analysis are contained in Table 2. It is seen that the results of the SFWM agree well with those of [8] except for Case 1. This discrepancy is attributed, in part, to the possible improper determination of the location and the intensity of maximum circulation. For this case the wind

**Table 3 Blade geometry and operating condition of MOD-OA for experimental comparisons**

Blade radius = 19.05 m RPM = 40			
% Blade radius	twist (degree)	chord (m)	thickness to chord ratio
22.4	4.2	1.58	0.295
32.0	3.43	1.44	0.269
41.8	2.65	1.345	0.243
51.5	1.87	1.228	0.218
61.2	1.10	1.11	0.192
70.9	0.33	0.994	0.166
80.6	0.45	0.875	0.140
90.3	-1.23	0.759	0.115
100.0	-2.0	0.64	0.090

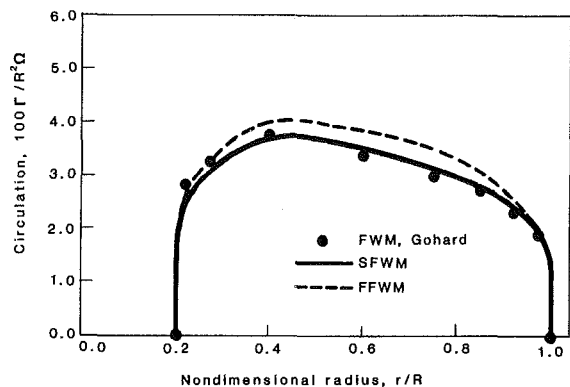


**Fig. 12 Computed nondimensional circulation distribution along the blade by three different methods for case 2 conditions, Table 1**

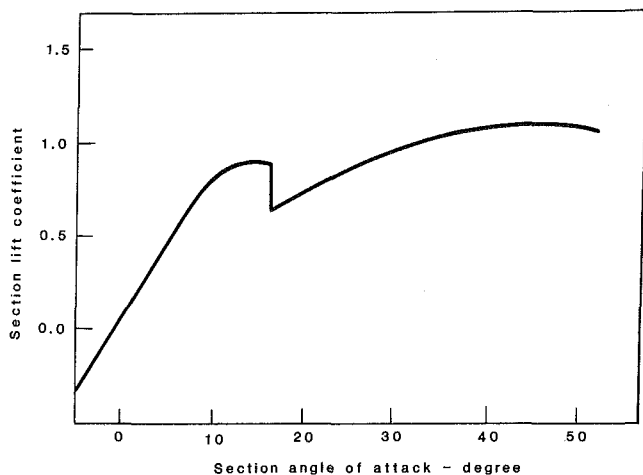


**Fig. 13 Lift coefficient versus angle of attack for a NACA 23024 airfoil**

velocity is low, hence, wake vortices remain in the vicinity of the rotor plane thereby greatly influencing the rotor induced flow. Consequently, a larger number of computation nodes on the blade (and therefore a larger number of trailing vortices) is required to represent the wake sheet more accurately.

Because the SFWM shares some of the same concepts as Miller's FFWM it is of some importance to contrast the methods. Both methods represent the rotor wake through a series of approximations applicable to different portions of the wake. In the FFWM, the wake is divided into three parts: a near wake region, an intermediate region, and a far wake region. Miller has developed both a three dimensional model which uses a series of vortex rings and cylinders and a two dimensional model which uses a pair of doubly infinite line vortices. In the SFWM, the wake is divided into near wake and

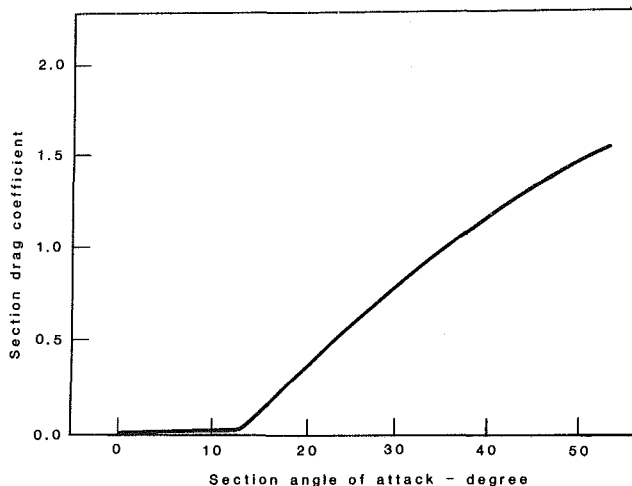


**Fig. 14 Drag coefficient versus angle of attack for a NACA 23024 airfoil**

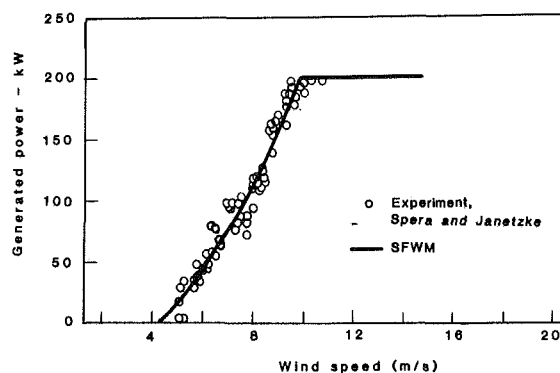


**Fig. 15 Comparison of experimental generated power versus wind speed with SFWM predictions**

far wake regions. Both contain inboard and outboard regions. However, it was found that overall performance and computed wake geometry are not affected appreciably by the inboard far wake. Omission of this region resulted in a computational savings.

Figure 12 was drawn in order to compare the predictions of the FFWM and the SFWM. This plot is the same as that of Fig. 6 only here the FFWM predictions have also been included. It can be seen that for this case the circulation distribution predicted by the SFWM is in better agreement with Gohard's results than are the FFWM predictions. Similar results were found for the other cases in Table 1 as well as for other computations. These other comparisons are presented in Afjeh [18]. On the other hand, the FFWM offers definite computer time savings. The average FFWM solution required approximately 30 seconds of CPU time whereas the SFWM solution required more than two minutes for the same problem.

**Comparisons With Experimental Data.** The total integrated performance of a more complicated rotor geometry with varying twist distribution and chord distribution was investigated to further verify the accuracy of the SFWM. The experimental data was obtained by Spera and Janetzke, [19] from a 200 kw wind turbine at the Plum Brook station in Sandusky, Ohio. Table 3 contains the pertinent rotor data and Figs. 13 and 14 are the lift and drag coefficients that were used in the calculations. Prestall coefficients were taken from Abbott and vonDoenhoff [20] and represent the average of rough and smooth airfoil data. Poststall coefficients represent an approximate modeling of this very complicated flow regime (refer to Afjeh [18]). A comparison of computed performance

against measured performance is shown in Fig. 15. It should be noted that drive train losses and generator efficiencies have been accounted for through the following empirical expression.

$$(\text{generated power}) = 0.945(\text{rotor power}) - 0.051(\text{rated power})$$

Examination of Fig. 15 reveals that the total integrated generated power is predicted very closely to the midpoint of the experimental data. As expected, however, the agreement is not as good for very low wind velocities. This is due to the fact that under these conditions the tip-vortex interaction effects are appreciable. The lifting line assumption is no longer valid for the sections close to the blade-tip under these operating conditions since large variations occur in the chordwise pressure distribution. The generated power curve for experimental data in Fig. 15 flattens out at the rated power as a result of the automatic tip control system employed. This is done by suitably changing the section pitch angle via a computer assisted control system. The power output of the alternator is monitored by this computer and the pitch is decreased so as to maintain the alternator power constant at the rated value.

### Concluding Remarks

The present investigation has adopted a simplified wake model for horizontal axis wind turbines coupled with numerical computations to study the aerodynamic loadings and performance of wind turbines. Detailed calculated results of performance parameters have been presented. Comparison of the results of a free wake analysis with those of the present model reveals that accurate results can be obtained, for operating conditions considered, with substantial savings of computer time. A typical run took approximately 2.5 minutes on the NAS 6650 computer system. This is more computer time than required by a companion fast free wake method but produced better agreement with an existing full free wake analysis. Although the present method of quantifying wind turbine performance may be expected to be less accurate than a full free wake method, it is encouraging to observe that a considerable degree of consistency exists between the results of the two methods. That the present method is a satisfactory predictor of aerodynamic performance of horizontal axis wind turbines is further supported by the experimental data.

### Acknowledgment

The research contained in this paper was performed under the auspices of the Wind Energy Section of the NASA Lewis Research Center, Cooperative Agreement No. NCC 3-5. The authors wish to thank Dr. Joseph Savino for the many helpful

discussions and encouragements throughout the course of their work.

### References

- 1 DeVries, O., "On the Theory of Horizontal-Axis Wind Turbines," *Annual Review of Fluid Mechanics*, Vol. 15, 1983, pp. 77-96.
- 2 DeVries, O., "Fluid Dynamic Aspects of Wind Energy Conversion," AGARDograph No. 243, July 1979.
- 3 Wilson, R. E., and Walker, S. N., "A Fortran Program for the Determination of Performance, Load and Stability Derivatives of Windmills," Dept. of Mechanical Engineering, Oregon State University. (RANN), Under Grant No. G1-41840, Oct. 25, 1974.
- 4 Jeng, D. R., Keith, T. G., and Aliakbarkhanafjeh, A., "Aerodynamic Analysis of a Horizontal-Axis Wind Turbine by Use of Helical Vortex Theory, Volume I: Theory," NASA CR-168054, Dec. 1982.
- 5 Landgrebe, A. J., "An Analytical and Experimental Investigation of Helicopter Rotor Hover Performance and Wake Geometry Characteristics," USAAMRDL Tech. Report 71-24, US Army Air Mobility Research and Development Lab., Fort Eustis, June 1971.
- 6 Landgrebe, A. J., "An Analytical Method of Predicting Rotor Wake Geometry," *J. of American Helicopter Society*, Vol. 14, No. 4, 1969.
- 7 Gray, R. B., and Brown, G. W., "A Vortex Wake Analysis of a Single-Bladed Hovering Rotor and a Comparison with Experimental Data," AGARD Conference Pre-print 111 on Aerodynamics of Rotary Wings, Marseilles, France, Sept. 1972.
- 8 Gohard, J. C., "Free Wake Analysis of Wing Turbine Aerodynamics," ASRL TR-184-14, Aero. and Struc. Research Lab., Dept. of Aeronautics and Astronautics, MIT, Sept. 1978.
- 9 Savino, J. M., and Nyland, T. W., "Wind Turbine Flow Visualization Studies: Tip and Root Vortices and Wind Stream Pattern at Low Power," PIR No. 241, *Wind Energy Project Office NASA Lewis Research Center*, Nov. 30, 1983.
- 10 Miller, R. H., "Application of Fast Free Wake Analysis Techniques to Rotors," *Vertica*, Vol. 8, No. 3, 1984, pp. 255-261.
- 11 Miller, R. H., "The Aerodynamics and Dynamic Analysis of Horizontal Axis Wind Turbines," *Journal of Wind Engineering and Industrial Aerodynamics*, Vol. 15, 1983, pp. 329-340.
- 12 Miller, R. H., "Rotor Hovering Performance Using the Method of Fast Free Wake Analysis," *AIAA Journal of Aircraft*, Vol. 20, No. 3, Mar. 1983, pp. 257-261.
- 13 Miller, R. H., "Simplified Free Wake Analysis for Rotors," FAA (Sweden) TN 1982-7 (Also MIT ASRL-TR-194-3).
- 14 Miller, R. H., "Free Wake Techniques for Rotor Aerodynamic Analysis: Volume I: Summary of Results and Background Theory," NASA CR-166434 (Also MIT ASRL-TR-199-1), 1982.
- 15 Hama, F. R., "Progressive Deformation of a Curved Vortex by Its Own Induction," *Physics of Fluids*, Vol. 5, No. 10, Oct. 1962, pp. 1156-1162.
- 16 Arms, R. J., and Hama, F. R., "Localized Induction Concept on a Curved Vortex and Motion of an Elliptic Vortex Ring," *Physics of Fluids*, Vol. 8, No. 4, Apr. 1965, pp. 553-559.
- 17 McCormick, B. W., *Aerodynamics of V/STOL Flight*, Academic Press, New York, 1967.
- 18 Afjeh, A. A., "Wake Effects on the Aerodynamic Performance of Horizontal Axis Wind Turbines," NASA CR-174920, 1984.
- 19 Spera, D. A., and Janetzke, D. C., "Performance and Load Data from Mod-OA and Mod-1 Wind Turbines," *Proceedings of a Workshop on Large Horizontal-Axis Wind Turbines*, July 28-30, 1981, pp. 447-468, NASA Conference Publication 2230 or DOE Publication CONF-810752, 1981.
- 20 Abbott, H., and VonDoenhoff, A. E., *Theory of Wing Sections*, McGraw-Hill, 1949.



**Y. Tsujimoto**

Research Associate.

**K. Imaichi**

Professor Emeritus.

Osaka University,  
Faculty of Engineering Science,  
Toyonaka, Osaka, Japan

**T. Moritani**

Engineer.  
Mitsubishi Electric Corp.,  
Kamakura Works,  
Kamakura, Kanagawa, Japan

**K. Kim**

Engineer,  
Mobil Sekiyu Corp.,  
Osaka Area Operations Office,  
Toyonaka, Osaka, Japan

# Measurements of Apparent Mass Torque Coefficients of Two-Dimensional Centrifugal Impellers

*Apparent mass torque coefficients for fluctuations of flow rate and angular velocity are determined experimentally for two-dimensional centrifugal impellers. Nearly sinusoidal fluctuations of flow rate and angular velocity are produced by using crank mechanisms, and the resulting unsteady torque on the impeller is measured. The torque is divided into components in-phase and out-of-phase with the displacements. The in-phase components are used to determine the apparent mass coefficients. Drag torque coefficients are defined and used to represent the out-of-phase components. The tests are conducted under various frequencies and amplitudes of the fluctuations with zero mean flow rate and rotational velocity. The apparent mass torque coefficients are compared with theoretical values obtained under the assumption of a two-dimensional potential flow. The experimental values are 5 to 20 percent larger than the theoretical ones and no appreciable effects of the frequency and the amplitude are observed within the range of the experiments.*

## Introduction

The introduction of the concept of apparent mass, or virtual mass, traces back at least to the early nineteenth century, and theoretical values have been given for various two and three dimensional bodies [1]. For bodies with simpler geometries such as circular cylinders or spheres, extensive studies have been made on the unsteady forces on oscillating bodies or on bodies in oscillatory flows [2]. The hydrodynamic mass due to a fluid annulus surrounding a rotating cylinder has been studied both theoretically and experimentally [3]. For an excellent review on unsteady fluid forces on bodies see Sarpkaya and Isaacson [4].

The estimation of the apparent moment of inertia of an impeller is inevitable in the designing of shaft systems of hydraulic machinery for the prediction of torsional critical speed, but, to our knowledge, publications on this problem have been few. Kito [5] has measured the apparent mass of a model runner of a water turbine and of two-dimensional straight vaned radial impellers for lateral oscillation. Later he made a theoretical analysis [6] of the apparent polar moment of inertia for two-dimensional straight vaned radial impellers. For marine propellers, Furuya and Ito [7] measured the apparent moment of inertia and proposed a method for prediction. In reference [8] we can find apparent mass coefficients of various two-dimensional bodies and airfoils. Among them the data for flat plate cascades might be used for the prediction of the apparent moment of inertia of axial flow rotors.

The present authors have made potential flow analyses [9,

10] of centrifugal impellers for flow rate and/or rotational velocity fluctuations. The resulting torque is divided into quasisteady, apparent mass and wake components and it is found that the wake component is usually smaller than the other two components. Apparent mass torque coefficients for the two types of fluctuations are defined and calculated for various logarithmic impellers. An approximate estimation of unsteady torque can be made easily by using the coefficients and the steady characteristics of the impeller. The apparent mass torque coefficient for rotational velocity fluctuation is proportional to the apparent moment of inertia and thus can be used for the prediction of torsional critical speed.

The main purpose of this paper is the experimental verification of the theoretical values of the apparent mass torque coefficients for two-dimensional centrifugal impellers. The unsteady torque resulting from the small sinusoidal flow rate fluctuation and/or torsional oscillation of the impeller is measured under a condition without mean flow rate and mean rotational velocity. By using a real time correlator the torque is divided into components in-phase and out-of-phase with the displacements. The in-phase component is used for the determination of the apparent mass torque coefficients. Drag torque coefficients are defined and used to represent the out-of-phase components.

## Apparent Mass Torque Coefficients

The apparent mass torque coefficients are defined for impellers with outer radius  $r_2$  and outer impeller breadth  $b_2$  as follows.

For flow rate fluctuation  $Q(t)$  under a constant angular velocity,

$$C_a^c = T_a / (\rho r_2^2 dQ/dt / 2\pi) \quad (1)$$

Contributed by the Fluids Engineering Division and presented at the Winter Annual Meeting, Anaheim, Calif., December 7-12, 1986 of THE AMERICAN SOCIETY OF MECHANICAL ENGINEERS. Manuscript received by the Fluids Engineering Division, March 28, 1985. Paper No. 86-WA/FE-2.

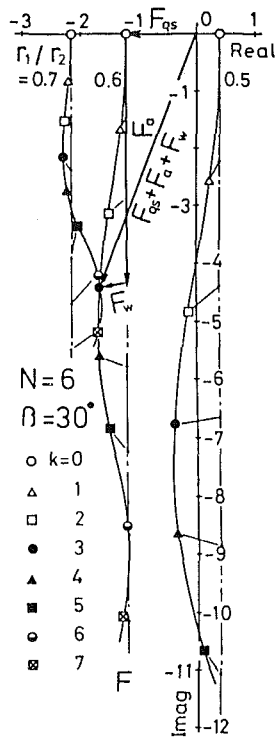


Fig. 1 Theoretical unsteady torque coefficient for small sinusoidal flow rate fluctuation [9]

and, for angular velocity fluctuation  $\Omega(t)$  under a constant flow rate,

$$C_a^{\Omega} = T_a / (\rho b_2 r_2^4 d\Omega/dt), \quad (2)$$

where  $T_a$  is the unsteady torque component caused by the apparent mass effect. The coefficient  $C_a^{\Omega}$  is related to the apparent polar moment of inertia  $I$  by

$$I = \rho b_2 r_2^4 C_a^{\Omega}. \quad (3)$$

From a theoretical point of view, both  $C_a^{\varphi}$  and  $C_a^{\Omega}$  are inherent to the geometry of the impeller and independent of the mean flow rate and of mean rotational velocity of the impeller as long as flow separation and cavitation are avoided. For spheres or circular cylinders, the flow separation, which might take place in cases with mean velocities, changes the apparent mass appreciably [4]. However, for centrifugal impellers, we will have many practical applications without severe separation and cavitation. Hence, it seems meaningful to determine

## Nomenclature

$a$  = amplitude parameter of flow rate fluctuation  
 $A$  = cross sectional area of cylinder  
 $b_2$  = impeller breadth  
 $C_a^{\varphi}, C_a^{\Omega}$  = apparent mass torque coefficients for fluctuations of flow rate and angular velocity  
 $C_{ath}^{\varphi}, C_{ath}^{\Omega}$  = theoretical values of  $C_a^{\varphi}$  and  $C_a^{\Omega}$   
 $C_d^{\varphi}, C_d^{\Omega}$  = drag torque coefficients for fluctuations of flow rate and angular velocity  
 $C_{df}, C_d$  = disk friction contributions to  $C_a^{\varphi}$  and  $C_a^{\Omega}$   
 $C_d$  = drag coefficient  
 $C_{x,T}(\tau)$  = cross correlation function of  $x$  and  $T$   
 $f$  = frequency  
 $F$  = fluctuating torque coefficient  
 $I$  = apparent polar moment of inertia  
 $I_0$  = polar moment of inertia of impeller  
 $i$  = imaginary unit

the apparent mass torque coefficients in the simplest situation without mean flow rate and mean rotational velocity of the impeller.

Figure 1 shows the theoretical unsteady torque [9] on logarithmic impellers with vane angle  $\beta = 30$  deg, vane number  $N = 6$  and inner to outer radius ratio  $r_1/r_2$  subjected to a small sinusoidal flow rate fluctuation around a shockless mean flow rate. The torque fluctuation  $T$  is normalized by

$$F = T / (\rho r_2^4 \Omega_0^2 b_2 \Delta \varphi e^{i\omega t})$$

and shown as a function of a normalized frequency  $k = \omega/\Omega_0$ , where  $\Omega_0$  is the constant angular velocity of the impeller and  $\Delta \varphi e^{i\omega t}$ , the assumed fluctuation of flow coefficient. The unsteady torque is composed of quasisteady  $F_{qs}$ , apparent mass  $F_a$  and wake  $F_w$  components. The wake component is smaller than the other two components. The quasisteady component can be estimated from the steady head-capacity characteristic and the apparent mass component by using the apparent mass torque coefficient. Hence, we can obtain an approximate estimate of the unsteady torque from the coefficient and the steady characteristic. The same is true also for the rotational velocity fluctuation.

The drag component of the unsteady torque has less importance for engineering purposes since it will be different in practical operation. However, since the drag component is not independent of the mass component and since it is useful in gaining the physical understanding, it is set aside for further discussions.

## Apparatus and Procedure

A schematic drawing of the apparatus is shown in Fig. 2. The impeller is supported by a driving mechanism to provide torsional displacements for the measurements of  $C_a^{\Omega}$ . On the occasion of the measurements of  $C_a^{\varphi}$ , the impeller is supported by a stationary frame through a torque pick up. A square water tank made of transparent acrylic resin is used. The dimension is 800 mm by 800 mm with the depth 250 mm.

The test impellers are made of transparent acrylic resin with thickness 2 mm. A schematic drawing is shown in Fig. 3 and dimensions are given in Table 1. The impellers have the same dimensions except for the number of vanes. Circular arc vanes are used to facilitate manufacturing. The theoretical model of reference [9] assumes a two dimensional unrestricted flow. In order to approximate the assumption, the radius of each shroud is extended to 4/3 the length of the outer radius of the impeller. The authors assume that the finiteness of the shrouds does not affect the measured apparent mass torque appreciably, since the velocity disturbance due to the impeller is insignificant at the outer radii of the shrouds. The impellers

$N$  = number of vanes  
 $Q$  = flow rate  
 $r_1, r_2$  = inner and outer radius of impeller  
 $R_1, R_2$  = inner and outer radius of shroud  
 $t$  = time  
 $T, T_a, T_d$  = torque, apparent mass and drag components of torque  
 $x, x_0$  = displacement, amplitude of displacement of piston  
 $\beta_1, \beta_2$  = vane angle from circumference at  $r = r_1, r_2$ , respectively  
 $\rho$  = density  
 $\nu$  = kinematic viscosity  
 $\theta, \theta_0$  = angular displacement and its amplitude  
 $\Omega$  = angular velocity of impeller  
 $\omega$  = angular frequency of fluctuation

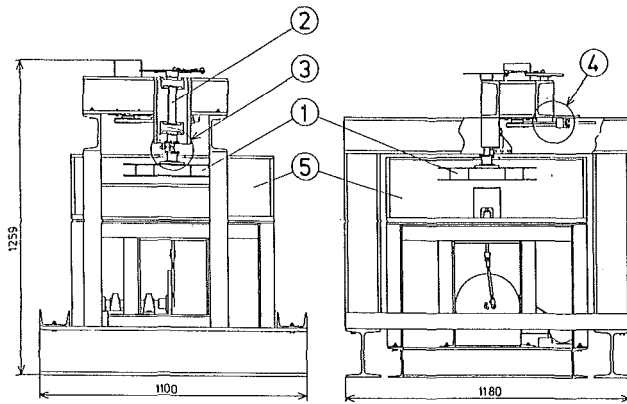


Fig. 2 Experimental apparatus: ① impeller ② shaft ③ torque-displacement pickups ④ frequency pickup ⑤ water tank

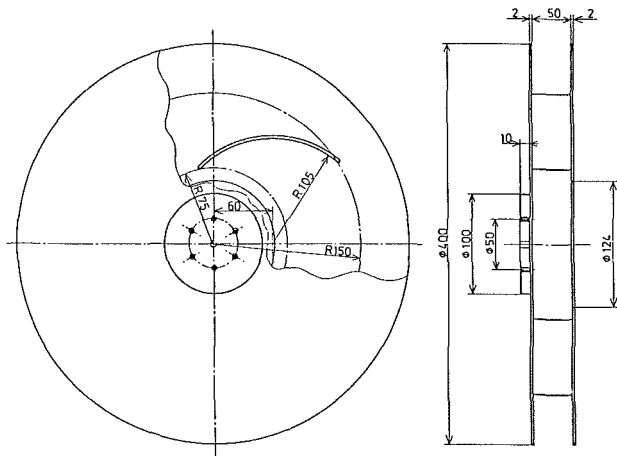


Fig. 3 Schematic drawing of test impellers

for the measurements of  $C_d^0$  have a circular opening at the center of the front shroud, while those for  $C_d^a$  are without an opening not to allow the flow through the impeller.

Water is used as the working fluid. Temperature is kept between  $17^\circ\text{C} \pm 1^\circ\text{C}$  throughout the experiment. The top of the tank is covered with a lid to prevent surface waves. The water level is lowered from time to time to remove air bubbles on the impeller so that the diameter of the bubbles may not exceed about 0.5 mm.

**Measurements of  $C_d^a$ .** Nearly sinusoidal flow rate fluctuation is produced by a piston-crank mechanism shown in Fig. 4. The length of the connecting rod is 200 mm while the maximum eccentricity used is 25 mm. The flywheel is driven by a D.C. motor through a toothed belt.

The impeller is supported by an upper frame through a torque pickup. The pickup has a cylindrical test section with diameter 20 mm and effective length 30 mm. Two strain gauge rosettes are attached to the test section on opposite sides. The measuring direction of each gauge element makes a 45 degree angle with the centerline of the pickup.

Attention is paid to secure perfect sealing in the piston-impeller flow system. An O-ring made of rubber is used between the cylinder of diameter 100 mm and the piston and silicon grease is applied for the purposes of lubrication and sealing. As a result, the sealing is found to be perfect even with static pressure difference of 5 KPa in the moving condition, which is about twice as large as the estimated maximum pressure difference in the experiments. The gap between the front shroud of the impeller and a spacer ring mounted on the

Table 1 Dimensions of test impellers

Inner radius	$r_1 = 75 \pm 0.3$ mm
Outer radius	$r_2 = 150 \pm 0.3$ mm
Impeller breadth	$b_2 = 50 \pm 0.3$ mm
Radius of vane curvature	$R = 105 \pm 2$ mm
Thickness of vanes	$t_v = 2 \pm 0.1$ mm
Inlet vane angle	$\beta_1 = 34 \pm 0.5$ deg
Outlet vane angle	$\beta_2 = 18.2 \pm 0.5$ deg
Number of vanes	$N = 4, 6, 10$
Inner radius of shroud	$R_1 = 62 \pm 0.3$ mm
Outer radius of shroud	$R_2 = 200 \pm 0.3$ mm

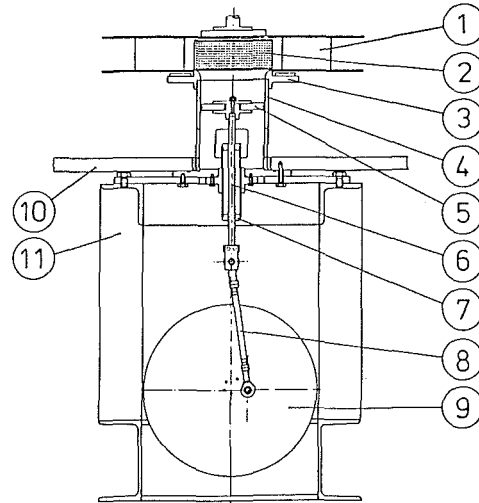


Fig. 4 Piston-crank mechanisms to produce flow rate fluctuation: ① impeller ② mesh ③ mouthpiece ④ cylinder ⑤ piston ⑥ shaft ⑦ guide ⑧ connecting rod ⑨ flywheel ⑩ bottom plate of tank ⑪ frame

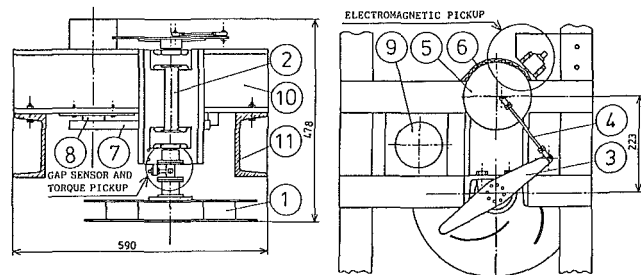
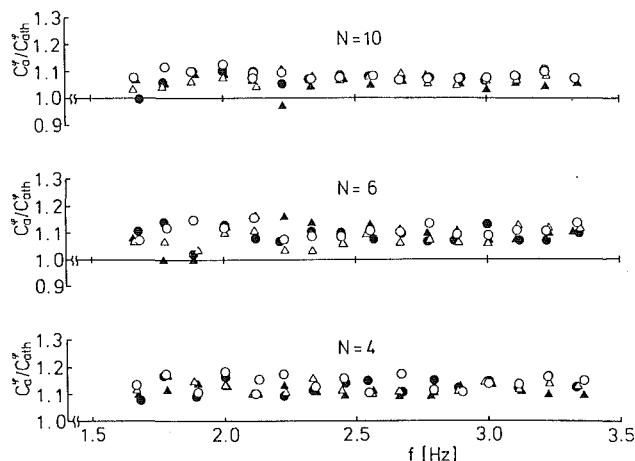


Fig. 5 Driving mechanisms to provide angular displacements: ① impeller ② shaft ③ control arm ④ connecting rod ⑤ flywheel ⑥ ⑦ toothed belt pulley ⑦ toothed belt ⑨ D.C. motor ⑩ ⑪ frame

mouthpiece is kept to be 1 mm and filled with silicon grease of viscosity 3000 cst for the purpose of sealing. After each run, the sealing condition is checked by visually ascertaining the existence of the grease. It is confirmed that the viscous force transmitted through the grease is negligible by comparing the results with those obtained by using a spacer ring with smaller diameter.

Thus securing the sealing in the piston-impeller flow system, we can estimate the instantaneous flow rate from the displacement of the piston. The estimated minimum pressure on the piston is well above the saturated vapour pressure to prevent cavitation. To detect the displacement of the piston, a circular cylinder of diameter 28 mm is attached on the other side of the flywheel axis with eccentricity 0.5 mm and a gap sensor is mounted on a stationary frame against the cylinder. The phase of the eccentricity is adjusted so that the output of the gap sensor is in phase with the displacement of the piston.



**Fig. 6 Apparent mass torque coefficient  $C_a^y$  for flow rate fluctuation**  
 $\circ, a = (2.78 \pm 0.02) \times 10^{-2}$ ;  $\triangle, a = (2.21 \pm 0.02) \times 10^{-2}$ ;  
 $\bullet, a = (1.69 \pm 0.02) \times 10^{-2}$ ;  $\blacktriangle, a = (1.14 \pm 0.02) \times 10^{-2}$ ;  
 (Uncertainty in  $C_a^y / C_a^y_0 = \pm 0.1$ , in  $f = \pm 0.05$  Hz at 20:1 odds)

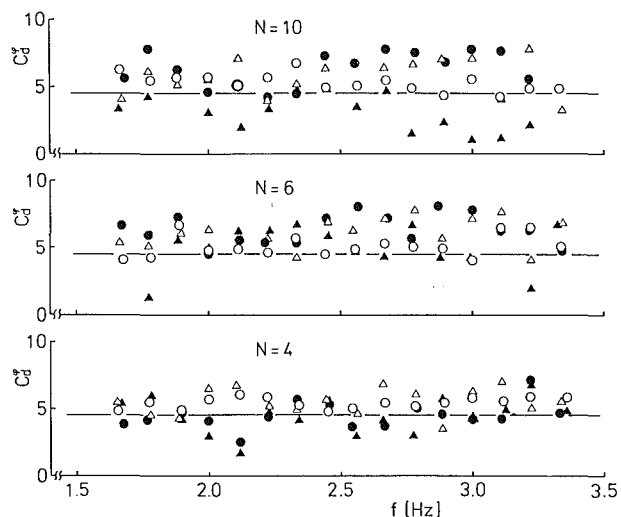


**Fig. 7 Drag torque coefficient  $C_d^y$  for flow rate fluctuation**  
 $\circ, a = (2.78 \pm 0.02) \times 10^{-2}$ ;  $\triangle, a = (2.21 \pm 0.02) \times 10^{-2}$ ;  
 $\bullet, a = (1.69 \pm 0.02) \times 10^{-2}$ ;  $\blacktriangle, a = (1.14 \pm 0.02) \times 10^{-2}$ ;  
 Equation (11)  
 (Uncertainty in  $C_d^y = \pm 5.0$ , in  $f = \pm 0.05$  Hz at 20:1 odds)

The frequency of the flywheel and the piston mechanism is determined by counting the pulses from an electromagnetic pickup responding to the passage of the teeth of a pulley driving the flywheel by a digital counter.

The torsional natural frequency of the impeller-support system is about 140 Hz with the impeller in water.

The signals of the torque on the impeller and of the displacement of the piston are put into a real time correlator which outputs digitally the crosscorrelation function between the torque and the displacement. Since the eccentricity of the target cylinder is small compared to its radius, the output of the gap sensor is nearly sinusoidal. The amplitude and phase of the first harmonic of the unsteady torque are determined by using the crosscorrelation function.

A cylindrical mesh is used for the realization of a two-dimensional flow. It is found, by a flow visualization, that the flow is nearly two dimensional without any flow separation.

**Measurements of  $C_a^y$ .** Figure 5 shows an apparatus to provide nearly sinusoidal angular displacement for the measurements of  $C_a^y$ . One end of the connecting rod of length 190 mm is connected to a flywheel with an eccentricity and the

other end to the control arm of the impeller axis. The maximum eccentricity used is 10 mm. The unsteady torque is measured by the same torque pickup as is used for the measurements of  $C_a^y$ . The angular displacement is determined by using a gap sensor to measure the distance between the stationary pickup and a target attached to a flange of the torque pickup. The frequency is determined by counting the pulses from an electromagnetic pickup responding to the passage of the teeth of the pulley.

The natural frequency of the system for torsional vibration of the impeller with  $N = 10$  is about 70 Hz with the impeller submerged.

As in the case of the measurements of  $C_a^y$ , the signals of the torque and the angular displacement are put into the real time correlator which outputs the crosscorrelation function between the torque and the displacement, which is used to determine the in-phase and the out-of-phase components of the torque. The values of  $C_a^y$  are determined by subtracting from the in-phase component the contribution of the polar moment of inertia  $I_0$  of the impeller which is approximately determined by tests with the impeller in air.

The torque pickup and the gap sensor are calibrated statically each time the impellers are replaced. Calibration constants and linearity seldom change. The fluctuation of the rotational velocity of the flywheel is kept within 3 and 1 percent of the average velocities for the measurements of  $C_a^y$  and  $C_d^y$ , respectively.

## Results and Discussions

**Flow Rate Fluctuation.** After Morison et al. [12] we assume that the unsteady torque can be represented by

$$T = -\frac{\rho}{2\pi b_2} \cdot C_d^y \cdot Q \cdot |Q| + \frac{\rho r_2^2}{2\pi} \cdot C_a^y \cdot \frac{dQ}{dt} \quad (4)$$

where we call  $C_d^y$  the "drag torque coefficient" for flow rate fluctuation. We represent the displacement  $x$  of the piston and the flow rate  $Q$  by

$$x = x_0 \cos \omega t$$

$$Q = A\dot{x} = -\omega x_0 A \sin \omega t = -Q_0 \sin \omega t \quad (5)$$

where  $A$  is the cross-sectional area of the cylinder. If we make use of the Fourier's expansion of  $\sin \omega t \cdot |\sin \omega t|$ , the crosscorrelation function  $C_{x,T}(\tau)$  between the displacement  $x$  and the torque  $T$  can be represented by

$$\begin{aligned} C_{x,T}(\tau) &= \lim_{T_m \rightarrow \infty} (1/T_m) \int_{-T_m/2}^{T_m/2} x(t) T(t+\tau) dt \\ &= (2\rho/3\pi^2 b_2) Q_0^2 C_d^y x_0 \sin \omega \tau \\ &\quad - (\rho r_2^2/4\pi) \omega Q_0 C_a^y x_0 \cos \omega \tau \end{aligned} \quad (6)$$

Hence, using the correlation function  $C_{x,T}(\tau)$  which is an output of the real time correlator, we can determine the value of  $C_a^y$  from the following relation.

$$C_a^y = 2\pi \{ C_{x,T}(\pi/\omega) - C_{x,T}(0) \} / (\rho r_2^2 \omega Q_0 x_0) \quad (7)$$

If we assume that  $C_{x,T}(\tau)$  attains its maximum at  $\omega\tau = \phi$  in the region  $0 < \omega\tau < \pi$ , the value of  $C_d^y$  is determined from

$$C_d^y = - (3\pi b_2 r_2^2 \omega / 8 Q_0) C_a^y \tan \phi \quad (8)$$

The amplitude of the fluctuation is represented by an amplitude parameter

$$a = Ax_0 / (2\pi r_2^2 b_2) = \Delta r / r_2 \quad (9)$$

where  $\Delta r = Ax_0 / (2\pi r_2 b_2)$  is the amplitude of radial displacement of the fluid particles at the outer radius of the impeller.

In Figs. 6 and 7,  $C_a^y$  and  $C_d^y$  are shown as functions of the frequency  $f$  for four different values of the amplitude parameter  $a$ . The apparent mass coefficient is shown as a ratio



**Table 2 Average values of  $C_a^\varphi/C_{ath}^\varphi$**

(Uncertainty in  $C_a^\varphi/C_{ath}^\varphi = \pm 0.1$ , in  $a = \pm 0.02 \times 10^{-2}$  at 20:1 odds)

$C_a^\varphi/C_{ath}^\varphi$	$a = 2.78 \times 10^{-2}$	$a = 2.21 \times 10^{-2}$	$a = 1.69 \times 10^{-2}$	$a = 1.14 \times 10^{-2}$
$N=4$	1.14	1.12	1.13	1.11
$N=6$	1.11	1.08	1.09	1.10
$N=10$	1.09	1.07	1.07	1.06

**Table 3 Average values of  $C_d^\varphi$**

(Uncertainty in  $C_d^\varphi = \pm 5.0$ , in  $a = \pm 0.02 \times 10^{-2}$  at 20:1 odds)

$C_d^\varphi$	$a = 2.78 \times 10^{-2}$	$a = 2.21 \times 10^{-2}$	$a = 1.69 \times 10^{-2}$	$a = 1.14 \times 10^{-2}$
$N=4$	5.19	5.88	4.53	4.07
$N=6$	5.15	6.40	6.40	5.15
$N=10$	5.35	6.14	6.38	3.41

**Table 4 Average values of  $C_a^\Omega/C_{ath}^\Omega$**

(Uncertainty in  $C_a^\Omega/C_{ath}^\Omega = \pm 0.15$ , in  $\theta_0 = \pm 0.06 \times 10^{-2}$  rad at 20:1 odds)

$C_a^\Omega/C_{ath}^\Omega$	$\theta_0 = 6.77 \times 10^{-2}$	$\theta_0 = 5.12 \times 10^{-2}$	$\theta_0 = 3.37 \times 10^{-2}$	$\theta_0 = 1.85 \times 10^{-2}$	$C_{df}/C_{ath}^\Omega$
$N=4$	1.27	1.30	1.26	1.26	0.0748
$N=6$	1.20	1.17	1.21	1.15	0.0508
$N=10$	1.13	1.16	1.09	1.18	0.0379

**Table 5 Average values of  $C_d^\Omega$**

(Uncertainty in  $C_d^\Omega = \pm 1.0$ , in  $\theta_0 = \pm 0.06 \times 10^{-2}$  rad at 20:1 odds)

$C_d^\Omega$	$\theta_0 = 6.77 \times 10^{-2}$	$\theta_0 = 5.12 \times 10^{-2}$	$\theta_0 = 3.37 \times 10^{-2}$	$\theta_0 = 1.85 \times 10^{-2}$
$N=4$	0.742	0.851	0.982	1.261
$N=6$	0.814	0.992	1.028	1.163
$N=10$	0.620	0.807	0.920	1.275
$C_{df}$	0.107	0.141	0.214	0.390

$C_a^\varphi/C_{ath}^\varphi$  where  $C_{ath}^\varphi$  is the theoretical value obtained by the method in [9] and is  $-1.56$ ,  $-2.28$  and  $-3.02$  for impellers with  $N = 4, 6$ , and  $10$ , respectively. Since there can be seen no meaningful effects of the frequency,  $C_a^\varphi/C_{ath}^\varphi$  and  $C_d^\varphi$  are averaged over the frequencies and shown in Tables 2 and 3. Using these averaged values of  $C_a^\varphi/C_{ath}^\varphi$  and  $C_d^\varphi$ , the total torque is reconstructed and its complex representation is shown in Fig. 8, where the torque  $T$  is represented by

$$T = \rho b_2 r_2^4 \omega^2 a \text{Re}(F e^{i\omega t})$$

$$F = -C_a^\varphi - (16/3) a C_d^\varphi i \tag{10}$$

for the displacement given by equation (5). The apparent mass component is in phase with the displacement and the drag component lags by  $\pi/2$  behind the displacement. Consequently, the total torque lags by about  $4 \sim 24$  deg behind the displacement.

As shown in Table 2, the measured values of  $C_a^\varphi$  are 5 – 15 percent larger than the theoretical values and no appreciable effects of the amplitude are observed. The difference between the experimental and theoretical values is larger for impellers with smaller numbers of vanes. Judging from the scatter of the plots in Fig. 6, the authors believe that the errors in the average values in Table 2 is less than 5 percent.

We have a large scatter in  $C_d^\varphi$  as shown in Fig. 7, which is caused by the difficulties in the precise determination of the phase difference between the displacement and the torque. No meaningful effects of the amplitude can be seen in the averaged values of  $C_d^\varphi$  given in Table 3.

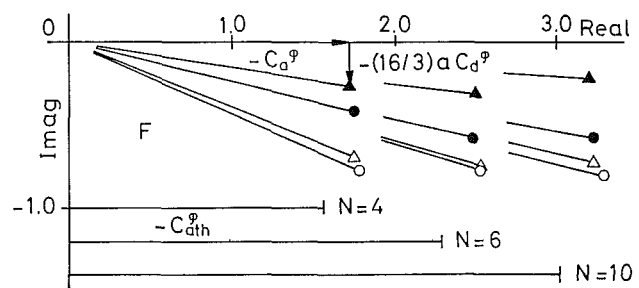


**Fig. 8 Vector plots of unsteady torque, flow rate fluctuation**  
 $\circ, a = (2.78 \pm 0.02) \times 10^{-2}$   
 $\Delta, a = (2.21 \pm 0.02) \times 10^{-2}$   
 $\bullet, a = (1.69 \pm 0.02) \times 10^{-2}$   
 $\blacktriangle, a = (1.14 \pm 0.02) \times 10^{-2}$

For the physical understanding of the drag component, let us consider about the angular momentum transfer across the inlet ( $r = r_1$ ) and the outlet ( $r = r_2$ ) of the impeller. If we assume that the number of the vanes is so large that the flow is discharged tangentially to the vanes, and that the angular momentum is retained until the re-entry of the discharged fluid into the impeller, the torque component due to the angular momentum transfer can be represented by the drag component with

$$C_d^\varphi = \cot \beta_1 + \cot \beta_2 \tag{11}$$

which is also plotted in Fig. 7. The measured values are scattering around this value. Hence, it might be concluded that the



contribution of  $C_{af}/C_{ath}^{\Omega}$ . No systematic effect of the amplitude is observed. Also the frequency has little effect on  $C_d^{\Omega}$  except for the case of  $N = 4$ , in which the measured values of  $C_d^{\Omega}$  are slightly smaller at higher frequencies. Since  $C_d^{\Omega}$  is obtained by subtracting the contribution of the moment of inertia of the impeller, we have a larger scatter than for the case of  $C_d^{\sigma}$ .

As shown in Fig. 10, we also have a large scatter in  $C_d^{\Omega}$  caused by the small phase lag of the torque. Hence, the following discussions on  $C_d^{\Omega}$  are only qualitative. Table 5 shows that the average values of  $C_d^{\Omega}$  are larger for cases of smaller amplitude. This tendency is partly caused by the effect of the disk friction. If we subtract  $2C_{df}$  from  $C_d^{\Omega}$ , we obtain an almost constant value. This means that the drag component contains a laminar type friction component approximately twice as large as that estimated from Rayleigh's solution and the rest can be represented by Morison's expression for the drag component. The "drag" component always has a damping effect on the torsional oscillation of the impeller, within the range of the experiments.

## Conclusions

Apparent mass torque coefficients for fluctuations of flow rate and rotational velocity are determined experimentally for two-dimensional centrifugal impellers and the results are compared with theoretical values obtained by assuming a two-dimensional potential flow. Experimental values are 5 to 20 percent larger than the theoretical values and no appreciable effects of the amplitude and the frequency are observed within the range of the experiments.

The drag torque component is also determined for the two types of disturbances. Although the scatter is large, the following tendencies are observed.

For flow rate fluctuation the drag component can be represented by Morison's expression without any meaningful effect of the frequency and the amplitude of the fluctuation on the drag torque coefficient. The drag component is for the most part explained by considering the angular momentum exchange across the inner and outer radius of the impeller.

In case of rotational velocity fluctuation, the effects of disk friction on the extended shroud of the test impellers are of non-negligible order and separate tests are conducted to deter-

mine the effects. It is found that Rayleigh's solution for an oscillating plate can be used for the evaluation of the disk friction effects. The disk friction can be one of the cause of the larger values of  $C_d^{\Omega}/C_{ath}^{\Omega}$  for impellers with smaller  $N$ . The drag component contains a laminar type friction component approximately twice as large as that estimated from Rayleigh's solution and the rest can be represented by Morison's expression for the drag component.

## Acknowledgements

The authors would like to express their sincere gratitude to Dr. Y. Murakami of Osaka University for his valuable discussions. His recommendation to use a real time correlator has made it possible to isolate the drag component. Acknowledgements are also to Messrs. Y. Koiso, M. Yasui, and H. Fukumoto for their supports in the experiments.

## References

- 1 Lamb, H., *Hydrodynamics*, Cambridge Univ. Press, London, 1st ed. 1879, 6th. ed. 1932.
- 2 Sarpkaya, T., "Forces on Cylinders and Spheres in a Sinusoidally Oscillating Fluid," *ASME Journal of Applied Mechanics*, Vol. 42, No. 1, Mar. 1975, pp. 32-37.
- 3 Fritz, R. J., "The Effects of an Annular Fluid on the Vibrations of a Long Rotor, Part 1—Theory, Part 2—Test," *ASME Journal of Basic Engineering*, Vol. 92, No. 4, Dec. 1970, pp. 923-929, 930-937.
- 4 Sarpkaya, T., Isaacson, M., *Mechanics of Wave Forces on Offshore Structures*, Van Nostrand Reinhold Company, N.Y., 1981.
- 5 Kito, F., "On Virtual Mass of Hydraulic Machinery," *Journ. Japan Soc. Mech. Engrs.* (in Japanese), Vol. 52, No. 373, Jan. 1950, pp. 14-18.
- 6 Kito, F., "On Virtual Mass of Vane Wheel having Radial Vanes which make Torsional Vibration in Water," *Trans. Japan Soc. Mech. Engrs.* (in Japanese), Vol. 18, No. 66, 1953, pp. 127-131.
- 7 Furuya, Y. and Ito, T., "Experiments on the Induced Moment of Inertia of Propellers," *Trans. Japan Soc. Mech. Engrs.* (in Japanese), Vol. 26, No. 162, Feb. 1960, pp. 194-202.
- 8 Sedov, L. I., *Two-Dimensional Problems in Hydrodynamics and Aerodynamics*, Interscience Publishers, N.Y., 1965.
- 9 Imaichi, K., Tsujimoto, Y., Yoshida, Y., "An Analysis of Unsteady Torque on a Two-Dimensional Radial Impeller," *ASME JOURNAL OF FLUIDS ENGINEERING*, Vol. 104, No. 2, June 1982, pp. 228-234.
- 10 Tsujimoto, Y., Imaichi, K., Tomohiro, T., and Gotoo, M., "An Analysis of Unsteady Torque on a Quasi-Three-Dimensional Centrifugal Impeller," *Bull. of Japan Soc. Mech. Engrs.*, Vol. 27, No. 232, Oct. 1984, pp. 2166-2172.
- 11 Schlichting, H., *Boundary-Layer Theory*, McGraw-Hill, N.Y., 4th ed. 1968.
- 12 Morison, J. R., et al., "The Force Exerted by Surface Waves on Piles," *Petroleum Trans.*, Vol. 189, 1950, p. 149-157.

**J. C. Dutton**

Associate Professor.  
Mem. ASME

**B. F. Carroll**

ONR Graduate Fellow.

Department of Mechanical and  
Industrial Engineering,  
University of Illinois  
at Urbana-Champaign,  
Urbana, Ill. 61801

# Optimal Supersonic Ejector Designs

*A technique based on a one-dimensional constant area flow model has been developed for solving a large class of supersonic ejector optimization problems. In particular, the method determines the primary nozzle Mach number and ejector area ratio which optimizes either the entrainment ratio, compression ratio, or stagnation pressure ratio given values for the other two variables and the primary and secondary gas properties and stagnation temperatures. Design curves for the common case of diatomic primary and secondary gases of equal molecular weight and stagnation temperature are also presented and discussed.*

## Introduction

Because of their flexibility and simplicity of operation, ejectors have been used in a variety of applications, ranging from high entrainment rate thrust augmentors for V/STOL aircraft to high compression ratio jet pumps for continuous wave (cw) chemical laser systems. For this reason, ejectors have also been widely studied over the years; in fact Porter and Squyers (1981) recently compiled a list of over 1600 references relating to ejector theory and performance. These research efforts have resulted in analytical models of varying degrees of sophistication and, in addition, extensive experimental investigations of ejector performance have been carried out.

The topic of ejector design optimization has also received some attention. Loth (1966, 1968) developed procedures for optimizing staged ejector systems using an experimentally derived empirical model for the operation of each stage. Loth defined an optimum design as one which required the minimum primary mass flowrate for given operating pressures at the ejector inlet and outlet. Emanuel (1976) utilized a simplified constant pressure mixing analysis to predict optimum performance of single stage ejectors. In this case, however, the optimal operating point was taken as that giving the largest exit-to-inlet compression ratio for given primary and secondary mass flowrates and inlet stagnation pressures. Mikkelsen et al. (1976) and Hasinger (1978) have both developed optimization procedures based on simplified one-dimensional flow models for the problem of minimizing the primary mass flowrate for given pressure conditions (i.e., similar to the problem considered by Loth). In addition, Mikkelsen et al. obtained ejector solutions which required a minimum value of the primary stagnation pressure and also presented results typical of supersonic wind tunnel and cw chemical laser applications. Dutton and Carroll (1983) considered an ejector optimization problem similar to the latter in connection with natural gas vapor recovery from oil storage tanks. In this case a constant area ejector flow model was

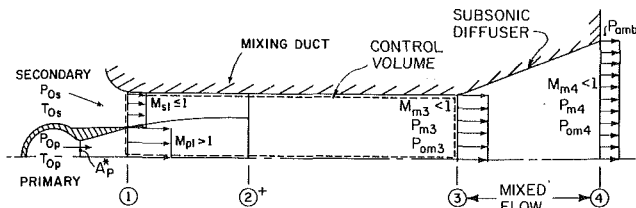
employed to find ejector designs which minimized the primary stagnation pressure required to pump given primary and secondary mass flows through a specified compression ratio. Recently, Wacholder and Dayan (1984) applied the adjoint sensitivity method to quantitatively predict the influence of various ejector design parameters on pressure recovery at a given operating point. These authors also briefly discussed the previously mentioned optimization problems of minimizing the primary mass flowrate for a given ejector compression ratio or, conversely, maximizing the compression ratio for a specified primary-to-secondary mass flow ratio.

Although a good deal of effort has been expended in developing procedures and solutions for optimum ejector designs, each of the previous studies has considered only special cases of ejector optimization. Clearly, a generalized procedure for obtaining optimal solutions for the entire class of problems mentioned above has not previously been presented. The objectives of this paper are to describe a solution methodology capable of parametrically determining optimum solutions for all of these problems and to present results for optimized ejector designs over a range of parameters typically encountered in practice.

## Flow Model

The ejector flow model used in this optimization study is based on the one-dimensional constant area analysis developed by Addy et al. (1981). The constant pressure mixing model is also sometimes used in the analysis of ejector flows, e.g., Emanuel (1976). However, previous experience (Addy et al., 1981) has shown that when based on the same values of area ratio and primary Mach number, both the constant area and constant pressure models predict very comparable performance. In addition, the constant area model has a broader range of possible solutions and is capable of predicting the well known aerodynamic choking phenomenon discussed below, whereas in the constant pressure model the wall contour necessary to produce constant pressure mixing is unknown. More sophisticated multi-dimensional models have also been developed, such as those of Chow and Addy (1964),

Contributed by the Fluids Engineering Division and presented at the Winter Annual Meeting, Anaheim, Calif., December 7-12, 1986 of THE AMERICAN SOCIETY OF MECHANICAL ENGINEERS. Manuscript received by the Fluids Engineering Division, July 19, 1985. Paper No. 86-WA/FE-3.



+ EXISTS ONLY FOR SUPERSONIC REGIME (SR)

Fig. 1 Schematic and nomenclature of the supersonic ejector-subsonic diffuser system

Chow and Yeh (1965), Hickman et al. (1972), Anderson (1974), Hedges and Hill (1974), and Shen et al. (1981), but these techniques are computationally much more cumbersome than the one-dimensional method and, therefore, are inappropriate for parametric design and optimization studies. In addition, the simplified constant area model has been found to agree quite well with experimental data when modified by a single empirical coefficient, as will be discussed below.

A schematic of the supersonic ejector system to be analyzed is shown in Fig. 1. The high velocity, high stagnation pressure supersonic primary stream entrains the lower velocity, lower stagnation pressure secondary stream by viscous interaction in the constant area mixing duct. At the exit of the duct the mixed flow is assumed to be uniform and subsonic. The pressure rise through the system may be increased by adding a subsonic diffuser as shown, to recover as large a fraction of the duct exit dynamic pressure as possible. In some practical ejector systems the exit of the primary nozzle may be located in a converging inlet section of the mixing duct. However, even in that case the constant area analysis has been found to agree reasonably well with experimental data when the minimum area of the mixing tube is used in the analysis (Addy et al., 1981). Given the operating conditions of the primary and secondary streams at inlet station 1, the analysis predicts the mixed flow properties at duct exit station 3, using control volume continuity, momentum, and energy principles. The usual assumptions of steady, frictionless, adiabatic flow of thermally and calorically perfect gases are made. However, to retain generality for various applications, the primary and secondary streams may be of different molecular weights and specific heat ratios and have different stagnation temperatures. A well known facet of supersonic ejector operation (Fabri and Sierstrunck, 1958) is that due to predominantly inviscid effects in the "initial interaction" region, aerodynamic choking of the secondary stream may occur at a location just downstream from the ejector inlet. This phenomenon occurs for operating points common to jet pump applications and thereby places an upper limit on the secondary inlet Mach number. The model of Addy et al. predicts this limiting value of  $M_{s1} < 1$  by writing a second set of control volume relations between inlet location 1 and

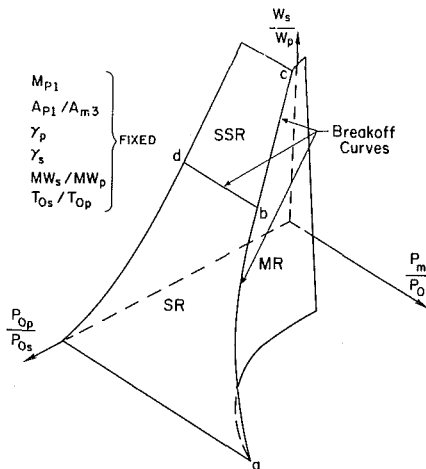


Fig. 2 Three-dimensional ejector operating surface depicting flow regimes

aerodynamic throat location 2 under the choking constraint  $M_{s2} = 1$ .

A useful way to visualize ejector performance for a given geometry, given secondary and primary gases, and given stagnation temperatures is by means of the three-dimensional surface presented in Fig. 2. The coordinates of this graph are the secondary-to-primary mass flow ratio (or "entrainment ratio"),  $W_s/W_p$ , the primary-to-secondary inlet stagnation pressure ratio,  $P_{0p}/P_{0s}$ , and the mixing duct exit static-to-secondary inlet stagnation pressure ratio (or "compression ratio"),  $P_{m3}/P_{0s}$ . The ejector is constrained to operate somewhere on this surface in one of the three regimes shown. In the "supersonic regime" (SR) the primary inlet static pressure exceeds that of the secondary,  $P_{p1} > P_{s1}$ , such that the primary stream expands against the secondary in the mixing duct forming the aerodynamic throat sketched in Fig. 1. In addition, the duct exit pressure  $P_{m3}$  is low enough in the supersonic regime to cause choking at this throat such that  $W_s/W_p$  is independent of  $P_{m3}/P_{0s}$ . The previously mentioned set of auxiliary control volume relations is used to predict the limiting value of  $M_{s1}$  for SR operation. In the "saturated supersonic regime" (SSR) the secondary inlet static pressure is greater than that of the primary,  $P_{s1} > P_{p1}$ , resulting in expansion of the secondary stream against the primary. Therefore, the secondary stream encounters an area minimum at the ejector inlet and for the low duct exit pressures occurring in the SSR, choking will occur at the inlet,  $M_{s1} = 1$ . As in the SR, the mass flow ratio is independent of the compression ratio for SSR operation. In the "mixed regime" (MR), on the other hand,  $P_{m3}/P_{0s}$  is high enough that choking of the secondary stream does not occur either at the inlet or

## Nomenclature

$A$ = cross-sectional area	$R_E$ = ejector pressure recovery coefficient, defined in equation (1)	amb = ambient
$B$ = quantity defined in equation (6)	SR = supersonic regime	$I$ = ideal
$C_p$ = diffuser pressure recovery coefficient, defined in equation (3)	SSR = saturated supersonic regime	$m$ = mixed
$D_h$ = hydraulic diameter	$T$ = temperature	$p$ = primary
$L$ = mixing duct length	$W$ = mass flowrate	$s$ = secondary
$M$ = Mach number	$\gamma$ = gas specific heat ratio	$0$ = stagnation
MR = mixed regime		1,2,3,4 = system locations in Fig. 1
MW = molecular weight		
$P$ = pressure		
	<b>Subscripts</b>	<b>Superscript</b>
	$A$ = actual	$*$ = sonic conditions, i.e., $M = 1$

aerodynamic throat locations. The mass flow ratio is therefore dependent on the compression ratio in this regime of operation.

The curves b-d and a-b-c which separate the various regimes in Fig. 2 are called "breakoff curves." Of particular importance to the present optimization study is breakoff curve a-b-c which separates SR and SSR operation from MR operation. In these regimes the entrainment ratio is respectively independent of and strongly dependent on the compression ratio. Consider a plane of constant  $P_{0p}/P_{0s}$  intersected with the surface of Fig. 2. Clearly, increasing  $P_{m3}/P_{0s}$  above its breakoff value results in a sharp drop in  $W_s/W_p$  due to the steepness of the MR surface. It is therefore advantageous to operate supersonic ejectors at or near breakoff curve a-b-c so that the highest possible compression ratio can be obtained with the mass flow ratio fixed at its maximum value. For this reason, the present optimization study considers only these breakoff operating points. By inspecting curve a-b-c in Fig. 2, SR operation (a-b) is seen to correspond to the relatively high compression ratio/low entrainment ratio cases while the opposite is true for operation in the SSR (b-c).

In an extensive experimental investigation of supersonic ejector performance, Petrie (1980) has demonstrated that the analysis described above provides excellent predictions of both the mass flow ratio,  $W_s/W_p$ , and inlet static pressure ratio,  $P_{s1}/P_{p1}$ , at breakoff. However, the compression ratio,  $P_{m3}/P_{0s}$ , at which the mass flow ratio begins to fall from its fixed SR or SSR value is less than that predicted, and the falloff is more gradual than that indicated in Fig. 2. In other words, the rather unsurprising experimental result was found that the sharp juncture between regimes indicated by breakoff curve a-b-c of the simplified analysis is actually more "rounded." To account for this phenomenon an empirical "ejector pressure recovery coefficient,"  $R_E$ , is introduced into the model,

$$\left[ \frac{P_{m3}}{P_{0s}} \right]_A = R_E \left[ \frac{P_{m3}}{P_{0s}} \right]_I \quad (1)$$

where the "A" subscript denotes actual conditions and the "P" denotes ideal conditions predicted by the original frictionless, adiabatic model. In essence,  $R_E$  is a loss coefficient which accounts for nonidealities such as wall friction, mixing layer, and unsteady shock wave/boundary layer/separation effects which are not accounted for in the simplified analysis. Previous experiments (Petrie, 1980 and Dutton et al., 1982) have shown that  $R_E$  is typically on the order of 0.75-0.85. When modified with  $R_E$  in this manner, the constant area theory has been found to be in good agreement with experimental results (Fabri and Siestrunk, 1958; Mikkelsen et al., 1976; Petrie, 1980; and Addy et al., 1981) over a relatively wide range of geometrical and operational parameters:  $0.13 \leq A_{p1}/A_{m3} \leq 0.93$ ,  $1.4 \leq M_{p1} \leq 3.1$ ,  $1.0 \leq P_{0p}/P_{0s} \leq 120$ ,  $0.35 \leq P_{m3}/P_{0s} \leq 18$ , and  $0 \leq W_s/W_p \leq 1.2$ . However, since the duct exit static pressure at breakoff,  $P_{m3A}$ , is less than the ideally predicted value, the Mach number and stagnation pressure at this location must also be adjusted from their ideal values for consistency. By writing continuity expressions at station 3 for the actual and ideal flows, the actual Mach number can be determined from

$$M_{m3A} = \left[ \frac{-1 + \left[ 1 + 2(\gamma_m - 1)(M_{m3I}/R_E)^2 \left( 1 + \frac{\gamma_m - 1}{2} M_{m3I}^2 \right) \right]^{1/2}}{(\gamma_m - 1)} \right]^{1/2} \quad (2)$$

and  $P_{0m3A}/P_{0s}$  is found from knowledge of  $P_{m3A}/P_{0s}$ ,  $M_{m3A}$ , and the usual isentropic relation.<sup>1</sup>

As previously mentioned and shown in Fig. 1, a subsonic diffuser is usually attached to the downstream end of the mixing duct to increase the system pressure recovery. Diffuser performance is generally reported in terms of the pressure recovery coefficient, defined in this application as

$$C_p \equiv \frac{P_{m4} - P_{m3}}{P_{0m3} - P_{m3}} \quad (3)$$

Given two of the three diffuser geometric parameters, area ratio, dimensionless length, or included angle,  $C_p$  can be estimated from any of several comprehensive experimental investigations of diffuser performance, e.g., Runstadler et al. (1975). Knowing  $C_p$ , the diffuser exit static pressure ratio can be obtained by manipulation of equation (3),

$$\frac{P_{m4}}{P_{0s}} = \frac{P_{m3}}{P_{0s}} + C_p \left( \frac{P_{0m3}}{P_{0s}} - \frac{P_{m3}}{P_{0s}} \right) \quad (4)$$

Likewise, with diffuser area ratio  $A_{m4}/A_{m3}$  known, the diffuser exit Mach number can be obtained by equating mass flow expressions at locations 3 and 4,

$$M_{m4} = \left[ \frac{-1 + [1 + 2(\gamma_m - 1)B^2]^{1/2}}{\gamma_m - 1} \right]^{1/2} \quad (5)$$

where

$$B \equiv \frac{\frac{P_{m3}}{P_{0s}} M_{m3}}{\frac{P_{m4}}{P_{0s}} \frac{A_{m4}}{A_{m3}}} \left[ 1 + \frac{\gamma_m - 1}{2} M_{m3}^2 \right]^{1/2} \quad (6)$$

The stagnation pressure ratio,  $P_{0m4}/P_{0s}$ , is determined from the isentropic relation with  $P_{m4}/P_{0s}$  and  $M_{m4}$  known. The analysis also gives information about the ejector flow in addition to the quantities already discussed; examples include the secondary-to-primary inlet static pressure ratio,  $P_{s1}/P_{p1}$ , and the mixed flow specific heat, molecular weight, and stagnation temperature ratios,  $\gamma_m$ ,  $MW_m/MW_p$ , and  $T_{0m}/T_{0p}$ . However, the control volume nature of the model precludes predictions of such flowfield details as the velocity profiles or pressure distributions at given locations in the mixing duct.

### Optimization Procedure

A useful feature of the one-dimensional model described above is that it identifies the pertinent dimensionless variables needed to describe ejector operation. In this *dimensionless* sense, the class of ejector optimization problems considered here can be stated as:

Given the specific heat, molecular weight, and stagnation temperature ratios of the primary and secondary streams,  $\gamma_s$ ,  $\gamma_p$ ,  $MW_s/MW_p$ , and  $T_{0s}/T_{0p}$ , it is desired to determine the primary Mach number,  $M_{p1}$ , and area ratio,  $A_{p1}/A_{m3}$ , such that any of the following three problems can be solved:

- Type 1: Given  $P_{0p}/P_{0s}$  and  $P_{m3}/P_{0s}$ , maximize  $W_s/W_p$
- Type 2: Given  $P_{0p}/P_{0s}$  and  $W_s/W_p$ , maximize  $P_{m3}/P_{0s}$
- Type 3: Given  $W_s/W_p$  and  $P_{m3}/P_{0s}$ , minimize  $P_{0p}/P_{0s}$

From a *dimensional* standpoint, and considering the second-

<sup>1</sup>From this point on, the "A" and "P" subscripts at station 3 will be dropped with the understanding that "actual" conditions are being referred to.

dary inlet stagnation pressure  $P_{0s}$  to be fixed, there are actually four problems contained in these categories: maximization of  $W_s$ , minimization of  $W_p$ , maximization of  $P_{m3}$ , and minimization of  $P_{0p}$ . As mentioned in the introduction, previous investigators have considered one or another of these special cases, although a unified methodology or typical results for the entire set of problem types above has not previously been presented.

It is recognized that other optimization problems are also possible. For example, in certain applications it may be possible by choice of the gases or their supply temperatures to vary  $\gamma_s$ ,  $\gamma_p$ ,  $MW_s/MW_p$ , or  $T_{0s}/T_{0p}$  to obtain improved performance. However, the specific heat and molecular weight ratios tend to be only discretely variable and it is usually only practical to vary the stagnation temperature ratio over a relatively narrow range. In any event, once the gases and stagnation temperatures have been chosen, one is still faced with the optimization problem considered here, i.e., choosing the ejector geometry which maximizes performance.

Note also that the characteristic compression ratio has been taken as the duct exit static pressure ratio  $P_{m3}/P_{0s}$ . This is because the diffuser which can be used in a given system is often subject to spatial constraints, making the choice of its geometry specific to each application. In addition, in many common uses the ejector flow exits directly to the ambient where the boundary condition for uniform subsonic flow is  $P_{m3} = P_{amb}$  (or  $P_{m4} = P_{amb}$  with a diffuser). In these cases, it is therefore the duct exit static, as opposed to the stagnation, pressure which is known. For this reason, and in order to avoid making an arbitrary assumption about the subsonic diffuser geometry, the following discussion and presentation of results will be given in terms of  $P_{m3}/P_{0s}$ . However, the same arguments can be made in terms of the  $P_{0m3}/P_{0s}$ ,  $P_{m4}/P_{0s}$ , or  $P_{0m4}/P_{0s}$  pressure ratios and, in fact, the optimization computer program which has been developed accepts any of these four ratios interchangeably.

In a previous paper (Dutton and Carroll, 1983), the authors presented a method for obtaining ejector designs which minimized  $P_{0p}/P_{0s}$  given  $W_s/W_p$  and  $P_{m3}/P_{0s}$ , i.e., Type 3 problems. Although the technique actually used is numerical, it is convenient to discuss it graphically as follows. For each three-dimensional operating surface, such as that given in Fig. 2, the design parameters  $M_{p1}$  and  $A_{p1}/A_{m3}$  are fixed as are  $\gamma_s$ ,  $\gamma_p$ ,  $MW_s/MW_p$ , and  $T_{0s}/T_{0p}$ . Intersecting this surface with a plane for the given value of  $W_s/W_p$  results in a single operating point along break-off curve a-b-c which, as previously mentioned, are the only points of interest here. Leaving  $M_{p1}$  fixed for the moment, additional breakoff points for this value of  $W_s/W_p$  can be generated from similar three-dimensional surfaces by varying  $A_{p1}/A_{m3}$ , where for each new point there are different values of the stagnation pressure ratio  $P_{0p}/P_{0s}$  and the compression ratio  $P_{m3}/P_{0s}$  (see Fig. 2). This series of breakoff points can then be plotted as a constant  $M_{p1}$  curve on a  $P_{0p}/P_{0s} - A_{p1}/A_{m3}$  graph where  $P_{m3}/P_{0s}$  varies along the curve. This process can then be repeated for new values of  $M_{p1}$  and the given value of  $W_s/W_p$  thereby generating a series of  $M_{p1}$  curves on this graph. In addition, contours of constant  $P_{m3}/P_{0s}$  can be drawn since the variation of the compression ratio along the  $M_{p1}$  curves is known.

An example is presented in Fig. 3, where the  $P_{m3}/P_{0s}$  contours are shown dashed. It is clear that the minimum point (marked with a cross) on each  $P_{m3}/P_{0s}$  contour is a solution to a Type 3 optimization problem. For the fixed  $W_s/W_p$  value of the figure and the  $P_{m3}/P_{0s}$  value of a given dashed contour, the cross point defines the minimum required value of the stagnation pressure ratio  $P_{0p}/P_{0s}$ . In addition, the optimum design Mach number and area ratio,  $M_{p1}$  and  $A_{p1}/A_{m3}$ , can be determined. Now consider a fixed value of  $P_{0p}/P_{0s}$  in Fig. 3, such as along line A-B. It can be seen that for this value of  $P_{0p}/P_{0s}$  and the fixed value of  $W_s/W_p$  for the figure, moving

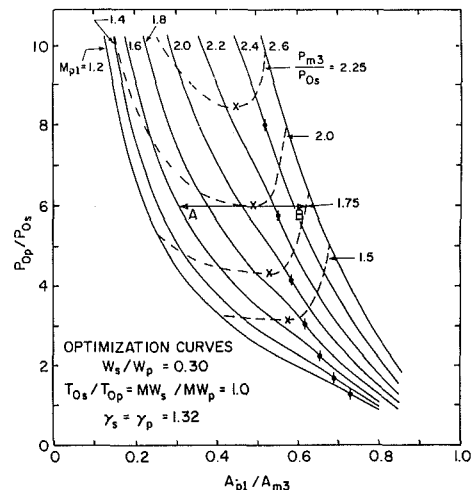


Fig. 3 Ejector optimization curves for fixed mass flow ratio,  $W_s/W_p = 0.3$

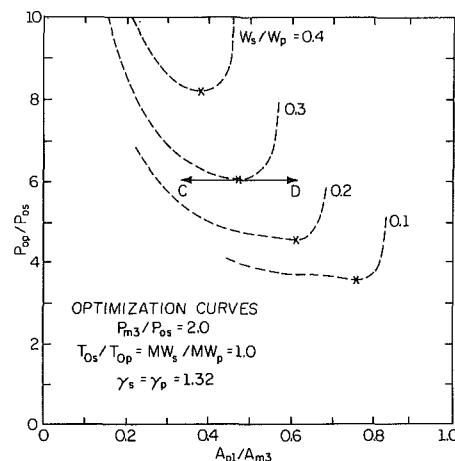


Fig. 4 Ejector optimization curves for fixed compression ratio,  $P_{m3}/P_{0s} = 2.0$

in either direction along A-B away from the minimum point on the dashed curve results in reduced values of the compression ratio  $P_{m3}/P_{0s}$ . Therefore, the cross points marked in the figure also define optimum solutions to Type 2 problems, i.e., maximized values of  $P_{m3}/P_{0s}$  for given values of  $P_{0p}/P_{0s}$  and  $W_s/W_p$ . Note that the solid symbols with the vertical bar through them in Fig. 3 mark the breakoff between the supersonic and saturated supersonic regimes; operating points to the left of this symbol are in the SR while those to the right are in the SSR.

Figure 3 has been generated for a fixed value of the mass flow ratio,  $W_s/W_p$ . Suppose that several such figures are obtained for various values of  $W_s/W_p$  and the same values of  $\gamma_s$ ,  $\gamma_p$ ,  $MW_s/MW_p$ , and  $T_{0s}/T_{0p}$ . Further, suppose that a given  $P_{m3}/P_{0s}$  contour (e.g.,  $P_{m3}/P_{0s} = 2.0$ ) is taken from each of these figures and placed on the same  $P_{0p}/P_{0s} - A_{p1}/A_{m3}$  graph. A typical result is shown in Fig. 4 where the  $P_{m3}/P_{0s} = 2.0$  contours for four values of  $W_s/W_p$  are given with the constant  $M_{p1}$  curves now omitted for clarity. Obviously, the minimum points on the dashed contours are still optimum solutions to Type 3 problems since they yield minimum values of the required  $P_{0p}/P_{0s}$  for given values of  $W_s/W_p$  and  $P_{m3}/P_{0s}$ . However, by considering a constant value of  $P_{0p}/P_{0s}$ , such as along line C-D, and the fixed value of  $P_{m3}/P_{0s}$  for the figure, the cross point is also seen to give the maximum entrainment ratio  $W_s/W_p$  for these conditions.



Thus, these points are also optimized solutions to Type 1 problems since they maximize  $W_s/W_p$  for given values of  $P_{op}/P_{os}$  and  $P_{m3}/P_{os}$ .

The conclusion to be reached from this discussion is that even though the method has been constructed to directly generate optimum solutions to Type 3 problems, it can also be used parametrically to yield optimized solutions to Type 1 and Type 2 problems. Therefore, by employing the technique to find a number of optimum ( $W_s/W_p, P_{m3}/P_{os}, P_{op}/P_{os}$ ) design points, i.e., cross points in Figs. 3 and 4, any of the three problem types can be solved over the range of parameters considered. A convenient way to represent these optimum points is by means of a three-dimensional surface plotted in  $W_s/W_p - P_{m3}/P_{os} - P_{op}/P_{os}$  space as shown in Fig. 5. Each point on the surface represents an optimized solution while points inside the surface are possible but nonoptimum and points outside the surface are not possible. This can be seen by starting at a given point on the surface such as  $E$ . Decreasing  $W_s/W_p$  or  $P_{m3}/P_{os}$ , or increasing  $P_{op}/P_{os}$  from the values at  $E$ , i.e., relaxing the performance requirements, moves one inside the surface to points which are possible but not optimum. The opposite variations in  $W_s/W_p, P_{m3}/P_{os}$ , and  $P_{op}/P_{os}$  move one outside the surface to performance levels which an ejector cannot meet. As previously discussed,  $M_{p1}$  and  $A_{p1}/A_{m3}$  are also determined by the method at each of the optimum points. Therefore, the optimized values of these variables could also be plotted as three-dimensional surfaces against any two of the three performance variables used in Fig. 5, e.g.,  $W_s/W_p$  and  $P_{m3}/P_{os}$ . However, for conciseness such plots are not included.

A FORTRAN computer program, CAEOPT2, has been developed to numerically determine the optimized ejector solutions. Input to the program consists of  $\gamma_s, \gamma_p, MW_s/MW_p, T_{os}/T_{op}, R_E, W_s/W_p$ , and one of the four characteristic compression ratios  $P_{m3}/P_{os}, P_{0m3}/P_{os}, P_{m4}/P_{os}^2$ , or  $P_{0m4}/P_{os}^2$ . If a diffuser is to be included, its pressure recovery coefficient and area ratio,  $C_p$  and  $A_{m4}/A_{m3}$ , must also be input. The optimal solution is then located iteratively yielding the following output parameters: the minimum required value of  $P_{op}/P_{os}$ , the optimum ejector design parameters  $M_{p1}$  and  $A_{p1}/A_{m3}$ , the inlet secondary Mach number and static pressure ratio,  $M_{s1}$  and  $P_{s1}/P_{p1}$ , and the exit Mach numbers and pressure ratios,  $M_{m3}, M_{m4}^2, P_{m3}/P_{os}, P_{0m3}/P_{os}, P_{m4}/P_{os}^2$ , and  $P_{0m4}/P_{os}^2$ . The mixed flow properties  $\gamma_m, MW_m/MW_p$ , and  $T_{0M}/T_{0p}$  are also printed. Further details concerning the numerical techniques and use of CAEOPT2 are contained in a separate report (Carroll and Dutton, 1985).

## Results and Discussion

Although the three-dimensional optimization surface shown in Fig. 5, and the companion surfaces for  $M_{p1}$  and  $A_{p1}/A_{m3}$  (not shown), are useful for qualitative discussions of optimum ejector operation, two-dimensional diagrams are more easily used for quantitative applications. Two series of design diagrams are presented in Figs. 6(a)–(c) and 7(a)–(c) for the commonly encountered case of diatomic primary and secondary gases,  $\gamma_s = \gamma_p = 1.4$ , with equal molecular weights and stagnation temperatures,  $MW_s/MW_p = T_{os}/T_{op} = 1.0$ . In addition, the ejector pressure recovery coefficient used in these results is  $R_E = 0.8$  (Petrie, 1980; Dutton et al., 1982). Figure 6 considers relatively high compression ratio/low entrainment ratio cases,  $0.75 \leq P_{m3}/P_{os} \leq 5$  and  $0.05 \leq W_s/W_p \leq 0.5$ , while Fig. 7 gives results for relatively high entrainment ratios and low compression ratios,  $0.5 \leq W_s/W_p \leq 2.5$  and  $0.75 \leq P_{m3}/P_{os} \leq 1.75$ . In both series the stagnation pressure range is limited to  $1.5 \leq P_{op}/P_{os} \leq 100$ .

<sup>2</sup>These quantities are meaningful only if a diffuser is present.

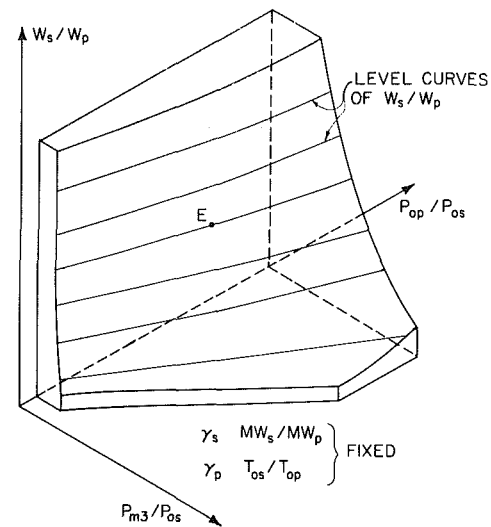


Fig. 5 Three-dimensional ejector optimization surface for performance variables  $W_s/W_p, P_{m3}/P_{os}$ , and  $P_{op}/P_{os}$

There are a large number of parametric trends embodied in the results of Figs. 6 and 7, and their discussion depends on the viewpoint taken, i.e., whether optimization problems of Types 1, 2, or 3 are of interest. Therefore, only a few general statements will be made. The performance tradeoffs inherent in a supersonic ejector system are evident in Figs. 6(a) and 7(a), which are projections of three-dimensional optimization surfaces such as Fig. 5 onto the  $P_{op}/P_{os} - P_{m3}/P_{os}$  base plane. As an example of the tradeoffs, if the stagnation pressure ratio  $P_{op}/P_{os}$  is fixed by system constraints, increasing the desired  $W_s/W_p$  entrainment ratio results in a reduced  $P_{m3}/P_{os}$  compression ratio and vice versa. Similar intuitively clear trends can be seen in Figs. 6(a) and 7(a) for fixed values of  $P_{m3}/P_{os}$  and  $W_s/W_p$ . Noting that a log scale is used for  $P_{op}/P_{os}$ , it is also seen that relatively small increases in  $P_{m3}/P_{os}$  can lead to quite large increases in the required values of  $P_{op}/P_{os}$ , especially for large  $W_s/W_p$ . The optimum values of the primary Mach number and ejector area ratio are presented in Figs. 6(b)–(c) and 7(b)–(c). These figures demonstrate the less obvious trends that for fixed  $P_{m3}/P_{os}$  and increasing  $W_s/W_p$  or vice versa (both requiring increased  $P_{op}/P_{os}$ ), the optimum value of  $M_{p1}$  increases while that for  $A_{p1}/A_{m3}$  is reduced. The change in slope evident in the curves of Figs. 6(b)–(c) and 7(b)–(c) occurs at a change in flow regime; to the left of the slope change the optimum operating point occurs in the SSR (along b–c in Fig. 2) while to the right the optimum point is in the SR (along a–b).

A design consideration not previously discussed is the static pressure ratio at the inlet location,  $P_{s1}/P_{p1}$ . Values of this parameter which differ greatly from unity are indicative of possible separation problems at the inlet and attendant poor ejector performance (Dutton et al., 1982). At the extreme left hand end points of the optimization curves in Figs. 6 and 7,  $P_{s1}/P_{p1}$  is in the range from 1.36 to 1.72. However, as  $P_{m3}/P_{os}$  is increased along each curve, the predicted value of  $P_{s1}/P_{p1}$  falls very rapidly such that it is very near unity for nearly the entire domain of optimized solutions plotted in Figs. 6 and 7. Other operating parameters of possible interest are the secondary inlet and mixing tube exit Mach numbers,  $M_{s1}$  and  $M_{m3}$ . For the optimized solutions plotted in Figs. 6 and 7, these variables are in the ranges  $0.51 \leq M_{s1} \leq 1.0$  and  $0.56 \leq M_{m3} \leq 0.88$ .

Also of interest is the computer time necessary to determine the optimized designs. Because of the simplified nature of the one-dimensional flow model, the calculation of any given

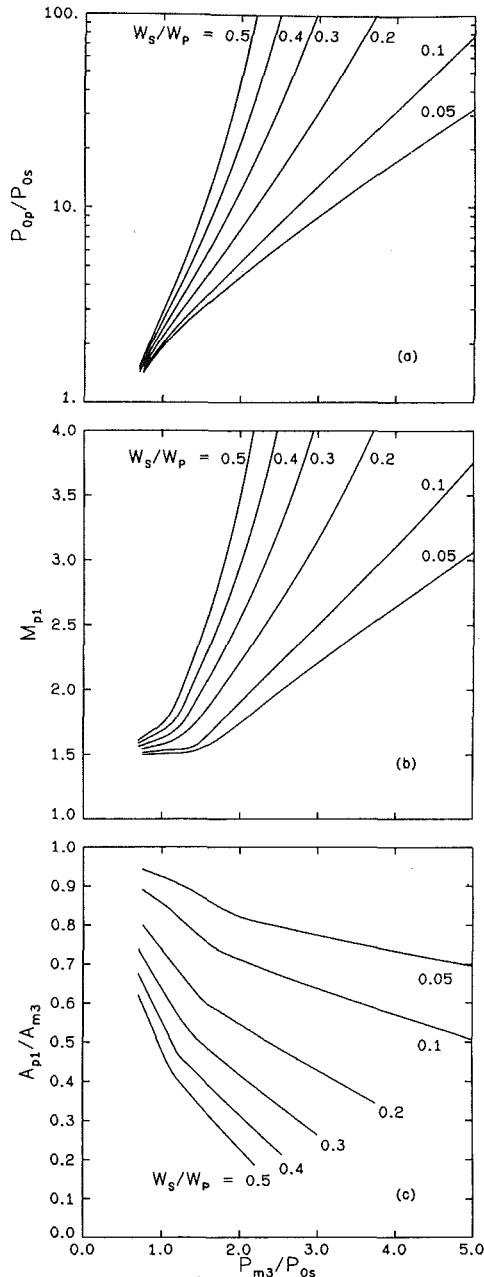


Fig. 6 Optimized ejector design curves for high compression/low entrainment ratios and  $\gamma_s = \gamma_p = 1.4$ ,  $MW_s/MW_p = T_{0s}/T_{0p} = 1.0$ ,  $R_E = 0.8$ : (a) performance variables, (b) primary Mach number, and (c) area ratio

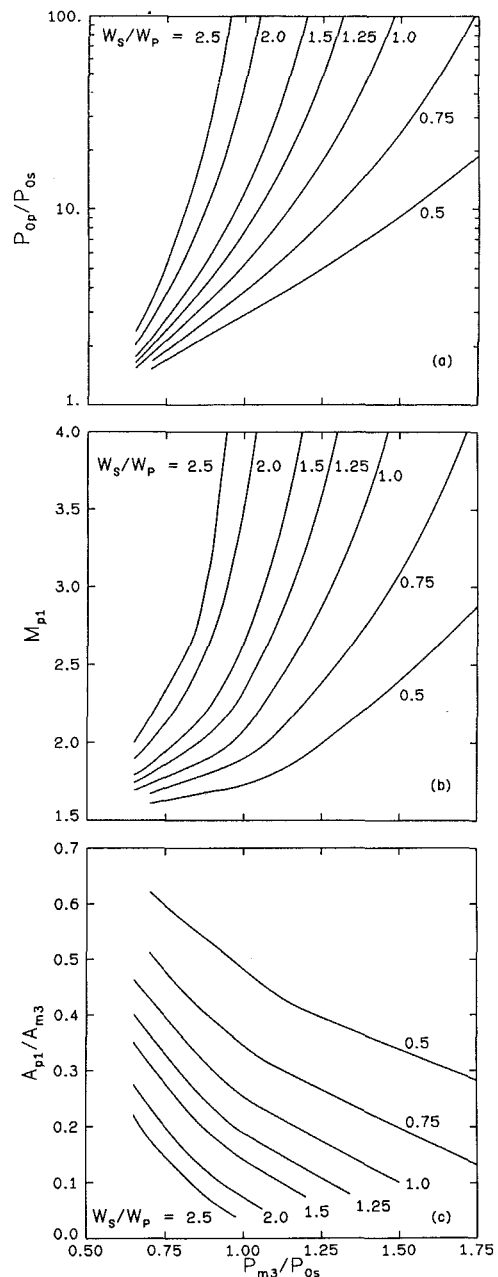


Fig. 7 Optimized ejector design curves for high entrainment/low compression ratios and  $\gamma_s = \gamma_p = 1.4$ ,  $MW_s/MW_p = T_{0s}/T_{0p} = 1.0$ ,  $R_E = 0.8$ : (a) performance variables, (b) primary Mach number, and (c) area ratio

operating point is extremely efficient. For example, to determine a typical SR breakoff point for fixed geometry along curve *a-b* in Fig. 2 requires approximately 0.05 CPU seconds on the University of Illinois CDC Cyber 175 computer. However, because of the large number of iterations required, determining optimized solutions is much more time-consuming. In fact,  $7\frac{1}{2}$  CPU minutes were required to generate the data for Fig. 6 (86 total optimization points) and nearly 10 minutes for Fig. 7 (84 total points) on the same computer. Use of more detailed, multi-dimensional flow models in the optimization method would clearly lead to exorbitant computational costs.

The results of Figs. 6 and 7 are directly and quantitatively useful to the ejector designer, provided the parameters are in the range of interest. Use of these results is straightforward and, hopefully, it is now clear that the key graph in each series is the first, Fig. 6(a) or 7(a). Given two of the three per-

formance parameters,  $W_s/W_p$ ,  $P_{m3}/P_{0s}$ , or  $P_{op}/P_{0s}$ , the optimized value of the third can be determined from these figures, i.e., maximized  $W_s/W_p$ , maximized  $P_{m3}/P_{0s}$ , or minimized  $P_{op}/P_{0s}$  for problem Types 1, 2, and 3, respectively. From a fundamental standpoint, this information tells the designer whether or not an ejector is even capable of accomplishing a proposed task or, alternately, quantifies its performance limits. Then with  $P_{m3}/P_{0s}$  and  $W_s/W_p$  known, the primary Mach number and area ratio,  $M_{p1}$  and  $A_{p1}/A_{m3}$ , of the optimized design can be determined from Figs. 6(b) and (c) or 7(b) and (c). As previously discussed, the system pressure recovery can also be increased above the level at mixing duct exit location 3 by addition of a subsonic diffuser.

Knowing the  $M_{p1}$  and  $A_{p1}/A_{m3}$  design variables, as well as the operating conditions, it is then a simple matter to determine the physical dimensions of the ejector system. Application of a mass flow expression, use of the isentropic area ratio

function, and knowledge of the optimum value of  $A_{p1}/A_{m3}$ , allow the successive determination of the primary nozzle throat and exit areas,  $A_p^*$  and  $A_{p1}$ , and the mixing tube area,  $A_{m3}$ . A geometric variable which cannot be specified by the analysis, due to its control volume form, is the mixing duct length,  $L$ . However, previous experiments (Petrie, 1980; Dutton et al., 1982; and Deleo et al., 1962) have shown that duct length-to-hydraulic diameter ratios in the range  $8 \leq L/D_h \leq 12$  are generally sufficient. For shorter ducts the mixing between the primary and secondary streams may not be complete at the exit (although such conditions may be mandated by length or weight constraints as in aircraft thrust augmentation), while longer ducts suffer unnecessary wall friction losses. An example of sizing an ejector system for a particular Type 3 optimization application has been given previously (Dutton and Carroll, 1983).

## Conclusions

A technique for determining optimized supersonic ejector designs for a large class of problems typically encountered in practice has been developed. Given the primary and secondary gases and their stagnation temperatures,  $\gamma_s$ ,  $\gamma_p$ ,  $MW_s/MW_p$ , and  $T_{0s}/T_{0p}$ , the method seeks the values of the design parameters  $M_{p1}$  and  $A_{p1}/A_{m3}$  which optimize one of the performance variables  $W_s/W_p$ ,  $P_{m3}/P_{0s}$ , or  $P_{0p}/P_{0s}$  given the values of the other two. Although the numerical method solves only  $P_{0p}/P_{0s}$  minimization problems directly, it can be employed to generate optimization surfaces in  $W_s/W_p - P_{m3}/P_{0s} - P_{0p}/P_{0s}$  space which can then be used for any of the three possible problem types. Example design curves are presented for the typical gas property values  $\gamma_s = \gamma_p = 1.4$  and  $MW_s/MW_p = T_{0s}/T_{0p} = 1.0$ . These curves show not only the quantitative performance limits of a supersonic ejector system but also give the optimum values of the design parameters  $M_{p1}$  and  $A_{p1}/A_{m3}$  necessary to achieve these limits. Knowledge of these two quantities, together with the primary and secondary gas properties, stagnation conditions, and mass flowrates, allow the determination of the physical dimensions of the optimal ejector system for the given application. The computer program, CAEOPT2, developed during this study can also be used to generate design curves for other parameter values and operating ranges of interest.

## Acknowledgments

This research was supported in part by an Office of Naval Research Graduate Fellowship for B. F. Carroll and by the Department of Mechanical and Industrial Engineering.

## References

- Addy, A. L., Dutton, J. C., and Mikkelsen, C. D., 1981, "Supersonic Ejector-Diffuser Theory and Experiments," Report No. UILU-ENG-82-4001, Department of Mechanical and Industrial Engineering, University of Illinois at Urbana-Champaign, Urbana, Ill.
- Anderson, B. H., 1974, "Computer Program for Calculating the Flowfield of Supersonic Ejector Nozzles," Report No. NASA TN D-7602, NASA-Lewis Research Center, Cleveland, Ohio.
- Carroll, B. F., and Dutton, J. C., 1985, "CAEOPT2: A Computer Program for Supersonic Ejector Optimization," Report No. UILU-ENG-85-4006, Department of Mechanical and Industrial Engineering, University of Illinois at Urbana-Champaign, Urbana, Ill.
- Chow, W. L., and Addy, A. L., 1964, "Interaction Between Primary and Secondary Streams of Supersonic Ejector Systems and Their Performance Characteristics," *AIAA Journal*, Vol. 2, No. 4, pp. 686-695.
- Chow, W. L., and Yeh, P. S., 1965, "Characteristics of Supersonic Ejector Systems with Nonconstant Area Shrouds," *AIAA Journal*, Vol. 3, No. 3, pp. 525-527.
- Deleo, R. V., Rose, R. E., and Dart, R. S., 1962, "An Experimental Investigation of the Use of Supersonic Driving Jets for Ejector Pumps," *ASME Journal of Engineering for Power*, Vol. 84, pp. 204-212.
- Dutton, J. C., Mikkelsen, C. D., and Addy, A. L., 1982, "A Theoretical and Experimental Investigation of the Constant Area, Supersonic-Supersonic Ejector," *AIAA Journal*, Vol. 20, No. 10, pp. 1392-1400.
- Dutton, J. C., and Carroll, B. F., 1983, "Optimized Ejector-Diffuser Design Procedure for Natural Gas Vapor Recovery," *ASME Journal of Energy Resources Technology*, Vol. 105, No. 3, pp. 388-393.
- Emanuel, G., 1976, "Optimum Performance for a Single-Stage Gaseous Ejector," *AIAA Journal*, Vol. 14, No. 9, pp. 1292-1296.
- Fabri, J., and Siestrunck, R., 1958, "Supersonic Air Ejectors," *Advances in Applied Mechanics*, Vol. V, Academic Press, New York, pp. 1-34.
- Hasinger, S. H., 1978, "Ejector Optimization," Report No. AFFDL-TR-78-23, Air Force Flight Dynamics Laboratory, Wright-Patterson Air Force Base, Ohio.
- Hedges, K. R., and Hill, P. G., 1974, "Compressible Flow Ejectors, Part I-Development of a Finite-Difference Flow Model," *ASME Paper No. 74-FE-1*.
- Hickman, K. E., Hill, P. G., and Gilbert, G. B., 1972, "Analysis and Testing of Compressible Flow Ejectors with Variable Area Mixing Tubes," *ASME Journal of Basic Engineering*, Vol. 94, pp. 407-416.
- Loth, J. L., 1966, "Theoretical Optimization of Staged Ejector Systems, Part I," Report No. AEDC-TR-66-2, Arnold Engineering Development Center, Arnold Air Force Station, Tenn.
- Loth, J. L., 1968, "Theoretical Optimization of Staged Ejector Systems, Part II," Report No. AEDC-TR-68-80, Arnold Engineering Development Center, Arnold Air Force Station, Tenn.
- Mikkelsen, C. D., Sandberg, M. R., and Addy, A. L., 1976, "Theoretical and Experimental Analysis of the Constant-Area, Supersonic-Supersonic Ejector," Report No. UILU-ENG-76-4003, Department of Mechanical and Industrial Engineering, University of Illinois at Urbana-Champaign, Urbana, Ill.
- Petrie, H. L., 1980, "An Experimental and Theoretical Investigation of Multiple Ducted Streams with a Periodic or a Steady Supersonic Driver Flow," M.S. thesis, Department of Mechanical and Industrial Engineering, University of Illinois at Urbana-Champaign, Urbana, Ill.
- Porter, J. L., and Squyers, R. A., 1981, "A Summary/Overview of Ejector Augmentor Theory and Performance," ATC Report No. R-91100/9CR-47A, Vought Corporation Advanced Technology Center, Dallas, Texas.
- Runstadler, P. W., Dolan, F. X., and Dean, R. C., 1975, *Diffuser Data Book*, 1st Edition, Creare Technical Information Service, Hanover, New Hampshire, pp. 1-88.
- Shen, H., Dong, E., Shyur, T., and Kee, M., 1981, "The Sweep Finite Element Method for Calculating the Flow Field and Performance of Supersonic Ejector Nozzles," *Proceedings: Fifth International Symposium on Airbreathing Engines*, available from M. S. Ramachandra, National Aeronautical Laboratory, Bangalore, India, pp. 15-1-15-5.
- Wacholder, E., and Dayan, J., 1984, "Application of the Adjoint Sensitivity Method to the Analysis of a Supersonic Ejector," *ASME Paper No. 84-WA/FE-2*.

# Cavitation Inception on a Circular Cylinder at Critical and Supercritical Flow Range

A. Ihara

Associate Professor,  
Institute of High Speed  
Mechanics,  
Tohoku University,  
Sendai, Japan

H. Murai

Professor,  
Hiroshima Institute of  
Technology,  
Hiroshima, Japan

*Cavitation tests were performed in the critical and supercritical flow range on circular cylinders with and without boundary layer trip. Mean and fluctuating static pressures were measured on the smooth circular cylinder from  $\theta = 0$  to  $180^\circ$  and on the tripped surface at  $\theta = 104$  and  $106^\circ$  corresponding to tripping wire location  $\alpha = 38$  and  $40$  deg. Through these measurements it was found that cavitation that closely resembles bubble ring cavitation reported on axisymmetric bodies took place in a reattachment region of the laminar separation bubble for the critical flow range where the laminar separation bubble was present. For the supercritical flow range where the laminar separation bubble disappeared, smooth cavitation with small irregular bubbles at its rear part took place at a location about  $100^\circ$  from the stagnation point.*

## Introduction

Since the work of Arakeri and Acosta [1] on a hemispherically-nosed body with the schlieren technique of flow visualization, viscous effects in inception of cavitation on axisymmetric bodies seems to have reinterested many investigators. Now it has been suggested that laminar separation and turbulent transition play a significant role in the mechanism of cavitation inception.

With regard to the viscous effect in inception of cavitation on two dimensional bodies, only a few works [2-4] can be found in spite of its industrial importance. This work has the intention of providing further understanding of the viscous effects on the inception of cavitation, in particular, on two dimensional bodies, in order to determine (1) the various types of limited cavitation which can occur at a particular state of the boundary layer, (2) the correlation between the incipient cavitation number and the pressure coefficient, (3) the dependency of the incipient cavitation number on cavitation nuclei, using circular cylinders for the test body. For these bodies the boundary layer is very sensitive to Reynolds number, surface roughness, and free-stream turbulence. Reynolds number effects on cavitation appearance have been reported by Wykes [5, 6] with changing water temperature but not quite so detailed because they have not included pressure fluctuation data. In this text, the critical flow means the presence of laminar separation bubble and the supercritical flow means the disappearance of laminar separation bubble. Supercritical flow conditions were realized by using a tripping device.

## Experimental Methods

**Test Models.** Two types of circular cylinders were used in

this experiment. One of them was a smooth circular cylinder made from brass with a diameter  $D=48$  mm and a length  $L=101.5$  mm. The accuracy of the cylinder diameter was within  $10 \mu\text{m}$ . The surface was polished so that the height of the roughness was within  $1 \mu\text{m}$ . The other was a circular cylinder with a tripping device on one side. A steel wire with a diameter  $d=0.19$  mm was installed with the help of contact cement in a groove which was machined on the surface. The height of the trip from the model surface was  $0.13$  mm. The location of the trip from the stagnation point was set at  $30, 36, 38, 40, 42,$  and  $44^\circ$  by rotating the cylinder around its longitudinal axis.

**Cavitation Tests.** The test bodies were mounted in the measuring section of  $101.6$  mm in width and  $260$  mm in height of the cavitation tunnel in the Institute of High Speed Mechanics, Tohoku University. Details of this facility can be seen in reference [7]. The free-stream turbulence level in this test section was  $0.73$  percent at a tunnel speed of  $9.04$  m/s as measured by a counter type Laser Doppler Velocimeter (55X System, DISA) connected to a minicomputer system (OKITAC 50/40, OKI Electric Company). Pressure measurements for the computation of free stream velocity and cavitation number were made with differential pressure transducers. The air content of the tunnel water was measured with a Van Slyke type air contentmeter which had been designed by Numachi [8] and was found to be between  $31$  and  $34$  PPM for the test run and was always oversaturated. Microscopic air bubbles in the tunnel water were monitored using a light scattering system in the  $161$  mm width and  $602$  mm height two dimensional section upstream of the test section. Details of the apparatus of the nucleus measuring system can be found in reference [9].

In general, the incipient cavitation conditions were observed by holding the tunnel velocity fixed and gradually reducing the

Contributed by the Fluids Engineering Division for publication in the JOURNAL OF FLUIDS ENGINEERING. Manuscript received by the Fluids Engineering Division February 19, 1985.

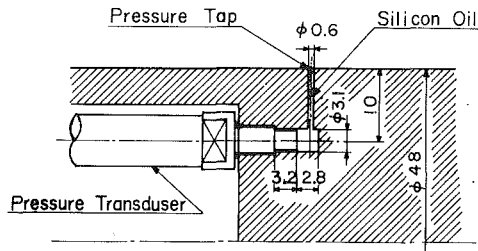
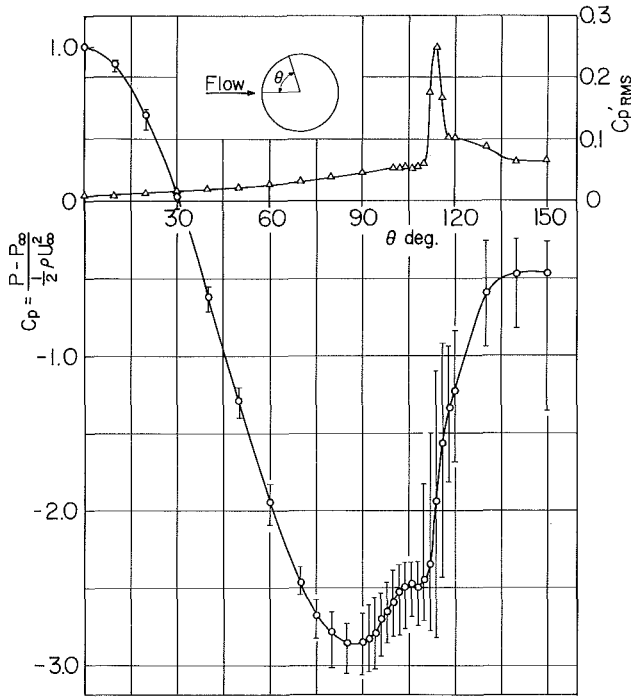
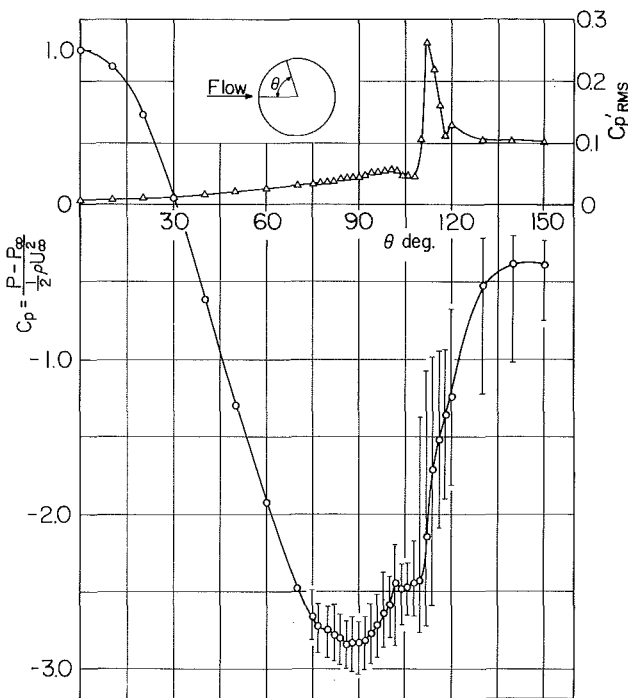


Fig. 1 Schematic diagram of the pressure transducer attached in the circular cylinder, unit is mm



(a)  $U_{\infty} = 8.31 \text{ m/s}$ ,  $Re = 2.83 \times 10^5$



(b)  $U_{\infty} = 9.72 \text{ m/s}$ ,  $Re = 3.20 \times 10^5$

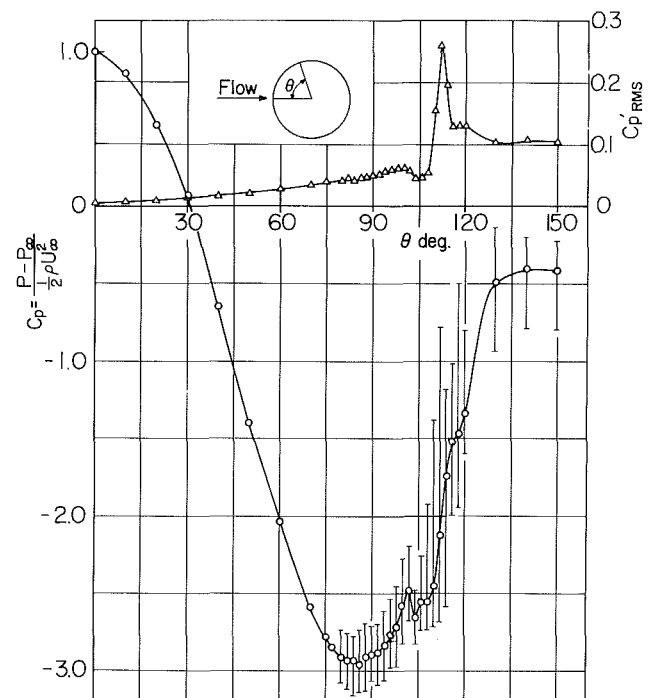
tunnel static pressure until the presence of cavitation near or on the body was visually observed under the illumination of stroboscopic light. At this point, all the indicator readings from differential transducers were recorded and the indicator readings of the light scattering system were photographed.

Cavitation number was calculated from the following equation

$$\sigma = 2(P_{\infty} - P_v) / \rho U_{\infty}^2 \quad (1)$$

where  $P_{\infty}$ ,  $P_v$ , and  $U_{\infty}$  are static pressure of the free stream, vapor pressure corresponding to the working water temperature and free-stream velocity, respectively. Cavitation tests were conducted for tunnel speeds from 8.3 m/s to 10.8 m/s and the tunnel water temperature was between 6.8 and 9.0°C.

**Mean and Fluctuating Static Pressure Measurements.** Static pressure measurements on a 48 mm diameter cylinder were performed in the test section. As illustrated in Fig. 1, a pressure hole of 0.6 mm diameter and 8.5 mm long, followed by a Helmholtz Chamber of 3.1 mm diameter and 2.8 mm long was employed. The hole and the Helmholtz Chamber was filled with silicon oil with kinematic viscosity of  $5.0 \times 10^{-4} \text{ m}^2/\text{s}$  (500cSt) at 15°C and degassed about one hour. A semiconductor type pressure transducer (PMS-3-2H, Toyoda Machine Work Company) with an active diameter of 3 mm and natural frequency of about 40 kHz was employed for measurements of the mean and fluctuating static pressures. The relation between an output through a linear amplifier (AA 1130, Toyoda Machine Work Company) and real pressure were calibrated using a standard pressure gauge. The outputs from the pressure transducer through the linear amplifier were processed on-line by the minicomputer described above. At the same time, outputs from the two differential pressure transducers were processed on-line by this minicomputer to calculate the tunnel speed and the static pressure at the test section. The signal from the pressure transducer was digitized at a rate of 4 kHz with an accuracy of 12 bits so that the peak could be found in the signal at about



(c)  $U_{\infty} = 10.81 \text{ m/s}$ ,  $Re = 3.63 \times 10^5$

Fig. 2 Pressure coefficients on the smooth surface, bar is range

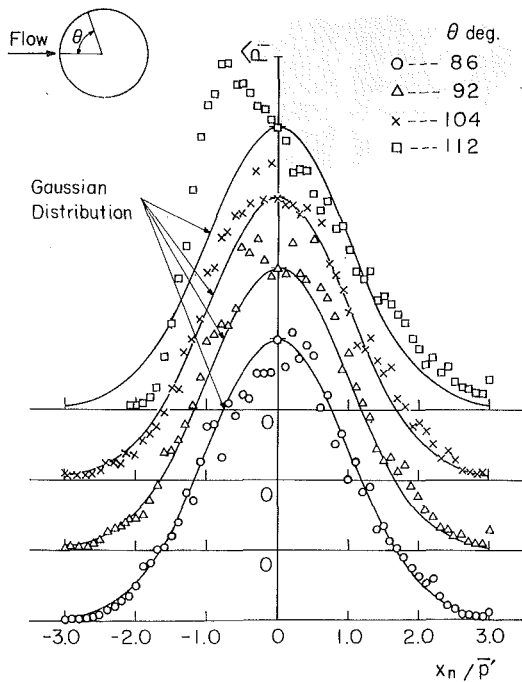


Fig. 3 Probability density distribution of fluctuating pressures on the smooth surface,  $x_n$  is fluctuating component,  $\bar{p}'$  is RMS of fluctuation  $U_\infty = 9.72$  m/s,  $Re = 3.20 \times 10^5$

2.3 kHz associated with Helmholtz resonance of the transducer/hole, chamber. Data were stored throughout 8 second to one location. The signals from the differential pressure transducers were also sampled to the same minicomputer at a rate of 500 Hz throughout 2 second with the same accuracy. The mean free-stream velocity and the mean static pressure at the test section were calculated from these data and used to calculate the pressure coefficient around the test body. The mean pressure coefficient  $\bar{C}_p$ , temporally maximum and minimum pressure coefficient  $C_{p_m}$ , root mean square of fluctuating pressure coefficient  $C_{p'RMS}$ , probability density distribution  $\hat{P}_i$  and power spectrum  $G(f)$  of the fluctuations were calculated from the sampled data using the following equations

$$C_{p_m} = 2(P_n - P_\infty) / \rho U_\infty^2 \quad (2)$$

$$\bar{C}_p = 2(\bar{P} - P_\infty) / \rho U_\infty^2 \quad (3)$$

where

$$\bar{P} = \left( \sum_{n=1}^N P_n \right) / N \quad (4)$$

$$C_{p'RMS} = 2\bar{p}' / \rho U_\infty^2 \quad (5)$$

where

$$\bar{p}' = \left[ \sum_{n=1}^N x_n^2 / (N-1) \right]^{1/2} \quad (6)$$

and

$$x_n = P_n - \bar{P} \quad (7)$$

$$\hat{P}_i = \text{Prob}[x_{i-1} < x < x_i] = N_i / \sqrt{2\pi N} \quad (8)$$

$$G(f) = |X_f|^2 / N^2 \quad (9)$$

where

$$X_f = \sum_{n=1}^N x_n \text{EXP}[-j2\pi fn / N] \quad (10)$$

Reynolds number was defined as follows

$$Re = DU_\infty / \nu \quad (11)$$

where  $\nu$  is kinematic viscosity of the test water.

Measurements were performed from  $\theta=0$  to  $180^\circ$  with pressure tap spacing of  $2^\circ$ , by turning the cylinder around its longitudinal axis from  $\theta=0$  (front stagnation point) to  $180^\circ$ . After the measurements on the smooth surface, a tripping wire was installed on the surface of the same test body so that the pressure hole would be located near to the region of a separation zone on the smooth surface. Measurements were performed between  $\theta=104$  to  $106^\circ$  turning the cylinder and changing the tunnel speed from 7.5 m/s to 10.5 m/s.

## Experimental Results

**Pressure Coefficients on the Smooth Surface.** The pressure distribution around a circular cylinder in a critical flow range has been measured by many authors [10-13]. Reported data, however, have been considerably different from each other even at the same Reynolds number. Moreover, existing data, Batham's [14] for example, have not revealed the precise aspect in or near a separation bubble, due to relatively large spacing of  $15^\circ$  between pressure taps. Therefore the necessity of measuring the mean and fluctuating pressure in detail over the range of Reynolds number tested arose. Figures 2(a), (b) and (c) show measured results of the mean static pressures and root mean squares of fluctuating pressure at the different Reynolds number in pressure coefficient form. From these figures, it can be seen that the flow separates at about  $106^\circ$  for  $Re=2.83 \times 10^5$ , and at about  $102^\circ$  for  $Re=3.20 \times 10^5$  and  $3.63 \times 10^5$ . Root mean squares of fluctuating pressure coefficients show the peaks at an angle of  $\theta=104$  and  $114^\circ$ , for  $Re=2.83 \times 10^5$ , at  $100$  and  $112^\circ$  for  $Re=3.20 \times 10^5$  and  $3.63 \times 10^5$ . It may be said that the former corresponds to just upstream of laminar separation and the latter corresponds to the center of the reattachment region of laminar separation. Maximum of  $C_{p'RMS}$  amounts to 27 percent of the dynamic head. Inside the laminar separation bubble there is a place where the mean static pressure and root mean squares of fluctuation become the minimum value, and fluctuations take relatively low values. Figure 3 shows the probability density distributions of fluctuating pressures for  $Re=3.20 \times 10^5$ . The distributions measured at  $\theta=86, 92$  and  $104^\circ$  are almost Gaussian. However, the distribution at  $112^\circ$ , that corresponds to the center of the reattachment region of laminar separation, is extremely skewed. It can be seen from this figure that the maximum occurrence of fluctuating pressure happens at  $x_n = -0.75 \bar{p}'$  and the occurrence at  $x_n < -2.0 \bar{p}'$  is considerably low in comparison with the Gaussian distribution. The fact that the maximum occurrence of fluctuating pressure happens at  $x_n = -0.75 \bar{p}'$  and  $\bar{p}'$  is about 27 percent of dynamic head suggests us that the nuclei may have mach chance of growing in a reattachment region. Figure 4 shows the power spectrum of fluctuating pressures for the same Reynolds number  $Re=3.20 \times 10^5$ , and it can be seen that at  $\theta=112^\circ$  the level of fluctuating pressures is considerably higher particularly in the high frequency range in comparison with the value at the other locations. Arakeri [15] found two peaks in the power spectrum of fluctuating pressure in the reattachment region for a hemispherically nosed body, and indicated that the peak pressure at higher frequencies may represent the most unstable transitional wave in the separated free shear layer and the peak at lower frequencies may represent the gross unsteadiness of the reattachment region itself. In our case, however, such a peak which represents the unstable transitional wave could not be found in the reattachment region for the frequency range measured, but a peak which may represent the gross unsteadiness of the separation point was found at about 110 Hz for  $\theta=86, 92$ , and  $104^\circ$ .

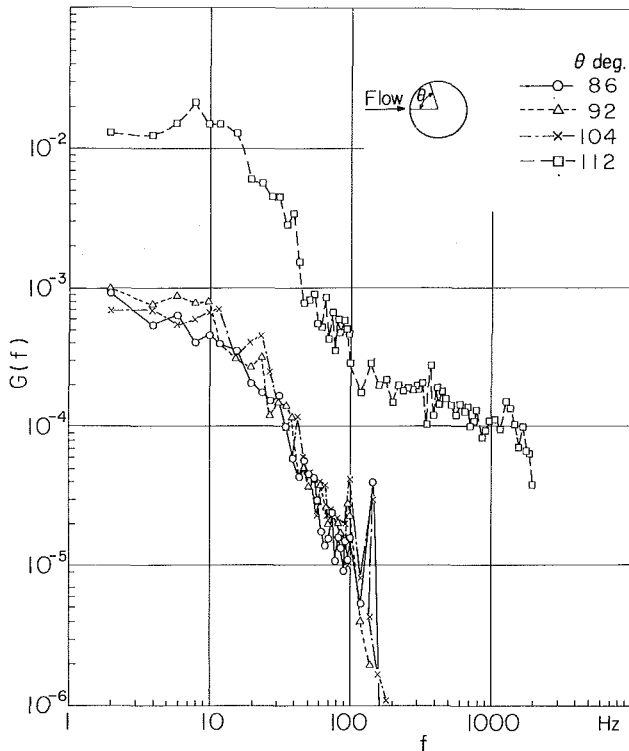


Fig. 4 Power spectrum of fluctuating pressures on the smooth surface,  $U_\infty = 9.72$  m/s,  $Re = 3.20 \times 10^5$

**Cavitation on the Smooth Surface.** The physical appearance of cavitation on the smooth surface are shown in Fig. 5 at different cavitation numbers. This cavitation appears for all Reynolds numbers tested as macroscopic irregularly-shaped bubbles (Fig. 5(a)) which appear and disappear within a very narrow region between  $\theta = 110$  and  $120^\circ$  where, as pointed out in preceding section, is a reattachment region of laminar separation. Under normal lighting, this type of cavitation appears as a fuzzy line fixed on the model. As this cavitation closely resembles the bubble ring cavitation, this cavitation will be called "bubble line" cavitation in the following. At lower cavitation numbers, smooth cavity can be found in some places (Fig. 5(c)) just upstream of bubble line cavitation. The beginning of this cavity originated at an angle of about  $104^\circ$  for the Reynolds number tested. This cavitation did not develop to the clear band-type cavitation as reported on the hemispherically nosed body. Incipient cavitation data for the bubble line cavitation are shown in Fig. 6 plotted with the pressure data measured in this experiment.

**Discussion of Bubble Line Cavitation.** In the recent analysis [16-18] of bubble ring cavitation based on bubble-dynamic consideration, Parkin hypothesized that a microbubble grows in a separation bubble by air diffusion, until the bubble has become large enough to interact with free shear layer. Then the bubble moves to the downstream end of the laminar bubble where the boundary layer becomes turbulent and being exposed to low pressures in turbulent eddies grows to a visible bubble vaporously. In order to confirm the applicability of his hypothesis to this type of cavitation found in this work, magnified still photographs were taken. From the photograph as shown in Fig. 7, a few visible bubbles can be found inside the laminar separation bubble but the most of them can be found in growing and being torn apart in the reattachment region where the fluctuation of the static pressure is violent. One can also recognize from the same figure that the

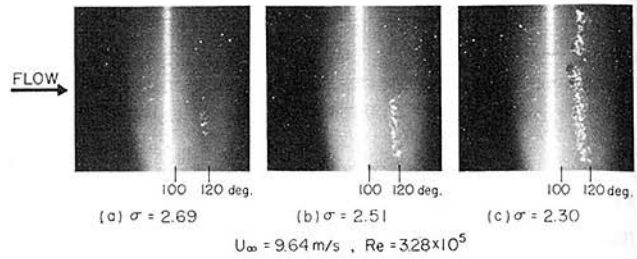


Fig. 5 Still photographs of bubble line cavitation on the smooth surface at  $Re = 3.28 \times 10^5$

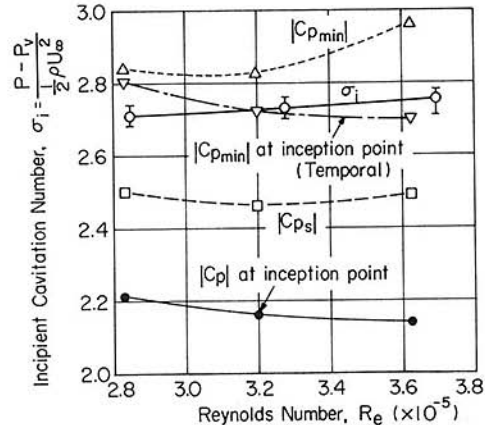


Fig. 6 Comparison of cavitation number and the pressure data for bubble line cavitation on the smooth surface, bar is range

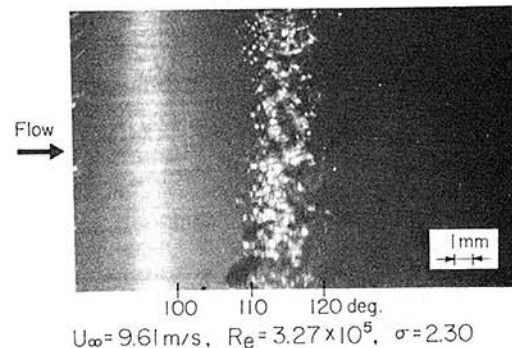


Fig. 7 Magnified still photograph of bubble line cavitation on the smooth surface

Table 1 Comparison of incipient cavitation indexes to predicted values

Reynolds Number $\times 10^{-5}$	2.83	3.27	3.63
Incipient Cavitation Number	2.71	2.73	2.75
$-C_p + C_{pRMS}$ at Transition Point	2.52	2.54	2.62
$-C_p + C_{pRMS}$ at Inception Point	2.19	2.42	2.40
$-C_{pMIN}$ at Inception Point	2.83	2.73	2.70

bubbles with about 0.06 mm in width at the front region of the reattachment region abruptly grow to about 2 mm in width at the center and disappear at the rear of the reattachment region. For bubble ring cavitation, Holl and Carroll [19] have proposed that  $\sigma_i$  can be expressed as follows

$$\sigma_i = |C_{PT}| + \Delta\sigma \quad (12)$$

where

$C_{PT}$ : the pressure coefficient at the transition point

$\Delta\sigma$ :  $2P'_R / \rho U_\infty^2$

$P'_R$ : is the fluctuating pressure in the reattachment region.

In their case,  $\Delta\sigma$  was about 0.03. In order to confirm the applicability of equation (12) to this type of cavitation, calculation using equation (12) was performed and compared with measured results, although a slight discrepancy in Reynolds



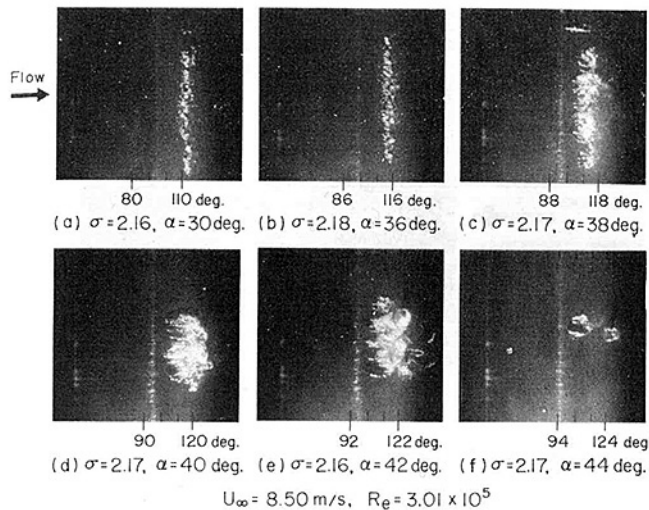


Fig. 8 Change in physical appearance of cavitation with angle  $\alpha$  of tripping wire

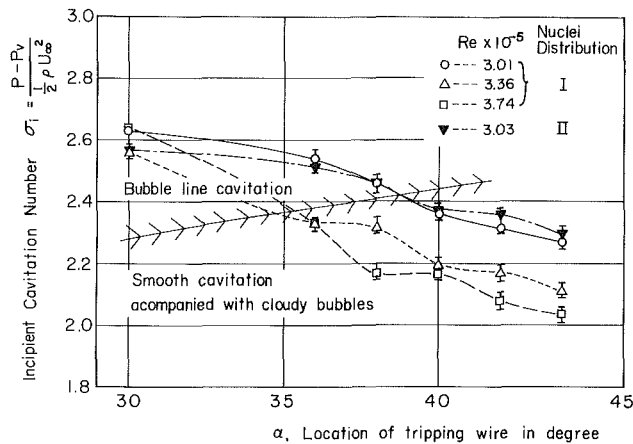


Fig. 9 Incipient cavitation number on the tripped surface, nuclei size distributions I and II are shown as conditions I and II in Fig. 11, bar size range

numbers exists between pressure measurements and inception measurements.

Results are shown in Table 1. The transition point was defined, following to Holl and Carroll [19], to be located where the mean pressure coefficients start to increase abruptly. In our case, it can be seen from Fig. 6 and Table 1, that  $\sigma_i$  closely coincides with the absolute value of the temporal minimum pressure coefficient at the location of inception.

**Cavitation on Tripped Surface.** The cavitation occurring on the tripped surface is shown in Figs. 8(a,b,c,d,e,f). The appearance of cavitation changed with Reynolds number and the location of the tripping wire. Two types of cavitation could be found in the normal nucleus condition whose size distribution is shown as condition I in Fig. 11.

One of them was the bubble line cavitation which was found at the wire location  $\alpha = 30, 36, 38$  and occasionally at  $40^\circ$  for  $Re = 3.01 \times 10^5$ , and at  $\alpha = 30^\circ$  for  $Re = 3.36 \times 10^5$  and  $3.74 \times 10^5$ . For this cavitation, the inception point proceeded slightly upstream with increasing  $\alpha$  but scarcely did with increasing Reynolds numbers. Its physical appearance changes gradually with the location of the tripping wire. For  $\alpha = 30$  and  $36^\circ$  (Figs. 8(a,b)), the cavitation could be seen to occur within a narrow band, indicating the presence of a narrow reattachment region of a laminar separation. However, for  $\alpha = 38^\circ$ ,

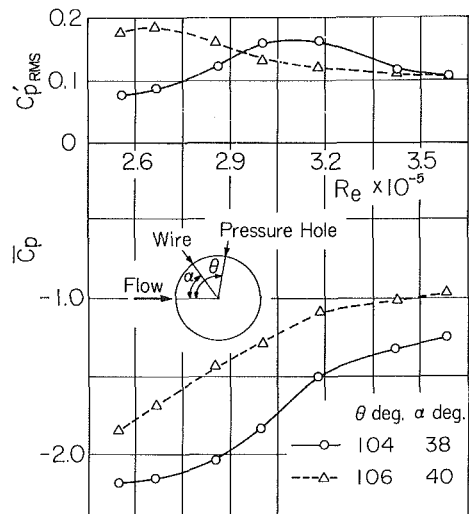


Fig. 10 Mean pressure coefficient and RMS of pressure coefficient fluctuation versus Reynolds number on the tripped surface

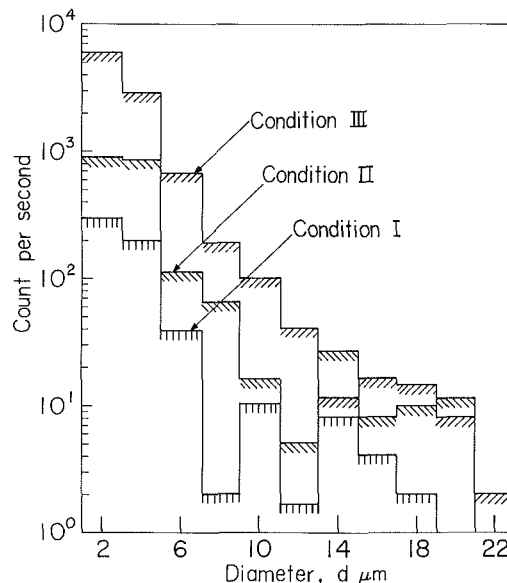


Fig. 11 Size distribution of cavitation nuclei. Condition I is normal test condition, condition II is the condition after about two hours with continuously cavitating on the test body, condition III is the condition soon after completion of the water supply to the water tunnel with cavitating to the inlet valve of water supply.

bubbles became to be distributed irregularly and widely in the free stream direction, indicating the expansion of the reattachment region. At lower cavitation numbers a smooth cavity accompanied by cloudy bubbles in its rear side could be found as shown in Fig. 8(c). The leading edge of this smooth cavitation was located at about  $\theta = 100^\circ$ . This cavitation resembled to the cavitation which has been found by Arakeri and Acosta [20] on the NSRDC body in the critical flow range.

The other was the smooth cavitation accompanied with cloudy bubbles as illustrated in Figs. 8(d,e,f). This type of cavitation was found for  $Re = 3.01 \times 10^5$  at the wire locations  $\alpha = 40, 42$ , and  $44^\circ$ , and for  $Re = 3.36 \times 10^5$  and  $3.74 \times 10^5$  at all wire location tested except  $\alpha = 30^\circ$ . When this type of cavitation took place, the bubble line cavitation did not take place. Leading edges of this type of cavitation was located at about  $\theta = 100^\circ$ . Incipient cavitation indexes for the smooth cavitation decreased with increasing Reynolds number and increasing angle of the tripping wire as can be seen in Fig. 9. Incipient cavitation indexes for the bubble line cavitation also decreased with increasing angle of the tripping wire.

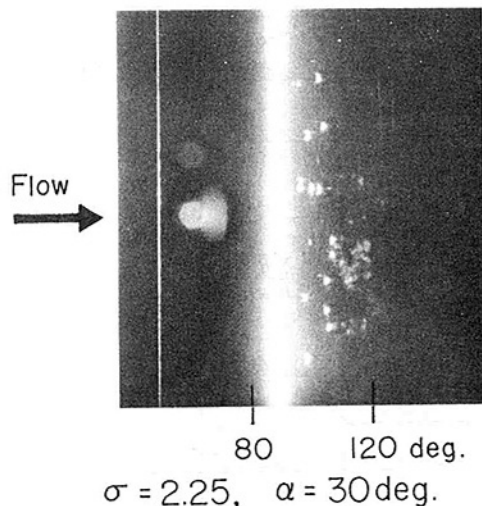


Fig. 12 Cavitation when a significant amount of free stream gas nuclei are counted,  $\alpha$  shows the wire location, nuclei size distribution is shown as condition III in Fig. 11

Dependency of the incipient cavitation indexes for these two types of cavitation on the size distribution of nuclei was also investigated for two types of nuclei distributions at about  $Re = 3.0 \times 10^5$ . For the two cases shown as conditions I and II in Fig. 11, as the number of the nuclei was increased, the incipient cavitation indexes for the smooth cavity increased, but those for the bubble line cavitation were scarcely affected as can be seen in Fig. 9. In the case of a significant number of nuclei whose population is shown as condition III in Fig. 11, cavitation which looked like travelling bubble cavitation was only found on the tripped surface at the side just downstream of the pressure minimum point. A few bubbles form a line almost parallel to the free stream direction with a small spacing between them, and the spacing of bubbles to the spanwise direction is almost constant as can be seen in Fig. 12. This phenomenon, as has been pointed out by Gates [21], can be understood that an existing laminar separation bubble can be eliminated by the presence of a significant number of macroscopic air bubbles, and this appearance of cavitation suggests to us that the cavitation just described might have taken place in a vortex core whose axis looks toward the free stream direction and stands side by side to the spanwise direction, although we could not confirm it. When cavitation was induced from the cavitation which was taken place on the tripping wire, the cavitation whose front form had a sharp wedge took place in the neighborhood of the pressure minimum point as illustrated in Fig. 13.

The mean pressure coefficient and RMS of the pressure fluctuations in normalized form at the pressure hole locations  $\theta = 104$  and  $106^\circ$  are shown in Fig. 10 for the tripped surface, corresponding to the wire locations  $\alpha = 38$  and  $40^\circ$ . The mean pressure coefficients at each point increased considerably as Reynolds number was increased. However RMS of the pressure fluctuations at  $\theta = 104^\circ$  for  $\alpha = 38^\circ$ , showed a peak value of about 16 percent of dynamic pressure head for the Reynolds number ranging from  $3.0 \times 10^5$  to  $3.2 \times 10^5$ . The physical appearance of cavitation corresponding to this condition is shown in Fig. 8(c) which shows a critical difference between the bubble line cavitation and the smooth cavitation. Though it could not be confirmed directly whether the peak of the pressure fluctuations was caused by the reattachment of the laminar separation or the transition after the disappearance of laminar separation bubble, it may be said that for  $Re = 3.0 \times 10^5$ , the location of the tripping wire at  $\alpha = 38^\circ$  is the critical position which divides the surface flow to the critical or supercritical condition. The absolute mean pressure

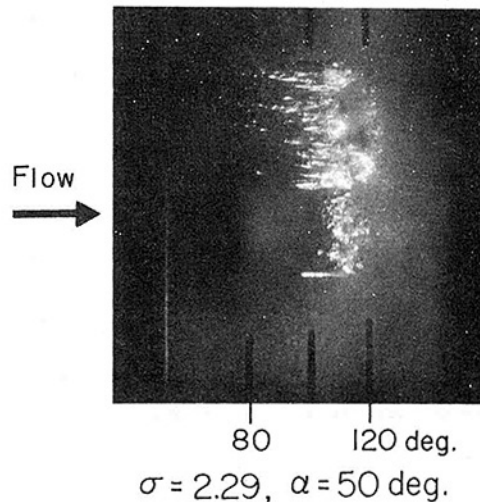


Fig. 13 Cavitation when the tripping wire is cavitating,  $Re = 3.09 \times 10^5$ ,  $\alpha$  shows the wire location

coefficient measured at  $\theta = 106^\circ$  for  $\alpha = 40^\circ$  is small in comparison with the value measured at  $\theta = 104^\circ$  for  $\alpha = 38^\circ$  in spite of taking into account the difference of the hole location. It may be said that the decrease of the cavitation index with an increase of  $\alpha$  in supercritical flow range is primarily caused by the increase in the pressure coefficient.

#### Experimental Uncertainty

The pressure data in Figs. 2, 3, 4, and 10 have a maximum uncertainty of about  $\pm 2$  percent. This maximum uncertainty is primarily due to the zero drift of the pressure transducer of the semiconductor type.

Cavitation data in Figs. 6 and 9 have a maximum uncertainty about  $\pm 1$  percent except the dispersion shown in figures. This uncertainty is associated with the fluctuation of indicator readings to calculate the free stream velocity and the static pressure.

#### Conclusions

Through the cavitation test using circular cylinders with and without trips, combined with the measurements of pressure distributions, and size distribution of gas nuclei, the following conclusions are obtained:

- 1 Cavitation which closely resembles bubble ring cavitation reported on axisymmetric bodies occurred in a reattachment region of a laminar separation bubble for the critical flow range.
- 2 The incipient cavitation number of the cavitation described in Conclusion 1 coincided closely with a temporal minimum pressure coefficient at the inception point, and was insensitive to free stream gas nuclei.
- 3 For the supercritical flow range smooth cavitation with small irregular bubbles in its neighborhood occurred at a location about  $100^\circ$  from the stagnation point.
- 4 Incipient cavitation number described in Conclusion 3 was sensitive to free-stream gas nuclei.
- 5 For the flow with a significant number of free stream gas nuclei, cavitation which looked like travelling bubble cavitation only occurred for the critical flow range.
- 6 Inside the laminar separation bubble on the circular cylinder, a location where the mean pressure coefficient and RMS of pressure fluctuations showed minimum existed.
- 7 RMS of pressure fluctuations measured in the reattachment region of the laminar separation amounted to 27 percent of the dynamic head.

## Acknowledgments

Authors are greatly indebted to Mr. Katagiri for his assistance with the experiments.

## References

- 1 Arakeri, V. H., and Acosta, A. J., "Viscous Effects in the Inception of Cavitation on Axisymmetric Bodies," *ASME JOURNAL OF FLUIDS ENGINEERING*, Vol. 95, No. 4, Dec. 1973, pp. 519-528.
- 2 Numachi, F., and Kawashima, O., "Theoretical Consideration Concerning the Boundary Layer and its Separation on Hydrofoils Suitable for Arrangement in Cascade," Report of the Institute of High Speed Mechanics, Tohoku University, Vol. 12, No. 114, 1960/1961, pp. 89-107.
- 3 Bailey, A. B., and Casey, M. V., "Cavitation Parameter for Inception on a Hydrofoil at Moderate Incidence," Report No. 1025/71, Oxford University Engineering Laboratory, 1971.
- 4 Van der Meulen, J. H. J., "Boundary Layer and Cavitation Studies of NACA16-012 and NACA4412 Hydrofoils," 13th Symposium on Naval Hydrodynamics, Oct. 1980, pp. II-5-1-II-5-23.
- 5 Wykes, M. E., "Cavitation Inception on a Two-Dimensional Circular Cylinder," *Proc. N.E.L. Fluid Mechanics Silver Jubilee Conference*, Nov. 1979, Paper No. 7.1, pp. 1-12.
- 6 Wykes, M. E., "The Development of Cavitation on a Circular Cylinder," *Proc. N.E.L. Fluid Mechanics Silver Jubilee Conference*, Nov. 1979, 2nd Paper, pp. 1-11.
- 7 Numachi, F., "Cavitation Tests on Hydrofoils in Cascade and its Theoretical Basis of Experiment," Report of the Institute of High Speed Mechanics, Tohoku University, Vol. 4, No. 5, 1954, pp. 125-157.
- 8 Numachi, F., "Über die kavitationsentstehung mit besonderem Bezug auf den Luftgehalt des Wassers," *Ingenieur-Archiv*, Bd. VII, 1936, pp. 396-406.
- 9 Murai, H., Watanabe, H., and Katagiri, K., "Suppression of Cavitation Inception in Water by Additives," *Proceedings of the 10th Symposium of IAHR*, Tokyo, 1980, pp. 65-76.
- 10 Fage, A., and Falkner, V. M., "Further Experiments on the Flow around a Circular Cylinder," Aeronautical Research Council R.&M. No. 1369, 1931.
- 11 Giedt, W. H., "Effects of Turbulence Level of Incident Airstream on Local Heat Transfer and Skin Friction on a Cylinder," *Journal of Aeronautical Science*, Vol. 8, 1951, pp. 725-730.
- 12 Roshko, A., "Experiments on the Flow Past a Circular Cylinder at very High Reynolds Number," *Journal of Fluid Mechanics*, Vol. 10, 1961, pp. 345-356.
- 13 Achenbach, E., "Distribution of Local Pressure and Skin Friction around a Circular Cylinder in Crossflow up to  $Re=5 \times 10^6$ ," *Journal of Fluid Mechanics*, Vol. 34, 1968, pp. 625-639.
- 14 Batham, J. P., "Pressure Distributions on Circular Cylinders at Critical Reynolds Numbers," *Journal of Fluid Mechanics*, Vol. 57, 1973, pp. 209-228.
- 15 Arakeri, V. H., "A Note on the Transition Observations on an Axisymmetric Body and Some Related Fluctuating Pressure Measurements," *ASME JOURNAL OF FLUIDS ENGINEERING*, Vol. 97, Mar. 1975, pp. 82-87.
- 16 Parkin, B. R., "A Possible Criterion for Cavitation Inception on Hemispherical Headforms," *ASME JOURNAL OF FLUIDS ENGINEERING*, Vol. 103, Dec. 1981, pp. 577-582.
- 17 Parkin, B. R., "The Initiation of Gaseous Microbubble Growth in Laminar Separation Bubbles," *ASME JOURNAL OF FLUIDS ENGINEERING*, Vol. 103, Dec. 1981, pp. 543-550.
- 18 Parkin, B. R., "The onset of Bubble-Ring Cavitation on Hemispherical Headforms," *ASME JOURNAL OF FLUIDS ENGINEERING*, Vol. 104, Mar. 1982, pp. 115-123.
- 19 Holl, J. W., and Carroll, J. A., "Observations of the Various Types of Limited Cavitation on Axisymmetric Bodies," *ASME JOURNAL OF FLUIDS ENGINEERING*, Vol. 103, Sept. 1981, pp. 415-424.
- 20 Arakeri, V. H., and Acosta, A. J., "Cavitation Inception Observations on Axisymmetric Bodies at Super Critical Reynolds Number," *Journal of Ship Research*, Vol. 20, No. 1, Mar. 1976, pp. 40-50.
- 21 Gates, E. M., "The Influence of Free Stream Turbulence, Free Stream Nuclei Populations and a Drag-Reducing Polymer on Cavitation Inception on Two Axisymmetric Bodies," California Institute of Technology, Report No. Eng. 183-2 Apr. 1977.

**S. Kamiyama**  
 Professor of Institute of  
 High Speed Mechanics,  
 Tohoku University,  
 Sendai, Japan

**T. Yamasaki**  
 Professor,  
 Faculty of Agriculture,  
 Kochi University,  
 Kochi Prefecture, Japan

# Critical Condition of Cavitation Occurrence in Various Liquids

*An experimental study of cavitation occurrence in benzene, kerosene, gasoline, and Freon 12 was conducted using a square-edged orifice. The experimental results of the desinent cavitation number are compared with the calculated values predicted from two-phase flow analogy. The predicted values show reasonable agreement with experimental data for benzene and gasoline but require some modifications for kerosene and Freon 12.*

## Introduction

Recently, cavitation occurrence in high speed flow of various liquids is of considerable and increasing importance in many fields, especially the design and development of fluid machinery for handling liquids other than water such as oils, liquid metals, organic and cryogenic liquids.

Several predicting methods for cavitation occurrence in such liquids have been theoretically studied taking into account liquid properties and flow condition. First, Stepanoff [1] proposed the B-factor method to explain the thermodynamic effects on the cavitation characteristics in pumps handling various liquids other than water. The B-factor theory has been developed by several researchers [2-5]. Also, an entrainment theory was proposed by Holl et al. [6]. However, these methods are mainly applicable to the states of fully developed cavitation and consider only a vapor volume produced by pressure reduction.

On the other hand, there are a few analyses of the thermodynamic effects on cavitation inception from the viewpoint of the bubble dynamics [7-8]. Moreover, the calculated values of the incipient (or desinent) cavitation number based on this method have not explained well the experimental results in water at various temperatures [7].

Concerning the air content effect on cavitation inception, Holl [9] has proposed a simple prediction method of critical cavitation number for gaseous cavitation, considering the effect of dissolved gas content on partial gas pressure by Henry's law though the partial gas pressure was assumed to be constant irrespective of the flow velocity.

The authors have already proposed another analytical method for predicting gaseous cavitation occurrence by analogy with the choked flow condition of homogeneous bubble mixture [10-11] and verified it by experimental studies for water [12] and turbine oil [13].

It is therefore the purpose of the present paper to confirm the applicability of the predicting method to the cases of organic liquids such as kerosene and gasoline as petroleum-based hydrocarbon mixtures and also Freon 12 which has fluid property showing a large thermodynamic effect.

The experimental study on the critical condition of cavitation

occurrence for these special liquids is carried out by using an orifice with a square edge and the test results are compared with the predicted values.

## Analysis

**Sonic Velocity in Bubble Mixture.** Flowing fluid must be regarded as a mixture composed of liquid, its vapor and foreign gas nuclei when it passes through lower pressure region where gaseous cavitation occurs due to the existence of free stream nuclei. Therefore homogeneous two-phase flow with a small void fraction is considered here.

The gas phase with void fraction  $\alpha$  is assumed to be thermal equilibrium with the liquid phase and consists of many tiny bubbles of the same equivalent radius  $R$ .

The slip velocity of bubble with respect to the liquid phase is negligible in these desinent states due to small void fraction as shown in reference [14]. Therefore, the apparent density  $\rho_T$  is expressed by

$$\rho_T = \rho_l \{ 1 - \alpha(p) \} \quad (1)$$

The equation of state of noncondensable gas is

$$p_g \rho_g^{-1} = \text{const} \quad \text{or} \quad p_g = p_{gref} r^{-3} \quad (2)$$

Also, from the definition of void fraction  $\alpha$  with gas volume  $V_g$  and liquid volume  $V_l$ , the following relation is obtained.

$$V_g = \frac{4}{3} \pi n R^3 = \frac{\alpha}{1 - \alpha} V_l \quad (3)$$

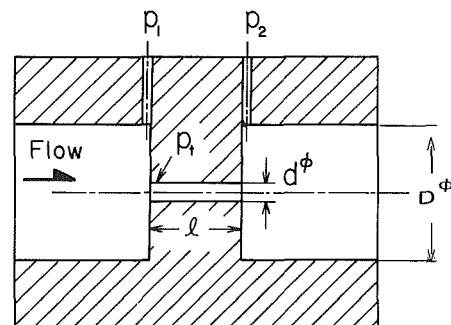


Fig. 1 Orifice with square edge

Contributed by the Fluids Engineering Division for publication in the JOURNAL OF FLUIDS ENGINEERING. Manuscript received by the Fluids Engineering Division, February 25, 1985.

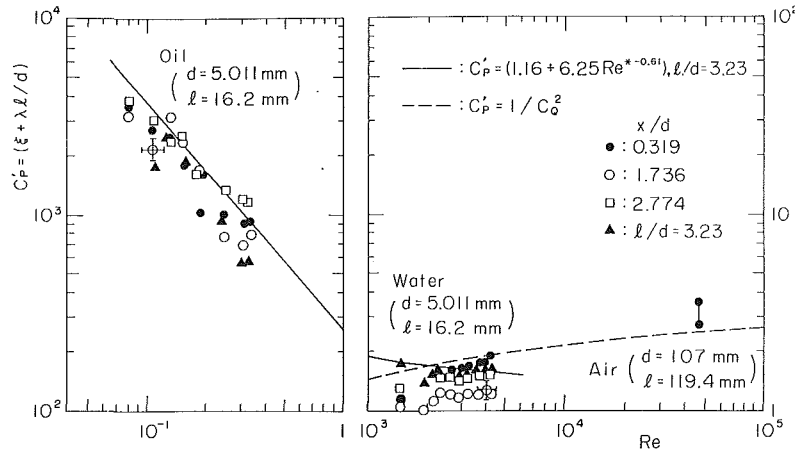


Fig. 2 Pressure coefficient of orifice with square edge

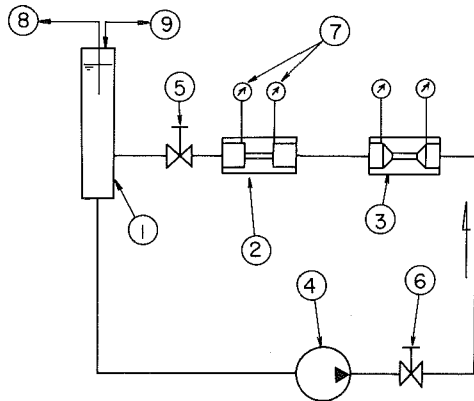


Fig. 3 Layout of experimental apparatus for benzene, kerosene and gasoline

- ① reservoir ② test section ③ flowmeter ④ pump ⑤, ⑥ valve ⑦ pressure gauge ⑧ air-content meter ⑨ compressor

In the reference state,

$$V_{g\text{ref}} = \frac{4}{3} \pi n R_{\text{ref}}^3 = \frac{\alpha_{\text{ref}}}{1 - \alpha_{\text{ref}}} V_l \quad (4)$$

Then, from equations (3) and (4),

$$\alpha = \beta_{\text{ref}} r^3 / (1 + \beta_{\text{ref}} r^3) \quad (5)$$

where

$$\beta = \alpha / (1 - \alpha) \quad (6)$$

$$r = R / R_{\text{ref}}$$

and  $n$  is number density of tiny bubbles. The subscripts  $l, g, T$

refer to liquid, noncondensable gas and two-phase mixture and also ref means the reference state (atmospheric condition).

In equation (2), no gas solubility and isothermal change of gas phase are assumed [10-11].

Pressure balance equation is simply given by

$$p_l + \frac{2\gamma}{R} = p_g + p_v \quad (7)$$

where  $\gamma$  is surface tension and  $p_v$  the vapor pressure.

Neglecting the effects of surface tension of gas bubble and liquid temperature depression due to evaporation, sonic velocity in a bubble mixture is obtained from equations (1)-(7) as follows [10]:

$$C = (dp_l / d\rho_T)^{1/2} = -\frac{1}{\rho_l} \left( \frac{d\alpha}{dp_l} \right)^{-1} \quad (8)$$

$$= -\frac{1}{\rho_l} \left( \frac{d\alpha}{dr} \frac{dr}{dp_l} \right)^{-1} = \frac{p_l - p_s + K}{\sqrt{\rho_l K}}$$

where  $p_s$  is saturated vapor pressure and  $K = \{(\alpha / (1 - \alpha)) p_g\}_{\text{ref}}$ .

### Calculating Method of Critical Cavitation Number

As stated in the previous papers [10-11], the local choking condition in homogeneous two-phase flow is adopted as a criterion of cavitation occurrence. That is, cavitation inception is defined as the state at which the throat velocity  $v_t$  of one dimensional flow in the orifice reaches the sonic velocity ( $v_t = C$ ) under pressure  $p_t$  and void fraction  $\alpha$ .

The critical cavitation number  $\sigma^*$  is written as follows:

### Nomenclature

$C$  = sonic velocity, m/s  
 $C_D$  = discharge coefficient  
 $d$  = inner diameter of orifice, mm  
 $D$  = diameter of tube, mm  
 $K = \left\{ \left( \frac{\alpha}{1 - \alpha} \right) p_g \right\}_{\text{ref}}$   
 $l$  = orifice length, mm  
 $p$  = pressure, kPa  
 $p_s$  = saturated vapor pressure, kPa  
 $Re$  = Reynolds number ( $v_0 d / \nu$ )  
 $Re^*$  = modified Reynolds number ( $Re(\pi d / 4l)$ )

$v$  = flow velocity, m/s  
 $v_0$  = mean velocity in orifice, m/s  
 $x$  = distance from inlet of throat, m  
 $\alpha$  = void fraction  
 $\lambda$  = resistance coefficient ( $= 64 / Re$ )  
 $\rho$  = density, kg/m<sup>3</sup>  
 $\nu$  = kinematic viscosity, m<sup>2</sup>/s  
 $\sigma$  = cavitation number  
 $\xi$  = additional expansion loss coefficient

### Super- and Subscripts

$g$  = gas  
 $l$  = liquid  
 $t$  = throat  
 $\text{ref}$  = state at standard temperature and pressure  
 $*$  = critical condition  
 $1$  = upstream  
 $2$  = downstream  
 $T$  = two-phase mixture

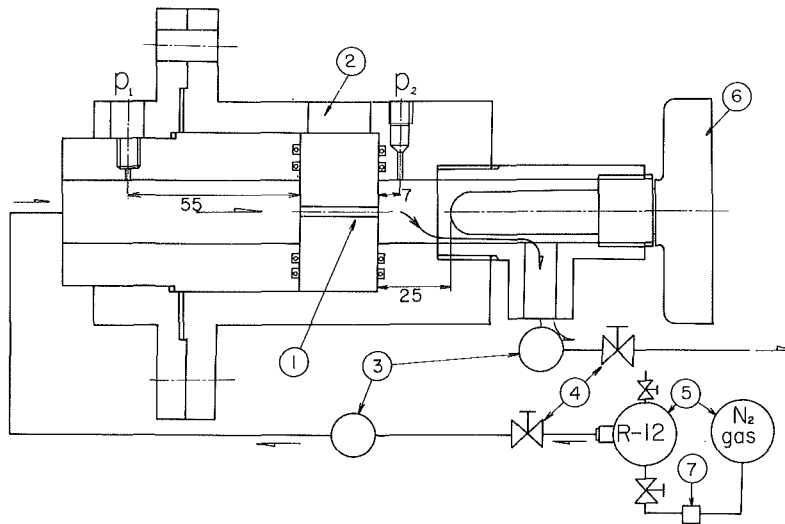


Fig. 4 Layout of experimental apparatus for Freon 12

- ① orifice ② window ③ sight-glass ④ valve ⑤ pressure vessel ⑥ thermometer ⑦ regulating valve

$$\sigma^* = \frac{2(p_1 - p_s)}{\rho_l C^2} \cong 2\alpha(1 - \alpha) \quad (9)$$

However, the pressures  $p_1$  and  $p_2$  are measured far from the position of cavitation occurrence in the case of orifice flow as shown in Fig. 1 and the relation between  $p_2$  and  $p_1$  is strongly influenced by the frictional and expansion losses in narrow passage. Then, if the critical cavitation number is defined by using downstream pressure  $p_2$  instead of  $p_1$ , it is necessary to take into account such pressure losses in the narrow passage.

The pressure difference in the viscous flow in the orifice is given by

$$p_1 - p_2 = \left( \lambda \frac{l}{d} + \xi \right) \frac{\rho_l v_0^2}{2} \quad (10)$$

where  $\lambda$  is pipe resistance coefficient,  $\xi$  the additional expansion loss coefficient, and  $v_0$  the mean velocity in the orifice.

The relation between  $p_1$  and  $p_2$  is assumed by using the discharge coefficient  $C_Q$  as,

$$v_0 = C_Q \sqrt{2(p_1 - p_2)/\rho_l} \quad (11)$$

Then, the critical pressure  $p_2^*$  for cavitation occurrence is obtained by assuming  $C \cong v_0$  as follows:

$$\frac{p_2^*}{p_1} = 1 - \frac{\left(1 + \xi \frac{Re^*}{16}\right) \left(\frac{32\mu l}{d^2}\right) \left(\frac{41Re^* \nu}{\pi d^2}\right)}{\left(\frac{41Re^* \nu}{\pi d^2}\right)^2 \left(\frac{\rho_l}{2C_Q^2}\right) + p_s - K + \left(\frac{41Re^* \nu}{\pi d^2}\right) \sqrt{\rho_l K}} \quad (12)$$

where  $Re^* = (\pi d/4l)(v_0 d/\nu)$  is modified Reynolds number and  $\nu$  the kinematic viscosity. The following relations are also used [13].

$$\xi = (1.16 + 6.25Re^{*-0.61})^2 - 16\pi/Re^* \quad \text{for } 1 < Re^* < 10^3$$

$$\xi = 1.0/(S_1 - 0.007911/d)^2 - 16\pi/Re^* \quad \text{for } Re^* > 10^3 \quad (13)$$

$$C_Q = 0.964/Re^{0.05} \quad \text{for } 8.0 < Re(=v_0 d/\nu) < 5000$$

$$C_Q = 0.63 \quad \text{for } Re > 5000 \quad (14)$$

Although the experimental constant of  $S_1 = 0.868$  is obtained in our experiment, another value of  $S_1 = 0.819$  for  $Re^* > 3.14 \times 10^4$  [15] is also used in the second of equation (13) for comparison.

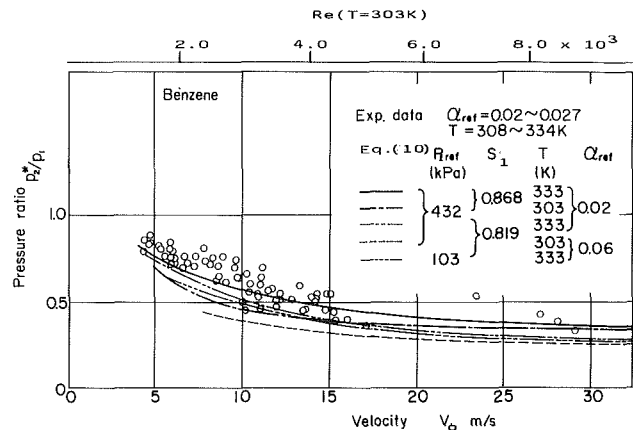


Fig. 5 Condition of desinent cavitation in benzene

Pressure ratio  $p_2^*/p_1$  is commonly used as a cavitation parameter instead of  $\sigma^*$  in oil hydraulic system because of its simplicity. One-dimensional flow analysis and assumption of  $C = v_0 \cong v_0$  seem to be very rough approximation for the actual flow in the orifice with sharp edge. However, one of the authors already confirmed the applicability of such approximation in the oil test [13].

Also, the propriety of equations (13) and (14) was examined by the test with different scale models. The pressure distribution in the orifice for various Reynolds number  $Re$  is shown in Fig. 2, where the solid line indicates the pressure loss coefficient  $C_p' (= \xi + \lambda l/d)$  obtained by equations (10) and (13), whereas the broken line is  $C_p'$  in the standard orifice. The experimental data show the pressure coefficient at various positions  $x/d$  within the orifice, where  $x$  is the distance from the inlet.

It is clear from Fig. 2 that equations (13) and (14) give reasonable estimation of  $C_p'$  for  $Re > 10^3$ , and sharp pressure decrease does not occur at the inlet for the small Reynolds number of  $Re < 1$ .

## Experimental Study

**Experimental Apparatus and Procedure.** The experimental apparatus for kerosene, gasoline, and benzene is shown in Fig. 3 where the test liquid is circulated in a closed loop by a

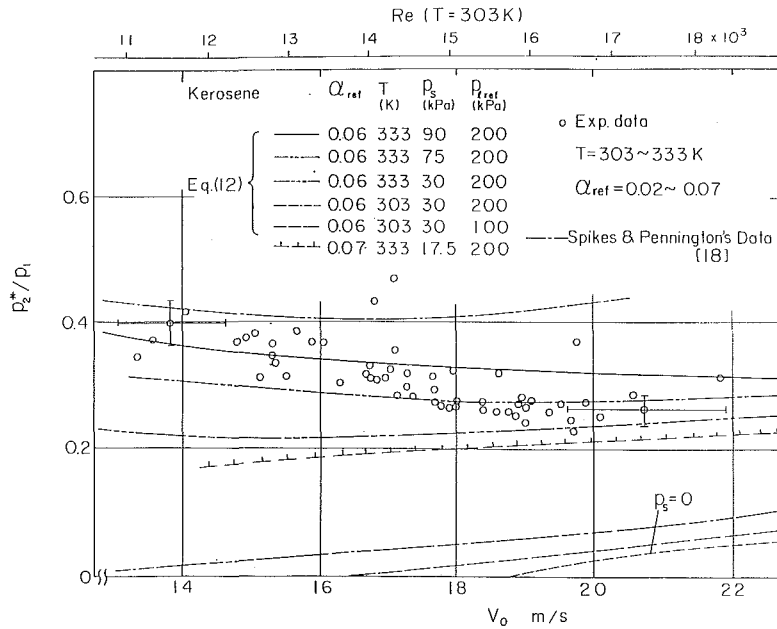


Fig. 6 Condition of desinent cavitation in kerosene

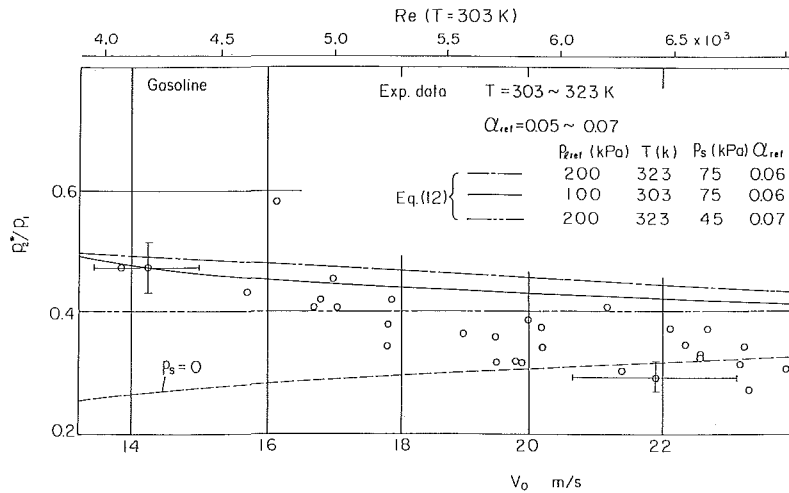


Fig. 7 Condition of desinent cavitation in gasoline

peripheral pump (4) ( $H = 50$  m,  $Q = 0.018$  m<sup>3</sup>/min,  $P = 1.5$  kW) through valves (5), (6), flowmeter (3), reservoir (1), and test section (2). An open circuit unit in small size as shown in Fig. 4 is also utilized in the case of Freon 12. In the case of Freon 12, nitrogen gas was introduced into the  $R - 12$  pressure vessel through the regulating valve (7) in order to pressurize Freon 12 at constant pressure of 10<sup>3</sup> kPa.

The test section is the orifice with square edge. The inner diameters  $D$ ,  $d$  and orifice length  $l$  are  $D = 26.5$  mm,  $d = 1.675$  mm,  $l = 25$  mm for gasoline, kerosene, benzene and  $D = 18.5$  mm,  $d = 0.436$  mm,  $l = 14.8$  mm for Freon 12, respectively.

Total air contents in the test liquids were measured by Numachi's method [16] and evaluated as  $\alpha_{ref}$  since the gas in a liquid is almost released and exists as small bubbles in low pressure region [12].

The apparent saturated vapor pressure  $p_s$  and kinematic viscosity of kerosene and gasoline were obtained by the actual measurement and for other fluid properties authors used reference [17].

As cavitation occurred downstream from orifice-exit in the case of Freon 12, the following critical cavitation number  $\sigma_d$  is defined.

$$\sigma_d = \frac{2(p_2 - p_s)}{\rho_l v_0^2} \quad (15)$$

## Experimental Results

The test results for the desinent cavitating condition are shown in Figs. 5–8 for benzene, kerosene, gasoline, and Freon 12, respectively. The curves in the figures show the predicted values from equation (12) except for the case of Freon 12 in which the thermodynamic effect is taken into consideration [11].

In Figs. 5–8, mean throat velocity  $v_0$  is taken as the abscissa since the predicted values of desinent condition are analytically found to be influenced by the flow velocity in a local state. For reference, the Reynolds number at a fixed temperature is also shown in the above line.

It is clearly shown that the experimental data are well predicted by equation (12) in the cases of benzene, kerosene and gasoline though a little modification in  $p_s$  values is necessary for kerosene in which a good prediction is obtained by using higher values of  $p_s = 75 - 90$  kPa than the measured saturated pressure of  $p_s = 17 - 30$  kPa in our experiment.



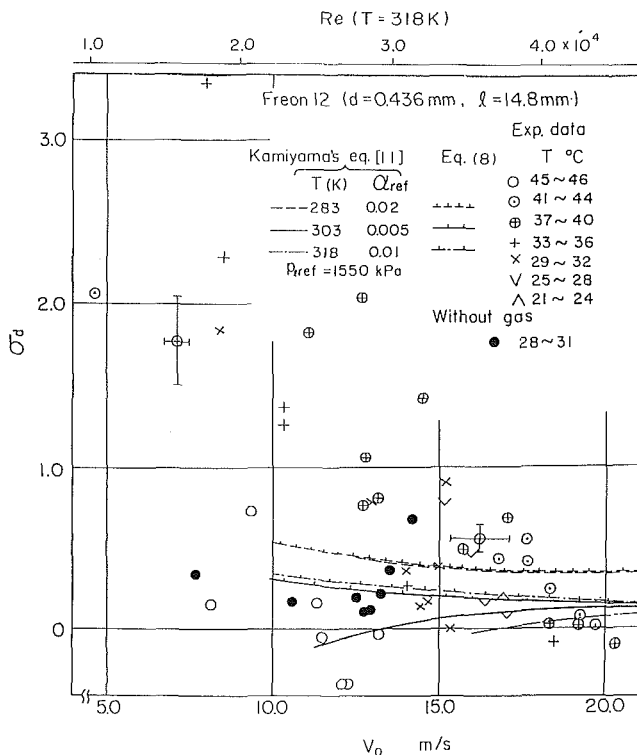


Fig. 8 Condition of desinent cavitation in Freon 12

Spikes and Pennington's data [18] are also shown in Fig. 6.

Curve with  $p_s = 0$  in kerosene and gasoline shows a simple prediction based on  $p_t = p_s = 0$  which gives lower values of  $p_2^*/p_1$  compared with the experimental data.

In the case of Freon 12, the predicted values explain only qualitatively the experimental data since there is large uncertainty in the experiment due to the small test facility and the unsteady heat conduction of thermodynamic depression by cavitation occurrence, which means that the uncertainty of cavitation event itself appears beyond the accuracy of velocity and pressure measurements. Therefore, the  $\sigma$ -values in the vicinity of  $\sigma = 0$  are masked by the experimental error and have no significant meanings though the analytical prediction indicates the possibility of negative  $\sigma$ .

Experimental error for the measurement of velocity and pressure is shown with error bands in each figure.

Anyhow, the thermodynamic effects on cavitation occurrence did not appear in these test liquids and equations (9) or (12) show good correlation with the present experimental results which suggest the importance of the existence of gas nuclei in cavitation occurrence in such liquids.

## Conclusion

A simple predicting method for gaseous cavitation occurrence is proposed based on an analogy with the choked flow condition of homogeneous bubble mixture.

Experimental data on desinent cavitation condition for benzene, kerosene, gasoline and Freon 12 are compared with the predicted values.

The main results obtained here are summarized as follows:

1. Experimental data on desinent condition of cavitation for benzene and gasoline show a good correlation with the predicted values.
2. The experimental values of desinent condition for kerosene show a little higher values compared with the prediction.
3. A thermodynamic effect on cavitation occurrence is not clearly shown in the experimental data for Freon 12 because of the scatter of experimental data though the predicted values show a clear thermodynamic effect.

## References

- 1 Stahl, H. A., and Stepanoff, A. J., "Thermodynamic Aspects of Cavitation in Centrifugal Pumps," *ASME Journal of Basic Engineering*, Vol. 78, No. 4, Nov. 1956, pp. 1691-1693.
- 2 Jakobsen, J. K., "On the Mechanism of Head Breakdown in Cavitating Inducers," *ASME Journal of Basic Engineering*, Vol. 86, No. 2, June 1964, pp. 291-305.
- 3 Spraker, W. A., "The Effects of Fluid Properties on Cavitation in Centrifugal Pumps," *ASME Journal of Engineering for Power*, Vol. 87, No. 3, July 1965, pp. 309-318.
- 4 Ruggeri, R. S., and Moore, R. D., "Method for Prediction of Pump Cavitation Performance for Various Liquids, Liquid Temperatures, and Rotative Speeds," TN D-5292, June 1969, National Aeronautics and Space Administration, Washington, D.C.
- 5 Thew, M. T., and Hadji-Sheikh, M., "Cavitation Behaviour of Water-Glycol Mixtures in Small Centrifugal Pumps," NEL Silver Jubilee Conference, Nov. 1979, East Kilbride, U.K.
- 6 Holl, J. W., Billet, M. L., and Weir, D. S., "Thermodynamic Effects on Developed Cavitation," *ASME JOURNAL OF FLUIDS ENGINEERING*, Vol. 97, No. 4, Dec. 1975, pp. 507-514.
- 7 Holl, J. W., and Kornhauser, A. L., "Thermodynamic Effects on Desinent Cavitation on Hemispherical Nosed Bodies in Water at Temperatures from 80 Deg F to 260 Deg F," *ASME Journal of Basic Engineering*, Vol. 92, No. 1, Mar. 1970, pp. 44-58.
- 8 Bonnin, J., "Theoretical and Experimental Investigations of Incipient Cavitation in Different Liquids," ASME Paper No. 72-WA/FE-31, Nov. 1972.
- 9 Holl, J. W., "An Effect of Air Content on the Occurrence of Cavitation," *ASME Journal of Basic Engineering*, Vol. 82, No. 4, Dec. 1960, pp. 941-946.
- 10 Kamiyama, S., and Yamasaki, T., "Prediction of Gaseous Cavitation Occurrence in Sodium and Water Based on Two-Phase Critical Flow Analogy," *Cavitation and Polyphase Flow Forum*, ASME, 1976, pp. 46-48.
- 11 Kamiyama, S., and Yamasaki, T., "Prediction of Gaseous Cavitation Occurrence in Various Liquids Based on Two-Phase Critical Flow Analogy," *ASME JOURNAL OF FLUIDS ENGINEERING*, Vol. 103, No. 4, Dec. 1981, pp. 551-556.
- 12 Kamiyama, S., and Yamasaki, T., "One Predicting Method of Gaseous Cavitation Occurrence in Water and Sodium," *Bull. of Japan Society of Mechanical Engineers*, Vol. 23, No. 183, Sept. 1980, pp. 1428-1434.
- 13 Yamasaki, T., "Condition of Cavitation Occurrence in Oil Flow in Narrow Passage," *Trans. JSME*, Series B, Vol. 47, No. 418, June 1981, pp. 976-981 (in Japanese).
- 14 Kamiyama, S., "Analysis of Two-Phase MHD Flow in Converging-Diverging Ducts," *Progress in Astro. and Aeronautics Series*, AIAA Inc., Vol. 100, 1985, pp. 304-316.
- 15 Hibi, A., Ichikawa, T., and Miyagawa, S., "Flow Characteristics of Cylindrical Chokes," *Yuatsu and Kuukiatsu*, (in Japanese), Vol. 2, No. 2, Apr. 1971, pp. 72-80.
- 16 Numachi, F., and Shiina, T., "A Contribution to the Mechanism of Cavitation Occurrence," *Trans. JSME* (in Japanese), Vol. 3, No. 11, May 1937, pp. 177-181.
- 17 Hatta, K., and Asanuma, T. (Ed.), *Handbook of Internal Combustion Engine*, Asakura Book Company, 1967 (in Japanese).
- 18 Spikes, R. H., and Pennington, G. A., "Discharge Coefficient of Small Submerged Orifices," *Proceedings of the Inst. of Mechanical Engineers*, Vol. 173, 1959, pp. 661-674.

# Contribution of Homogeneous Condensation Inside Cavitation Nuclei to Cavitation Inception

Y. Matsumoto

Associate Professor,  
Department of Mechanical Engineering,  
University of Tokyo,  
Tokyo, Japan

*The response of a small gas bubble, so-called cavitation nucleus, to the reduction of ambient pressure is investigated theoretically and experimentally. Numerical results show that the gas mixture inside the bubble expands adiabatically and the temperature of the mixture decreases rapidly at the first stage, however the temperature recovers soon to the surrounding liquid temperature by homogeneous condensation which forms a mist inside the bubble. Consequently, the bubble grows almost isothermally. Experiments have been performed using a hydro-shock tube. The radius of a small bubble has been measured by a light-scattering method whose time resolving power is one micro-second. The experimental results are found to be in good agreement with the numerical results calculated using the ambient pressure change measured in the test section.*

## Introduction

It is generally understood that cavitation bubble is formed from small air bubbles in water (cavitation nuclei). In this sense, the cavitation can be recognized as a process of rapid growth and collapse of a gas bubble with phase change. Concerning the cavitation inception around a body, the relation to the nuclei and the flow structure like laminar separation has been studied by many researchers such as Arakeri and Acosta [1]. Katz and Acosta [2] have shown that the number density of nuclei in a recirculating region behind a step on an axisymmetric body is much higher than in the main flow. Ito and Oba [3] observed the process of cavitation inception in a separated region. The nuclei grows to cavitation bubbles depending on the surrounding flow condition. Therefore, the pressure response of a small gas bubble like a cavitation nucleus is an important problem for cavitation inception. The pressure response of a gas bubble has been calculated by Sato and Shima [4] and Lin [5]. Recently the author [6] analyzed the response of a small gas bubble to the ambient pressure reduction taking the mist formation by homogeneous nucleation inside the bubble into consideration. Following are the conclusions from the study: (i) The gas mixture inside the bubble expands adiabatically at the first stage, however the temperature of the mixture recovers soon to the surrounding liquid temperature due to mist formation inside the bubble by homogeneous condensation. Consequently, the bubble grows almost isothermally. (ii) When the initial bubble radius is larger than  $8\ \mu\text{m}$ , the relation between the initial bubble radius and the critical pressure for cavitation inception due to step-wise pressure reduction becomes very close to the one under the assumption of the isothermal change in the gas mixture inside the bubble.

In 1949, Plesset [7] observed the behavior of a bubble around a 1.5 caliber ogive and compared experimental observations with the calculation using the assumption that the pressure inside a bubble is equal to the saturated vapor pressure. The agreements of the results were good except for the first and last stage. Recently, Fujikawa and Akamatsu [8] observed bubble growth in a liquid shock tube and found that a hydrogen bubble grew isothermally with the ambient pressure reduction. However, the observation seems to be limited by its instrumentation, especially insufficient time resolving power and short period.

The response of a small gas bubble, so-called cavitation nuclei, to the ambient pressure reduction is investigated theoretically and experimentally in this paper. Experiments have been performed using a hydro-shock tube. The radius of a small bubble has been measured by a light scattering method whose time resolving power is one micro-second. The experimental results are found to be in good agreement with the numerical results calculated using the ambient pressure change measured in the test section.

## Theoretical Analysis

A response of a small gas bubble is calculated numerically assuming the following model [6].

**Calculation Model.** The following phenomena are taken into consideration in the model.

- (1) Nonequilibrium heat and mass transfer by evaporation and condensation on the bubble wall.
- (2) Formation of condensed droplets by homogeneous nucleation, their growth, evaporation and deposition onto the bubble wall.
- (3) Change of pressure and temperature inside the bubble by the above mentioned phenomena.

The following assumptions are used to formulate the governing equations.

Contributed by the Fluids Engineering Division for publication in the JOURNAL OF FLUIDS ENGINEERING. Manuscript received by the Fluids Engineering Division February 26, 1985.

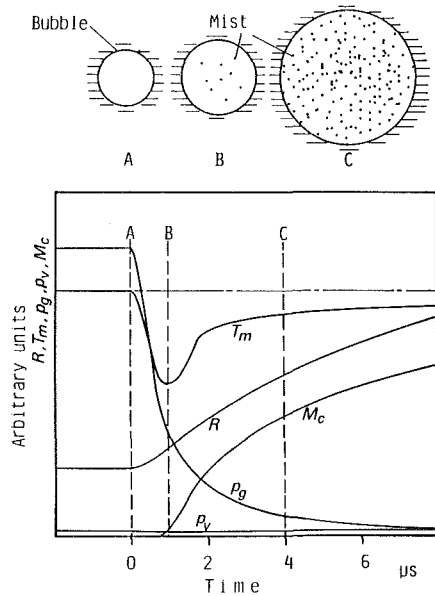


Fig. 1 Schematic explanation for calculation model

- (1) The bubble and the surrounding liquid move spherically and symmetrically.
- (2) The pressure, temperature and concentration inside the bubble are assumed as uniform except for the thin boundary layer near the bubble wall.
- (3) The inside boundary layer is thin enough compared with the bubble radius.
- (4) Vapor and noncondensable gas obey a perfect gas law.
- (5) Movement of the bubble wall by condensation or evaporation on the wall is assumed to be very small and therefore ignored.
- (6) The noncondensable gas obeys Henry's law.
- (7) The components inside the bubble, generated by electrolysis at the bottom of shock tube, are in equilibrium conditions with the surrounding liquid except for hydrogen.
- (8) Coalescence and fragmentation of droplets are neglected.
- (9) Slip between the droplets and the gas mixture is assumed to be small and ignored.
- (10) The diffusion process between the vapor and the noncondensable gas is assumed to be fast enough for the gas mixture inside the bubble to have uniformity, because the pressure inside the bubble is generally low and the size of the bubble is small.

**Calculated Results.** Main results will be shown in the section of Experimental Results and Discussion. The calculation model is shown schematically in Fig. 1. A bubble whose initial radius is  $10 \mu\text{m}$  starts to grow with stepwise pressure reduction from  $100 \text{ kPa}$  to the saturated vapor pressure ( $2.3 \text{ kPa}$ ,  $20^\circ\text{C}$ ). At the same time, the temperature inside the bubble decreases by adiabatic expansion of the gas mixture. Soon mist is formed by homogeneous condensation and the temperature recovers due to heat release of the condensation. Consequently the bubble behavior can be simulated by an isothermal

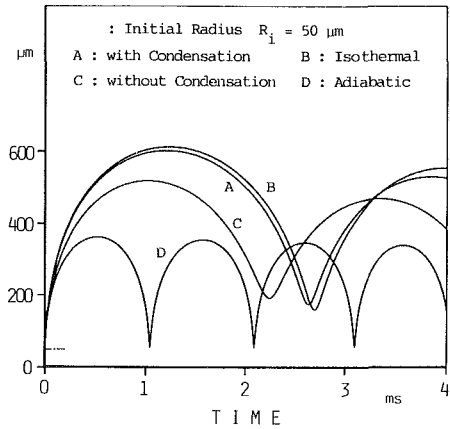


Fig. 2 Comparison of bubble motions depending on the inner conditions

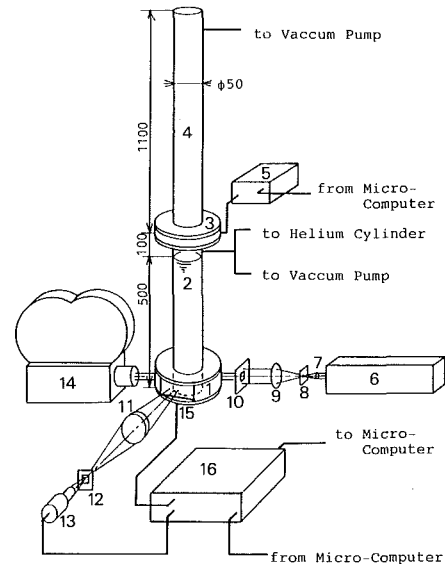


Fig. 3 Experimental apparatus consisting of a hydro shock tube and a bubble radius measuring system

- |                                     |                                       |
|-------------------------------------|---------------------------------------|
| 1: Test Section                     | 9: Lens ( $f = 100$ , $\phi 30$ )     |
| 2: High pressure chamber            | 10: Aperture ( $\square 6 \times 8$ ) |
| 3: Diaphragm                        | 11: Lens ( $f = 100$ , $\phi 50$ )    |
| 4: Low pressure chamber             | 12: Aperture ( $\square 6 \times 8$ ) |
| 5: Rupturing device                 | 13: Photomultiplier                   |
| 6: He-Ne Laser (25 mW)              | 14: High-speed camera                 |
| 7: Objective ( $f = 16.3$ )         | 15: Pressure transducer               |
| 8: Pinhole ( $\phi 5 \mu\text{m}$ ) | 16: Digital memory                    |

change inside the bubble. Figure 2 shows the calculated bubble behavior under various conditions. The initial radii are  $50 \mu\text{m}$  and the surrounding pressures are reduced from  $100 \text{ kPa}$  to the saturated vapor pressure ( $2.3 \text{ kPa}$ ,  $20^\circ\text{C}$ ). The bubble motion with the mist formation shown by *A* in the figure is close

### Nomenclature

$C$  = dissolved gas content,  $\text{kg}/\text{m}^3$   
 $I$  = output voltage of photomultiplier,  $\text{V}$   
 $P$  = pressure,  $\text{Pa}$   
 $M$  = mass inside the bubble,  $\text{kg}$

$R$  = radius of the bubble,  $\text{m}$   
 $T$  = temperature,  $\text{K}$   
 $k$  = constant,  $\text{V}/\text{m}^2$   
 $\alpha_M$  = mass accommodation factor  
 $\kappa$  = ratio of specific heat

### Subscripts

$g$  = noncondensable gas  
 $i$  = initial condition  
 $m$  = mixture  
 $v$  = vapor

to the curve *B* obtained from the assumption of isothermal change inside the bubble. When the radii are large the difference between assumption *A* and *B* is trivial, because the characteristic time of bubble motion is much longer than that of nonequilibrium condensation and evaporation inside the bubble. The motion without mist formation inside the bubble shown by *C* in the figure becomes smaller and faster than that with the mist formation. Curve *D* in the figure shows the motion under the assumption that the inside pressure consists of vapor pressure,  $P_v$ , and noncondensable gas pressure,  $P_g$ , where  $P_v$  is assumed to be constant and  $P_g$  to change adiabatically (ratio of specific heat  $\kappa = 1.4$ ). The motion of *D* is much smaller and faster than those of former cases.

## Experiments

**Experimental Apparatus and Procedures.** The experimental apparatus shown in Fig. 3 consists of a longitudinal hydroshock tube with its test section at the bottom. The shock tube has a high pressure chamber, made of a glass tube, in the lower part, a low pressure chamber, made of stainless steel tube, in the upper part and a rupturing device. The high pressure chamber contains distilled water whose surface is about 100 mm below the diaphragm. A pressure transducer and an electrode to generate a hydrogen bubble are installed at the bottom. The side wall of test section is made of acrylic resins and is polished sufficiently for laser light measurement.

The measuring system is as follows: The laser beam is expanded by two lenses and a pinhole. The expanded beam reaches the test section through a rectangular aperture. Scattered light from the bubble is focussed by lenses to a photomultiplier through a rectangular aperture. The control volume formed by the apertures has a shape of regular prism (6 mm  $\times$  6 mm  $\times$  8 mm). The output voltage of the photomultiplier,  $I$ , is related to the bubble radius,  $R$ , by  $I = kR^2$ . The constant  $k$  is calibrated in the following manner: The bubble radius is estimated from the measured rising speed and then the output  $I$  is related with the value of the radius. The signals of the photomultiplier and the pressure transducer are stored in the digital memories. After the run, the data are sent to a microcomputer and processed. The signal of the photomultiplier is stored simultaneously in three digital memories (1  $\mu$ s, 8 bit, 2 kword) whose input ranges are 0.1 V, 1 V and 10 V in order to increase the accuracy in low output region. The dynamic behavior of the cavitation bubble is photographed using high-speed motion pictures to confirm that there is one bubble in the control volume. The typical uncertainty levels are estimated as  $\pm 1$  percent for the pressure measurement and  $\pm 8$  percent for the bubble radius from their calibration data.

The experiment is performed according to the following procedures:

(1) The high pressure chamber is evacuated in order to remove air from pits and scratches on the inner wall and then the distilled water is poured into the chamber.

(2) After the water is stabilized at atmospheric pressure, the pressures of both chambers are adjusted, the high pressure to about 100 kPa (gauge) and the low pressure to  $-50$  kPa (gauge). The high pressure chamber is pressurized by helium in order to sharpen the pressure change.

(3) The time sequence of experiments is controlled by a microcomputer. Namely, when the hydrogen bubble formed by electrolysis enters the control volume, the high-speed camera is started and after 0.5 second the diaphragm is ruptured. The outputs of the photomultiplier and the pressure transducer are stored in digital memories.

(4) After the above experiments, the test water is sampled from the test section and the dissolved air content is estimated from oxygen content measured by a DO-meter.

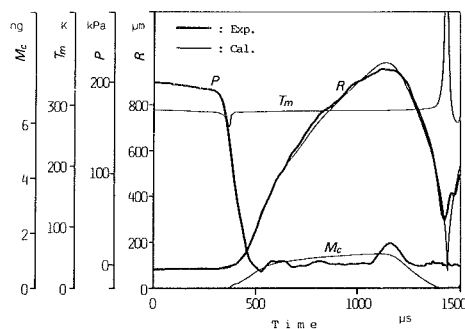


Fig. 4 Response of a small gas bubble to the ambient pressure change. The comparison between the experimental results and the calculated ones. The initial bubble radius is 80  $\mu$ m, the initial temperature is 16.5°C, the gas content is 18 ppm and the mass accommodation factor is 0.4.

**Experimental Results and Discussions.** The experimental results when the initial bubble radius is 80  $\mu$ m, the initial temperature is 16.5°C and the air content is 18 ppm, are shown in Fig. 4 together with the numerical results. The surrounding pressure decreases from 200 kPa (absolute) to the saturated vapor pressure and fluctuates around it. A tensile strength is observed at about 500  $\mu$ s. A small pressure rise about 1200  $\mu$ s is a reflected expansion wave at the gas-liquid interface in the tube. The bubble grows gradually at the first stage with the ambient pressure reduction and then accelerates its expanding rate. The bubble starts to shrink with the pressure rise and rebounds at 1420  $\mu$ s.

The bubble motion is calculated numerically using the experimental time history of pressure in the test section. The numerical results are shown by fine lines in the figure. The initial bubble radius used in the calculation is adjusted to a value, which is within the uncertainty level of measured data up to 100  $\mu$ s and gives the best fitting with the experimental result. The mass accommodation factor is assumed as 0.4. The agreement between the calculated time history of the bubble radius and the experimental one is very good except in the rebounding period. The temperature inside the bubble  $T_m$ , decreases with the bubble growth to a certain level, then it recovers to the surrounding liquid temperature due to the latent heat release caused by homogeneous condensation, which forms mist inside the bubble. The mass of condensed droplets  $M_c$ , increases with the bubble growth. When the bubble shrinks, the inside temperature tends to increase by the compression of the gas mixture, however the temperature is kept constant due to the evaporation of the mist. The mass of the condensed droplets decreases and then disappears by the evaporation and the deposition onto the bubble wall with the shrinking. The inside temperature increases adiabatically because of the absence of the mist. Subsequently the bubble rebounds and the temperature decreases rapidly.

The disagreement between experimental result and numerical one in the rebounding region may be caused by the following reasons: (1) The calculation model is inadequate to the interaction between the noncondensable gas and the vapor near the bubble wall in the shrinking period. When the pressure inside the bubble is high and the diffusion coefficient is small, the noncondensable gas accumulates near the bubble wall and the condensation rate of the vapor decreases due to the accumulation. (2) The bubble wall is deformed from the spherical shape by the instability in the shrinking period. The irregular surface may scatter laser light more than a spherical surface. So that, the bubble radius is measured larger than it is.

Figure 5 shows the case in which the initial radius is 82  $\mu$ m, the temperature is 16°C and the air content is 20 ppm. The

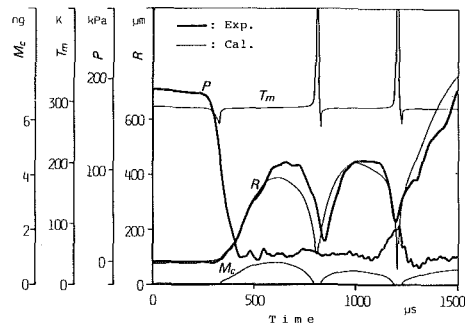


Fig. 5 Response of a small gas bubble to the ambient pressure change. The comparison between the experimental results and the calculated ones. The initial bubble radius is  $82 \mu\text{m}$ , the initial temperature is  $16^\circ\text{C}$ , the gas content is  $20 \text{ ppm}$  and the mass accommodation factor is  $0.4$ .

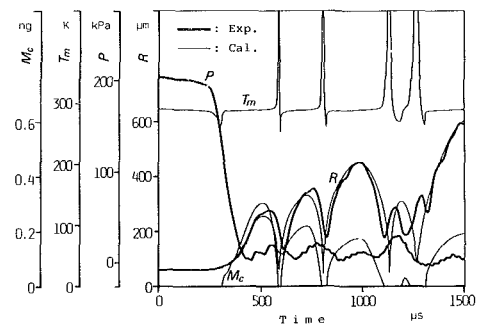


Fig. 6 Response of a small gas bubble to the ambient pressure change. The comparison between the experimental results and the calculated ones. The initial bubble radius is  $59 \mu\text{m}$ , the initial temperature is  $16^\circ\text{C}$ , the gas content is  $20 \text{ ppm}$  and the mass accommodation factor is  $0.4$ .

pressure does not decrease as in Fig. 4. The bubble does not grow as the former case and the rebound is observed in the middle. In the second cycle of the bubble motion, it rebounds and grows to the same size as the first cycle, then rebounds again by the compression wave and grows larger by the low pressure at about  $1300 \mu\text{s}$ . The complicated fluctuations overlapped on the main motion are observed in the bubble motion with the pressure fluctuations. The agreement between the experimental result and calculated one is not so good, however, the calculated bubble motion shows the characteristics of the experimental one. The bubble grows due to the pressure reduction and oscillates with higher order fluctuations by the complicated pressure variation. The mist is formed inside the bubble and the inside temperature is kept almost at the initial level, then the temperature increases rapidly due to the disappearance of mist inside the bubble in the rebounding period as shown in the former case. The mass of condensed droplets after the rebound is smaller than the first one. The reasons are explained as follows: The condensed droplets formed in the first cycle increase the enthalpy of the gas mixture due to the latent heat release, however many of them deposit onto the bubble wall without the absorption of enthalpy by the evaporation during the shrinking period. By these phenomena, the enthalpy has been transported into the bubble through the wall. The mass of condensed droplets in the third cycle is in the same order as in the second cycle, though the bubble radius in the third cycle is much larger than in the second cycle. The bubble motion is much influenced by the mist formation and disappearance inside the bubble.

Figure 6 shows the case in which the reduction of the ambient pressure has the same order as in Fig. 5 and the initial bubble radius is smaller. The bubble radius is  $59 \mu\text{m}$ , the temperature is  $16^\circ\text{C}$  and the air content is  $20 \text{ ppm}$ . Two rebounds are observed in the bubble motion until a compression wave reaches the test section. Comparison of the pressure change and the bubble motion reveals that the bubble expands when the pressure is lower than a certain value (about  $10 \text{ kPa}$ ) and it shrinks when the pressure is higher than the value. The bubble motion is resonant with the mode of pressure variation and grows to the same size as the bubble in Fig. 5 in spite of a smaller initial bubble radius. Ito and Oba [3] have observed that the bubbles trapped in a separation bubble circulate in it and oscillate complicatedly. Some of them explode to cavitation bubbles. Their observation seems to suggest that there are pressure fluctuations in the separated region, consequently, some bubbles explode and some collapse depending on the resonance. In this case, the response of bubbles to variable pressure fields play an important role in the cavitation inception.

The calculated results agree with the experimental ones except in the rebounding region. As to the mist formed inside the

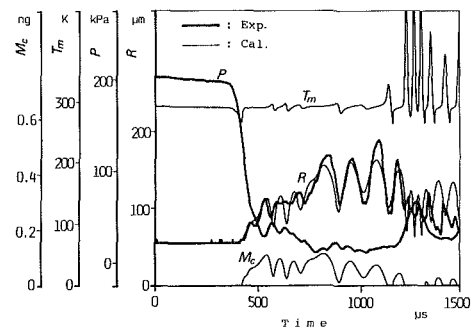


Fig. 7 Response of a small gas bubble to the ambient pressure change. The comparison between the experimental results and the calculated ones. The initial bubble radius is  $53 \mu\text{m}$ , the initial temperature is  $18^\circ\text{C}$ , the gas content is  $14 \text{ ppm}$  and the mass accommodation factor is  $0.4$ .

bubble, the maximum amount of the mass in each cycle decreases in spite of the increase of the bubble radius as shown in the former figure. It is understood that the mist formation and disappearance transport an enthalpy into the bubble. The temperature inside the bubble rises sharply when the bubble rebounds. At this moment, the inside gas mixture is compressed and expanded nearly adiabatically because there is no mist inside the bubble. The isothermal change and the adiabatic change appear alternately in the bubble during its oscillation due to the mist formation and disappearance. The resonance frequency of the bubble to a certain degree of pressure variation is much influenced by the mist formed inside the bubble. Namely, the behavior of the mist formed inside the bubble must be considered if the bubble motion is to be predicted exactly.

The last figure shows the case in which the pressure reduction is less than the former cases. The initial bubble radius is  $53 \mu\text{m}$ , the temperature is  $18^\circ\text{C}$  and the dissolved air content is  $14 \text{ ppm}$ . The bubble grows gradually with oscillation due to the slow pressure reduction. The experimental and calculated results agree with each other except in the period when the compression wave reaches the test section. The mist inside the bubble do not disappear and the mass of the condensed droplets oscillate with the bubble motion. The inside temperature is kept almost constant by the mist which works as a kind of a buffer.

A noncondensable gas inside a bubble plays an important role during its collapse. The authors et al. [9] have shown that dissolved air in water diffuses through a bubble wall when the bubble grows rapidly. The amount of noncondensable gas becomes 1.09 times of the initial condition in the case of Fig. 4 when the compression wave reaches the test section. In the case of Fig. 6, the ratio is 1.03. The quantity has no contribu-

tion to the bubble growth, however it may have many influences on the bubble collapse.

## Conclusions

Experiments and numerical calculations on the pressure response of small gas bubbles, so-called cavitation nuclei, to the ambient pressure change have been performed. The motions of hydrogen bubbles due to the ambient pressure reduction and increase have been observed in distilled water using a hydro-shock tube and a light scattering method. The measurement has been done for 2 ms and with  $1\mu\text{s}$  time resolving power. The bubble motion has been calculated numerically using the experimental time history of pressure in the test section. The thermodynamic effects by the mist formation inside the bubble are taken into consideration in this calculation. The calculated results are in good agreement with experimental ones. The following dynamic behavior of a small bubble is clarified:

(1) A small gas bubble grows almost isothermally due to the mist formation inside the bubble with the ambient pressure reduction.

(2) At the last stage of the bubble shrinking, the mist disappears from the inside by the evaporation and the deposition onto the bubble wall, so that the bubble rebounds nearly adiabatically.

(3) A bubble grows resonantly with the ambient pressure variation. The resonant bubble motion is much influenced by the mist formation and disappearance. The isothermal change and the adiabatic change appear alternately inside the bubble during its oscillation.

As mentioned above, it is necessary for the exact prediction of a bubble motion with the ambient pressure variation to consider the behavior of mist formed inside the bubble.

## Acknowledgments

The author wishes to express his gratitude for the helpful suggestions by Prof. H. Ohashi of University of Tokyo in preparing the manuscript. He also wishes to express his thanks to Messrs. M. Nagasaka and N. Goto for help with the experiments.

## References

- 1 Arakeri, V. H., and Acosta, A. J., "Viscous Effects in the Inception of Cavitation on Axisymmetric Bodies," *ASME JOURNAL OF FLUIDS ENGINEERING*, Vol. 95, 1973, pp. 519-528.
- 2 Katz, J., and Acosta, A., "Observations of Nuclei in Cavitating Flows," *Mechanics and Physics of Bubbles in Liquids*, Martinus Nijhoff Publishers, The Hague, 1982, pp. 123-132.
- 3 Ito, Y., and Oba, R., "A Limit in "Separation-Bubble Role" on Cavitation Inception," *Proceedings of Cavitation and Polyphase Flow Forum 1982*, ASME, 1982, pp. 9-11.
- 4 Sato, Y., and Shima, A., "The Growth of Bubbles in Viscous Incompressible Liquids," *Reports of the Institute of High Speed Mechanics*, Tohoku University, Japan, Vol. 40, 1979, pp. 23-49.
- 5 Lin, S. C., "Role of Microair Bubbles on Cavitation," *Proceedings of IAHR 10th Symposium of the Section on Hydraulic Machinery, Equipment and Cavitation*, 1980, pp. 27-38.
- 6 Matsumoto, Y., and Beylich, A. E., "Influence of Homogeneous Condensation inside a Small Gas Bubble on its Pressure Response," *ASME JOURNAL OF FLUIDS ENGINEERING*, Vol. 107, 1985, pp. 281-286.
- 7 Plesset, M. S., "The Dynamics of Cavitation Bubbles," *ASME Journal of Applied Mechanics*, Vol. 16, 1949, pp. 277-282.
- 8 Fujikawa, S., and Akamatsu, T., "On the Mechanisms of Cavitation Bubble Collapse," *Proceedings of IAHR 10th Symposium of the Section on Hydraulic Machinery, Equipment and Cavitation*, 1980, pp. 91-102.
- 9 Matsumoto, Y., and Shirakura, M., "Mechanisms of Cavitation Nuclei Suspension," *Proceedings of IAHR 11th Symposium of the Section on Hydraulic Machinery, Equipment and Cavitation*, Vol. 1, Paper No. 3, 1982.

## APPENDIX

### Uncertainty Analysis for Measurement of Bubble Radius

In this experiment which is a single-sample experiment, bias errors are debugged as much as possible. The random errors are considered in this analysis. The scattered light intensity from a bubble is proportion to the surface area of the bubble if the size is not too small. So that, the output voltage of the photomultiplier,  $I$ , may be related to the bubble radius,  $R$ , by  $I = kR^2$ . The constant  $k$  is estimated as follows: If the density and the viscosity inside the bubble is much smaller than those of water, the rising speed of the bubble in water,  $u$ , is written as

$$u = \frac{1}{3} \frac{g}{\nu} R^2 \quad (A1)$$

where  $\nu$  is kinematic viscosity and  $g$  is gravitational acceleration. The rising speed,  $u$ , is found to be proportion to the output voltage,  $I$ , and the proportional constant  $c$  is calibrated by the experiment. The bubble radius,  $R$ , can be expressed as follows using equation (A1) and the constant  $c$ .

$$I = \frac{g}{3\nu c} R^2 \text{ or } R = \sqrt{\frac{3}{g}} \cdot \sqrt{\nu c I} \quad (A2)$$

The relative uncertainty in the bubble radius is

$$\frac{\delta R}{R} = \frac{1}{2} \sqrt{\left(\frac{\delta \nu}{\nu}\right)^2 + \left(\frac{\delta c}{c}\right)^2 + \left(\frac{\delta I}{I}\right)^2} \quad (A3)$$

The  $\delta \nu / \nu$  is estimated as 0.02 because the temperature is measured as  $16 \pm 0.8^\circ\text{C}$  in 95 percent confidence level. The  $\delta c / c$  is estimated as 0.14 from the standard deviation  $s$  of the calibration data. The value of  $s/c$  is 0.07. The typical relative noise level of the output voltage of the photomultiplier is found as 0.04 and the relative uncertainty in the output,  $\delta I / I$ , is estimated as 0.08. The relative uncertainty in the bubble radius measurement,  $\delta R / R$ , is estimated as 0.08 in 95 percent confidence level from the above values.





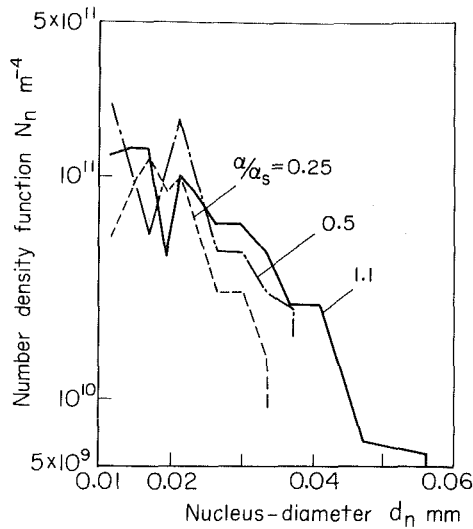


Fig. 2 Typical nuclei-size-distribution (uncertainties of  $\alpha/\alpha_s$  and  $N_n$  are  $\pm 5$  and  $\pm 10$  percent, respectively)

tent,  $\alpha/\alpha_s$ . The existing blow-down tunnel [5] shown in Fig. 1 is very suitable for these purposes.

In order to keep the cavitation nuclei as well as the physical properties of test water as uniform as possible for the entire experimental range, sufficiently clean water was once poured into the upstream reservoir. The test water, whose typical nuclei-size-distributions are shown in Fig. 2, was directly poured into the test section, changing the cavitation number,  $\sigma$ , very slightly to make a series of test runs for several values of  $\sigma$ . The test section is made of lucite, and the reservoir as well as all pipes of the tunnel is of plastic resin to keep the water as clean as possible by removing from the wall, any attached solid particles, which can be a source of cavitation nuclei.

The brass test-orifice [5, 6] of 8 mm diameter in conformity to the JIS Standards and the test section shown in Fig. 3 are the same as that described elsewhere [5], so that the acoustical and vibrational characteristics around the test orifice has to be the same as those reported previously [5, 7]. Since no feed pump is installed here, and since the flow starts from still water in the upstream reservoir, any additional disturbances become very small. The upstream and the downstream pressures,  $P_1$ , and  $P_2$ , were measured at the points,  $b_1$  and  $b_2$ , respectively, by the pressure transducer through the pressure chambers of about 2.6 kHz in natural frequency.

The cavitation acoustic pressure pulses were detected by means of the PZT-probe [5] with natural frequencies of 2.25 MHz (thickness mode) and 400 kHz (radial mode), which was

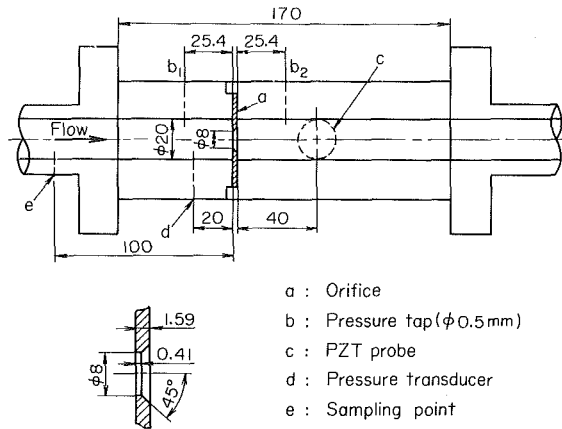


Fig. 3 Lucite orifice and test section

fixed at the point,  $c$ , on the outer surface of lucite wall whose acoustic impedance is very close to that of water. The directivity of the 20 mm diam-probe is broad enough to cover the entire occurrence zone of cavitation.

### Experimental Procedures

The cavitation number,  $\sigma$ , is defined by the downstream state where the cavitation takes place as follows:

$$\sigma = 2(P_2 - P_v) / \rho V_2^2$$

where  $P_v$ ,  $\rho$ , and  $V_2$  are the vapor pressure, the density of water, and the mean throat velocity, respectively.

The water was refined by the previously mentioned degassing process [7] for several air saturation rates  $\beta$  or several relative air contents  $\alpha/\alpha_s$ . The following three kinds of water were tested: (i) natural water as  $\beta = 2.8$  and  $\alpha/\alpha_s = 1.1$ , (ii) degassed water which is very often used in the ITTC Experiments [1] as  $\beta = 1.2$  and  $\alpha/\alpha_s = 0.5$ , and (iii) extremely degassed water as  $\beta = 0.8$  and  $\alpha/\alpha_s = 0.25$ .

Similar experimental procedures have followed for each run as described elsewhere [7]. For each run, a small amount of test water was sampled from the tap,  $e$ , located 100 mm upstream from the orifice. It was then checked whether or not  $\beta$ ,  $\alpha/\alpha_s$ , and the nuclei distribution were as prescribed. The cavitation number,  $\sigma$ , was continuously changed very slowly, considering the stochastic behavior of desinence as will be shown in Fig. 4. The rate,  $\Delta\sigma/\Delta t$ , was just as small as  $(1.6 \sim 3) \times 10^{-3}/s$ . Simultaneously, we tried to measure the pressure pulses, the cavitation aspects, and the corresponding flow conditions in order to analyze them statistically.

The number of pulses,  $n$ , and the time interval between suc-

### Nomenclature

$D$	= pipe diameter
$d_n$	= diameter of cavitation nuclei
$N_n$	= number-density distribution-function of the nuclei
$n$	= number of pulses per second
$n_i$	= number of pulses within a small $\sigma$ -range within a small $T_p$ -range
$n_t$	= total number of $n_i$ within the small $T_p$ -range
$P_1, P_2$	= 25.4mm upstream and downstream pressure from an orifice
$P_{TH}$	= threshold level selected for the pulse-detection
$P_v$	= vapor pressure of test water
$Re_{c,D}$	= Reynolds number based on $D$
$T_p, \bar{T}_p, \hat{T}_p$	= time interval between successive pulses, the

	mean, and the standard deviation within the small $T_p$ -range
$t_w$	= water temperature
$V_1, V_2$	= upstream velocity and mean throat velocity
$\alpha/\alpha_s$	= relative air content of water under the standard temperature and pressure
$\beta$	= air-saturation-rate under $\sigma_{d10}$
$\nu, \rho$	= kinematic viscosity and density of water
$\sigma$	= cavitation number, $2(P_2 - P_v) / \rho V_2^2$
$\sigma_d, \bar{\sigma}_d, \hat{\sigma}_d$	= desinent cavitation number, the mean, and the standard deviation within the small $T_p$ -range
$\sigma_{d10}$	= desinent cavitation number at $\bar{T}_p \approx 10s$
$\Delta\sigma/\Delta t$	= time-changing rate of $\sigma$

cessive pulses,  $T_p$ , were analyzed by a pulse-height-analyzer (1024 channels in resolving power,  $0.1 \sim 5 \mu\text{s}$  in rise time,  $1 \mu\text{s}$  in minimum duration, and  $3.3 \mu\text{s}$  in double-multiple resolution), and a digital memory ( $50\text{ns} \sim 1\text{s}$  per word in sampling speed).

For nuclei-size-measurement, the acoustical characteristics of the PZT-probe, and high-speed photography are described in detail elsewhere [5, 7-9].

In the present experiments, the upstream pressure,  $P_1$ , was fixed at about 144 kPa, and the water temperature,  $t_w$ , remained within  $286 \sim 288^\circ\text{K}$  ( $\approx 13 \sim 15^\circ\text{C}$ ). Since the Reynolds number,  $R_{c,D} = DV_1/\nu$ , lies within  $(2.2 \sim 3.0) \times 10^4$ , the orifice-flow must be turbulent.  $V_1$  and  $\nu$  are upstream mean flow-velocity, and the kinematic viscosity of water, respectively.

## Results

Cavitation bubbles having various sizes as well as shapes are clarified into several types having their own special characteristics, and are very randomly distributed both in space and in time, accompanied with their characteristic

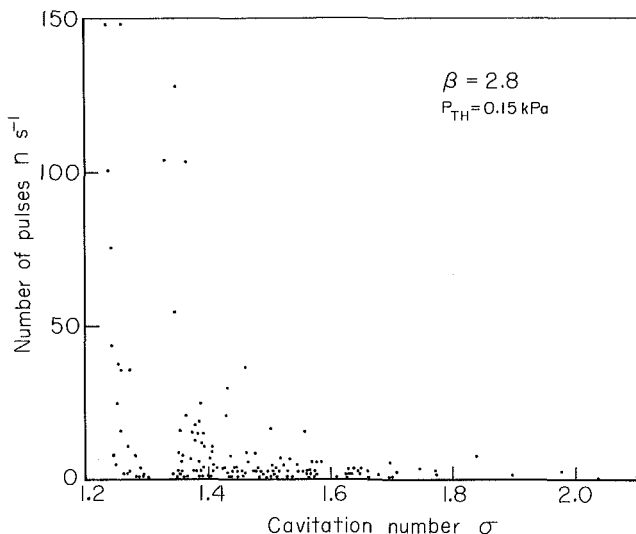


Fig. 4(a) Typical pressure-pulse frequency-distribution in the desinent state (uncertainties of  $\sigma$  and  $P_{TH}$  are  $\pm 5$  and  $\pm 0.5$  percent, respectively)

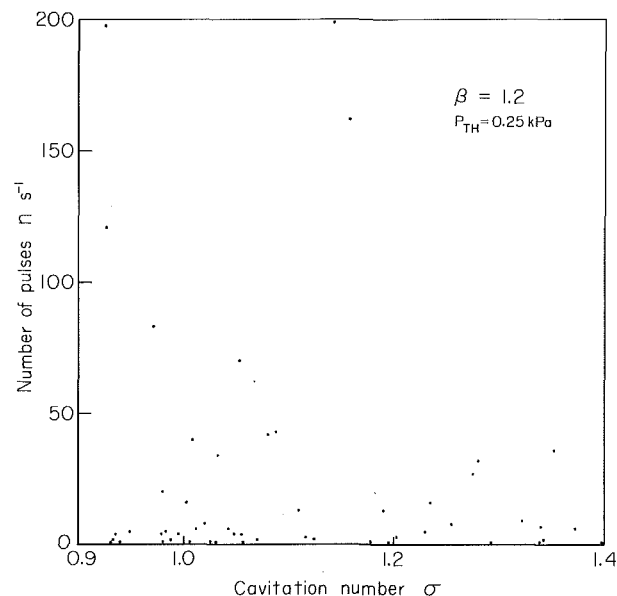


Fig. 4(b) Typical pressure-pulse frequency-distribution in the desinent state

pressure pulses with several microsecond durations in their collapsing stage. First, let us investigate the stochastic behavior of desinence through the pressure pulses, i.e., the acoustic energy flux coming out of the collapsing bubbles.

These pulses exhibit a wide variety both in height and in time interval between successive pulses. In the past experiments on such a cavitation desinence, however, the most essential parameters, such as the time interval,  $T_p$ , as well as the threshold level of the pulse height,  $P_{TH}$ , which is closely related to the time resolution of desinence detection, have arbitrarily been selected or almost ignored, resulting in an extremely wide variation in desinent cavitation number.

**Range of Desinence.** To date, desinence has roughly been regarded as a desinent point without deviation, and its stochastic behavior has almost been ignored. Here, we will study whether or not such an existing concept is essentially acceptable.

With the above-mentioned continuous small rate of  $\Delta\sigma/\Delta t$ , we first searched for the pulse-frequency-distribution in the desinent state, where only a small number of pulses per second,  $n$ , such as several hundreds or less, could be countable, as illustrated in Figs. 4(a)-(c), in a wide range in air-saturation-rate,  $\beta$ , from undersaturation to oversaturation, for low threshold levels,  $P_{TH}$ .

It is noted that in the oversaturated water ( $\beta > 1$ ), the nature of the desinent point is not necessarily shown. However, the desinence is unexpectedly distributed widely with respect to  $\sigma$ , showing its significant stochastic behavior. In our future studies, therefore, we must evaluate the random parameters clearly. With a decrease in  $\beta$ , however, the stochastic behavior vanishes rapidly, and disappears almost completely in undersaturated water ( $\beta < 1$ ). This shows the

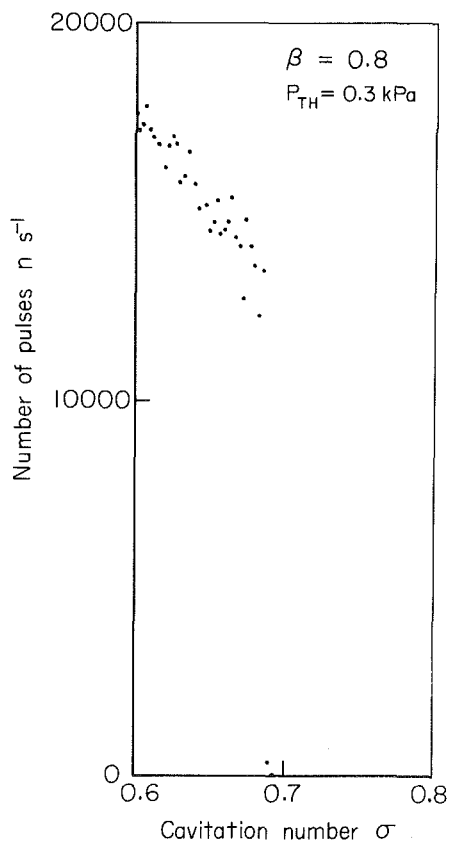


Fig. 4(c) Typical pressure-pulse frequency-distribution in the desinent state

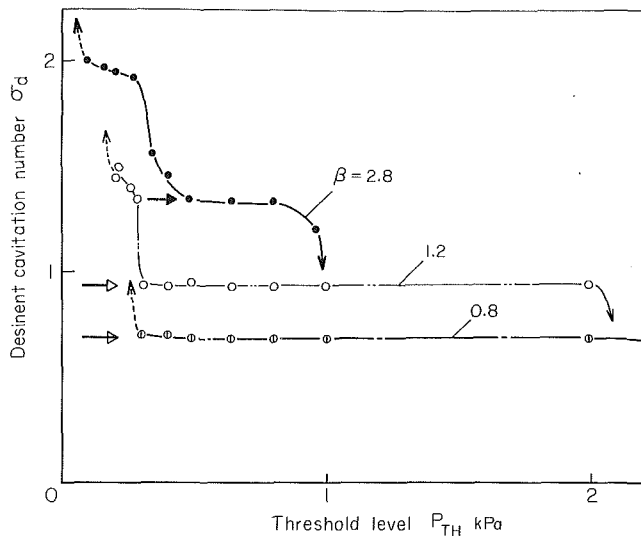


Fig. 5 Threshold level  $P_{TH}$  versus desinent cavitation number  $\sigma_d$  ( $\leftarrow$ ,  $\rightarrow$  and  $\rightarrow$  show the desinent cavitation number  $\sigma_{d10}$ )

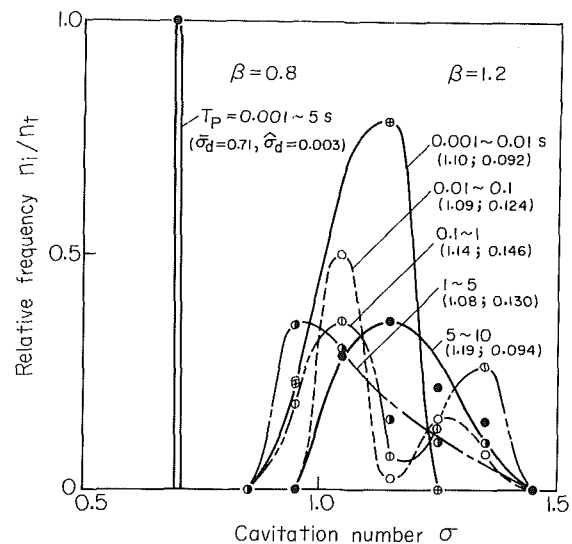


Fig. 7 Relative frequency distribution within a small  $T_p$ -range

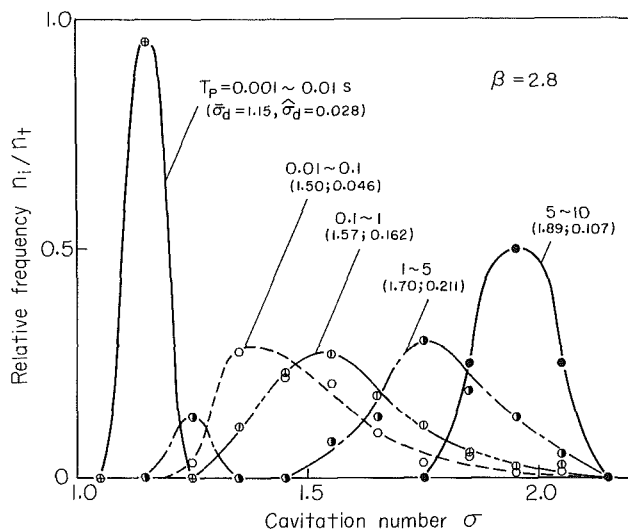


Fig. 6 Relative frequency distribution within a small  $T_p$ -range (uncertainty of  $T_p$  is  $\pm 5$  percent)

nature of the desinent point where  $n$  decreases sharply at a fixed value of  $\sigma$ .

The threshold level,  $P_{TH}$ , is still arbitrarily selectable. Here, we define the desinent cavitation number  $\sigma_{d10}$ , which corresponds to  $\bar{\sigma}_d$  at  $\bar{T}_p \approx 10$  s as shown later in Figs. 8–9. The observed values of  $\sigma_{d10}$  are shown in Fig. 5. The upper limit of  $P_{TH}$  is the maximum pulse height, and the lower one to be detected in the present experiment, as shown by dotted lines, is the electric noise level. For example, in a range of  $0.5 \text{ kPa} < P_{TH} < 0.9 \text{ kPa}$  for  $\beta = 2.8$ , there exists a marked range of constant  $\sigma_{d10}$ , where  $\sigma_{d10}$  is expected to be close to so-called desinent cavitation number,  $\sigma_d$ , having been regarded as a desinent point [7]. As  $\sigma_d$  varies principally in the lower  $P_{TH}$ -side, it is therefore presumed that the stochastic behavior results mainly from rather low pulses.

**Recognition Parameters for Desinence.** Next, let us clarify the detailed aspects of these frequency distributions. The individual pulses were first classified into small groups with respect to  $T_p$  as well as  $\sigma$ . Then the relative frequency distribution,  $n_i/n_T$  versus  $\sigma$  relation shown in Figs. 6 and 7, was searched for, where the pulse number,  $n_i$ , was counted within a small  $\sigma$ -range and a small  $T_p$ -range,  $n_T$  was the total number

of  $n_i$  within the small  $T_p$ -range. The mean values  $\bar{T}_p$ ,  $\bar{\sigma}_d$ , as well as the standard deviations  $\hat{T}_p$ ,  $\hat{\sigma}_d$  were also evaluated. Clearly these distributions tend to shift toward the high  $\sigma$ -side with an increase in  $T_p$ . Thus detected desinence depends on the method of detection, since its time resolving power is still almost arbitrarily selectable. Being fairly close to the normal distribution, these distributions also illustrate the marked stochastic evidence. With a decrease in  $\beta$ , however, such a shift becomes rapidly narrower and is expected scarcely to be seen in undersaturated water.

For various values of  $P_{TH}$  and  $\beta$ , Figs. 8–9 illustrate the mean desinent cavitation number,  $\bar{\sigma}_d$ , the mean time interval,  $\bar{T}_p$ , and their standard deviations,  $\hat{\sigma}_d$ ,  $\hat{T}_p$ , as shown by symbols  $\square$ ,  $\square$ , respectively. The extrapolated values of  $\bar{\sigma}_d$  are also shown for  $\bar{T}_p = 1$  day, 1 year, and 10 years. Clearly, both  $\bar{\sigma}_d$  and  $\hat{\sigma}_d$  vary significantly not only with respect to the known parameter,  $\beta$ , and/or  $\alpha/\alpha_s$  [10, 11], but also to the new recognition parameters,  $\bar{T}_p$  and  $P_{TH}$ . Therefore, it is doubtful to the authors that the existing approach can result in the precise evaluation of desinence. Thus, in our future experiments, it will be absolutely necessary to show the selected values of  $\bar{T}_p$  and  $P_{TH}$ , or to use the standard values internationally decided.

The time resolving power detecting such desinence thus depends on the method of detection with the naked eye, the ear, photography, and acoustic-and optical techniques. It is thus necessary that a very wide variety of  $\sigma_d$  be observed on the ITTC Standard Body, since the variations of  $\bar{\sigma}_d$  and  $\hat{\sigma}_d$  are comparable to those reported by Johnsson [1]. Some readers may wonder why the substantial cavitation variation on desinence was found only very recently [1, 2]. Because of recent rapid improvements in time resolving power of acoustic and optical detection, however, such findings are expected, because  $\bar{\sigma}_d$  and  $\hat{\sigma}_d$  increase rapidly with a decrease in  $P_{TH}$ , as shown in Fig. 8.

In Figs. 8 and 9,  $\bar{\sigma}_d$  is almost linearly related to  $\ln(\bar{T}_p)$ , thus  $\bar{\sigma}_d = a \ln(b\bar{T}_p)$ , where the constants,  $a$  and  $b$ , are positive. The relation essentially indicates that  $\bar{\sigma}_d$  becomes much higher when the desinence is detected only through very intermittent pulses. From the viewpoint of absolute safety from cavitation troubles, it may be advisable that a safety factor should be 3 or so at the entrance to nozzles or bends as in an atomic reactor, in which even extremely intermittent cavitation events, say, once a hundred years must be avoided completely.

It is also significant that the stochastic behavior takes place predominantly in a range of  $0.01 \text{ s} < \bar{T}_p < 1 \text{ s}$ , and it tends to

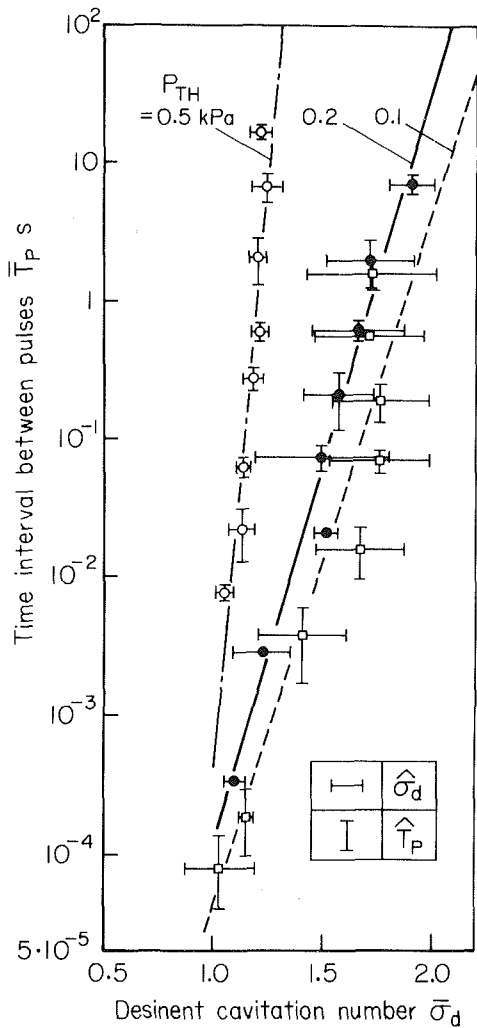


Fig. 8 Effects of recognition parameters,  $T_p$  and  $P_{TH}$ , upon the desinence (case of  $\beta = 2.8$ )

vanish for an increase in the interval away from this range. Thus, when desinence is detected with a low time resolving power of  $T_p \approx 0.1s$  (for example, that for the naked eye), significant scatter in the observed  $\sigma_d$  is inevitable.

Finally, we will consider the mechanism by which such stochastic behavior is directly related to  $\beta$  (Fig. 9). Then  $\sigma_d$  varies scarcely with  $T_p$  for undersaturated water ( $\beta = 0.8$ ), so that such behavior can be said to vanish there. Such a marked change with respect to  $\beta$  can be explained sufficiently only by a rather small difference in cavitation nuclei contained within the upstream reservoir (Fig. 2).

According to the present theory of cavitation nucleation [12, 13], observed cavitation bubbles must be closely related to initial nuclei sizes. Any nucleus may grow into sufficient size to cavitate in the downstream dead water space, since such nuclei, moving within this space could have sufficient time to grow. In oversaturated water, where any bubble (say, a gaseous bubble) may be stable, nucleus sizes are much more densely distributed than in undersaturated water, where only bubbles smaller than those with a critical radius (say, vaporous bubbles) are stable. Thus nuclei are much larger in oversaturated water than in undersaturated water. This is the reason, therefore, why a marked change of stochastic behavior with respect to  $\beta$  takes place. Nucleation theory also indicates that gaseous bubbles can be produced with much smaller tension than vaporous ones.

**Aspects of Desinence.** The desinent aspects were

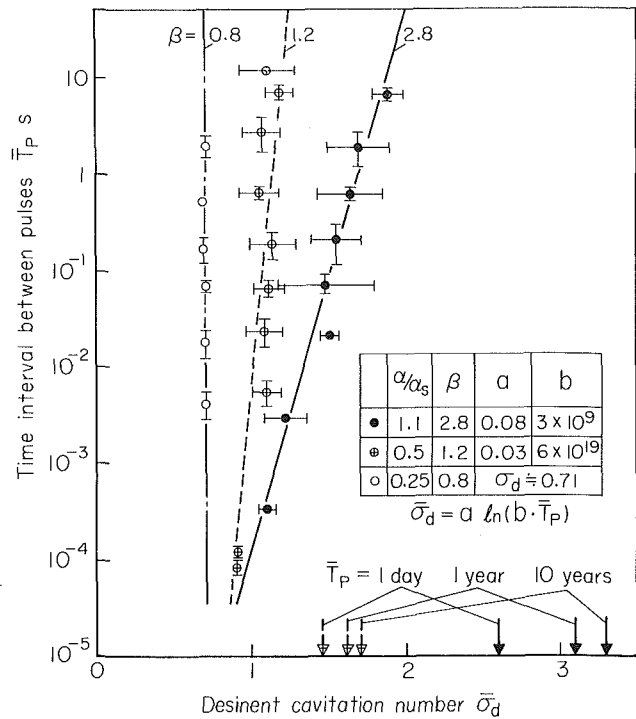


Fig. 9 Effects of recognition parameters,  $T_p$  and  $\beta$  upon the desinence (case of  $P_{TH} = 0.3 \text{ kPa}$ )

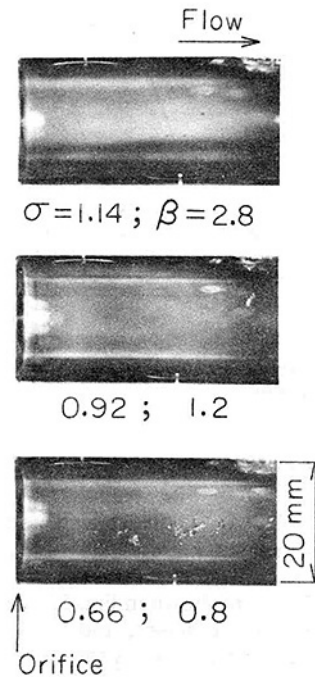


Fig. 10 Aspects of desinence (exposure time  $3 \mu s$ )

photographed with a xenon flash lamp with exposure time of  $3 \mu s$ , for various  $\beta$ , as shown in Fig. 10. Clearly, most of these consist of nonspherical bubbles, as previously reported [7, 9], but their nonsphericity is small. We have described elsewhere [7, 9] the cavitation aspects for the entire range from the desinence to the developed state, for various air saturation rates, the frequency distributions for several types of bubbles, and the spectra of cavitation-shock-sound-pressures.

## Conclusion

To make clear the stochastic behavior of desinence in low

turbulence water flow through an orifice, the acoustic pressure pulses associated with cavitation were statistically analyzed for various random stochastic quantities, and various states of the test water. The results obtained are summarized as follows:

(1) For oversaturated water ( $\beta > 1$ ), desinence is distributed widely on  $\sigma_d$ , scarcely showing the nature of a desinent point for little deviation. Strong stochastic behavior and predominantly exhibited as variations of  $\bar{\sigma}_d$  and  $\hat{\sigma}_d$  are made large enough with respect to  $P_{TH}$ ,  $\bar{T}_p$ , and  $\beta$ , explaining  $\sigma_d$ -deviation partly on the ITTC Standard Body. In our future experiments, therefore, it is desirable to decide the standard values of the recognition parameters,  $P_{TH}$  and  $\bar{T}_p$ .

(2) The relation  $\bar{\sigma}_d = a \ln(b\bar{T}_p)$  holds true for a fixed  $P_{TH}$  and  $\beta$ . A safety factor of at least 3 from cavitation troubles is advisable, for example, for the entrance nozzles of an atomic reactor.

(3) It is remarkable that  $\hat{\sigma}_d$  becomes much larger in a range of  $0.001s < \bar{T}_p < 1s$ , which is close to that of the time resolving power, detecting desinence with the naked eye, the still photographs, and/or high-speed movies under the framing rate of 1000 fps.

(4) In undersaturated water ( $\beta < 1$ ), the stochastic behavior almost disappears, indicating the desinent point actually where it decreases sharply, regardless of the difference in the desinence detection.

## References

1 Johnsson, C. A., "Cavitation Inception on Head Form. Further Test,"

*Proceedings of the 12th International Towing Tank Conference*, Rome, 1969, pp. 381-392.

2 Oba, R., and Ito, Y., "Cavitation Aspects in a Venturi "Johnson Effects" in a Low Turbulent Flow," The Report of the Institute of High Speed Mechanics, Tohoku Univ., Vol. 46, 1983, pp. 89-102.

3 Arakeri, V. H., and Acosta, A. J., "Viscous Effects in the Inception of Cavitation on Axisymmetric Bodies," ASME JOURNAL OF FLUIDS ENGINEERING, Vol. 95, 1973, pp. 519-528.

4 Ito, Y., and Oba, R., "Several Types of Cavitation Bubbles, Especially Streamer-Bubbles," 1981 Cavitation and Polyphase Flow Forum, ASME, Boulder, Colo., 1981, pp. 14-16.

5 Oba, R., Ito, Y., and Uranishi, K., "Effect of Polymer Additives on Cavitation Development and Noise in Water Flow Through an Orifice," ASME JOURNAL OF FLUIDS ENGINEERING, Vol. 100, 1978, pp. 493-499.

6 Japanese Industrial Standard, Z8762, "Measurement of Fluid Flow by Means of Orifice Plates and Nozzles," Japanese Industrial Committee, 1979.

7 Oba, R., Kim, K. T., and Uranishi, K., "Singular Behavior of Cavitation in Undersaturated Water," The Report of the Institute of High Speed Mechanics, Tohoku Univ., Vol. 46, 1983, pp. 75-88.

8 Oba, R., Kim, K. T., Niitsuma, H., Ikohagi, T., and Sato, R., "Cavitation-Nuclei Measurements by a Newly Made Coulter-Counter Without Adding Salt in Water," The Report of the Institute of High Speed Mechanics, Tohoku Univ., Vol. 43, 1981, pp. 163-176.

9 Oba, R., and Uranishi, K., "Cavitation Bubble Observation in Dilute Polymer Flow Through an Orifice," The Report of the Institute of High Speed Mechanics, Tohoku Univ., Vol. 39, 1979, pp. 47-62.

10 Numachi, F., "Über die Kavitationsentstehung mit besonderem Bezug auf der Luftgehalt des Wassers," *Ingenieur-Archiv*, Bd.7, 1936, S.396-406.

11 Holl, J. W., "An Effect of Air Content on the Occurrence of Cavitation," ASME *Journal of Basic Engineering*, Vol. 82, 1960, pp. 941-946.

12 Kamiyama, S., and Yamazaki, T., "Prediction of Gaseous Cavitation Occurrence in Various Liquids Based on Two-Phase Flow Analogy," *Proceedings of IAHR Symposium*, Tokyo, 1980, pp. 53-63.

13 Holl, J. W., and Wislicenus, G. F., "Scale Effects on Cavitation," ASME *Journal of Basic Engineering*, Vol. 87, 1961, pp. 385-398.

# Bubble Dynamics and Cavitation Inception in Cavitation Susceptibility Meters

G. L. Chahine

Tracor Hydronautics, Inc.,  
Laurel, MD

Y. T. Shen

David W. Taylor Naval Ship Research  
and Development Center,  
Bethesda, MD

*To improve the understanding of the scaling effects of nuclei on cavitation inception, bubble dynamics, multibubble interaction effects, and bubble-mean flow interaction in a venturi Cavitation Susceptibility Meter are considered theoretically. The results are compared with classical bubble static equilibrium predictions. In a parallel effort, cavitation susceptibility measurements of ocean and laboratory water were carried out using a venturi device. The measured cavitation inception indices were found to relate to the measured microbubble concentration. The relationship between the measured cavitation inception and bubble concentration and distribution can be explained by using the theoretical predictions. A tentative explanation is given for the observation that the number of cavitation bursting events measured by an acoustic device is sometimes an order of magnitude lower than the number of microbubbles measured by the light scattering detector. The questions addressed here add to the fundamental knowledge needed if the cavitation susceptibility meter is to be used effectively for the measurement of microbubble size distributions.*

## Introduction

Pure liquids at ambient temperature are known to withstand very large tensile stresses before they are ruptured into cavities. However a "real" liquid contains weak spots or nuclei, which allow phase change of the liquid at much lower tensile stresses or even at positive pressures. Cavitation is the physical phenomenon describing this phase change under hydrodynamic conditions. Stream nuclei or microbubbles have been shown experimentally to be a very important source for cavitation inception (see review by Holl, 1979), and a significant influence of bubble concentration on cavitation inception has been observed experimentally. The development of techniques to measure cavitation nuclei distribution in laboratories and oceans has been intensified in recent years. Review studies on the subject have been presented recently by Shen and Peterson (1983) and Billet (1984). One of the devices being developed and which will be studied here is the Cavitation Susceptibility Meter (CSM). This is a venturi system with a specially tailored geometry for cavitation nuclei measurements (Oldenzel, 1982 and Lecoffre and Bonnin, 1979). Microbubbles entering the venturi grow at the throat and are detected either optically or acoustically. In the first case they have to exceed a certain size to be perceived, while in the second case the noise generated during the implosion of these bubbles has to exceed a certain acoustical level. Therefore in this method a "critical pressure,"  $P_{cr}$ , at the venturi throat, below which cavitation events are detected by the CSM, is measured.

The classical cavitation number,  $\sigma$ , has been widely used in scaling cavitation inception between model and prototype:

$$\sigma = \frac{P_{\infty} - P_v}{\frac{1}{2} \rho V_{\infty}^2} \quad (1)$$

In this expression  $P_{\infty}$  and  $V_{\infty}$  are the characteristic pressure and velocity,  $\rho$  the liquid density, and  $P_v$  the liquid vapor pressure. This definition assumes that cavitation inception occurs when the liquid pressure drops below vapor pressure. However, it has been recognized for a long time, using static equilibrium theory, that there exists for each initial nuclei size a critical pressure, usually much lower than  $p_v$ , below which unstable bubble growth occurs. Since in a liquid nuclei are distributed in a relatively wide range of sizes, the definition of a "liquid critical pressure" can only be done by introducing an inception criterion such as a threshold amplitude and rate of the detected cavitation "events." It has been demonstrated experimentally that if  $p_v$  is replaced by such a "critical pressure" of the liquid, the correlation of cavitation inception observed experimentally between different model sizes is greatly improved (Keller, 1984). It is implied that by doing so one accounts for differences in the nuclei population without having to determine the actual bubble size distribution. With the CSM a "critical pressure" at the venturi throat is determined by varying the throat velocity and counting the occurrence of cavitation bursting optically or acoustically. If, in addition, there exists a thorough theoretical knowledge of the relationship between fluid flow characteristics, nuclei initial size and needed critical pressures to initiate cavitation events the CSM

Contributed by the Fluids Engineering Division for publication in the JOURNAL OF FLUIDS ENGINEERING. Manuscript received by the Fluids Engineering Division, December 17, 1985.

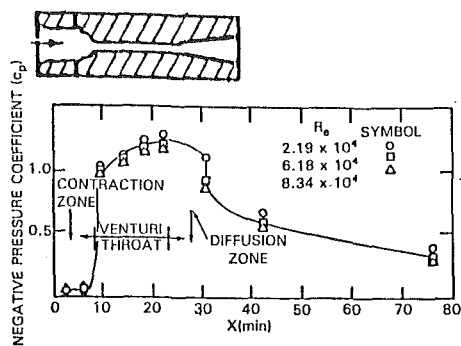


Fig. 1 Pressure distribution along the Venturi throat

might be useful as a bubble nuclei size detector. In this paper we attempt to improve on this knowledge by considering bubble dynamics and interactions between bubbles and with the main flow into the venturi. This investigation is to be added to earlier studies by d'Agostino and Acosta (1983) and Shen, Gowing, and Pierce (1984).

To obtain the critical pressure and bubble size distribution of ocean waters, measurements were carried out in the straits of Florida and the coastal waters of the Bahamas. The critical pressure of the ocean water was determined by detecting the onset of cavitation in the CSM venturi system. Ocean measurements (Shen, Gowing, and Pierce, 1984) showed that at a given depth (ambient pressure) there exists a critical venturi throat velocity below which no cavitation bursting is detected. A slight increase of throat velocity above this critical value results in a jump in the recurrence of cavitation bursting. The same qualitative trend is predicted from the static equilibrium theory of a single spherical bubble. The dynamic bubble behavior should give a more accurate quantitative comparison to the experiments since it allows a more effective screening of the bubble sizes which contribute to the cavitation events detected by the CSM. Bubble Growth or collapse can then be related to cavitation inception dependent on the event detection system used. The inclusion of interactions is important for the reasons presented below.

Cavitation susceptibility meters are designed in such a way that when in operation there is only one bubble in the venturi throat at a given time (see, for instance, the paper of d'Agostino and Acosta, 1983). However, in practice multibubbles appear occasionally in the venturi and invalidate the method of detection. The subject of multibubble interaction and its influence on the dynamics of an individual bubble is of great interest in many fluid engineering fields. In this paper multibubble interaction when the nuclei entering the venturi are clustered together is included in the study of cavitation inception in the CSM venturi system and its influence on the inception criterion is investigated. This part of the analysis follows earlier studies by Chahine (1981, 1982, and 1985).

Due to the restriction of the pipe wall, the velocity field and the pressure field in a venturi system are altered when the microbubbles begin to grow. This subject has been studied by d'Agostino and Acosta (1983) for a single spherical bubble entering from a reservoir into a semi-infinite pipe of constant cross-section. In the present paper we consider the case where multiple bubbles are present in a venturi and we derive an expression for the pressure correction due to the wall restriction. This correction is included in a symmetrical multibubble code when the bubbles are grouped together as a cloud. The growth and collapse of a single bubble and multibubbles in a venturi system with contraction, throat, and diffuser zones of various diameters are computed considering the venturi wall restriction.

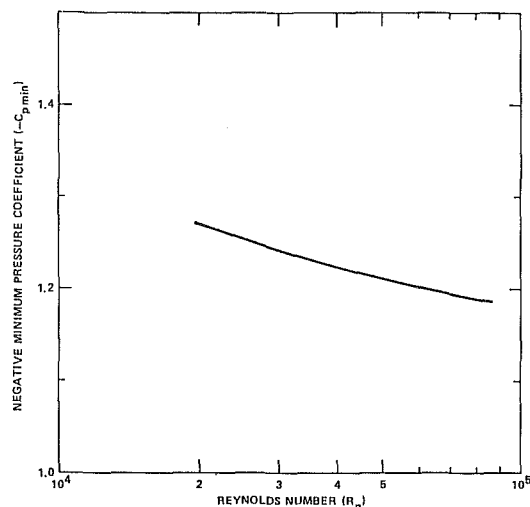


Fig. 2 Minimum pressure coefficient in the Venturi throat

### Experimental Study

At-sea measurements were conducted in March and April of 1983 off the coast of Florida and in coastal waters near the Bahamas (Shen, Gowing, and Pierce, 1984). The test program included cavitation susceptibility measurements using a venturi system, and microbubble measurements using a light scattering detector. The occurrence of cavitation was detected by acoustic pulses from collapsing cavitation bubbles. After completion of the sea trip, the same venturi system was attached to the DTNSRDC 12-in. water tunnel to correlate venturi cavitation with the microbubble distributions measured by the light scattering device. The ocean microbubble spectra were measured by examining the microbubbles in large water samples retrieved from depth. For the 12-in. water tunnel tests the bubble detector was connected to a pipe that bypassed water from the center of the tunnel test section to the detector. Detailed descriptions of the tests and procedures are given in the paper by Shen, Gowing, and Pierce (1984).

The venturi used as a cavitator for these studies had a 16 to 1 area contraction ratio and a throat diameter of 2.02 mm. A three-times scaled up model of this venturi was fabricated at DTNSRDC to facilitate pressure distribution measurements. Ten pressure taps of 0.41 mm diameter were flush mounted along the venturi wall. The measured pressure distributions are shown in Fig. 1 for several Reynolds numbers. The pressure coefficients,  $c_p$ , shown in the figure are defined by:

$$c_p = \frac{P - P_o}{\frac{1}{2} \rho V_t^2} \quad (2)$$

where  $P$  is the local pressure,  $P_o$  the reference upstream pressure, and  $V_t$  is the mean velocity at minimum throat diameter. The negative minimum pressure coefficient as a function of Reynolds number is shown in Fig. 2. The values decrease with increasing Reynolds number as expected. Due to the small throat diameter and high throat velocity, the boundary layer becomes turbulent and results in a wall shear region near the entrance. A significant energy loss can be expected. A pressure coefficient of as low as  $-1.22$  was measured. This fact must be properly considered when a venturi is used for cavitation investigations. We have accounted for this energy loss in our computations presented below.

The at-sea trials venturi unit was deployed to a specified depth while monitoring the pressure transducers. Once at depth, the flow rate was set just below the critical speed such

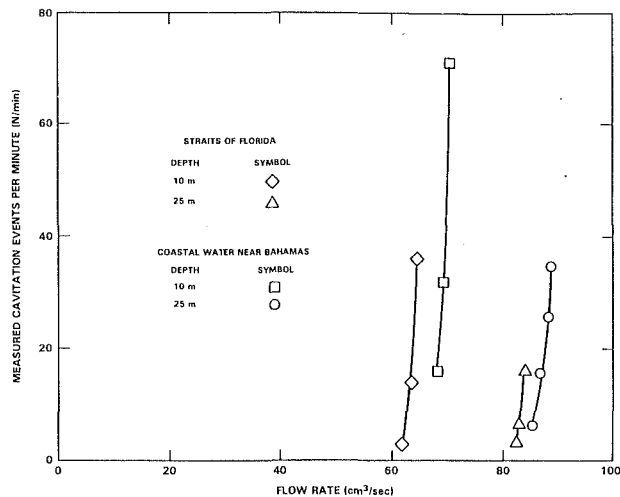


Fig. 3 Measured cavitation events at sea

that no acoustic signals were detected for three to five minutes. The flow rate was then increased until high amplitude acoustic signals were detected, and then tuned to attain a specific frequency of cavitation events. The flow rate, ambient pressure, and acoustic signals were recorded on tape and displayed on the shipboard readout unit for 3 to 5 minutes, with a few 10 minute runs.

The measured frequencies of cavitation events as a function of flow rate at 10 and 25 meter depths are shown in Fig. 3. At a given depth there exists a threshold flow rate below which no cavitation bursting signals were detected, yet a slight increase in flow rate resulted in a large increase in the frequency of cavitation events. This sensitive dependence of cavitation event frequency on flow rate was also observed at other test sites. The tensile strength of the liquid is related to the threshold flow rate at which bursting events start to be detected and the inception of cavitation occurs. This flow rate can be obtained for example by extending the inception curves in Fig. 3 to the zero event per minute rate. The measured cavitation inception indices were found to be quite different from the measured  $-C_{pmin}$ , depending on the depth and the test sites. The measured values of the cavitation number at inception were about 1.08 in the straits of Florida and about 0.90 in the coastal water near the Bahamas at the 10 meter depth. These measurements relate to the different bubble size distributions in the two locations (see Shen, Gowing, and Pierce, 1984). Those values are substantially lower than the value of  $-C_{pmin}$  of 1.22. Another observation was that fewer cavitation events were measured than would be predicted by optically determined bubble concentrations.

In the water tunnel tests the air content conditions could be varied from very low to supersaturated. At the supersaturated conditions, the throat pressure was higher than the vapor pressure when the cavitation acoustic signals were detected. The measured cavitation inception indices were then higher than  $-C_{pmin}$ . Even without going through explosive growth, adequate acoustic signals can be generated if the larger sizes of cavitation nuclei are available. With the tunnel water deaerated, tension occurred at the venturi throat when cavitation inception was detected. The tensile strength increased with reduced air content. At the intermediate air contents, a tensile strength of 0.4 bars was measured. This value is compatible with the values measured in sea water at 10 and 25 meter depths. Similarly the bubble distributions are compatible. At an extremely low air content, a tensile strength of 1.69 bars was measured. This corresponds to a cavitation inception number of 0.48. Additional data and information can be found in Shen, Gowing, and Pierce (1984).

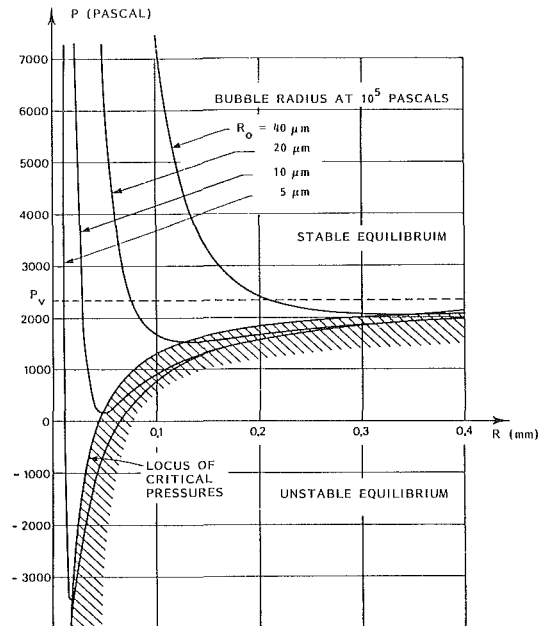


Fig. 4 Variation of bubble radius with ambient pressure

### Single Bubble Static Equilibrium and Dynamics

We have earlier defined the critical pressure of a liquid as the pressure (or tension) below which significant bubble growth or activity is detectable. In fact, as can be deduced from the dynamic stability analysis of the static equilibrium of isolated spherical bubbles, there is a different critical pressure for each initial bubble size considered. The balance of pressure across the bubble interface can be written:

$$P = P_v + P_g - 2\gamma/R, \quad (3)$$

where  $P$  is the ambient pressure,  $P_v$  and  $\gamma$  are the liquid vapor pressure and surface tension, and  $R$  is the equilibrium bubble radius.  $P_g$  is the pressure of noncondensable gas inside the bubble. The gas is usually assumed to behave ideally with the law of compression:

$$P_g R^{3K} = \text{constant}. \quad (4)$$

The polytropic constant  $K$  lies between 1 (isothermal case) and  $c_p/c_v$  (adiabatic case). The relationship between the ambient pressure,  $P$ , and the equilibrium radius,  $R$ , is therefore univocally defined for a given reference value  $R_o$ , or  $P_{g_o}$ , corresponding to a reference pressure  $P_o$ :

$$P = P_v + P_{g_o} \left(\frac{R_o}{R}\right)^{3K} - \frac{2\gamma}{R}, \quad (5)$$

with

$$P_{g_o} = P_o - P_v + \frac{2\gamma}{R_o}. \quad (6)$$

Figure 4 shows an example of the static equilibrium curves  $P(R)$  for the isothermal case,  $K=1$ .

The unstable portions of these curves correspond to  $dP/dR > 0$ , while the critical pressure,  $P_{cr}$ , and radius,  $R_{cr}$ , are given by  $dP/dR = 0$ . These critical values are related to each other and to the initial conditions by the relations:

$$R_{cr}^{3K-1} = \frac{3K P_{g_o} R_o^{3K}}{2\gamma}, \quad (7)$$

$$P_v - P_{cr} = \frac{3K-1}{3K} \cdot \frac{2\gamma}{R_{cr}}. \quad (8)$$

Therefore a bubble of initial size  $R_o$  at the ambient pressure  $P_o$  would explosively grow (no static equilibrium) if the



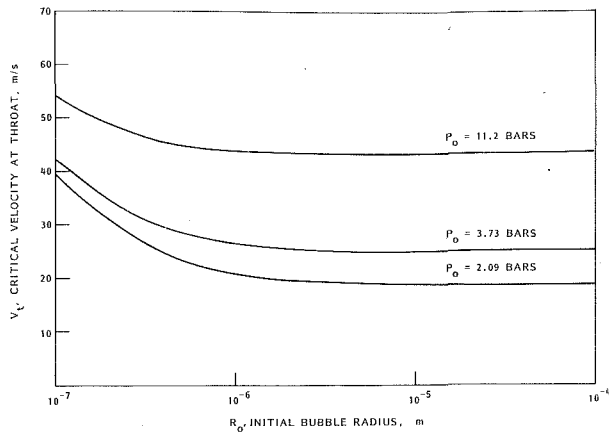


Fig. 5 Critical velocity at Venturi throat as a function of the initial bubble radius. Static equilibrium case,  $K = 1.4$ .

pressure around it drops below  $P_{cr}$ . One should note that  $P_{cr}$  is always lower than  $P_v$  and tends toward it when  $R_o$  is very large.

An information of great interest to the venturi CSM as an eventual bubble size detector is, for a given reference pressure,  $P_o$  (depth of submergence) and throat velocity,  $V_t$ , what is the initial radius of the bubble or nuclei which would reach the critical size at the throat pressure,  $P_{th}$ ? All bubbles of larger radius would then be unstable, while smaller bubbles would remain undetectable. In terms of the maximum throat velocity (accounting for pressure loss by viscous effects)  $P_{th}$  can be written

$$P_{th} = P_o + \frac{1}{2} C_{pmin} \rho V_t^2, \quad (9)$$

and the relation between  $R_o$  and the critical throat velocity,  $V_{tc}$ , is

$$P_{th} - P_v = P_o + \frac{1}{2} \rho C_{pmin} V_{tc}^2 - P_v = \frac{2\gamma(1-3K)}{3KR_o} \left[ 3K + \frac{R_o(P_o - P_v)}{2\gamma} \right]^{\frac{-1}{3k-1}}. \quad (10)$$

For a given critical throat velocity,  $V_{tc}$ , any bubble larger than  $R_o$  would grow explosively. Conversely for a given bubble size any  $V_t$  larger than the critical velocity would render the pressure at the throat below the bubble critical pressure. Figure 5 shows the relationship between  $R_o$  and  $V_t$  for various ambient pressures and for  $K = 1.4$ . Note the sensitivity to the critical velocity for relatively "large" radii (e.g.,  $R_o > 1 \mu\text{m}$ ). Very small changes in  $V_t$  induces large changes in  $R_o$ . This underlines the major practical problem in the use of the CSM as a bubble size detector. Much less sensitivity would be obtained if  $P_{th}$  was the variable controlled in the experiments (see Fig. 4).

The original concept for the use of the venturi cavitation susceptibility meter was based on the above static equilibrium approach. Actually, the above reasoning can be invalidated when bubble dynamics is taken into account in the two following configurations (Darrozes and Chahine, 1983):

(a) The pressure in the throat drops below the critical pressure but the considered bubble does not remain long enough in this region to grow explosively.

(b) The imposed pressure is always above the critical pressure but pressure variations are great enough for an intense collapse and therefore a strong acoustical signal to be generated.

In order to account for the above phenomena, the complete bubble dynamical equation has to be solved for the particular

venturi CSM pressure field. In the case of a single bubble of negligible size as compared to the throat diameter, the classical Rayleigh-Plesset equation adequately describes the bubble radius variations.

$$\rho \left[ R\ddot{R} + \frac{3}{2} \dot{R}^2 \right] + 4\mu \frac{\dot{R}}{R} = P_{g_o} \left( \frac{R_o}{R} \right)^{3K} - P(t) + P_v - \frac{2\gamma}{R}. \quad (11)$$

Dots denote time derivatives. This differential equation relates the bubble radius time variations as a function of the driving pressure function  $P(t)$ .  $P(t)$  is the pressure "felt" by the bubble during its traverse of the venturi. With the above assumptions  $P(t)$  is the pressure in the liquid in absence of the bubble at the location of its center. The bubble position  $x(t)$  is obtained from the bubble translation velocity  $V_b(t)$

$$x(t) - x(0) = \int_0^t V_b(t) dt. \quad (12)$$

If we neglect relative velocity between the bubble and the liquid the coupling between (11) and (12), knowing the fluid velocity variations along the venturi, is straightforward. Actually the slip velocity could be important and should be included in future developments of this study.

When the bubble growth rate is large enough to significantly modify the liquid flow rate into the venturi, the pressure term in equation (11) has to be modified to account for the resulting pressure variations. Similarly as described below, equation (11) alone is not adequate to describe the case where interaction between several bubbles crossing the venturi simultaneously is considered.

## Multiple Bubble Dynamics

If a finite number of nuclei clustered in a cloud crosses the venturi then bubble interaction during the growth and collapse stages come into play. If the characteristic size,  $r_{b_o}$ , of a bubble in the cloud is small compared to its characteristic distance  $l_o$ , from its neighbors then a first order approximation consists in neglecting interactions. In the absence of relative velocity with the surrounding fluid, each of the individual bubbles reacts to the local pressure variations spherically, as if isolated. When the spacing between the bubbles in the cloud is small compared to the external flow and pressure field characteristic length, the excitation pressure felt in first approximation by all bubbles in the cloud can be considered to be the same. Variations of this pressure due to the position of each bubble are only seen at the higher orders. This assumption was adopted for the numerical examples presented below. In a more general case, the pressure felt by each bubble is dependent on both its location and the modification of the mean flow field in the venturi by the presence of the other bubbles as addressed in the following section. This case can be treated similarly to the case presented here as long as the basic method (asymptotic expansions) is applicable; that is as long as the spacing between bubbles is large compared to their characteristic size. At higher orders of approximation, or when  $r_{b_o}/l_o$  increases from zero, mutual bubble interactions and individual bubble motions and deformations come into play. These various approximations are studied by means of the method of matched asymptotic expansions. The "outer problem" is that considered when the reference length is chosen to be  $l_o$ . This problem is concerned with the macrobehavior of the cloud, and the bubbles appear in it only as singularities. The "inner problem" is that considered when the lengths are normalized by  $r_{b_o}$ . The solution of this problem applies to the microscale of the cloud, i.e., to the vicinity of an individual bubble of center  $B^i$ . The presence of the other bubbles, all considered to be at infinity in the "inner problem," is sensed only by means of the matching condition

with the "outer problem." The boundary conditions at infinity for the "inner problem" are obtained, at each order of approximation, by the asymptotic behavior of the outer solution in the vicinity of  $B^i$ . Thus, if one knows the behavior of all the bubbles except  $B^i$ , the motion, deformation and pressure field due to this cavity can be determined. In first approximation  $\epsilon = r_{b_o}/l_o$  is equal to zero, all the bubbles behave as in an infinite medium and the time dependence of their radii,  $a_o(t)$ , is given by the Rayleigh-Plesset equation, (11). This first determination of the whole flow field sets the boundary conditions at infinity for the following order of approximation. The same process is then repeated for the successive high orders. One can show (Chahine, 1981 and 1982) that up to the order  $\epsilon^3$ , concerning the dynamics of a bubble centered at  $B^i$ , the remaining cavities can schematically be replaced by a unique equivalent bubble centered at  $G^i$ , and whose growth rate and position are determined by the geometrical distribution and the growth rate of these cavities. If  $\theta^{ij}$  is the angle between  $B^i G^i$  and a field point,  $M$ , the equation of the surface of the axisymmetric bubble  $B^i$  can be written in the form:

$$R(\theta^{ij}, \phi, t) = a_1^i(t) + \epsilon a_2^i(t) + \epsilon^2 [a_2^i(t) + f_2^i(t) \cos \theta^{ij}] + \epsilon^3 [a_3^i(t) + f_3^i(t) \cos \theta^{ij} + g_3^i(t) P_2(\cos \theta^{ij})] + \dots \quad (13)$$

where  $P_2$  is the Legendre polynomial of order 2 and argument  $\cos \theta^{ij}$ . The first component,  $a_0(t)$ , is given by the Rayleigh-Plesset differential equation, while the other components,  $a_n$ ,  $f_n$ , and  $g_n$  are given by similar differential equations of the second order which can be written in a symbolic form as follows:

$$D_2(y_n^i) = \sum_j \left( \frac{l_0}{l_{ij}} \right)^m f_j^i(y_0^i, \dots, y_{n-1}^i) P_m(\cos \theta^{ij}) \quad (14)$$

$D_2(y_n^i)$  represents a differential equation of the second order of the radius component  $y_n^i$  of the bubble  $i$ .  $l_{ij}$  is the initial distance between the bubbles  $B^i$  and  $B^j$ ,  $f_j^i(y_0^i, \dots, y_{n-1}^i)$  is a known function of the terms  $y_k^i$ , determined at the preceding orders, and  $m$  is an integer.  $\theta^{ij}$  is the angle between the direction  $B^i B^j$  connecting the bubbles' center and the direction of motion of the bubble  $i$  toward the cloud center,  $B^g$ , and  $n$  is an integer.

The behavior of  $B^i$  can then be computed by solving the obtained differential equations using a multi-Runge-Kutta procedure. The behavior of the whole cloud is then obtained.

Earlier studies (Chahine, 1981 and 1982; Chahine and Liu, 1985) have shown that collective bubble behavior can have a dramatic effect on both bubble growth and implosion. Specifically bubble growth is inhibited by bubble interaction while bubble collapse is enhanced. This cumulative effect comes from the fact that the interaction reduces the driving pressure drop for bubble growth, while it increases the collapse driving pressure. Due to the cumulative effects of the collapse of all the bubbles in the cloud, each bubble ends its collapse under the influence of a pressure which is orders of magnitude higher than that for an isolated bubble.

### Multibubble Interaction With Venturi Mean Flow

Under the basic assumption of small bubble radius size relative to bubble spacing and to flow characteristic length (for instance throat radius), in first approximation each bubble behaves independently and the basic flow is undisturbed by the presence of the cloud. With this approach and at this order of approximation, the pressure field to which each bubble in the cloud reacts is that existing at the location of its center in its absence. At higher orders bubbles interact with each other, and in addition due to the restricted nature of the flow in the venturi they modify the main flow into the venturi. The influence of the cloud dynamics on the basic flow becomes important when the cloud volume rate attains a significant fraction of the mean volume flow rate. We will try here to account for this correction since its implementation is rather simple.

Let  $\nabla(t)$  be the total volume of bubbles present at time  $t$  in the venturi (these bubbles could be either a certain number of isolated separated bubbles or a bubble cloud). The difference between the upstream and downstream flow rates into the venturi is equal to  $\dot{\nabla}$ . With a unidimensional approach to the venturi flow it is reasonable to write that the mean flow entering the venturi is then modulated as follows:

$$V_o = U_o - \alpha \dot{\nabla} / A_o, \quad (15)$$

where  $A_o$  is the area of the venturi at its entrance and  $U_o$  the undisturbed velocity at this location.  $\alpha$  is the fraction of the displaced liquid volume rate during the bubble growth which propagates upstream. We will assume from here on that  $\alpha = 0.5$ . If all bubbles were concentrated at  $x = X$  then between the venturi entrance ( $x = 0$ ) and  $X$  the velocity in the venturi can be related to the undisturbed velocity  $U(x)$  by an equivalent relation to (15), valid in the small perturbation approach:

$$V(x) = U(x) - \frac{\dot{\nabla}}{2A(x)}; \quad x \leq X. \quad (16)$$

If in addition the flow is assumed to be potential, then the velocity potential can be written:

$$\phi(x) = \phi_o(x) - \int_{-\infty}^x \frac{\dot{\nabla}}{2A(s)} ds \quad (17)$$

Bernoulli's theorem between  $x$  and a field point upstream where the pressure is  $P_a$  and the fluid is at rest can be written:

$$\frac{P_a}{\rho} = \frac{P(x)}{\rho} + \frac{\partial \phi(x)}{\partial t} + \frac{1}{2} \left[ \frac{\partial \phi(x)}{\partial x} \right]^2 \quad (18)$$

We can now define a perturbation pressure  $p'(x)$  such that

$$P(x) = P_{st}(x) + p'(x), \quad (19)$$

where  $P_{st}$  is the steady state pressure in absence of bubbles. Combining (17), (18), and (19) one obtains the following expression for  $p'(x)$  where a higher order term in  $(\dot{\nabla}/A)^2$  has been neglected.

$$\frac{p'(x)}{\rho} = \int_{-\infty}^x \frac{\dot{\nabla}}{2A(s)} ds + U(x) \frac{\dot{\nabla}}{2A(x)}. \quad (20)$$

In a matched asymptotic approach the imposed pressure field around any bubble or cloud at location  $X$  is given by (19) and the corresponding first order bubble equation. The imposed pressure term combines with the undisturbed pressure in the venturi at the bubble location and the correction  $p'(x)$  given by (20).

If the bubble cloud is composed of  $N$  bubbles of equal size then

$$\nabla = 4 \pi N R^3 / 3, \quad (21)$$

and the Rayleigh Plesset equation becomes:

$$\rho \left[ R \ddot{R} + \frac{3}{2} \dot{R}^2 \right] + 4\mu \frac{\dot{R}}{R} = P_{g_o} \left( \frac{R_o}{R} \right)^{3K} + P_v - \frac{2\gamma}{R} + \left[ P(X(t)) + 2\pi \rho N \left( \frac{R^2 \dot{R} U(X)}{A(X)} + \int_{-\infty}^X \frac{2R \dot{R}^2 + R^2 \ddot{R}}{A(x)} dx \right) \right]. \quad (22)$$

D'Agostino and Acosta (1983) derived a similar equation for a semi-infinite pipe of constant cross section  $A_o$ .

If the bubbles are not all concentrated at a given location, or more precisely if their spacing is large compared to the venturi scale (throat radius for instance), then equations (16) and (17) have to be generalized by introducing  $\nabla_x(x, t)$  the total volume of bubbles present between the venturi entrance and the section  $x$ . In addition, the above assumption ( $\alpha = 0.5$ ) becomes invalid and should be replaced by a time and space dependent  $\alpha$  determined by the inertances of the upstream and downstream bubble-liquid mixture. Such a generalization is

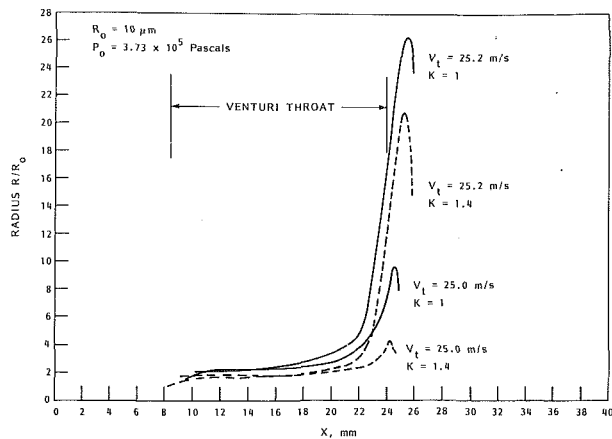


Fig. 6 Bubble radius variation during its traverse through the Venturi. Influence of throat velocity and polytropic constant  $K$ .

not attempted here and we concentrate instead on the relatively simple case of a single bubble cluster with small overall dimensions relative to the venturi flow field characteristic length.

Equation (22) combined with the system of equations (14) and, using a multi-Runge-Kutta procedure, can be solved numerically to investigate interaction of bubbles with the venturi main flow and with each other.

### Numerical Results and Interpretation

A series of computer runs were made using the above described method. The objective of this investigation was to compare the behavior of an isolated spherical bubble with that of a bubble in a cloud. Both sets of cases were considered for the venturi shown in Fig. 1 with and without pressure correction due to the modification of the mean flow by the presence of the bubbles. The results obtained are illustrated in the following examples and figures.

The bubble wall motion during its traverse through the venturi is illustrated in Fig. 6 for a bubble of  $10 \mu\text{m}$  initial radius. In most cases computations were started at the throat entrance ( $X \approx 0.825 \text{ cm}$ ) in order to reduce computation time. This is acceptable since comparative tests have shown that no significant error is then introduced. A typical bubble radius history can be described as follows. Near the throat entrance the bubble radius oscillates for a certain number of cycles which decreases with increasing flow velocity. Then, if this velocity is large enough a continual growth is observed until the bubble reaches the venturi expansion area. This is followed by a more or less violent bubble implosion which may be detected acoustically. Since this behavior is primarily controlled by a balance between gas pressure inside the bubble and the imposed ambient pressure, a key factor is the polytropic constant,  $K$ . The isothermal case ( $K=1$ ) is the most easily manageable mathematically and has therefore been studied by many investigators. Its use is justified when the bubble wall motion is slow enough so that the gas temperature remains constant. However; the value of  $K$  can vary widely during the bubble history (see Plesset and Prosperetti, 1977 and Chahine 1986). Figure 6 shows the importance of  $K$  by comparing the results for the two classical values of  $K$ : 1 and 1.4. Larger maximum radii are obtained with  $K=1$ . Two velocities at the throat are also considered in Fig. 6. Here we see that for a slight variation of  $V_t$  the maximum bubble radius can be doubled. Therefore, if the criterion of cavitation inception is when the bubble radius exceeds, let us say,  $150 \mu\text{m}$  then  $V_t = 25.0 \text{ m/s}$  would be below inception and  $V_t = 25.2 \text{ m/s}$  would be slightly above it. The static equilibrium curves (Fig. 5) derived from Equation (10) give, however, a lower value for the critical throat velocity,  $V_t \approx 24.95 \text{ m/s}$ . This relatively

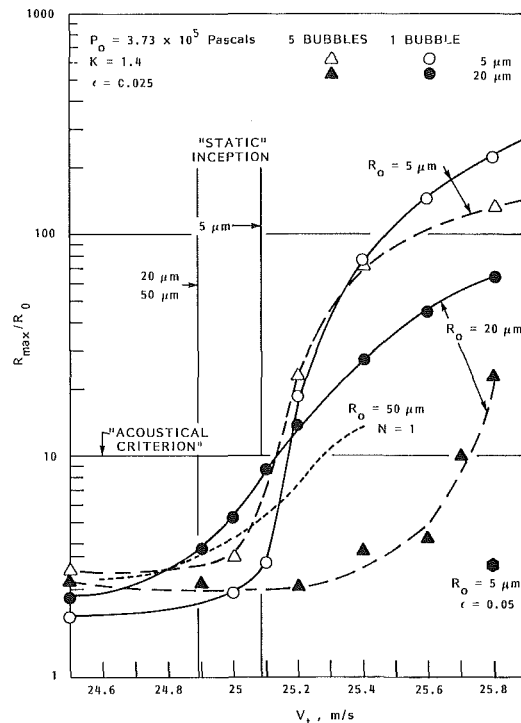


Fig. 7 Normalized maximum bubble radius as a function of the throat velocity. Influence of bubble size and bubble number.

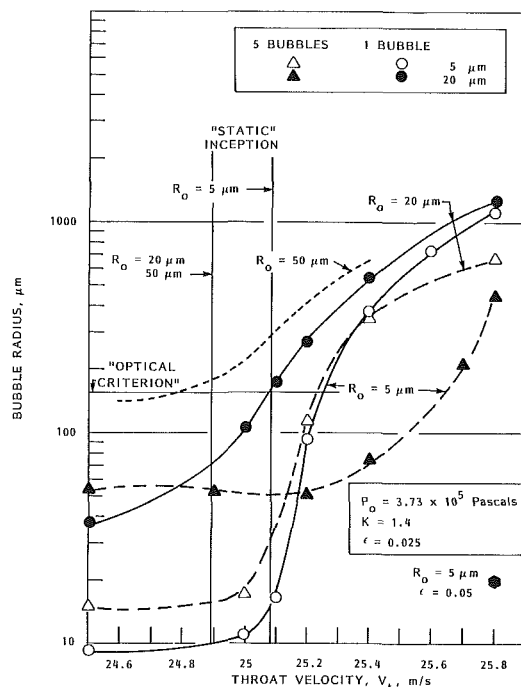


Fig. 8 Maximum bubble radius as a function of the throat velocity. Influence of bubble size and number.

small difference of about 0.8 percent is significant for the precision needed in the measurement of  $V_t$  in order to use the CSM venturi effectively. Note that if the throat velocity at inception was  $24.95 \text{ m/s}$  the critical pressure would be  $-500 \text{ pascals}$  while one obtains  $-8000 \text{ pascals}$  with  $25.2 \text{ m/s}$ . The difference in the critical pressure is therefore very significant between the static and dynamic approaches.

Figures 7 and 8 show the maximum size attained by a bubble crossing the venturi CSM as a function of the velocity at the throat. Bubbles of different initial sizes at the same initial

reference pressure are considered. Single bubble results are compared with symmetrical multibubble configurations. Several very interesting observations can be made from contemplating these figures and the corresponding computer run results. Bubble size scaling effects are observed as follows. At the lower velocities bubbles exhibit an oscillatory behavior all the way through the venturi (e.g.,  $V_t < 25.1$  m/s for  $R_o = 5 \mu\text{m}$ ;  $V_t < 24.8$  m/s for  $R_o = 20 \mu\text{m}$ ). Their radius oscillates between a fraction of  $R_o$  and a maximum radius of a few times  $R_o$ . At the higher velocities the bubbles experience an explosive growth followed by a strong implosion. Bubble size scaling effects are expressed by the fact that while initially larger bubbles have a larger growth rate at the low venturi throat velocities, the trend is reversed at higher velocities (Fig. 7). The result of this scaling effect is that at large velocities (e.g.,  $V_t \approx 25.8$  m/s for the cases considered) single isolated bubbles of 5, 20, and 50  $\mu\text{m}$  initial size attain the same maximum size. This could be seen on Figure 8 where the dimensional variables are represented for the same data points as in Fig. 7. This result is also related to the fact that the considered venturi has a long enough throat to allow the above bubbles to grow to significant sizes.

The effects of bubble interactions and restricted mean flow correction show up in a similar way when single bubble and multibubble results are compared. At lower velocities bubble oscillations in the throat area close to the entrance are amplified when the collective behavior of the bubble cloud is considered (see Figure 10 for details). As a result larger maximum sizes are obtained with multibubbles but also very early collapses are achieved in the throat section before reaching the expansion. At higher velocities the opposite phenomenon is observed. An explosive bubble growth is then achieved and multibubble effect is to inhibit the growth rate of each bubble in the cloud. This is mostly due to a reduction of the pressure drop around each bubble induced by the motion of the other bubbles. One can notice in both Figs. 7 and 8 that while multibubble effects weakly modifies the 5 micron bubble curves, a dramatic change is seen with the 20 micron bubble. In the latter case bubble interactions are much stronger and shift the behavior of the bubble from an explosive growth to strong oscillations which induce an early collapse even for velocities as high as 25.6 m/s. At higher values of  $\epsilon$  (bubbles closer to each other) this effect can be seen even for the 5  $\mu\text{m}$  bubble at  $V_t = 25.8$  m/s (case  $\epsilon = 0.05$  on Figures 7 and 8).

Figures 7 and 8 could also be used to determine dynamic cavitation inception. This could be done by using either an "acoustical" criterion,  $R_{\text{max}}/R_o$  greater than a certain value, or an "optical" criterion, the actual bubble size exceeding a given value. If we adopt criteria used earlier in the literature the values for  $V_t$  at inception as compared to static equilibrium values are shown in the following table.

Criterion	$R_o$ $\mu\text{m}$	Static		Dyn. Single Bubble		Dyn. Five Bubbles	
		$V_t$ , m/s	$P_{cr}$ , $10^3 p_a$	$V_t$ , m/s	$P_{cr}$ , $10^3 p_a$	$V_t$ , m/s	$P_{cr}$ , $10^3 p_a$
$R/R_o > 10$	5	25.08	-4.4	25.17	-7.1	25.13	-5.9
$R > 150 \mu\text{m}$	5	25.08	-4.4	25.24	-9.2	25.22	-8.9
$R/R_o > 10$	20	24.89	1.3	25.13	-5.9	25.70	-23.3
$R > 150 \mu\text{m}$	20	24.89	1.3	25.08	-4.4	25.62	-20.8

From Table 1 one can notice that predictions with static theory are conservative. For a given bubble size they show earlier inception. Similarly, for a given velocity, static theory predicts the activation of a broader range of nuclei. For instance at 25.08 m/s all bubbles initially larger than 5  $\mu\text{m}$  are predicted to be unstable while dynamics show that only those initially above 20  $\mu\text{m}$  will be observed with the optical criterion. Larger differences between statics and dynamics

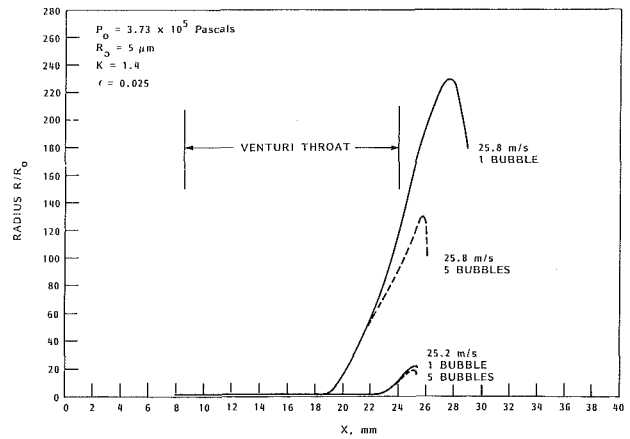


Fig. 9 Influence of throat velocity and bubble number on bubble radius history during its motion through the Venturi

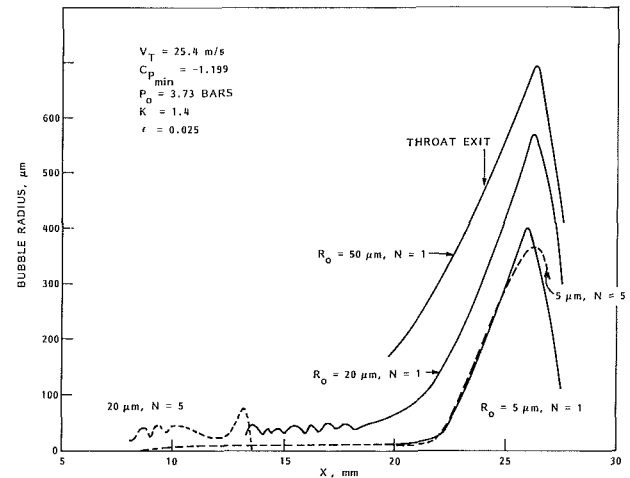


Fig. 10 Bubble growth and collapse in the Venturi system at three different initial bubble sizes

result for the case of a multibubble system. One should however recognize that differences in  $V_t$  are relatively small especially when considering present practical considerations in the control of this velocity. On the other hand, note that the resulting critical pressure varies in a very wide range between the various approaches. The difference between these values becomes very important in predicting full scale performance from cavitation tunnel tests where the ambient pressure is low. This encourages an effort toward a better control of  $V_t$  or  $P_{cr}$ . This, as well as additional information given below, might explain the discrepancies between optical and CSM measurements of bubble distributions. Large size bubbles in a cloud formation are not excited at the velocities expected from static theory and are therefore not counted when interpreting experimental CSM results.

Figures 9 and 10 illustrate some details of the results presented in Figs. 7 and 8. The influence of the velocity at the venturi throat on the dynamics of a bubble of initial radius 5  $\mu\text{m}$  can be seen in Fig. 9. One can observe an earlier explosive growth of the bubble at the higher velocity as well as the achievement of a greater maximum bubble radius. The bubble reaches its maximum size after leaving the throat in the venturi diffuser zone. This is due to its response time to a change in the ambient pressure. At higher velocities the maximum is achieved farther downstream. This conclusion has to be tempered by the fact that the response time is also a function of  $V_t$ . Influence of multibubble interaction and of restricted mean flow modification on the bubble dynamics can also be

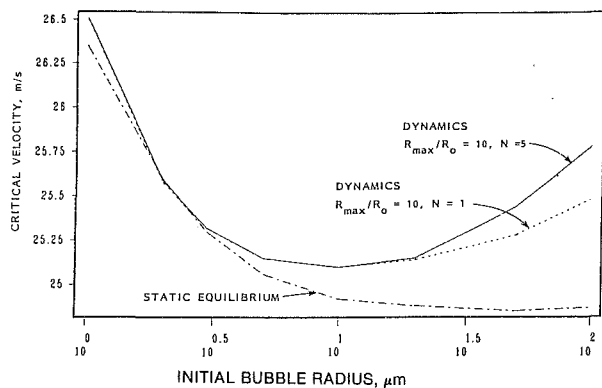


Fig. 11 Comparison between dynamics and static critical velocity at Venturi throat as a function of initial bubble radius

seen in Fig. 9. The explosive growth, as observed in Figs. 7 and 8, is inhibited by multibubble interaction more significantly at the higher velocities. The location,  $x$ , of maximum radius and the location of the collapse are then closer to the throat exit. This effect increases with the ratio between bubble size and distance,  $\epsilon$ . For a larger  $\epsilon$  the influence of oscillations is very much increased and the bubble collapses much earlier in the venturi throat (e.g., for  $\epsilon = 0.05$ , the collapse is  $x = 1.30$  cm instead of  $x = 2.8$  cm).

Figure 10 shows the influence of the initial size of a bubble on its dynamics and the modification of the behavior by inter-bubble and mean flow interactions. All cases are considered for the same ambient pressure and throat velocity. The larger bubbles achieve their maximum size further downstream inside the venturi diffusion section. When interactions are considered the bubble of initial radius  $R_0 = 5 \mu\text{m}$  has its behavior moderately modified, similar to what is shown in Fig. 9. However, for the  $20 \mu\text{m}$  bubble the modification of the behavior is dramatic. Large oscillations are induced through interactions and an early collapse at  $X \approx 1.30$  cm occurs inside the venturi throat. Such a bubble cloud would not be detected optically and probably not acoustically if the intensity of the collapse was not strong enough.

For the present user of the Venturi Cavitation Susceptibility Meter the curves relating the initial radius of a detectable bubble to the critical velocity at the throat are the most useful. Figure 5 showed those curves based on static equilibrium considerations. Any bubble of initial radius larger than that given by these static predictions would grow explosively at the corresponding velocity. The discussions above pertaining to Figs. 7 to 10 have shown that the problem is more complex when dynamics and interactions are taken into account. This fact can be illustrated, as in Fig. 11, by comparing  $R_0$  versus  $V_t$  obtained by both static and dynamic considerations. Here one can observe significant discrepancies at the larger bubble radii and also at the higher velocities. Again these theoretical differences are relatively small when expressed in terms of  $V_t$  but reflect very large differences in the critical pressures. The most interesting result seems to be the presence of a minimum in the dynamic curve. This implies that at a given velocity above a minimal value (25.1 m/s in the case of Fig. 11) only a finite range of bubbles radii are excited. Compare this prediction with the conclusion from statics that all bubbles above a critical radius become active. This may also explain the lower number of detected bubble in the venturi CSM as opposed to the scattering method.

### Statement of Uncertainty Estimate for the Numerical Results

All computations were performed up to order  $\epsilon^3$  included.

In addition, the RUNGE-KUTTA procedure used was an ENGLAND method where numerical errors were computed at each time step. The time step varied in order to impose an upper limit on the error of  $10^{-5}$ . However, errors due to the analytical model became sometimes significant but difficult to evaluate during the bubble collapse. The curves were stopped when these instabilities occurred. The marks on figures 7, 8 and 11 indicate actual computation points. In between these points an arbitrary interpolation curve is plotted.

### Conclusions

We have considered in this paper the behavior of a single bubble and of multibubbles in a Venturi Cavitation Susceptibility Meter. Results on bubble growth and dynamics were compared with those obtained from static equilibrium curves. In some ranges of fluid velocities and initial bubble radii statics and dynamics, with and without multibubble and mean flow interactions, give about the same results. However, significant differences are found elsewhere. Those differences are mostly due to the relative importance between bubble dynamics characteristic time and the time the bubble takes to cross the low pressure throat region. The CSM is however too sensitive to small variations in the velocities which introduce large variations in the critical pressures. A highly accurate control of the flow is desirable.

Dynamics and interactions seem to account for the lower number of detected bubbles in the venturi CSM as compared to optical scattering test results. Larger interacting bubbles could implode in the venturi throat and probably subdivide into a multitude of very fine bubbles which do not have the time to grow again in the throat. This is reflected by the fact that the critical velocity versus initial bubble radius curve exhibits a minimum (Figure 11). This implies that the venturi CSM excites only a part of the actually active nuclei spectrum in the field and does not, therefore account for the larger of them.

The information obtained in this work on bubble size history in the venturi as a function of the imposed flow conditions and initial bubble radii should be complemented and could be used to determine nuclei population. This could be implemented if the venturi CSM is instrumented to measure the size of the grown bubble at several locations in the venturi. This could be done by simple optical sensors.

The analyses should be refined and extended to include bubble-liquid slip velocity and a fine description of bubble collapse. Slip velocity could modify the bubble time response and quantitatively change the results obtained. A precise description of the implosion would allow us to accurately compute the pressures generated and therefore would be very helpful for acoustic detection.

### Acknowledgments

This work was supported by Naval Sea Systems Command, General Hydrodynamic Research Program, Element No. 61153N, Task Area SR0230101 and David Taylor Naval Ship Research and Development Center Contract No. N00167-85-D-0013.

We would like to thank colleagues at both our organizations, particularly Dr. Han-Lieh Liu for their contributions and helpful discussions.

### References

- Billet, M. L., (1984) "Cavitation Nuclei Measurements," *International Symposium on Cavitation Inception*—1984, ASME FED-Vol. 16, pp. 33–42.
- Chahine, G. L., (1981) "Asymptotic Theory of Collective Bubble Growth and Collapse," *Proc. 5th International Symposium on Water Column Separation*, Obernach, Germany.

- Chahine, G. L., (1982) "Cloud Cavitation Theory," *14th Symposium on Naval Hydrodynamics*, Ann Arbor, Mich.
- Chahine, G. L., and Liu, H. L., (1985) "A Singular Perturbation Theory of the Growth of a Bubble Cluster in a Superheated Liquid," *Journal of Fluid Mechanics*, Vol. 156, pp. 257-279.
- Chahine, G. L., (1986), "Cloud Cavitation and Bubble Interaction," 21st American Towing Tank Conference, Washington, D.C., August 1986.
- d'Agostino, L., and Acosta, A. J., (1983) "On the Design of Cavitation Susceptibility Meters," 20th American Towing Tank Conference.
- Darozes, J. S., and Chahine, G. L., (1983), "Less Recherches sur le Phénomène de Cavitation Effectués a l'Ecole Nationale Supérieure des Techniques Avancées," Sciences et Techniques de l'Armement 1er Fascicule.
- Holl, J. W., (1979) "Nuclei and Cavitation," *ASME Journal of Basic Engineering*, December, pp. 681-688.
- Keller, A. P., (1984), "Scale Effects at Beginning Cavitation Applied to Submerged Bodies," *International Symposium on Cavitation Inception*, ASME, FED-Vol. 16, pp. 43-47.
- Lecoffre, Y., and Bonnin, (1979), "Cavitation Tests and Nucleation Control," *International Symposium on Cavitation Inception*, The ASME Winter Annual Meeting, New York, New York, December 2-7, pp. 141-147.
- Oldenziel, D. M., (1982), "A New Instrument in Cavitation Research: The Cavitation Susceptibility Meter," *ASME JOURNAL OF FLUIDS ENGINEERING*, Vol. 104, June, pp. 136-142.
- Plesset, M. S., and Prosperetti, A., (1977), "Bubble Dynamics and Cavitation," *Ann. Rev. Fluid Mechanics*, Vol. 9, pp. 145-185.
- Shen, Y. T., and Gowing, S., (1985), "Scale Effect on Bubble Growth and Cavitation Inception in Cavitation Susceptibility Meters," *Cavitation and Multiphase Flow Form-1985*, ASME, FED-Vol. 23, pp. 14-16.
- Shen, Y. T., Gowing, S., and Pierce, R., (1984), "Cavitation Susceptibility Measurements by a Venturi," *International Symposium on Cavitation Inception*, ASME, FED-Vol. 16, pp. 9-19.
- Shen, Y. T., and Peterson, F. B., (1983) "Cavitation Inception - A Review - Progress Since 19th ATTC," 20th American Towing Tank Conference.

# Casing Headloss in Centrifugal Slurry Pumps

**M. C. Roco**  
Professor,  
Mem. ASME

**P. Nair**  
Research Assistant.

Department of Mechanical Engineering,  
University of Kentucky,  
Lexington, KY 40506-0046

**G. R. Addie**  
Professional Engineer,  
GIW Industries, Inc.

*The headlosses in slurry pump casings are caused by the energy dissipation in the flowing liquid-solid mixture, and the particle-casing wall interaction. This paper presents a quasi-three-dimensional flow analysis, in two steps: (1) the casing width-averaged parameters are obtained from the two-dimensional flow simulation in a normal plane to the pump axis, (2) the results are then used for flow computation in the casing radial cross-sections. The governing equations are averaged over the typical time interval for the periodic flow in the casing caused by the finite number of impeller blades. Finite element techniques with linear three-node and quadratic nine-node elements are used in the numerical simulation. The effect of the casing shape on the headlosses is illustrated by comparing the performances of three centrifugal slurry pumps with quasi-spiral, semi-annular and annular casings at various flowrates. The flow recirculated between the casing tongue and impeller shrouds is shown to play a major role in the overall headloss. The flow results may also be used for determining the wear in the casing and thrust on the impeller, as well as for optimizing the casing dimensions.*

## Introduction

The dimensions of the centrifugal pump casing affect the overall pumping performance, especially at operating points different from the nominal flowrate (BEP). The variation of the energy and wear indices with the casing shape is more pronounced for slurry pumps as compared to water pumps. This paper focuses on the prediction of the velocity and concentration distributions plus the frictional headlosses in the casing.

The headlosses in the pump casing have been estimated in previous work mainly by using one-dimensional models [1], [2], and only for single-fluid flow (water). Here the velocity distributions were assumed constant in the radial cross-sections, and the secondary flows were neglected.

The quasi-three-dimensional analysis proposed in the present work aims to simulate with some simplifying assumptions the turbulent flow pattern in the casing, including the secondary currents. The velocity and concentration profiles obtained from this analysis can be used to find the pressure distribution around the impeller and the thrust on it, as well as the wear rate on the casing wall. The proposed approach combines finite element flow simulations in a normal section to the pump axis (Figs. 1(b) and 2(d-e)) and in the radial cross-sections (Figs. 1(c) and 2(a-c)). The governing equations are averaged over a specific time interval and local averaging volumes to diminish the computational work. Simplifying assumptions are adopted in the suggested engineering algorithm for casing headloss.

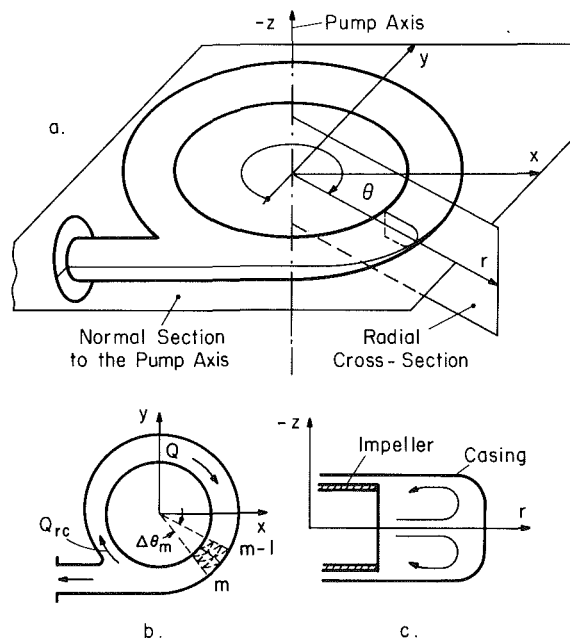


**Fig. 1 Casing cross section used in flow analysis:**  
(a) General view, (b) Normal section to the pump axis, (c) Radial cross section

## General Approach

The casing headloss analysis is a part of a more general research program on centrifugal slurry pump performance initiated in the University of Kentucky and applied at pump manufacturer, mining and dredging companies. The effects of solids on the pump performance have been investigated in five areas:

Contributed by the Fluids Engineering Division of THE AMERICAN SOCIETY OF MECHANICAL ENGINEERS and presented at the Joint ASCE/ASME Mechanics Conference, Albuquerque, 1985. Manuscript received by the Fluids Engineering Division July 25, 1985.

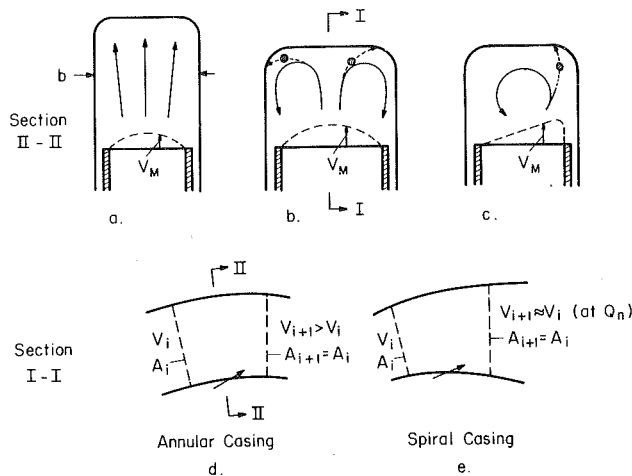


Fig. 2 Typical flow pattern in pump casing: (a, b, c) = radial cross section; (d, e) = normal sections

- (a) Basic two-phase flow equations starting from the analysis at particle scale [3], [4],
- (b) Pump hydraulic performance [2], [5],
- (c) Erosion wear [6], [7],
- (d) Mechanical, and
- (e) Metallurgical aspects.

The flow and wear phenomena (above (a), (b), and (c)) are strongly interdependent. Special attention is given in this

work to dense slurry flows, in which the particle-particle and particle-wall stresses are of the same order of magnitude or even predominant compared to the fluid and fluid-particle stresses.

The general approach combines experimental and computational steps, and is carried out in three main steps:

- Preliminary prediction of the pump performance using dimensional analysis and statistical correlations from experiments [2], [7];
- Detailed numerical analysis for individual pump areas and phenomena (blade-to-blade flow [5], casing flow [6], typical wear mechanisms [8]) by solving the governing field equations with some simplified boundary conditions;
- Prediction of the individual pump performances by assembling the computational algorithms from each pump component: inlet, impeller, casing. The performances of interest are the characteristic curves for head, power and efficiency versus flowrate; as well as the wear rate and the necessary thickness of the pump component walls.

The interaction with the pipeline system (pipeline curve, other pumps or hydraulic equipment mounted in series or parallel), and the effects of the secondary phenomena (cavitation, corrosion, scaling, vibrations), should be analyzed for each operational situation.

The numerical analysis in the pump casing presented in this paper corresponds to the second main step of the general approach outlined above. The computational algorithm for the design of the pump casing is sketched in Fig. 3. First, the velocity and concentration distributions are calculated in the

## Nomenclature

$A$ = area of casing radial cross section	$\psi$ equation, acting on the flow component $K$ due to all other flow components and bounding wall	$\xi_1, \xi_2, \xi_3$ = coefficients defined in equation (11)
$b, B_c$ = local and maximum casing width, respectively	$Re_{mesh}$ = mesh Reynolds number	$\psi$ = flow field quantity
BEP = best efficiency point	$S_\psi$ = source term for $\psi$	$\lambda$ = penalty parameter
$c_{2u}$ = tangential fluid velocity at impeller exit	$S_{\psi\theta}, S_{m\theta}$ = source-like terms in equations (6a) and (8), respectively	<b>Subscripts</b>
$C$ = perimeter of the casing contour in a radial section	$V$ = velocity	$A$ = averaged over the casing cross-section ( $A$ )
$d$ = dimension of solid particles	$W_i$ = weighting function about node $i$	$b$ = averaged over the casing width ( $b$ )
De = Dean number	$x, y, z$ = Cartesian coordinates	cas = casing
$\mathbf{J}$ = flux vector	$Z$ = number of impeller blades	$m$ = refers to the $m$ th casing section
$(E_{TV})_K$ = dispersion term over the time interval $\Delta T$ (equation (4))	$\alpha, \alpha_\Sigma$ = volumetric and superficial solid concentration, respectively	$\mathbf{f}$ = denotes a vector
$f_D$ = Darcy's friction coefficient (in Moody diagram)	$\alpha_M$ = maximum packing concentration, by volume	$L, S, M$ = denotes liquid, solid and mixture, respectively
$g$ = gravitational acceleration	$\Delta$ = technical wall roughness (mm)	$K$ = averaged over the flow component $K$ ( $K = L$ for the liquid, $K = S$ for solid)
$H$ = pump head	$\Delta\dot{s}$ = wear rate (mm/h)	$n$ = nominal, or Best Efficiency Point (BEP)
$l$ = circumferential length, defined in equation (11)	$\rho_L, \rho_S$ = density of liquid and solid phase, respectively	$rc$ = recirculation
$m$ = radial section	$\sigma_{SL}, \tau_{SL}$ = normal and shear stress due to supported load, respectively	$r, \theta, z$ = projections on the cylindrical coordinates
$N$ = pump rotational speed, rpm	$\xi_1, \xi_2$ = local isoparametric coordinates	$x, y, z$ = projections on the Cartesian coordinates
$N_s$ = pump specific speed	$\eta$ = pump efficiency	$\psi$ = refers to quantity $\psi$
$N_i$ = interpolation function	$\epsilon_S$ = solids diffusion coefficient	<b>Superscripts</b>
$p$ = pressure	$\nu, \nu_{art}$ = viscosity and artificial viscosity, respectively	$\bar{f}$ = denotes the time average of $f$ (equation (3))
$r, \theta, z$ = cylindrical coordinates		$i$ = $i$ th iteration
$Q$ = flowrate		
$R_2$ = impeller exit radius		
$R_{\psi K}$ = interaction term in the		



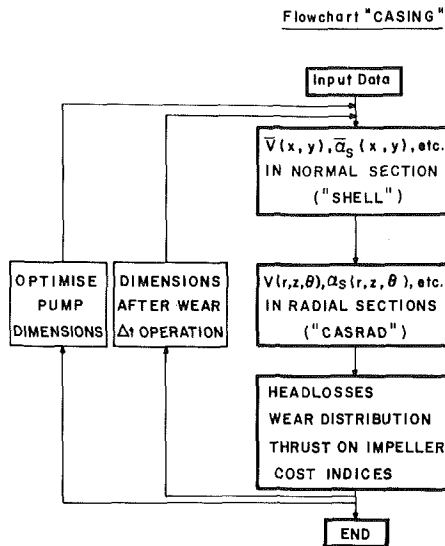


Fig. 3 Flowchart "CASING"

gaps between the impeller shrouds and casing shell with a two-dimensional  $x$ - $y$  model (subroutine "SHELL"). Then a quasi-three-dimensional marching approach in successive radial cross-sections is applied (subroutine "CASRAD"). On this basis, the energy dissipation and wear distribution in the casing, as well as the overall economical indices may be determined. The casing dimensions and wall roughness change during operation. The evolution of the tongue shape is especially important. Once the wear is calculated after an operation time  $t$ , the corresponding reduction of the thickness wall is introduced in the computation for the next interval of time  $\Delta t_{\text{operation}}$ . The time interval is taken in the order of one tenth of the life expectancy, which may vary from few weeks to one-two years. The time evolution of the wall thickness and the corresponding effects on the pump performance can be estimated for any new casing geometry. By successively changing the initial shape of the pump casing one can find the most efficient design for the pump during the whole operational life. This task is completed by the loop "optimize pump dimensions" shown in the numerical code "CASING" (Fig. 3).

### Casing Headloss Analysis

The flow in a slurry pump casing is three-dimensional, two-phase, turbulent and cyclic. The cycle is determined by the passage of two successive impeller blades through the same location ( $\Delta T = 60/N/Z$ ). The flow recirculated in the normal plane ( $Q_{rc}$  in Fig. 1(b)), the inflow from impeller and the secondary currents in the radial cross sections (Figs. 1(c) and 2) are expected to play a significant role. A time efficient approach for casing flow including these basic phenomena is the object of the present work.

(a) The momentum and concentration conservation equations should be space/time averaged over each flow component to express the phase interactions and two-phase space nonuniformities [3]. The conservation equation for a field quantity  $\psi$  ( $V_x, V_y, V_z, \alpha$ , etc.) averaged over a flow component  $K$  ( $K = L$  for liquid, or  $K = S$  for solid) can be written (including the mass exchange between components) in the form:

$$\frac{\partial(\alpha\rho\psi)_K}{\partial t} + \nabla(\alpha\rho\mathbf{V}\psi)_K - \nabla(\alpha_\Sigma\mathbf{J}_\psi)_K - (S_\psi)_K + R_{\psi K} = 0 \quad (1)$$

where:

$$\begin{aligned} \alpha &= \text{spatial concentration, by volume} \\ \alpha_\Sigma &= \text{superficial concentration, by area} \end{aligned}$$

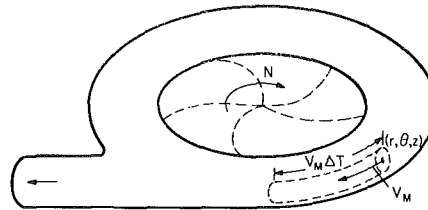


Fig. 4 Averaging volume in casing

$\mathbf{J}_\psi, S_\psi$  = flux vector and source term for  $\psi$ , respectively  
 $R_{\psi K}$  = interaction term, due to all other flow components and bounding walls.

Equation (1) shows the fluid mass conservation for  $\psi = 1$ , momentum conservation for  $\psi = V_x, V_y, V_z$  or  $V_r, V_\theta, V_z$ , or generally the conservation equation for any other flow contaminant.

(b) A specific flow nonuniformity in the casing is due to the limited number of impeller blades, causing the quasi-periodical fluctuations of the velocity and concentration distributions at a point in time. As an alternative to transient flow analysis, the governing equations are averaged over the interval of time  $\Delta T = 60/N/Z$  and the problem is formally treated as a steady-state flow. An equivalent averaging volume can be defined (Fig. 4). The new term denoted by  $(E_{T\psi})_K$  shows the dispersion effects over  $\Delta T$  in the governing equations, and yields from the corresponding nonlinear terms:

$$\nabla(\bar{\alpha}\bar{\rho}\bar{\mathbf{V}}\bar{\psi})_K - \nabla(\bar{\alpha}_\Sigma\bar{\mathbf{J}}_\psi)_K - (\bar{S}_\psi)_K + \bar{R}_{\psi K} + (E_{T\psi})_K = 0 \quad (2)$$

where the overbar is defined by

$$\begin{aligned} \bar{f} &= \frac{1}{\Delta T} \int_0^{\Delta T} f dt \\ &= \text{time average of } f \text{ over the time interval } \Delta T \end{aligned} \quad (3)$$

and

$$(E_{T\psi})_K \equiv \nabla[(\bar{\alpha}\bar{\rho}\bar{\mathbf{V}}\bar{\psi})_K - \bar{\alpha}\bar{\rho}\bar{\mathbf{V}}\bar{\psi}]_K - \nabla(\bar{\alpha}_\Sigma\bar{\mathbf{J}}_\psi)_K - \bar{\alpha}_\Sigma\bar{\mathbf{J}}_\psi]_K \quad (4)$$

The dispersion term  $(E_{T\psi})_K$  can be estimated from the velocity and concentration distributions at the impeller outlet or directly from experiments. Since the solid particles have the tendency to segregate in the impeller channel, a reasonable assumption is to consider a cyclic variation of solid concentration in  $\Delta T$ .

The overbar showing the averaging over  $\Delta T$  is omitted in the following equations to simplify the notations. We also assume no mass exchange between phases, i.e.,  $(S_\psi)_K = 0$ , and that the volumetric and superficial concentrations are equal  $\alpha = \alpha_\Sigma$ .

(c) The three-dimensional flow analysis is reduced to two simpler problems, in the  $x$ - $y$  plane and selected  $r$ - $z$  radial sections (Fig. 1).

Equation (2) can be averaged over the casing width  $b$  to solve the two-dimensional problem in the "normal plane" ( $x$ - $y$  plane), as suggested in [6] and [7]. Equation (2) averaged over the casing width  $b$  is:

$$\begin{aligned} \nabla(\alpha_b\rho_b\mathbf{V}_b\psi_b)_K - \nabla(\alpha_{\Sigma b}\mathbf{J}_{\psi b})_K + R_{\psi Kb} + (E_{T\psi b})_K \\ + \frac{1}{\alpha_b\rho_b b} \int_0^b \nabla[\alpha\rho(\mathbf{V} - \mathbf{V}_b)(\psi - \psi_b)] dz \\ \text{(dispersion effects over } b) \approx 0 \end{aligned} \quad (5)$$

The index  $b$  denotes the average over  $b$ . The dispersion effects over  $b$  due to the second term,  $\nabla(\alpha_{\Sigma}\mathbf{J}_\psi)_K$ , are neglected in equation (5).

Since the inertial forces are the predominant forces in the

casing, it is reasonable for most applications to adopt an inviscid flow solution for the analysis in the normal plane, from where the average velocities in the radial cross-sections  $V_{KA}$  are computed. The mean flow velocity  $V_{MA} = \sum_K \alpha_K V_{KA}$  is

used as a constraint in each radial section to obtain the pressure gradient and energy dissipation. Only the recirculation between impeller and casing tongue,  $Q_{rc}$ , is effectively employed in the marching approach.

In the next step the analysis is reduced to a two-dimensional domain in the radial section ( $r$ - $z$  in Fig. 1(c)), without losing some three-dimensional features (i.e., the three velocity components and upstream effects), by rearranging equation (2) to the following form in cylindrical coordinates:

$$\nabla_{rz}(\alpha \rho \mathbf{V} \psi)_K - \nabla_{rz}(\alpha_S \mathbf{J} \psi)_K - (S_{\psi\theta})_K + R_{\psi K} + (E_{T\psi})_K = 0 \quad (6a)$$

where:

$$\begin{aligned} \nabla_{rz}(\ast) &= \text{same as } \nabla(\ast) \text{ for the three-dimensional flow,} \\ &\text{but without the derivatives with respect to } \theta; \\ &\text{i.e., } \nabla_{rz}(\mathbf{V}) = (1/r) \partial(rV_r)/\partial r + \partial(V_z)/\partial z \\ (S_{\psi\theta})_K &= \text{source-like term, equal to the sum of the} \\ &\text{derivatives of } \psi \text{ with respect to } \theta \text{ from the} \\ &\text{operators } \nabla(\ast) \text{ in equation (2).} \end{aligned}$$

The term  $(S_{\psi\theta})_K$  accounts for the variation of  $\psi$  and its derivatives in the  $\theta$  direction, and is estimated from the  $\psi$  distribution in the upstream radial section in the marching approach. The corresponding steady-state momentum ( $\psi = V_r$ ,  $V_\theta$  and  $V_z$ ) and solid mass ( $\psi = \alpha_s$ ) conservation equations for the flow component  $K$  are:

- Momentum,  $r$  projection ( $\psi = V_r$ ):

$$\begin{aligned} \left[ \rho \left( V_r \frac{\partial V_r}{\partial r} - \frac{V_\theta^2}{r} + V_z \frac{\partial V_r}{\partial z} \right) - \rho \nu \left( \frac{\partial^2 V_r}{\partial r^2} + \frac{1}{r} \frac{\partial V_r}{\partial r} + \frac{\partial^2 V_r}{\partial z^2} \right) \right. \\ \left. - \frac{V_r}{r^2} + \frac{\partial p}{\partial r} \right]_K + \frac{\left( \frac{\rho V_\theta}{r} \frac{\partial V_r}{\partial \theta} - \frac{2\rho \nu}{r^2} \frac{\partial V_\theta}{\partial \theta} - \frac{\rho \nu}{r^2} \frac{\partial V_r^2}{\partial \theta^2} \right)_K}{(= S_{\psi\theta})} \\ + R_{rK} + (E_{Tx})_K = 0 \quad (6b) \end{aligned}$$

- Momentum,  $\theta$  projection ( $\psi = V_\theta$ ):

$$\begin{aligned} \left[ \rho \left( V_r \frac{\partial V_\theta}{\partial r} + \frac{V_\theta V_r}{r} + V_z \frac{\partial V_\theta}{\partial z} \right) - \rho \nu \left( \frac{\partial^2 V_\theta}{\partial r^2} + \frac{1}{r} \frac{\partial V_\theta}{\partial r} \right) \right. \\ \left. + \frac{\partial^2 V_\theta}{\partial z^2} - \frac{V_\theta}{r^2} + \frac{1}{r} \frac{\partial p}{\partial \theta} \right]_K \\ + \frac{\left( \frac{\rho V_\theta}{r} \frac{\partial V_\theta}{\partial \theta} + \frac{2\rho \nu}{r^2} \frac{\partial V_r}{\partial \theta} - \frac{\rho \nu}{r^2} \frac{\partial^2 V_\theta}{\partial \theta^2} \right)_K}{(= S_{\psi\theta})} \\ + R_{\theta K} + (E_{Ty})_K = 0 \quad (6c) \end{aligned}$$

- Momentum,  $z$  projection ( $\psi = V_z$ ):

$$\begin{aligned} \left[ \rho \left( V_r \frac{\partial V_z}{\partial r} + V_z \frac{\partial V_z}{\partial z} - \rho \nu \left( \frac{\partial^2 V_z}{\partial r^2} + \frac{1}{r} \frac{\partial V_z}{\partial r} + \frac{\partial^2 V_z}{\partial z^2} \right) \right) \right. \\ \left. + \frac{\partial p}{\partial z} \right]_K + \frac{\left( \frac{\rho V_\theta}{r} \frac{\partial V_z}{\partial \theta} - \frac{\rho \nu}{r} \frac{\partial^2 V_z}{\partial \theta^2} \right)_K}{(= S_{\psi\theta})} \\ + R_{zK} + (E_{Tz})_K = 0 \quad (6d) \end{aligned}$$

Solid concentration equation ( $\psi = \alpha_s$ ):

$$\begin{aligned} \frac{\partial(\rho_S V_{Sr} \alpha_S)}{\partial r} + \frac{\rho_S V_{Sr} \alpha_S}{r} + \frac{\partial(\rho_S V_{Sz} \alpha_S)}{\partial z} \\ - \rho_S \epsilon_S \left( \frac{\partial^2 \alpha_S}{\partial r^2} + \frac{1}{r} \frac{\partial \alpha_S}{\partial r} + \frac{\partial^2 \alpha_S}{\partial z^2} \right) \\ + \frac{1}{r} \frac{\partial(\rho_S V_{S\theta} \alpha_S)}{\partial \theta} - \rho_S \epsilon_S \frac{1}{r} \frac{\partial^2 \alpha_S}{\partial \theta^2} \\ (= S_{\psi\theta}) \end{aligned}$$

$$+ R_{\alpha K} + (E_{T\alpha})_K = 0 \quad (6e)$$

The underlined terms in equations (6b)–(6f) are the source-like terms  $S_{\psi\theta}$  containing the derivatives with respect to  $\theta$ . The second derivatives with respect to  $\theta$  are simply neglected, or estimated by using the variables from the previous interval  $\Delta\theta$ .

Let us consider equations (6b)–(6d) for mixture flow ( $K = M$ ) and equation (6e) for solid phase ( $K = S$ ) written in cylindrical coordinates, and a finite differentiation with respect to  $\theta$ . An angular interval  $\Delta\theta_m = \theta_m - \theta_{m-1}$  is defined between two radial cross-sections  $m-1$  and  $m$  (see Fig. 1(b)).

The continuity equation for an incompressible mixture is

$$\Delta V_M = \nabla_{rz} V_M + S_{m\theta} \quad (7)$$

The three mixture velocity components in a section are obtained by solving equations (6b)–(6d) and the continuity equation (7). The pressure is replaced in the momentum equations by using a slightly modified penalty approach:

$$p = -\lambda_e (\nabla_{rz} \mathbf{V}_M + S_{m\theta}) \quad (8)$$

where:  $\lambda_e$  = penalty function defined in each finite element ( $e$ )

$S_{m\theta}$  = source-like term in the  $r$ - $z$  continuity equation caused by the mass flux gradient in the  $\theta$  direction.

In the proposed marching approach the pressure gradient  $\partial p/\partial\theta$  may vary between the corresponding points in two successive sections [9]. However, in this paper, the pressure gradient is imposed constant between two successive sections to reduce the computational time and improve the stability of solutions for the same mesh. Large secondary currents and the lateral inflow are not restricted by this condition.

The penalty function  $\lambda$  depends on the area of the finite element  $e$  [10]:

$$\lambda_e = 10^6 \cdot (\text{element area})/(\text{mean area of all elements}) \quad (9)$$

A portion of the solid particles can not be maintained in suspension by the hydrodynamical forces and are centrifuged toward the peripheral casing wall. The effect of the direct interaction by friction between solid particles and the casing wall is introduced in the momentum equation (6a) through the interaction term  $(R_{\psi K})$ . The corresponding supported load shear stress  $\tau_{SL}$  was estimated in [6].

Following the marching approach the computation in the  $r$ - $z$  radial sections originates from the tongue area. From the analysis in the  $x$ - $y$  plane only the  $Q_{rc}$  value is used.

The solid velocity relative to the mixture can be obtained from equation (2), by taking  $\psi = \mathbf{V}_s$ . This corresponds to the dynamic equilibrium of a cloud of solid particles within a differential control volume, as explained in [6]. The centrifugal effect due to the curvature of the particle trajectory in the casing cross-section is small compared to the centrifugal forces in the normal plane to the pump axis, and it is neglected in the present tests.

The concentration distribution is determined from the same

**Table 1 Test pumps (runs 1-6)**

Run no.	Pump (GIW)	Impeller	Casing	$Q_m$ (m <sup>3</sup> /h)	$\Delta$ (mm)	$N$ (rpm)	$N_s$ (-)
1	8 × 10 LSA32	Simple curvature (RV 535 C)	Annular (1029 D)	950	0.25	590	1200
2	8 × 10 LSA32	Medium efficiency (ME 2377 D)	Semi-annular (1233 D)	1010	0.25	590	1200
3	8 × 10 LSA32	High efficiency (HE)	Spiral (1903 D)	790	0.25	590	1200
4a	26 × 26 LHD50	Medium efficiency ( $R_2 = 0.635m$ )*	Semi-annular	6350	0.25	270	3200
4b	26 × 26 LHD45	Medium efficiency ( $R_2 = 0.571m$ **)	Semi-annular	5400	0.25	270	3760**
4c	26 × 26 LHD45	Medium efficiency ( $R_2 = 0.571m$ **)	Spiral	5510	0.25	270	3680**

( )\* Nominal dimension of the impeller.  
 ( )\*\* Reduced dimension of the impeller.

transport equation (6a) but for  $\psi = \alpha_s$ , equation (6e). The source-like term is  $(S_{\psi\theta})_s = S_{m\theta} \cdot \alpha_s$ .

The mixture eddy viscosity and solid eddy diffusivity were approximated in the tests below to their casing with average [6]. The laws of variation of these coefficients with the solid concentration were extrapolated from the slurry pipe results. This is a computation saving alternative to solving equation (2) for the diffusion coefficients. The point distributions of the diffusion coefficients for mass and momentum can be obtained from the corresponding transport equations of type (2), as it was presented elsewhere [4].

The field solutions for concentration, solids eddy diffusivity, eddy-viscosity and velocity are obtained in this order following an iterative scheme at each radial section  $m$  starting from the tongue area. Three to four global iterations were sufficient for convergence in all test cases (i.e., the maximum difference of concentration between two successive iterations less than 0.2 percent). The initial guess for concentration is the average discharge concentration.

The relative loss in the pump efficiency due to the headlosses in casing is:

$$\Delta\eta_{cas} = \left\{ \sum_m \left[ \Delta p_m \frac{Q_m + Q_{m-1}}{2g} - \rho_m (Q_m - Q_{m-1})^2 c_{2u} \right] + \rho_{rc} \Delta H_{rc} Q_{rc} \right\} / \rho Q H_{th} \quad (10)$$

where:

- $\Delta p_m$  = pressure gradient between the radial sections  $m-1$  and  $m$  (see Fig. 1(b))
- $Q_{m-1}, Q_m$  = mixture flowrate through sections  $m-1$  and  $m$ , respectively
- $c_{2u}$  = tangential velocity at impeller exit
- $Q$  = pump discharge flowrate
- $H_{th}$  = theoretical pump head
- $Q_{rc}$  = recirculation flow rate (see Fig. 1(b))
- $\Delta H_{rc}$  = local headloss due to the bifurcation at the pump tongue [11].

(d) An alternative to the algorithm (2)-(10) is a global formulation for  $\Delta p_m$ . By taking the integral of equation (2) with  $\psi = V_M$  over the casing radial cross-section and  $\Delta\theta_m$ , one obtains the linear momentum equation for a sector  $m$ , which may be brought to the following approximate form:

$$\Delta p_m = \left[ (1 + \zeta_1 + \zeta_2 + \zeta_3) f_D \frac{\rho^2 Q}{A^2/C} \right]_m + \left( \tau_{SL} \frac{C}{A} \right)_m + [(\rho Q V)_m - (\rho Q V)_{m-1}] + \rho (Q_m - Q_{m-1}) \cdot c_{2u} \quad (11)$$

- where:  $\zeta_1$  = positive coefficient due to the nonuniform distribution of the circumferential velocity
- $\zeta_2$  = positive coefficient due to the energy dissipated by secondary currents in cross-section. The secondary currents are caused by both the inflow from impeller and centrifugal effects
- $\zeta_3$  = positive coefficient due to the nonuniform solid concentration
- $f_D$  = Darcy's friction coefficient (used in the Moody's diagram)
- $l, A, C$  = the mean circumferential length, cross-sectional area and casing wall perimeter in the cross-section
- $\tau_{SL}$  = averaged supported load shear stress on the casing wall.

This last formula (11) can be used only after the coefficients  $\zeta_1, \zeta_2, \zeta_3$ , and stress  $\tau_{SL}$  are modeled employing the differential algorithm (2)-(10).

### Experimental Work

The experimental work was performed in the slurry pump and pipeline laboratory built to investigate hydraulic and wear performances. Twelve pumps of various types and dimensions (annular, semiannular, and spiral casings), flowrates and specific speeds ( $N_s = 1200 - 3200 (m^3/h)^{0.5} (rpm)^1 (m_{H_2O})^{-0.75}$ ) were tested, from which four are listed in Table 1. A view of the slurry pump and pipeline laboratory system is given in Fig. 5. A special feature of this facility is the capability to test at full scale slurry pumps with flowrates up to 10,000 m<sup>3</sup>/h and power up to 1500 kW. The laboratory is equipped with special circuits for rheological tests, erosion wear in elbows and particle degradation. The flowrate is controlled by the pump rotational speed and when necessary by throttling valves. The experimental loops include a vertical pipe section for measuring concentration and flow. Horizontal ( $D = 76 - 760$  mm) and variable slope pipe (0 - 90 deg) sections, valves, joints, and erosion probes may be introduced in the circuit. The instrumentation measuring the pump performance is connected to a computer data acquisition system to record and interpret the results. The experimental uncertainty for all main measurements was brought by careful calibrations to under 1 percent. The symbols used in Fig. 5 have the following meaning:  $V$  = tank volume,  $D$  = pipe diameter,  $Q_M$  = mixture flowrate,  $N$  = pump rotational speed,  $\Delta p$  = pressure difference,  $i$  = hydraulic slope,  $T$  = temperature,  $\alpha_s$  = solid concentration,  $V_{cr}$  = critical sediment velocity in pipes,  $\theta$  =

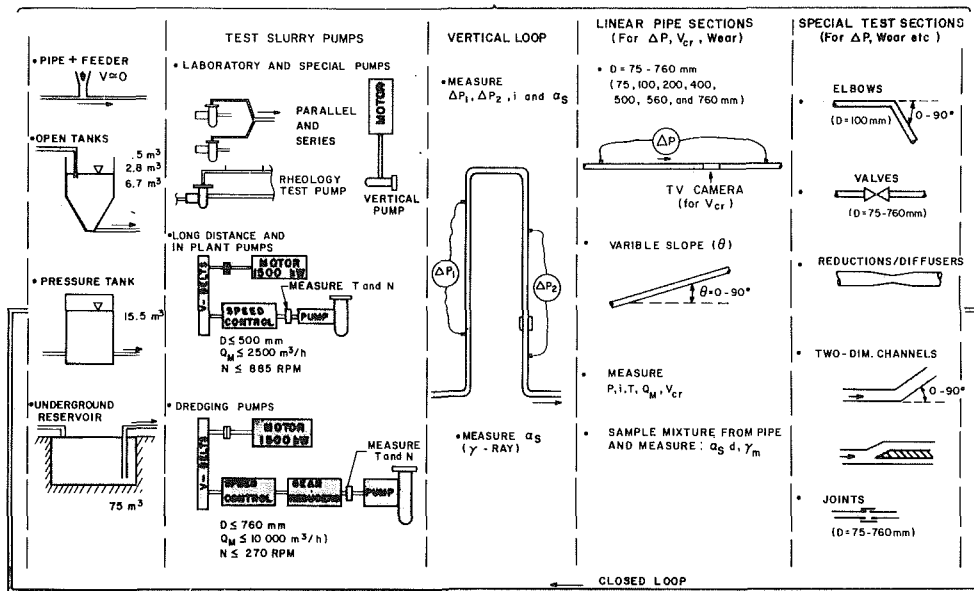


Fig. 5 Slurry pump and pipe laboratory loop scheme

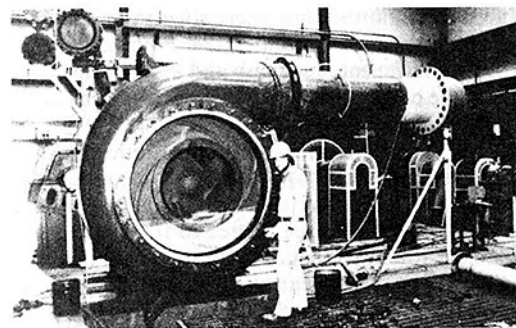
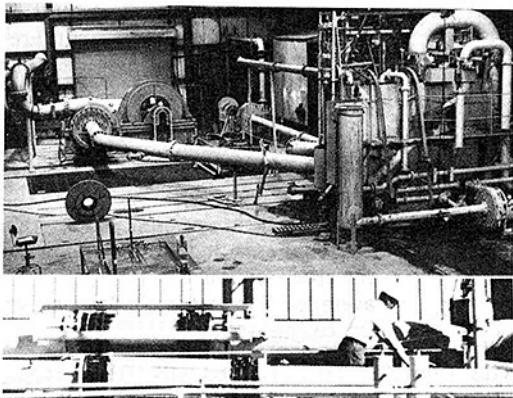


Fig. 6 Partial views of the laboratory facility

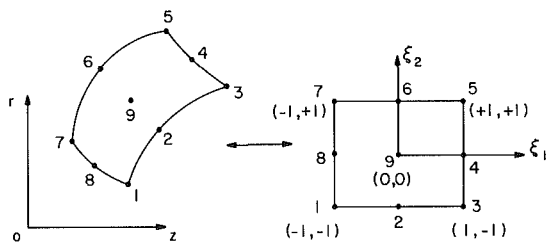


Fig. 7 Nine-node quadratic finite element (Q9)

pipe inclination. Partial views of the laboratory facility with the 26 × 26 LHD 50 pump (Run 4 in Table 1) are shown in Fig. 6.

The relative effect of different casing on the characteristic curve was determined by keeping all other pump components the same and changing only the casing. The shape in the normal plane and radial cross-sections, as well as the casing wall roughness, were modified from one test to another. Measurements on the pressure fluctuations and distributions along the casing wall will be reported in future work.

**Finite Element Flow Simulation**

Finite element method is successively applied in two typical domains:

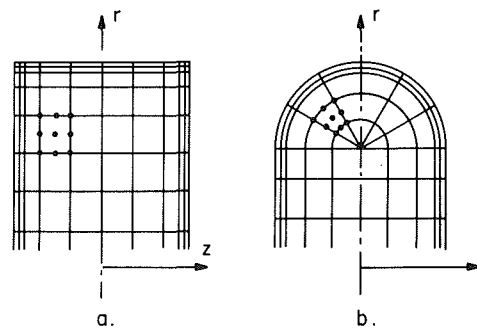


Fig. 8 Samples of mesh generation in the radial cross section

(a) In the normal plane ( $x-y$  in Fig. 1) to the pump axis. The average flow parameters over the casing width ( $b$ ) are computed with a two-dimensional model (equation (5)). The numerical simulation for velocity (using stream function formulation, triangular elements, parametric solution to find  $Q_{rc}$ ) and solid concentration (using up-winding triangular elements) was presented in [6]. The main global result is the recirculation flowrate  $Q_{rc}$  about the impeller, which crosses the gap between the impeller shrouds and the casing tongue.

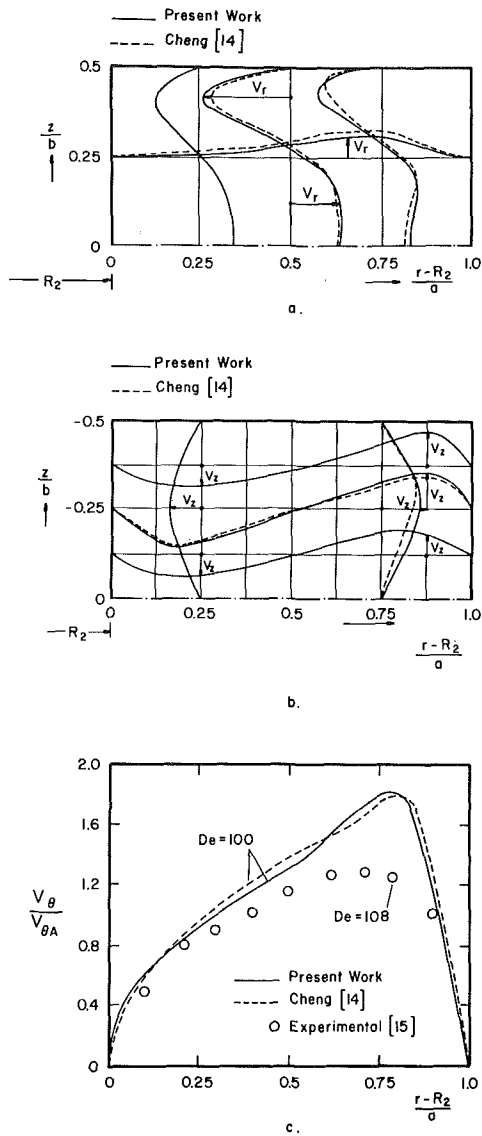


Fig. 9 Comparison of the present method to Cheng et al. [14] and experiments ( $V_\theta$ ) [15]:  
 (a) Radial velocity profiles ( $V_r$ ),  
 (b) Axial velocity profiles ( $V_z$ ),  
 (c) Circumferential velocity profiles ( $V_\theta$ )

The typical number of elements in the normal section (Fig. 1(b)) is between 200 and 250, which corresponds to six rows of triangular element between the impeller and casing shell. By increasing the number of elements up to five times the recirculation flow remains in the acceptable range of 2.0 percent.

(b) In the radial cross-sections ( $r - z$  in Fig. 1) of the pump casing. The point distributions of the mixture velocity vector (three projections  $V_r$ ,  $V_\theta$ ,  $V_z$ ; equations (6b)–(6d)) and solid concentration (equation (6e)) are obtained. The turbulent flow simulation in the casing radial cross section is performed with nine-node quadratic elements (Fig. 7). Since the velocities have relatively large values caused by the circumferential velocities (in the  $\theta$  direction), the “artificial viscosity” approach [12] was adopted to damp the non-physical oscillations of the numerical solutions. This approach was preferred to the more time expensive “up-winding” techniques. The artificial viscosity  $\nu_{art}$  is adjusted in each element as a function of the element mesh Reynolds number ( $Re_{mesh} = u\Delta h/\nu_M$ ,  $u$  = average velocity on the element,  $\Delta h$  = element dimension) in the flow direction:

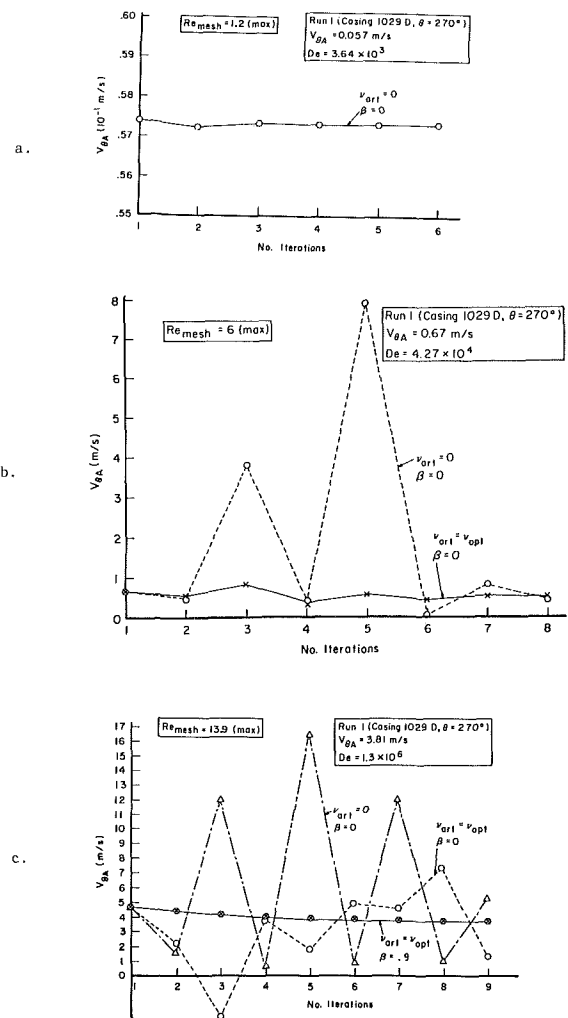


Fig. 10 The effect of the number of iterations on the numerical solution for  $V_{\theta A}$

$$\nu_{art} = \nu_M[(Re_{mesh}/2) \cdot \coth(Re_{mesh}/2) - 1] \quad (12)$$

where  $\nu$  denotes the mixture viscosity (physical parameter). The computational viscosity is  $\nu_M + \nu_{art}$ .

Equations (6) are solved for the mixture momentum equation (which is obtained by summing the momentum equations for  $\psi = \mathbf{V}_L$  and  $\psi = \mathbf{V}_S$ ) and concentration ( $\psi = \alpha_S$ ). The typical boundary conditions are imposed at the casing solid wall and at the inlet sections from impeller. The velocity profile at the inlet boundary was estimated from the casing width flow simulation by imposing the radial velocity component. The concentration distribution at the same inlet section in the casing results from the impeller flow pattern. In the present test work we assume a constant concentration at the inlet. Samples of mesh generation are shown in Fig. 8.

The variable  $\psi$  is interpolated in a nine node curvilinear element as a function of the intrinsic system of coordinates  $\xi_1, \xi_2$  (see Fig. 7):

$$\psi = \sum_{i=1,9} [N_i(\xi_1, \xi_2)] \{\psi_i\} \quad (13)$$

where  $N_i$  are the interpolation function for the 9-node quadratic element [13]:

$$N_i = \frac{1}{4} \xi_{1i} \xi_{2i} (1 + \xi_{1i} \xi_1)(1 + \xi_{2i} \xi_2) \xi_1 \xi_2,$$

$$\begin{aligned}
 & \text{for } i=1,3,5,7 \\
 & = \frac{1}{2} \xi_{2i} (1 + \xi_{2i} \xi_2) (1 - \xi_1^2) \xi_2, \\
 & \qquad \qquad \qquad \text{for } i=2.6 \\
 & = \frac{1}{2} \xi_{1i} (1 + \xi_{1i} \xi_1) (1 + \xi_2^2) \xi_1, \\
 & \qquad \qquad \qquad \text{for } i=4.8 \\
 & = (1 - \xi_1^2) (1 - \xi_2^2), \\
 & \qquad \qquad \qquad \text{for } i=9
 \end{aligned}
 \tag{14}$$

The Galerkin weighted residual method applied to the governing differential equations yields a system of nonlinear equations for the velocity components and concentration. The Newton-Raphson method is used for numerical solutions. The finite element simulation tests in the radial cross-sections were performed with three meshes of 169 nodes (36 quadratic elements), 81 nodes (16 quadratic elements), and 25 nodes (4 quadratic elements), respectively.

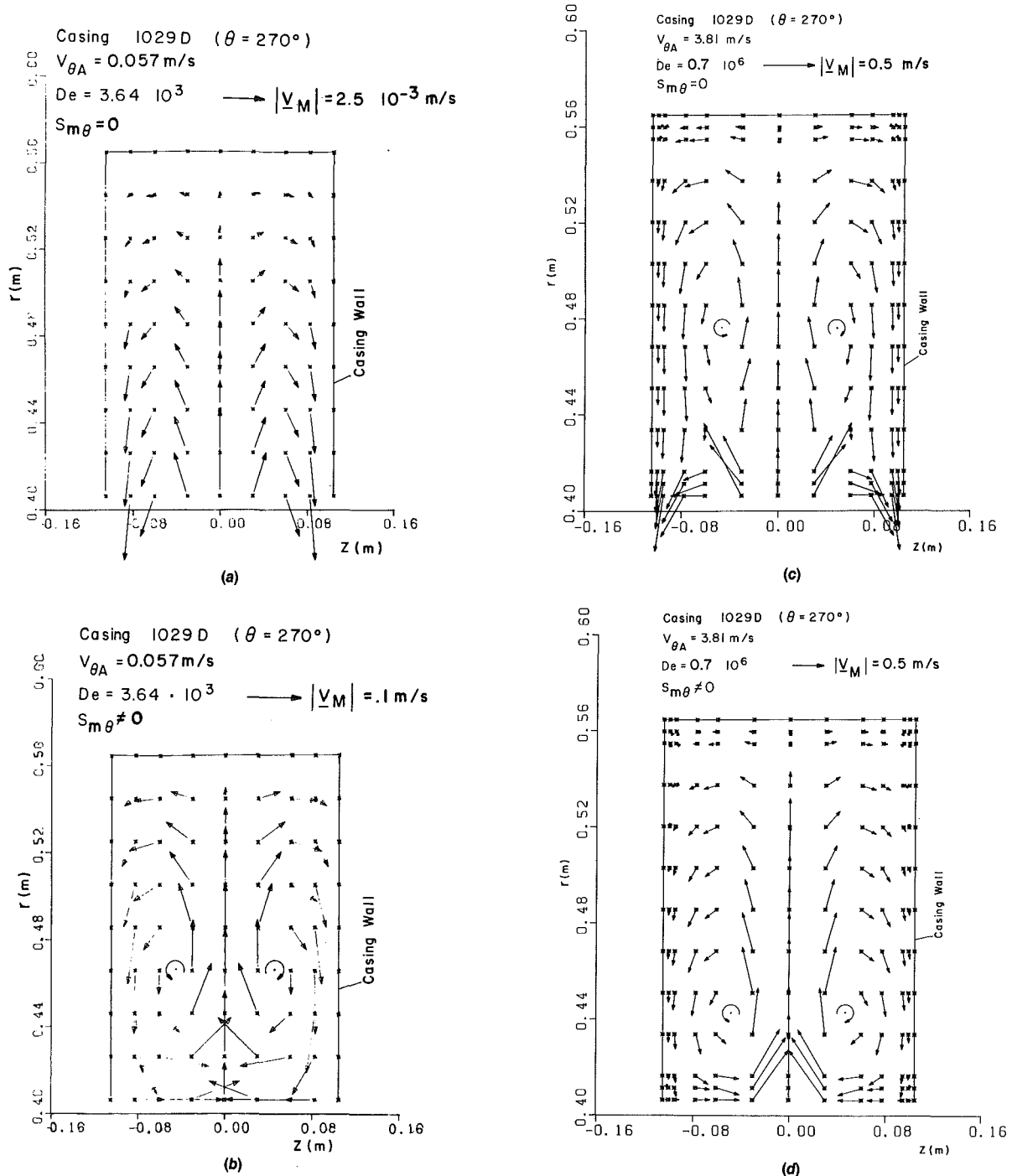


Fig. 11 Velocity distribution in the annular casing,  $\theta = 270$  deg,  $\alpha_S = 0$  (Run 1), assuming:  
 (a, b, c, d) Symmetric velocity distribution at the impeller outlet (see scheme Fig. 2(b)),  
 The source term  $S_{m\theta}$  (equation (8)) was neglected in the calculations presented in Figs. a and c.

## Application

The algorithm to determine  $\Delta\eta_{cas}$  follows the steps:

1. Calculate the casing width mixture velocity and concentration distributions in the normal section to the pump axis, including the recirculation flowrate  $Q_{rc}$ ;
2. Divide the casing in a suitable number of domains  $m$  ( $\approx 25$ ) and find the corresponding mean velocity  $V_{\theta A}$  in the radial cross-sections  $A_m$ ;
3. Calculate the normal and shear stresses caused solid particles in Coulombic contact ("supported load" stresses);
4. Solve the differential equations (equations (6)) to obtain the mixture velocity and concentration distributions in the radial cross sections  $m$ , and find  $\Delta p_m$  at which the mean velocity is  $V_{\theta A}$ ; here the computation starts from the tongue area where the recirculation flowrate was previously obtained;
5. Calculate  $\Delta\eta_{cas}$  with equation (10).

The numerical model was initially tested for simple flow situations. The calculated velocity distributions and headlosses in closed pipes with rotational motion and in curved channels were compared with results to other predictions and experimental data published in literature [14]–[16]. Figure 9 illustrates the agreement obtained with the data published by Cheng et al. [14] and Mori et al. [15] for the laminar flow of a homogeneous fluid in curved rectangular channels. The Dean number (De) is defined by the product between the Reynolds number in the curved channel multiplied by the square root of the ratio between the equivalent diameter of the cross-section and the radius of curvature.

The spurious oscillations of the velocity solutions in the radial sections at high De numbers are damped by: reducing the mesh size (i.e., reducing  $Re_{mesh}$ ) using the artificial viscosity approach (equation (12)), and an iterative scheme with a specific "breaking factor". The numerical solutions are stable at  $Re_{mesh}$  less than 2 (see Fig. 10(a)). The artificial viscosity approach alone has a satisfactory "smoothing" effect for flows characterized by  $Re_{mesh}$  between 2 and 10. A "breaking factor"  $\beta$  (similar to [17]) is used in the iterative scheme at  $Re_{mesh} > 8$ –10. The  $i$ th iteration of the velocity  $V^{(i)}$  is a linear combination of the  $(i-1)$ th iteration  $V^{(i-1)}$  and the new calculated velocity  $V^i$ :

$$V^{(i)} = (1 - \beta)V^i + \beta V^{(i-1)} \quad (15)$$

The iteration follows a specific pattern: in the first approximation the secondary flows are neglected ( $V_r = V_z = 0$ , and the solution is unconditionally stable); then, the velocity components  $V_r$ ,  $V_z$  are introduced in the iteration successively without and with the source terms caused by the flow parameter change in the  $\theta$  direction. The convergence of the velocity computation is checked by the condition

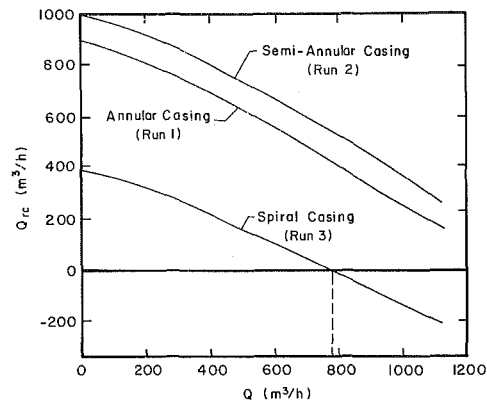
$$100 \cdot \Sigma (V^{(i)} - V^{(i-1)})^2 / \Sigma (V^{(i)})^2 \leq 0.5 \text{ percent} \quad (16)$$

where the sum  $\Sigma$  is taken over all the nodes.

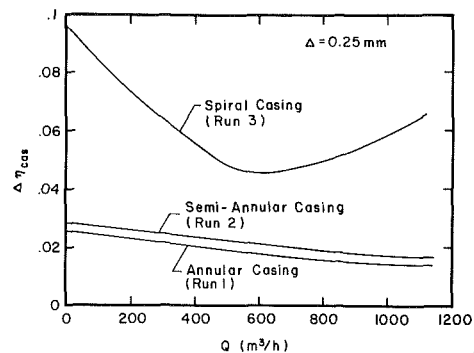
Three to four iterations are sufficient for the convergence of concentration solutions, to reach the maximum difference of concentration between two successive iterations less than 0.2 percent.

The pump efficiency reduction due to the casing headloss  $\Delta\eta_{cas}$  was calculated for seven pumps with specific speeds varying between  $N_s = 1200$  and 3200. Table 1 lists some of the runs, each run being performed for flowrates from 0 to 1.2  $Q_n$ .

Figures 11–14 give comparative results obtained for six casings of various shapes (runs 1–4 in Table 1). The same casings were previously used for wear tests [6]. The secondary currents obtained in the radial section  $\theta = 270$  deg of the annular pump (position E in Fig. 13) for different computational assumptions are illustrated in Fig. 11. The flow pattern changes with



(a) Recirculation flowrate ( $Q_{rc}$ ) versus pump discharge flowrate ( $Q$ )



(b)  $\Delta\eta_{cas}$  versus  $Q$  ( $\alpha_S = 0$ )

Fig. 12 Comparative results for runs 1–3

the Dean number (see Figs. 11(c) and (d) versus Figs. 11(a) and (b)), and the use of the source term  $S_{m\theta}$  in the computation (Figs. 11(a) and (c) versus Figs. 11(b) and (d)). The source term  $S_{m\theta} = 0$  corresponds in Fig. 11, (a) and (c), to the uniform casing flow in which the clearance recirculation flow between the impeller shrouds and casing lateral walls is equal to the inflow from impeller. The test cases from Fig. 11, (b) and (d), correspond to zero clearance recirculation. The applicative situations are generally between these two limits. Only symmetrical flow patterns are shown in Fig. 11. Other test cases, including asymmetrical flow configurations, were presented in [9]. The first three casings considered were mounted on three pumps having close nominal flowrates. The relative dissipation of energy  $\Delta\eta_{cas}$  in the spiral casing was obviously larger compared to the annular and semiannular casings (Fig. 12). At the same time, the headlosses in the spiral casing are more sensitive to the flowrate deviation from  $Q_n$  compared to the annular and semiannular casings. The headlosses in the spiral casing seems to reach a minimum in the neighborhood of the nominal pump flowrate. The recirculation flow  $Q_{rc}(Q)$  between the casing tongue and impeller shrouds plays an important role. Computational results are given in Figs. 12(a) and 14(a). The truncation error is 2.0 percent. By changing the shape of the casing tongue, the recirculation flow and  $\Delta\eta_{cas}$  are strongly affected. To improve the efficiency at smaller flow rates (0.3–0.7  $Q_n$ ) it is justifiable in many cases to reduce the casing width and the tongue dimensions (increasing the radial gap between the casing and impeller shrouds). These changes generally will produce a smaller recirculation flow about the impeller, and then lower velocities in casing.

Besides the headlosses, the two-phase flow pattern determines the rate of erosion wear on the casing wall. Both parameters are then considered in design, and a compromise

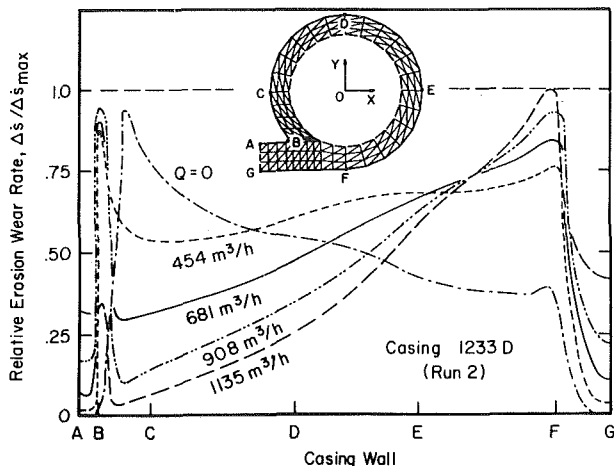


Fig. 13 Peripheral wear rate distribution in casing 1029D (run 2) for different flowrates ( $\alpha_s = 30$  vol percent, sand  $d = 0.27$  mm)

between the requirements of minimum losses and wear is necessary. An energy approach was previously suggested to predict the wear rate caused by solid-liquid mixture flow on solid boundaries [6]. The wear rate distribution on the peripheral wall of the semiannular casing (run 2 in Table 1) is illustrated in Fig. 13. The wear curves are obtained for different pump flowrates, but for the same slurry characteristics (sand/water mixture,  $\alpha_s = 30$  vol percent, sand size  $d = 0.27$  mm) and rotational speed ( $N = 590$  rpm). The predictive approach was experimentally verified in previous work [6]. Figure 13 shows the change of the location of maximum wear

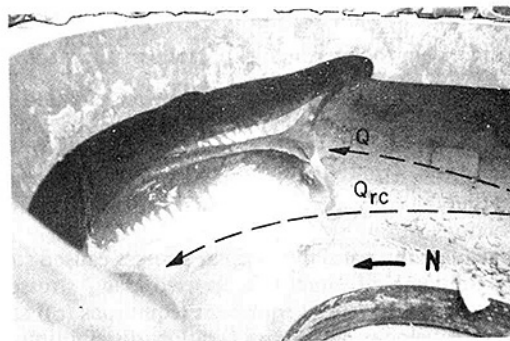
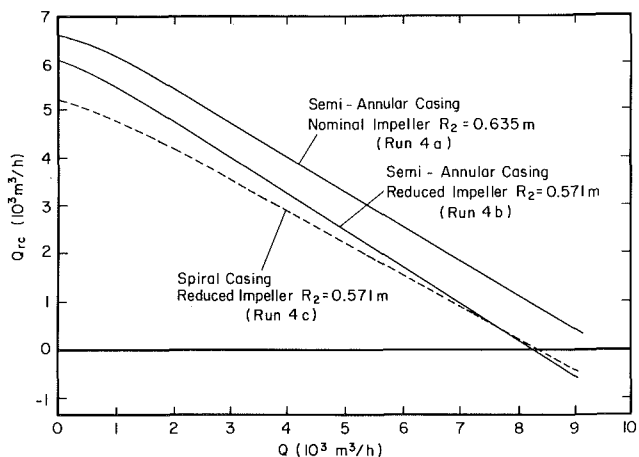


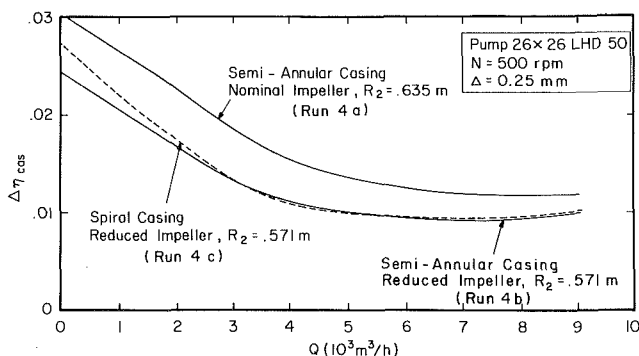
Fig. 15 Sample of the wear pattern in radial section ( $\alpha_s = 30$  vol percent, copper tailings  $d = 0.3$  mm)

with the flowrate. Besides the flowrate, the wear profiles depend on the casing shape, particle characteristics, rotational speed and the pair of wearing/worn materials. No general wear profile can be assumed a priori based on an individual parameter, without considering the assembly of data. The wear rate distribution is considered together with the energy losses to obtain the optimum casing design, as it is suggested by the flowchart "CASING" (Fig. 3). This design is found by optimizing the casing shape for minimum cost including the wear damage and the energy dissipation rate.

Figure 14 illustrates the effects of changing the impeller exit diameter, and then the casing shape (runs 4a-4c in Table 1). By reducing the impeller diameter from the design value  $R_2 = 0.635$  m to  $0.571$  m the recirculation and headloss in the casing diminish (see computational results in Figs. 14(a) and (b); here



(a) Recirculation flowrate ( $Q_{rc}$ ) versus pump discharge flowrate ( $Q$ )



(b)  $\Delta\eta_{cas}$  versus  $Q$  ( $\alpha_s = 0$ )

Fig. 14 Comparative results for runs 4a-4c from Table 1



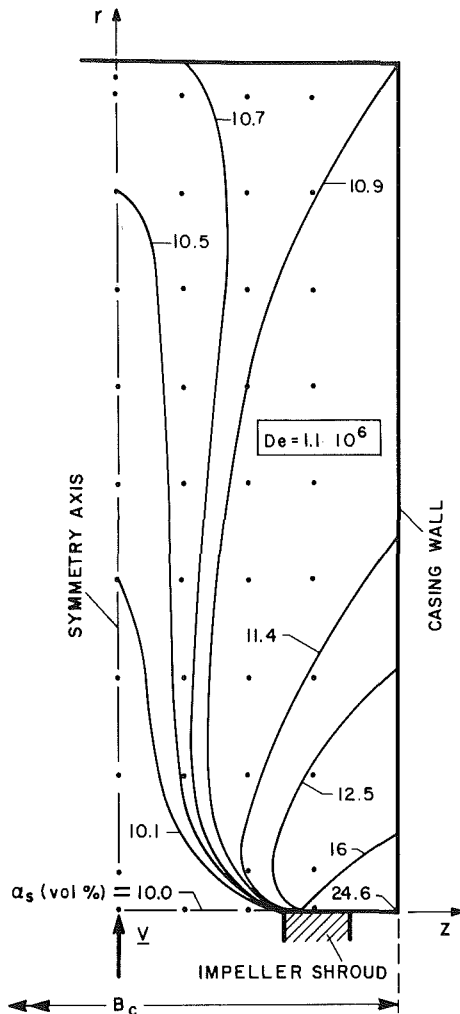


Fig. 16 Concentration distribution in a radial cross-section (the mixture velocity distribution  $V_M$  is given in Fig. 11(c),  $\alpha_S = 10$  vol percent, sand  $d = 0.165$  mm)

the truncation error is: 2.0 percent for  $Q_{rc}$ , and 3 percent  $\Delta\eta_{cas}$ ). When the gap between the impeller and casing is larger, as it occurs in the last case, a reduced effect of the casing shape is observed (compare runs 4b and 4c in Figs. 14).

The wear pattern shown in Fig. 15 (photo of a worn casing from a mining site) suggests the existence of a symmetrical double helicoidal flow in the gaps between casing and the impeller shrouds. The double helicoidal flow may be replaced by single (see Figs. 2(c) and 11(e)) or multiple helicoidal motions as a function of the three dimensional velocity distribution at the impeller exit, casing shape and Dean number. A symmetric velocity distribution (as between two parallel walls) is assumed as the impeller outlet if no flow simulation in the impeller is available.

The concentration generally increases in the radial direction, and progressively from the tongue area toward the discharge [6]. The concentration distribution in a radial cross-section is illustrated in Fig. 16.

The overall objective of the present work was to propose a computational engineering algorithm for  $\Delta\eta_{cas}$  starting from the two-phase flow equations [3], [4], with a time efficient calculation schemes. A detailed fully three dimensional analysis in the tongue area will be the next step of the present investigation. That study will include the flow separation and local recirculations, characteristic for a corner flow pattern.

The present approach can be extended to investigate the pressure distribution and thrust on the pump impeller, the wear profile in a radial cross-section and the impeller/casing

flow interaction. The first industrial application of the algorithm outlined in Fig. 3 (Flowchart "CASING") was the design of a new slurry pump of higher efficiency for phosphate mining [17]. The new design resulted from the initial computer analysis in the University of Kentucky (the reduction of the casing width, the tongue size, etc.) was adopted by the GIW Industries, Inc. Recent field measurements on a phosphate slurry line in Florida confirm the predicted uniform wear distribution and improved efficiency. The economy estimated per pump unit ( $P \approx 1000$  kW,  $H = 76$  m,  $Q = 2700$  m<sup>3</sup>/h,  $\alpha_S = 18$  vol percent phosphate,  $d = 0.2$  mm) is over \$20,000/year.

## Conclusions

1. A new quasi-three-dimensional approach is proposed for slurry flow simulation, with application to centrifugal pump casings. The governing equations are averaged over the typical interval of time for the periodic flow caused by the finite number of impeller blades,  $\Delta T = 60/N/Z$ , and over local averaging volumes to reduce the computational work.

The proposed marching approach was particularly formulated for use on pump casings and works well for large secondary currents and lateral inflow. Mass and momentum transfer are fully considered between the adjacent computational stream tubes connecting two successive radial sections. Source-like terms in the momentum and concentration equations (equations (6)) and a modified continuity constraint (equation (8)) were adopted to account for the upstream effects in a radial cross-section.

2. The recirculation flowrate  $Q_{rc}$  was for the first time calculated in the centrifugal pump casing (Figs. 12(a) and 14(a)). Its value is very sensitive to the casing shape in the normal plane, casing width, inflow from impeller and ratio  $Q/Q_n$ . The internal recirculations ( $Q_{rc}$ , secondary currents in a radial cross-section) determine higher headlosses and wear rates, especially at flowrates  $Q$  different from the nominal flowrate  $Q_n$ .

3. The casing headloss was obtained as a function of the casing geometry, flowrate, pump rotational speed, concentration, solids characteristics and inflow boundary conditions from the pump impeller. The approach can be used for parametric studies and casing geometry optimization, taking into account both the energy dissipation and erosive wear. The laboratory facility (Fig. 5) is equipped to provide reliable data for testing the model development.

## Acknowledgments

Partial support received in the University of Kentucky from NSF Grant CBT is acknowledged. The University of Kentucky Computing Center provided assistance to the first two co-authors to develop the numerical codes on flow and wear in pump casings, as a part of a research program on centrifugal pump performance prediction. Some research results were adopted and implemented in design by the GIW pump manufacturer. A simplified version of the two-dimensional program for uniform particle size was also transmitted from the University of Kentucky to the GIW Industries, Inc. for internal use in the pump design. Figure 15 originates from a field study of the first co-author sponsored by OAS in Chile.

## References

- 1 Hamkins, C. P., "Correlation of a One-Dimensional Centrifugal Pump Performance Analysis Method," Paper 84-WA/FM-10, 1984.
- 2 Roco, M. C., Marsh, M., Addie, G. R., and Maffett, J., "Dredge Pump Performance Prediction," *Proc. 8-th ETCE*, Vol. ASME "Synfuels and Coal Energy," 1985, pp. 31-40, also *Journal of Pipelines*, Vol. 5, 1986, pp. 171-190.
- 3 Roco, M. C., and Shook, C. A., "Turbulent Flow on Incompressible Mixtures," *Proc. 4th International Symp. on Turbulent Shear Flows*, NSF/ONR/USAF/ASME, Karlsruhe, pp. 12-1-12.8, 1983 (also in *JOURNAL OF FLUIDS ENGINEERING*, Vol. 107, 1985, pp. 224-231).

- 4 Roco, M. C., and Balakrishnan, N., "Multi-dimensional Flow Analysis of Solid-Liquid Mixtures," *Journal of Rheology*, Vol. 29, 1985, pp. 431-456.
- 5 Roco, M. C., and Reinhard, E., "Calculation of Solid Particle Concentration in Centrifugal Pump Impellers Using Finite Element Techniques," *BHRA*, Vol. Hydrotransport 7, 1980, pp. 359-376.
- 6 Roco, M. C., Nair, P., Addie, G. R., and Dennis, J., "Erosion of Concentrated Slurries in Turbulent Flow," *J. of Pipelines*, Vol. 4, No. 3, 1984, pp. 213-221.
- 7 Roco, M. C., Nair, P., Addie, G. R., and Dennis, J., "Modeling Erosion Wear in Centrifugal Slurry Pumps," *Hydrotransport 9*, BHRA Fluid Engineering, Cranfield 1984, pp. 291-316.
- 8 Roco, M. C., and Addie, G. R., "Test Approach for Dense Slurry Erosion," 1984 Wear Symposium, Denver, 1984, p. 57, also in ASTM Vol. *Slurry Erosion*, in press.
- 9 Roco, M. C., and Dehaven, S., "Marching Approach for Channels with Lateral Inflow and Secondary Currents," (University of Kentucky, 1986), Proc. 2-nd ASME/JSME Thermal Engineering Conference, ASME, Vol. "Thermo-Fluid Dynamics in Rotating Machinery.
- 10 Khesghi, H. S., and Scriven, L. E., "Finite Element Analysis of Incompressible Viscous Flow by a Variable Penalty Function Method," Vol. *Penalty Finite Element Methods in Mechanics*, ASME-AMD 51, 1981, pp. 67-73.
- 11 *Heat Transfer and Fluid Flow Data*, Publ. by General Electric, New York, Section 6403.3, 1984.
- 12 Thomasset, F., *Implementation of Finite Element Methods for Navier-Stokes Equations*, Springer Verlag, New York, 1981, p. 37
- 13 Zienkiewicz, O. C., *The Finite Element Method*, McGraw-Hill, London, 1977.
- 14 Cheng, K. C., Lin, R. C., and Ou, J. W., "Fully Developed Laminar Flow in Curved Rectangular Channels," *ASME JOURNAL OF FLUIDS ENGINEERING*, 1976, p. 41.
- 15 Mori, Y., Uchida, Y., and Ukon, T., "Forced Convective Heat Transfer in a Curved Channel with a Square Cross-section," *Intl. J. of Heat and Mass Transfer*, Vol. 14, 1971, p. 1787.
- 16 Ito, H., and Nambo, K., "Flow in Rotating Straight Pipes of Circular Cross-Section," *ASME Journal of Basic Engineering*, Vol. 93, 1971, pp. 383-394.
- 17 Kawahara, M., Yoshimura, N., and Nakagawa, K., "Analysis of Steady Incompressible Viscous Flow," In: *Finite Elements in Flow Problems*, Ed. Oden, J. T. et al., UAH Press, Huntsville, 1974, pp. 107-120.
- 18 Roco, M. C., Addie, G. R., Visintainer, R., and Ray, E. L., "Optimum Wearing High Efficiency Design of Phosphate Slurry Pumps," 11-th Int'l. Conference on Slurry Technology, Vol. STA, 1986, pp. 277-286.

# Automatic Remeshing Scheme for Modeling Hot Forming Process

H. P. Wang

Automation Systems Lab.,  
General Electric R&D Center,  
Schenectady, New York 12345

R. T. McLay

The University of Texas at Austin,  
Dept. ASE-EM,  
Austin, TX 78712

*Many intrinsic problems associated with the modeling of hot forming processes are described. In the updated Lagrangian finite element technique both the momentum and energy equations are formulated to accommodate moving meshes. Forming processes have several characteristics: no-slip conditions with transient free surfaces; strong thermal and flow coupling; and moving fluid/solid contact points. Due to the no-slip condition at the walls, the Lagrangian mesh is distorted. Two related numerical algorithms, an automatic remeshing scheme and a moving contact point definition, are developed and incorporated into a finite element code for incompressible viscous flow with temperature-sensitive viscosity. The application of this newly developed code for analyzing the glass pressing process demonstrates the capability of this powerful engineering tool.*

## Introduction

Hot forming processes such as pressing, molding, and forging play a major role in manufacturing processes. The basic characteristics are transient free surfaces, strong thermal and flow coupling, moving fluid/solid contact points and material constitutive formulation. Because of these nonlinearities the process mechanics can only be analyzed through numerical modeling. This paper discusses some of the intrinsic problems associated with transient-free surface modeling and presents a method to simulate the complex interactions among the processing conditions, the thermal/flow coupling, and the mold/die geometry in hot forming.

The model of the glass pressing process discussed in this paper serves as an example to illustrate its practical applications. The average production yield of the glass pressing process is relatively low due to many kinds of defects, such as incomplete filling, and warpage. A computer program was developed to better understand the physics of this coupled heat and fluid flow process and to increase the yield.

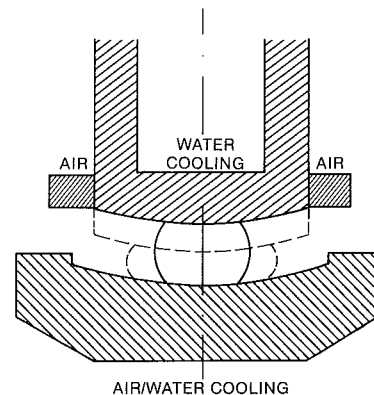
**The Physical Process and Its Implications.** Figure 1 shows a close-up view of the plunger, the gob of molten glass, and the mold. There is water cooling on the plunger and air/water cooling on the mold. When the plunger lowers, the gob deforms like dough. Glass at these molten temperatures is a newtonian fluid. The result section discusses examples of how the gob distorts during forming.

The effect of this flow has many implications on the modeling effort. The outer free surface must be tracked to determine if the glass gob fills the mold. Moving all the nodes with their computed velocity will accurately predict the position of the free surface. This leads to using a Lagrangian frame of reference. However, due to the continuous motion of nodes in the Lagrangian coordinates, severe numerical difficulties, such as element shearing, node tangling, and negative Jaco-

bian, are generally encountered in modeling of large deformation problems in two or more dimensions.

Another transient-free surface modeling technique is the rubberband stretching coordinate technique, in which all interior nodes are moved proportionally to the free surfaces or interfaces. It is very useful to construct moving meshes when the primary boundary motion is in one direction, where there is no complication due to a moving fluid/solid contact point, and the no-slip condition [1-3].

However, in the glass pressing process, the glass sticks to the top and bottom surfaces of the plunger and mold during deformation. This fact means that the free surface will flow toward the two walls, thus changing the contact point where the outer edge of the glass touches the wall. This moving contact must be accurately computed so as to conserve mass.



COUPLED GLASS FLOW AND HEAT TRANSFER

Fig. 1 Gob, plunger, and mold heat transfer

Contributed by the Fluids Engineering Division and presented at the Symposium on Grid Generation, ASME Joint Conference, Houston, Texas, May 1983. Manuscript received by the Fluids Engineering Division, August 3, 1983.

Also, the no-slip condition will lead to mesh tangling, especially at the elements which one side on the wall and another on the free surface. Automatic remeshing has been developed during the course of this work to prevent the mesh from tangling during this time-dependent computation.

The properties of glass are not constant but are a strong function of temperature, especially viscosity. The viscosity decreases drastically with increasing temperatures. A 10°C change in temperature changes the viscosity to 10 to 20 percent; a 50°C change causes an 80 to 100 percent change in viscosity. The temperature-dependent properties along with the transient terms mean that when remeshing, the old solution must be carried over to the new mesh.

While the discussions in this paper mainly concern the glass pressing process, the ideas and the process modeler developed in this work can be applied to many of the hot forming processes, including the forming of shear-rate-dependent materials.

### Finite Elements Formulation

The material of the glass pressing process is treated as a incompressible newtonian fluid with temperature-sensitive viscosity. The geometry of the workpiece can be either axisymmetric or two-dimensional. Since this is a free surface problem, as discussed above, the conservation equations must be reformulated to accommodate the moving meshes. The time derivative for the velocities and the temperature in the moving mesh system become:

$$\begin{aligned} \frac{\partial u_i}{\partial t} \Big|_M &= \frac{\partial u_i}{\partial x_j} \Big|_M \frac{\partial x_j}{\partial t} + \frac{\partial u_i}{\partial t} \Big|_E \\ \frac{\partial T}{\partial t} \Big|_M &= \frac{\partial T}{\partial x_j} \Big|_M \frac{\partial x_j}{\partial t} + \frac{\partial T}{\partial t} \Big|_E \end{aligned} \quad (1)$$

where the subscript  $M$  denotes the moving mesh, the subscript  $E$  the Eulerian description, and  $\partial x_j / \partial t$  the velocity of the mesh. The first term in each of the above equations is due to the moving nodes. The element convection  $\partial x_j / \partial t$  can also be approximated in terms of the velocity of the nodal coordinates and the basis function [1].

$$\frac{\partial x_j}{\partial t} = \Phi^T(x, t) \mathbf{U}_j(t) = U_j^e \quad (2)$$

Using the conventional Galerkin formulation, the continuity, momentum, and energy equation in the moving mesh yield are

$$\int \Psi \left( \frac{\partial \hat{u}_i}{\partial x_i} \right) dV = 0 \quad (3)$$

$$\begin{aligned} \int \Phi \left[ \frac{\partial \hat{u}_i}{\partial t} + (\hat{u}_j - U_j^e) \frac{\partial \hat{u}_i}{\partial x_j} \right] dV \\ + \int \tau_{ij} \frac{\partial \Phi}{\partial x_j} dV - \int \rho g_i \Phi dV - \int \Phi \tau_{ij} n_j dA = 0 \end{aligned} \quad (4)$$

### Nomenclature

$u_i$  = velocity components  
 $\rho$  = mass density  
 $\tau_{ij}$  = stress tensor  
 $p$  = pressure  
 $\mu$  = viscosity  
 $C_p$  = specific heat  
 $q_i$  = heat flux  
 $k$  = thermal conductivity

$\Phi(x_i, t)$  = vector form of the basis function for velocity  
 $\Psi(x_i, t)$  = vector form of the basis function for pressure  
 $\Theta(x_i, t)$  = vector form of the basis function for velocity  
 $\mathbf{U}_i$  = velocity of moving node  
 $U_j^e$  = element convection

$v$  = velocity on free surface or plunger  
 $N_i(s, t)$  = shape function in local coordinates  
 $R_p, Z_p$  = coordinates for fluid/solid contact location  
 $\hat{\phantom{x}}$  = finite element approximation, i.e.,  $\hat{u}_i(x_i, t)$

$$\int \Theta \rho C_p \left[ \frac{\partial \hat{T}}{\partial t} + (\hat{u}_j - U_j^e) \frac{\partial \hat{T}}{\partial x_j} \right] dV + \int q \frac{\partial \Theta}{\partial x_i} dV - \int \Theta q n_j dA = 0 \quad (5)$$

When the element velocity  $U_j^e = 0$ , these equations are Eulerian, and when  $U_j^e = \hat{u}_j$ , these equations are Lagrangian.

In the literature, there has been much discussion of the choice of an element for this mixed formulation of velocity and pressure [4]. If one wants to use quadrilaterals there are three main choices: four velocity nodes and one pressure node in the center ( $4 \times 1$ ); eight velocity nodes and four pressure nodes at the corners ( $8 \times 4$ ); and nine velocity nodes and four pressure nodes at the corners ( $9 \times 4$ ). The  $4 \times 1$  element is the simplest but it has an oscillatory mode known as a "checkerboard" mode in the pressure. This mode can be removed by post-processing techniques under certain conditions [5]. The  $9 \times 4$  element is known to be stable but has the extra velocity node in the middle [4]. We have chosen the  $8 \times 4$  element because it is the simplest element that allows for curved sides. Sani et al. showed that  $8 \times 4$  element can have bad or oscillatory pressures [5]. One of the authors of this paper has shown, however, that the  $8 \times 4$  element has as accurate results as the  $9 \times 4$  element, provided that there are enough elements and that the boundary data is reasonably smooth [6]. In the study of glass pressing, there have been no pressure oscillations.

### Automatic Remeshing Scheme

The details of the matrix formulation and the numerical integrations are referred to in references [7 and 8]. The flowchart, as shown in Fig. 2, illustrates the two major tasks developed during this work: the automatic remeshing scheme and the moving contact algorithm. They are discussed in this and the following section.

There are three major tasks involved in this automatic remeshing scheme: automatic mesh generation, boundary node initialization, and element searching technique and local coordinate calculation.

**Automatic Mesh Generation.** Automatic interior mesh generation for finite element modeling has been investigated for many years [9]. Several of the two-dimensional schemes are based on the theory of mapping node space  $(I, J)$  into real space  $(x_i, x_j)$  through solving a differential operator. The present scheme developed for the hot forming modeling follows Caswell's fourth order operator approach [10] in which the  $x_1(I, J)$  and  $x_2(I, J)$  of the interior nodes are computed by solving the finite difference form of

$$\frac{\partial^4 f}{\partial^2 I \partial^2 J} = 0 \quad (6)$$

where  $f$  can be either  $x_1$  or  $x_2$ . The coordinates of specified boundary nodes serve as the boundary conditions for this equation. Most fourth order operators require the specification on the boundary of at least one derivative in addition to the function itself. By using Green's theorem, it can be shown

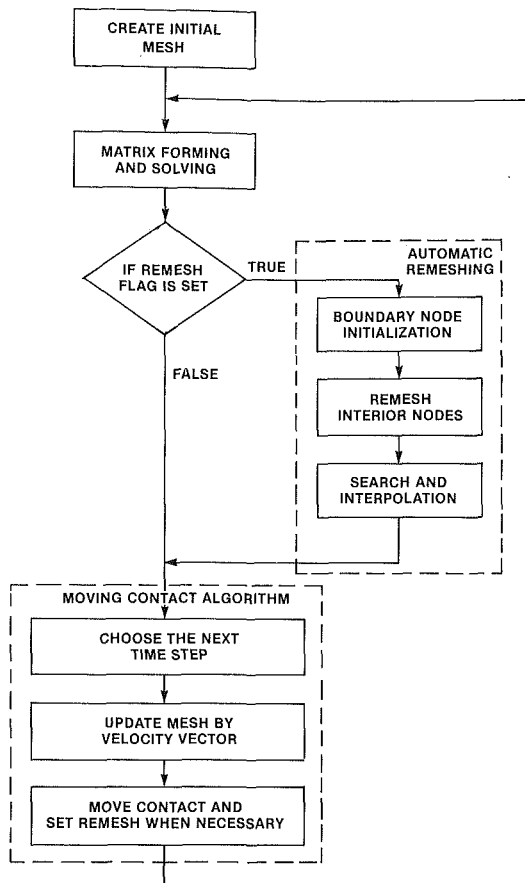


Fig. 2 Flowchart of automatic remeshing scheme

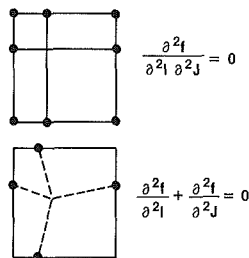


Fig. 3 Comparison of interior node position between two schemes

that this operator only needs the function itself provided the boundaries in  $I$ - $J$  space are straight lines (which is the identity of the  $I$ - $J$  space in the first place).

The central finite difference approximation for node  $(0,0)$  is

$$f_{1,1} + f_{-1,1} + f_{1,-1} + f_{-1,-1} - 2f_{0,0} - 2f_{1,0} - 2f_{-1,0} - 2f_{0,1} + 4f_{0,0} = 0 \quad (7)$$

It is noted that the center node is influenced by eight surrounding nodes while the Laplace scheme is calculated with four nodes, as shown in Fig. 3. The finite difference equation is solved by Gauss-Seidel iteration with an optimum over-relaxation factor of 1.53. The mesh generation scheme developed by Winslow [9] uses a weighted average of the surrounding eight nodes with proper weighting factors for different meshes. For glass pressing the mesh generated by Caswell's approach is more desirable because the nodes are closer to the curved boundary. However, the fourth order operator has no maximum principal, unlike Winslow's equipotential approach, meaning that an interior node could

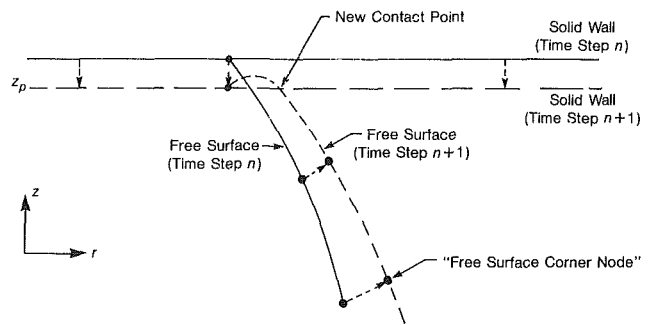


Fig. 4 Moving contact point definition

be repositioned outside the boundary for some concave domains.

**Boundary Node Initialization and Element Searching.** Since automatic internal mesh generation [9] is really a boundary value problem, the initialization of the nodes on the boundary are crucial to the placement of the interior nodes. The algorithm implemented here can redistribute the boundary nodes of a fairly arbitrary shape. In glass pressing the nodes are evenly redistributed along each of the four sides.

There are two techniques to determine in which old mesh element the node is located (after remeshing). The method implemented is the cross product scheme, in which the cross product between the new nodal vector and the four sides of each element is checked. If it is positive with all four sides, the node is inside that element. The other scheme is to check the number of intersections in one direction; an odd number means it is inside the element.

In order to continue the computation, the unknowns on the new nodes have to be interpolated from the local coordinates of the old mesh. The eight-node quadrilateral elements are used in this forming model. The local coordinates,  $s$  and  $t$ , can be determined by solving the following nonlinear simultaneous equations.

$$Z = \sum N_i(s,t)z_i$$

$$R = \sum N_i(s,t)r_i \quad (8)$$

where  $Z$  and  $R$  are nodal locations. The standard Newton-Raphson method is used. The starting values of  $s$  and  $t$  were calculated exactly by assuming that the element is a bilinear element.

### Moving Contact Algorithm

As noted in the introduction, the no-slip boundary condition causes element shearing. Element shearing is the greatest at the element on the corner of the free surface and the solid wall. This shearing moves the free surface towards the wall, changing where the fluid/solid contact is located.

**Contact Point Definition.** The procedure for finding the contact is shown clearly in Fig. 4. The dotted lines show both the plunger and the free surface at the updated position. The program computes the new contact where the wall and the free surface meet. The intersection of the free surface shape and the solid wall is determined by this equation:

$$Z_p = \sum N_i(1,t)z_i \quad (9a)$$

$$R_p = \sum N_i(1,t)r_i \quad (9b)$$

where  $t$  is the local coordinate and  $N_i(t)$  are the shape functions, where  $s=1$ . Since the eight node quadrilateral elements

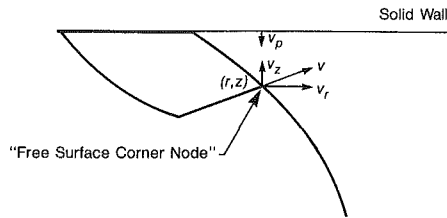


Fig. 5 Variable time step computation

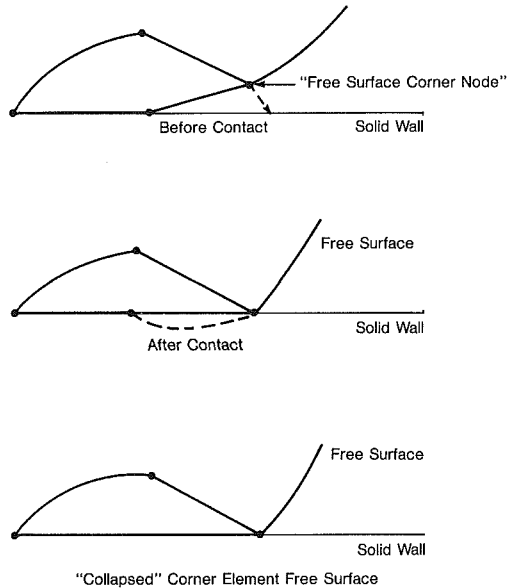


Fig. 6 "Collapsed" free surface on contact element

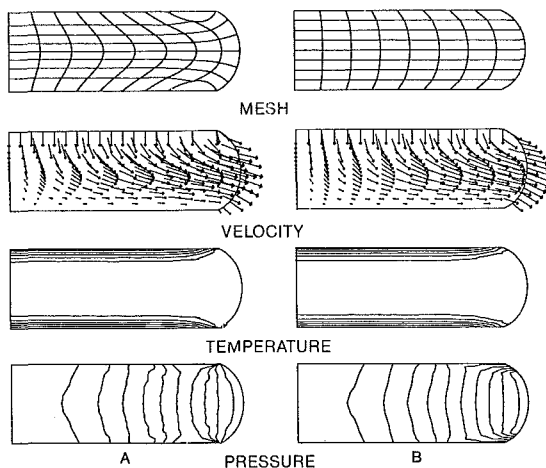


Fig. 7 Comparisons of solutions before (A) and after (B) remeshing

are used in this forming model, the free surface is a quadratic curve. The local coordinate,  $t$ , is found by (9a). The radial distance,  $R_p$ , is computed by using  $t$  in the shape function for  $r$  (9b). The mid-point nodes are moved back to the average distance and the values are interpolated at the new position. The same scheme is used on both the moving plunger at the top and the fixed mold on the bottom. As is clear from Fig. 4, there is some material loss. In practice, however, the loss has proved to be very small, as shown in the result section.

**Variable Time Step Selection.** This approach works fine until the corner node on the free surface passes the solid boundary. Preventing this node from traveling through the solid is solved by reducing the time step. Once the solution is computed, the choice of the time step is independent of the

previous one. If the velocity and the previous time step would push the "free surface corner node" past the solid wall, the time step is reduced to the time that the node would just contact the solid wall (see Fig. 5). Knowing the solution, the mesh, solid wall position, and velocity, the time step for the free surface corner node to contact is

$$\Delta t = \frac{Z_p - Z}{v_z - v_p} \quad (10)$$

**Collapsed Free Surface on Contact Element.** Once the free surface corner node has met the solid wall, the element's free surface is against the wall and has a 180 deg angle with the side stuck to the plunger. To match the solid boundary conditions for the old free surface on the corner element, the free surface is collapsed to a single point. Figure 6 outlines the steps. The top figure is before the free surface corner node contacts. The second picture shows the element after the free surface corner node contacts. In the bottom picture, what was formerly the free surface side is now collapsed to a single point. This collapsed element retains all the degrees of freedom except the velocity, which is forced to have the same velocity as the wall. There is no problem with the Jacobian.

## Evaluation and Results

There are two ways to evaluate how well this scheme works. In glass pressing, the volume is constant. Also, it is important for the calculation to accurately interpolate the new nodal values after remeshing.

The volume losses are very small and are due to three different causes: remeshing, the moving contact, and the explicit time step for moving the mesh. The overall change in volume is  $-0.19$  percent for 140 time steps. The major part of this is due to remeshing ( $-0.26$  percent). The moving contact is a small part of that with  $0.03$  percent. At the beginning, the explicit scheme causes very insignificant volume changes; however, at the end the explicit scheme actually adds volume. The long elements at the end of the calculation do not give as accurate a velocity distribution as at the beginning. Overall the explicit scheme increases the volume  $0.1$  percent. The volume is calculated by numerical integration using gauss quadrature.

The discussion above shows that the changes in volume are very small. It is useful also to check the contours to see if the solution field remains nearly the same after remeshing as before. Figure 7 shows these two cases. The shape of the boundary is the same, and the velocity and temperature fields look identical. The pressure contours are different at the free surface. The cause of the change is due to the collapsed free surfaces on the corner elements. The pair of pressure nodes on the collapsed side have different answers but are at the same location. Looking at the pressure contours before remeshing shows that the pressure along the free surface is approximately uniform. When the free surface corner node solution values are interpolated, they are about the same values as before but at a different location. This causes the contours to spread out. The spreading of the solution is limited to this corner element. With a smaller mesh, the influence of this effect will be diminished.

The results of applying this process modeler are shown in the next two figures. Figure 8 shows the transient temperature distributions. The initial gob temperature for this case is  $1200^\circ\text{C}$ . Figure 8 clearly indicates that the outer radial ring is hotter than the center region on the mold and the plunger surfaces at the end of the pressing stage. This is due to the fountain effect: the center core flows radially then toward the top and bottom surfaces. This information is very useful for a proper cooling design. The thermal boundary layer penetrating into the gob center from both the plunger side and the mold side definitely affects the viscosity distribution and, subsequently, the required load on the plunger.

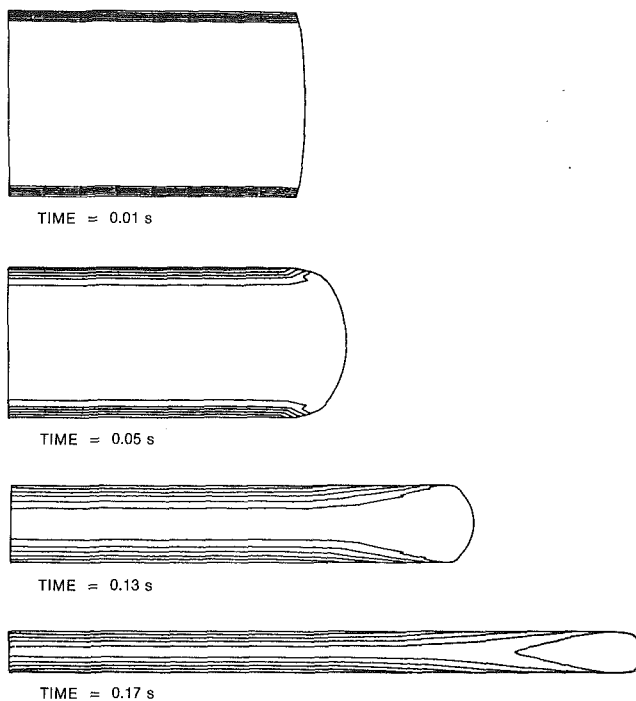


Fig. 8 Temperature contours for four time steps

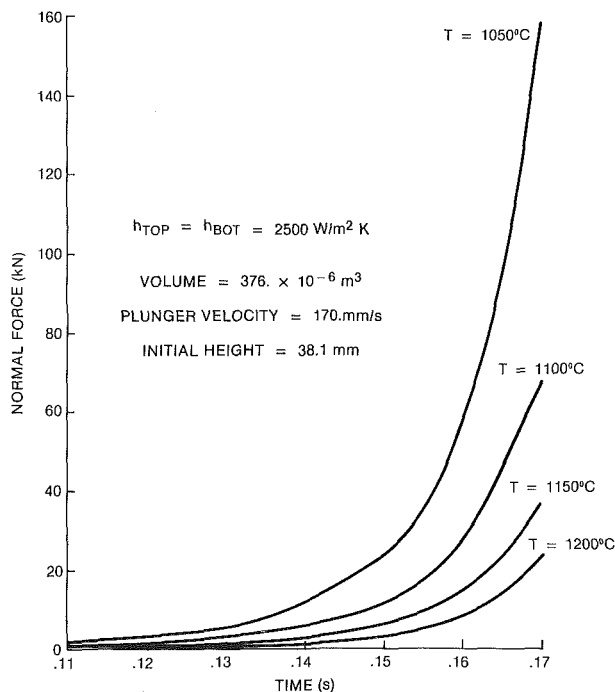


Fig. 9 Load curves for different critical temperatures

The following parametric study gives technical insight into the forming process. The sensitivity of the initial gob temperature is shown in Fig. 9. There are two nonlinear characteristics involved here. First, the required load is approximately proportional to the third power of the thickness as shown by each individual curve. Second, the glass viscosity increases exponentially with the decreasing temperature, as seen by comparing curves with different initial temperatures. Other results can be seen in reference [11]. Without this numerical model, it would be extremely difficult to evaluate this coupling effect. The CPU time for one run with 140 time steps and 64 elements is 5 minutes on a CRAY-1 computer.

## Conclusion

The finite element formulation of momentum and energy equations using moving meshes is presented. The element shearing problem of the hot forming model are solved by using this automatic remeshing scheme integrated with the moving contact algorithm. The numerical techniques developed and implemented in this work are quite general; their application to the glass pressing process is an example used to demonstrate this new method. Using different material constitutive equations, the current model can be directly applied to metal forming and other processes. Additional work on the comparison between using the convective adjustment and search and interpolation technique discussed in this paper is in Reference 12. Adaptive meshing techniques based on the solution and/or the solution gradients is still under development for fixed geometry. A recommended area of research involves further work integrating the above outlined remeshing technique, which has moving boundaries, with the adaptive meshing.

## References

- Lynch, D. R., "Unified Approach to Simulation on Deforming Elements with Application to Phase Change Problems," *Journal of Computational Physics*, Vol. 47, 1982, pp. 387-411.
- Murray, W. D., and Landis, R., "Numerical and Machine Solutions of Transient Heat-Conduction Problem Involving Melting or Freezing, Part 1," *ASME Journal of Heat Transfer*, 1959, pp. 106-112.
- Patzek, T. W., Benner, R. E., and Scriven, L. E., "Nonlinear Oscillations of Inviscid Free Drops," *The American Physical Society*, Vol. 27, No. 9, 1982.
- Sani, R., Gresho, P., Lee, R., and Griffiths, D., "The Cause and Cure of the Spurious Pressures Generated by Certain FEM Solutions of the Incompressible Navier-Stokes Equations," *Int. J. of Numerical Methods in Fluids*, Part 1, 1981, pp. 17-44, Part 2, pp. 171-204.
- Carey, G. F., and Oden, J. T., *Finite Elements: A Second Course*, Prentice-Hall, Englewood Cliffs, NJ, Chapter 3, 1983.
- Carey, G. F., and McLay, R. T., "Some Numerical Comparison Studies for the Eight-node Quadrilateral," *Int. J. for Numerical Methods in Fluids*, Vol. 6, 1986, pp. 165-172.
- Zienkiewicz, O. C., *The Finite Element Method in Engineering Science*, McGraw-Hill, London, 1977.
- Gartling, D. K., and Nickell, R. E., "Finite Element Analysis of Free and Forced Convection," *Finite Elements in Fluids*, First Edition, Vol. 3, Wiley, New York, 1978, pp. 105-121.
- Winslow, A. M., "Equipotential Zoning for Two-dimensional Meshes," University of California, Lawrence Radiation Laboratory Report, UCRL-7312, 1963.
- Caswell, B., private communication, Brown University, Providence, RI.
- Wang, H. P., and McLay, R. T., "A Finite Element Model for the Glass Pressing Process," *Glastechn. Ber.* (W. Germany) 56K, 1983, pp. 289-294.
- Wang, H. P., and McLay, R. T., "Remeshing Schemes for Convective Elements with Application to Hot Forming Process," edited by G. Carey and J. T. Oden, Fifth International Symposium of Finite Elements and Flow Problems, January 1984, Austin, TX.

# Calculation of Boundary Layers With Sudden Transverse Strain

M. M. Gibson

B. A. Younis

Mechanical Engineering Department,  
Imperial College of Science & Technology,  
London SW7 2BX, England

*Modifications to a Reynolds stress closure are proposed in which the weighting of the two components of the pressure-strain correlation is adjusted: the turbulence part is increased to conform with measured rates of return to isotropy and the contribution from the mean-strain part is reduced. Consequential changes are then needed in the other closure assumptions. Their effect is to make the model more generally applicable and to improve predictions of turbulent flows in complex strain fields. The revised model is tested here against the measured response of axisymmetric boundary layers to suddenly imposed rotation. The wall region of this flow is resolved by means of wall functions where it is assumed that the directions of the shear stress and the mean-strain rate are coincident.*

## 1 A Modified Turbulence Model

The transport equations for the Reynolds stresses contain time-averaged products of the fluctuating parts of the pressure and the strain rate that must be modelled in order to close the equations for turbulent flow calculation. Probably the most widely used model is one of two originally proposed by Launder et al. [1], in which the pressure-strain correlation:

$$\frac{p}{\rho} \left( \frac{\partial u_i}{\partial x_j} + \frac{\partial u_j}{\partial x_i} \right) = -C_1 \frac{2\epsilon}{q^2} \left( \overline{u_i u_j} - \frac{1}{3} \delta_{ij} \overline{q^2} \right) - C_2 \left( P_{ij} - \frac{2}{3} \delta_{ij} P \right) \quad (1)$$

is expressed as the sum of components representing the nonlinear interaction of turbulence with itself and the interaction with the mean strain rate [2]. With what appeared to be suitable choices for the constants  $C_1$  and  $C_2$  the model has given good results for many simple shear flows. Performance for more difficult flows has, however, been less satisfactory. For example, the model does not properly account for the effects of longitudinal curvature in boundary layers or the effects of swirl about an axis of symmetry when the accepted values of the constants are used. A reassessment of the criteria to be met in calibration shows that the model constants may be altered in a logical way to improve the accuracy of predictions of complex flows without loss of accuracy in simple shear flow prediction.

Launder et al. [1] identified three basic criteria to be met: (a) theoretical results for suddenly distorted turbulence, (b) the measured rate of return to isotropy in the absence of mean strain and, (c) measured stress levels in homogeneous shear flow. The usual practice [1, 3-5] has been to set  $C_2 = 0.6$  in order to satisfy (a) when the turbulence is initially isotropic. Then  $C_1$  must be specified in the range 1.5-1.8 in order to obtain approximately the measured stress levels in homogeneous shear flow [6]. On the other hand, condition (b) requires a

value of about 3.0 to agree with the measured rate of return to isotropy [7].

Use of these constants (1.8, 0.6) has given good results for buoyant shear layers [3, 4] but, for the analogous case when the streamlines are curved [5], only in a curvilinear coordinate system. The model with these constants also fails badly to predict the development of weakly swirling jets, with results very similar to those obtained [8] with  $C_1$  set equal to 1.5 in the alternative model of Launder et al. [1]. Some modification is therefore needed to account for the effects of extra strain in flows of this description. There is little to be gained by replacement: the alternative model of Launder et al. [1] does not perform significantly better and is less amenable to changes in the constants, and other proposals are either inconveniently complicated or problem dependent. The alternative approach is to see whether the results given by equation (1) can be improved by changes in the constants that alter the balance of the two components.

The basis for a different choice of model constants has been presented in detail, and by reference to curved flow, in an earlier paper [9]. There it was argued that too much importance had been attached to the exact result for suddenly distorted isotropic turbulence as a limiting case. Calculations in practice will always be of anisotropic turbulence for which no single value of  $C_2$  is obtainable from rapid-distortion theory [10, 11]. Moreover, Lumley [12] has argued that the rapid-distortion problem has little to do with Reynolds-stress modelling anyway. It is surely not logical to insist that the first requirement of a pressure-strain model is that it satisfy one particular result of a theory of questionable relevance. This constraint is therefore abandoned.

For turbulent shear flow in local equilibrium at high Reynolds numbers, the use of (1) in the stress equations produces stress/energy ratios that are simple functions of the single parameter  $(1 - C_2)/C_1$  which, for consistency with the data [6], must assume a value in the range 0.2-0.24. Consideration of the extinction of shear stress in highly curved flow [9] produces a second relationship between the constants. These two conditions are satisfied approximately when

Contributed by the Fluids Engineering Division for publication in the JOURNAL OF FLUIDS ENGINEERING. Manuscript received by the Fluids Engineering Division February 25, 1985.



**Table 1 Influence of model constants on stress levels calculated for free and wall flow in local equilibrium**

Reference	1	3,5	Present work
$C_1$	1.5	1.8	3.0
$C_2$	0.6	0.6	0.3
$(1 - C_2)/C_1$	0.267	0.222	0.233
$C_1'$	—	0.50	0.75
$C_2'$	—	0.30	0.50
$-\overline{uv}/\overline{q^2}$	free	0.181	0.170
	wall	—	0.130
$\overline{u^2}/\overline{v^2}$	free	2.08	1.86
	wall	—	4.40
			3.60

$C_1 = 3.0$ ,  $C_2 = 0.3$  and  $(1 - C_2)/C_1 = 0.23$  and the new value of  $C_1$  also satisfies condition (b): the rate of return to isotropy.

Additional terms must be added to the right side of equation (1) to account for increased anisotropy in turbulence near a wall. It is not necessary to write these terms out in full; they are the same as in our previous studies [3, 5] but with the constants  $C_1'$  and  $C_2'$  changed to 0.75 and 0.5, respectively, as a result of the changes to  $C_1$  and  $C_2$ . New and old values of the model constants are summarized in Table 1 together with the stress levels obtained for local-equilibrium turbulence in free flow and near a wall.

The remaining closure approximations can be dealt with briefly. Turbulent transport of Reynolds stress is modeled as before [5] by gradient diffusion:

$$\overline{u_i u_j u_k} = -C_t \frac{\overline{q^2}}{2\epsilon} \overline{u_k u_m} \frac{\partial \overline{u_i u_j}}{\partial x_m} \quad (2)$$

with the value of  $C_t$  left unchanged at 0.22. The equation for the turbulent energy dissipation rate is [1, 5]

$$\frac{D\epsilon}{Dt} = C_\epsilon \frac{\partial}{\partial x_k} \left( \frac{\overline{q^2}}{2\epsilon} \overline{u_k u_m} \frac{\partial \epsilon}{\partial x_m} \right) + \frac{2\epsilon^2}{\overline{q^2}} \left( C_{\epsilon_1} \frac{P}{\epsilon} - C_{\epsilon_2} \right) \quad (3)$$

in which the constants  $(C_\epsilon, C_{\epsilon_1}, C_{\epsilon_2}) = (0.15, 1.4, 1.8)$  differ slightly from the traditional values of the  $k-\epsilon$  model and those originally chosen by Launder et al. (0.18, 1.44, 1.9) [1]. The use of return-to-isotropy data [7] to calibrate the model involves only  $C_1$  and  $C_2$ . The increase in  $C_1$  to 3.0 necessitates a wholly beneficial decrease in  $C_2$  to 1.8, the value also chosen by Hanjalic and Launder [13], because it gives a better agreement with the rate of decay of grid turbulence. Small changes in the stress levels in near-wall turbulence (Table 1) modify the relationship between the constants [1] to  $C_\epsilon = 0.35 (C_{\epsilon_2} - C_{\epsilon_1})$ , and the value of  $C_{\epsilon_1}$  is specified as the result of a large number of calculations for two-dimensional shear flows [14].

These changes do not impair the accuracy of calculation of the standard shear flows (plane and round jets, wakes, mixing

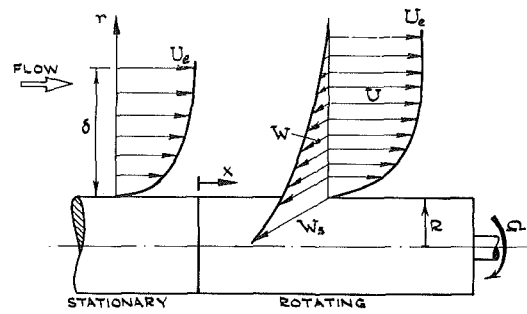


**Fig. 1 Experimental arrangement and notation**

layers and flat-plate boundary layers) because there is no significant change in the ratio  $(1 - C_2)/C_1$  and the optimum values have been used for the other model constants. Flows with extra rates of strain are more difficult. The changes are essential for calculations of curved flows (mixing layers, boundary layers and wall jets) that are independent of the coordinate system [14] and they greatly improve predictions of swirling jets [9].

## 2 Flow on a Spinning Cylinder

**2.1 Description.** Three-dimensional boundary layers on bodies of revolution rotating in axial stream occur on the hubs turbomachines and on spinning projectiles. The flow is also of interest as a special type of three-dimensional boundary layer which resembles the yawed boundary layer on a swept wing in some respects, but differs from it in that the transverse motion is not driven by pressure gradients. The effects of spin have been investigated by Bissonnette and Mellor [15] and Lohmann [16] for the flow sketched in Fig. 1 and the conditions of Table 2. An axisymmetric boundary layer develops first on the surface of a stationary cylinder of radius  $R$  whose axis is aligned to the free-stream direction. The transverse motion is suddenly applied at  $x=0$  where the after part of the cylinder rotates with angular velocity  $\Omega$ , surface velocity  $W_s = R\Omega$ . An internal, transverse, boundary layer is formed, the developed oncoming flow is distorted, and the turbulence has gradually to adjust to the new strain field. More recent LDA measurements by Driver and Hebbar [17] also confirm the finding [18] that the flow toward the end of the rotating section approaches the collateral condition  $W/W_s = 1 - U/U_e$ . One effect of the rotation is to increase turbulent activity in the boundary layer. The Lohmann flow [16] is an established test case for three-dimensional boundary-layer calculation [19] that has been used [20] to compare results of computations

## Nomenclature

$A, B$	= constants in the law of the wall, equation (4)
$C_1, C_2, C_1', C_2'$	= constants in the pressure-strain model
$C_t$	= turbulent diffusion coefficient, equation (2)
$C_\epsilon, C_{\epsilon_1}, C_{\epsilon_2}$	= constants in the $\epsilon$ equation, (3)
$P$	= production rate of turbulent kinetic energy
$P_{ij}$	= production rate of Reynolds stress $\overline{u_i u_j}$
$p$	= pressure
$\overline{q^2}$	= (turbulent kinetic energy) $\times 2$
$R$	= cylinder radius
$U, u$	= mean and fluctuating axial velocity components
$u_\tau$	= friction velocity
$V, v$	= mean and fluctuating radial velocity components

$W, w$	= mean and fluctuating circumferential velocity components
$x$	= axial distance measured from start of rotating cylinder
$y$	= radial distance measured from the cylinder surface
$\beta$	= angle of the shear stress to axial direction
$\delta$	= boundary-layer thickness
$\epsilon$	= dissipation rate of turbulent energy
$\nu$	= kinematic viscosity
$\rho$	= fluid density
$\tau$	= shear stress
$\Omega$	= angular velocity

## Subscripts

$r$	= resultant
$s$	= surface
$e$	= edge (free stream)

**Table 2 The experimental conditions**

	Experiments	
	Bissonnette and Mellor [15]	Lohmann [16]
Free-stream velocity, $U_e$ (m/s)	19.4	16.8
Rotation number, $W_s/U_e$	0.936	1.45
Body diameter, $D$ (cm)	12.7	26.8
Reynolds number, $U_e D/\nu \times 10^{-5}$	1.6	2.9
Initial boundary-layer thickness, $\delta_0$ (cm)	1.6	2.0
Maximum $x/\delta_0$	36.5	20.3

with eddy-viscosity and Reynolds-stress models where the integrations were carried through the sublayers to the surface.

**2.2 Flow Calculation.** Previous attempts to treat the low-Reynolds-number turbulence close to a wall by empirical modifications to second-order closures have not been convincing, and there are obvious advantages to be gained from the use of wall functions in preference to integrating the transport equations to the wall. Wall functions have been used [21, 22] to calculate yawed boundary layers on swept wings where it is also necessary to account for pressure-gradient and inertial effects that are negligible in the present flow.

The shear stress at the wall changes direction abruptly at the start of the spinning section with effects that diffuse through the viscous layer into the main body of the boundary layer. A constant-stress layer may be assumed to exist close to the surface in which the shear stress acts in the same direction as the strain rate [21-23]. The velocity distribution can be obtained by substituting the resultant velocity and wall shear vectors in the two-dimensional wall law to give

$$\frac{V_r}{(\tau_s/\rho)^{1/2}} = A \ln \left[ \frac{(\tau_s/\rho)^{1/2} y}{\nu} \right] + B \quad (4)$$

where the subscript  $r$  is a reminder that the relative velocity is to be used; if the surface velocity of the spinning cylinder is  $W_s$ , the appropriate tangential component of  $V_r$  is  $(W_s - W)$ . The constants are the same as for two-dimensional flow:  $A=2.44$ ,  $B=5.0$ . The shear stress and velocity can now be resolved in the axial and tangential directions to obtain

$$\frac{U}{(\tau_{sx}/\rho)^{1/2}} = A(\cos\beta)^{1/2} \ln \left[ \frac{(\tau_{sx}/\rho)^{1/2} y}{\nu} \right] + (\cos\beta)^{1/2} \left[ B - \frac{1}{2} A \ln(\cos\beta) \right] \quad (5)$$

$$\frac{W_s - W}{(\tau_{sz}/\rho)^{1/2}} = A(\sin\beta)^{1/2} \ln \left[ \frac{(\tau_{sz}/\rho)^{1/2} y}{\nu} \right] + (\sin\beta)^{1/2} \left[ B - \frac{1}{2} A \ln(\sin\beta) \right] \quad (6)$$

where  $\tan \beta = \tau_{sz}/\tau_{sx}$ . These relationships are used to evaluate the wall shear stresses in the same way as for two-dimensional flow [24].

A modified version of the Patankar and Spalding "GEN-MIX" computer code [24] was used to solve six modeled equations for the Reynolds stresses [8, 9], the equations of the mean flow and the dissipation-rate equation (3). The main features of the method are that: (a) the radial mean momentum equation is solved implicitly to determine the pressure field; (b) numerical instabilities are eliminated through the use of a staggered grid on which values of the shear stresses are calculated at one set of points and values of all other variables at another set; (c) values of the normal stresses  $v^2$  and  $w^2$  are found from equations for their sum and difference; (d) gradients of the shear stresses are treated as source terms in the

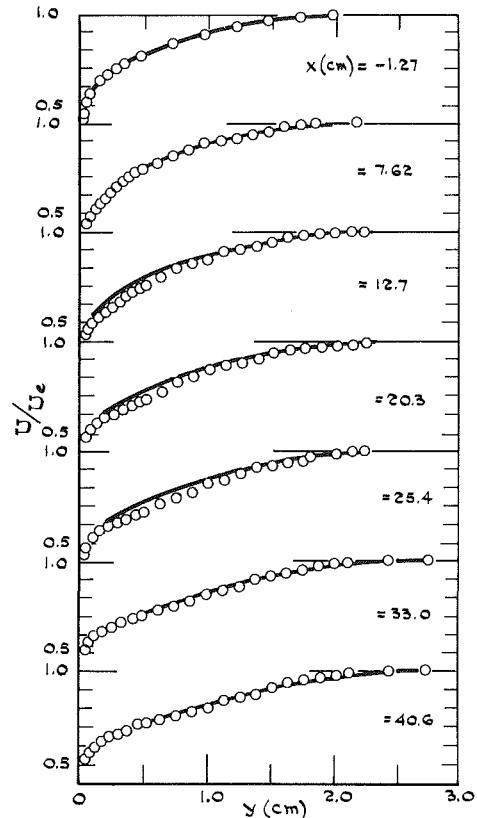


**Fig. 2 Measured and calculated axial-velocity profiles; data of Lohmann**

momentum equations and not, as is a common practice, used only to evaluate eddy viscosities.

Calculations were made with the old model constants proposed by Gibson and Launder [3] and with the revised values of the previous section. The procedure was the same in each case. 35 grid nodes were used in the radial direction with spacing increasing with distance from the cylinder surface. The step size in the axial direction was limited to about 3 percent of the boundary-layer thickness by the approximate method used to obtain the axial pressure gradient from the radial mean momentum equation. The transition from the stationary forward part of the cylinder to the rotating after part was accomplished gradually in 100 steps over a length of 1mm on either side of the boundary.

**2.3 Comparison With Measurements.** The calculations were started 15.2cm and 1.27cm upstream of the spinning cylinder for the Bissonnette-Mellor and Lohmann flows, respectively. The comparisons are made chiefly between Lohmann's measurements and the results obtained using the revised model constants. The profiles of Fig. 2 show that the initial effect of the transverse strain is to reduce the axial velocity close to the wall. Further downstream this velocity-deficit region moves radially outward while the velocity closer to the wall relaxes to the values typical of the non-rotating approach flow. This behavior is reproduced in the calculations and is attributable to increased turbulence generation by the

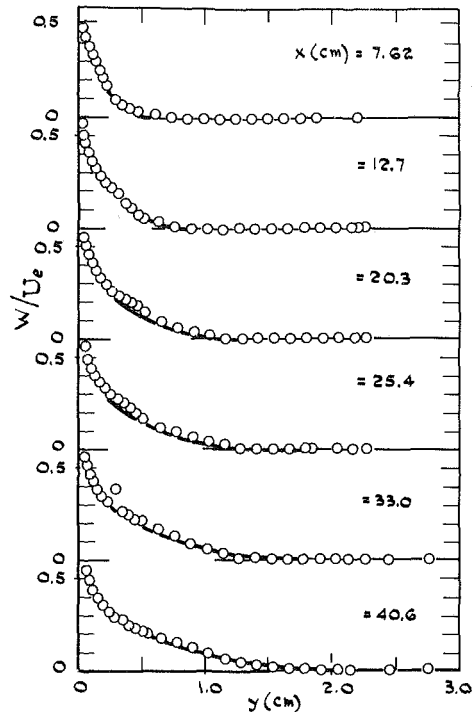


Fig. 3 Measured and calculated tangential-velocity profiles; data of Lohmann

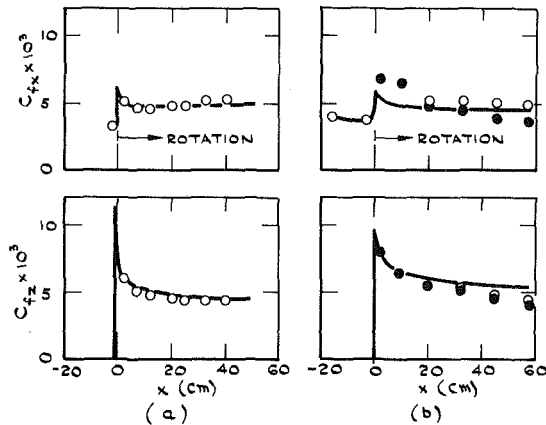


Fig. 4 Measured and calculated axial variation of the skin-friction coefficients. (a) data of Lohmann, (b) data of Bissonnette and Mellor.

extra strains rather than to the small axial pressure caused by the swirl. The results of calculations with the pressure set at the free-edge value show only slight changes to these distributions. Figure 3 shows the growth of the transverse boundary layer with the measured profiles predicted to about the accuracy of the yaw measurements with a single hot wire, estimated by Lohmann to be from about 1.5 to 2.0 deg.

Figure 4 is a plot of the surface shear stresses which are reasonably well predicted for the Lohmann flow but apparently less well so the less demanding conditions of the Bissonnette-Mellor flow. The differences in the former reflect the differences in the measured and predicted velocity profiles because Lohmann also used equation (4) to determine the skin friction. The data of Bissonnette and Mellor must be regarded as suspect here because they found that "it is impossible to find a skin-friction coefficient that would allow a reasonable fit with a law-of-the-wall curve." Instead, the skin friction was estimated, first by extrapolating the measured shear-stress profiles to the wall and second, from the integral momentum equations. The values obtained for  $c_{f_x}$  from the two methods are scattered and show opposite trends to the Lohmann results. While Lohmann's  $c_{f_x}$  falls to a minimum at  $x=10$ cm

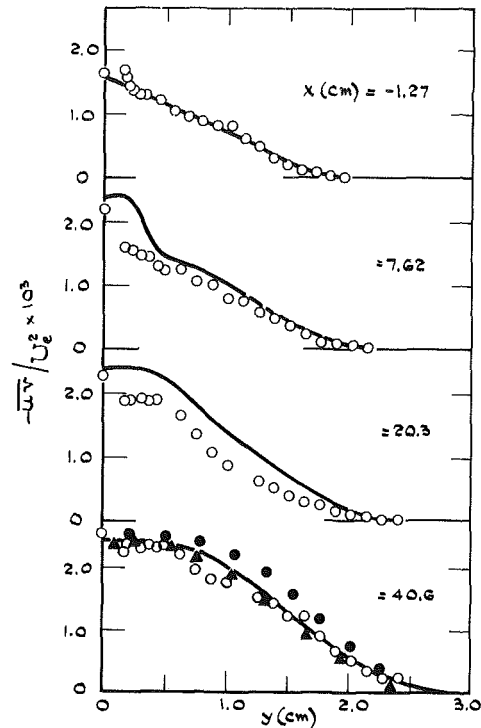


Fig. 5 Measured and calculated profiles of the shear stress  $\overline{uv}$ ; data of Lohmann.  $\bullet$ ,  $\blacktriangle$  GYC and Wilcox and Rubesin model predictions from reference [20].

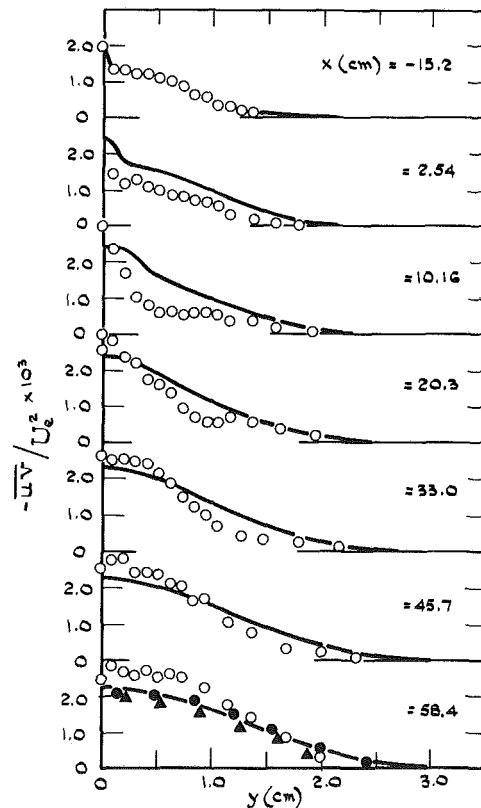


Fig. 6 Measured and calculated profiles of the shear stress  $\overline{uv}$ ; data of Bissonnette and Mellor. Symbols as in Fig. 5.

and then to rise gradually; the values obtained by Bissonnette and Mellor are either constant or falling monotonically. The predictions agree with Lohmann's values of  $c_{f_z}$  which becomes approximately constant for  $x>20$ cm in contrast to the steady fall shown in the Bissonnette and Mellor results.

Figures 5 and 6 show that the shear stress  $uv$  is increased in

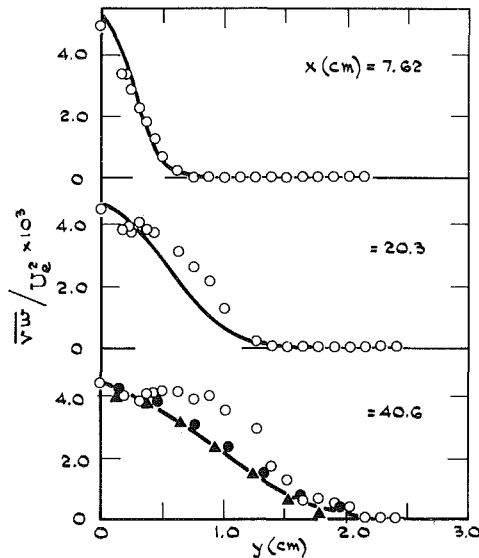


Fig. 7 Measured and calculated profiles of the shear stress  $\overline{vw}$ ; data of Lohmann. Symbols as in Fig. 5.

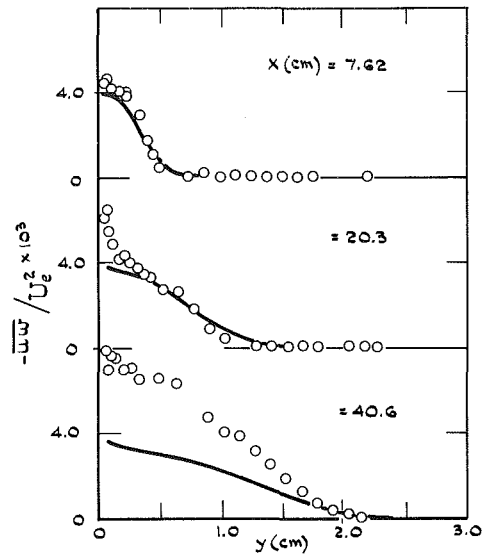


Fig. 9 Measured and calculated profiles of the shear stress  $\overline{uw}$ ; data of Lohmann.

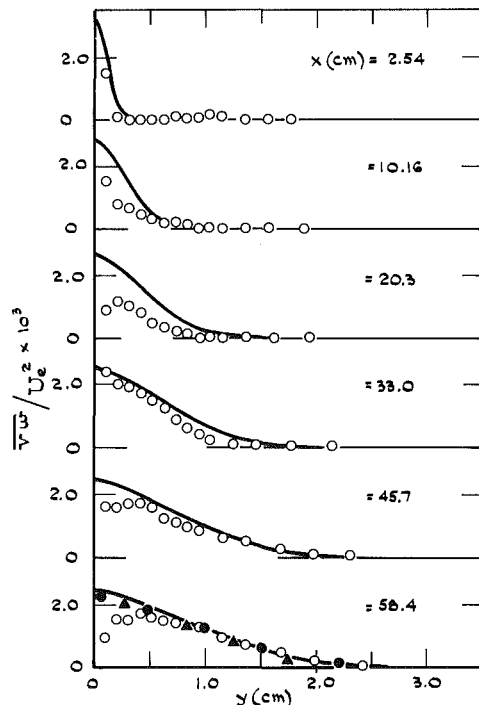


Fig. 8 Measured and calculated profiles of the shear stress  $\overline{vw}$ ; data of Bissonnette and Mellor. Symbols as in Fig. 5.

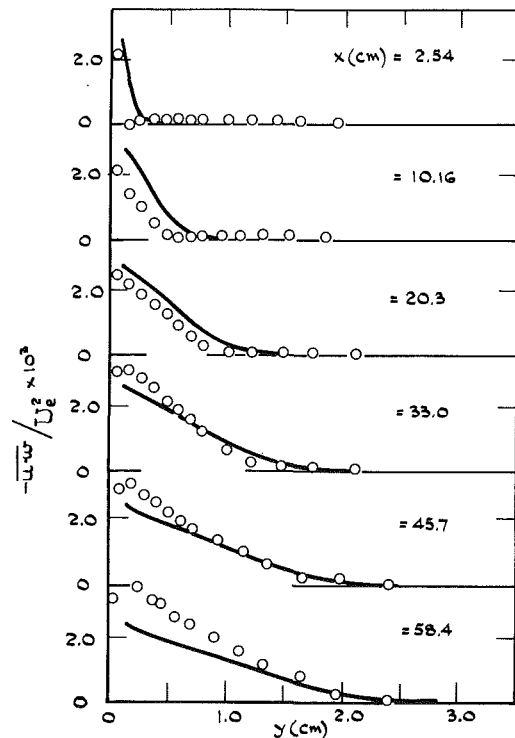


Fig. 10 Measured and calculated profiles of the shear stress  $\overline{uw}$ ; data of Bissonnette and Mellor

the swirling flow. The apparent overpredictions close to the surface may be due in part to the recognised tendency of hot-wire sensors to record low values in this region. The shear-stress profiles in the Bissonnette and Mellor flow are not so closely predicted, but there are also considerable discrepancies here between the measurements and values deduced from the integral momentum equation that are shown in the skin-friction results, Fig. 4. Also shown in the figures are predictions by Higuchi and Rubesin [20] from two Reynolds-stress models in which the wall-function method was replaced by numerical integration through the sublayers.

The other two components of shear stress are plotted in Figs. 7-10 with the Higuchi and Rubesin [20] calculations of  $\overline{vw}$  at one station shown for comparison. The overall level of agreement is fair, except in the downstream  $\overline{uw}$  distributions where the calculated values near the wall are well below those measured in both flows. The shear stress  $\overline{uw}$  exerts some in-

fluence on the development of swirling flows which is explained by its appearance, in  $\overline{uw}W/r$ , as a production term in the equation for  $\overline{uv}$ . Higuchi and Rubesin [20] did not present calculated  $\overline{uw}$  profiles but reported only that "the correct sign of the quantity is predicted, but the quantitative agreement is generally poor."

The effects of spin increase preferentially the turbulent energy in  $w^2$ . In the near-wall, energy-production, region of the Lohmann flow for example, the levels of  $\overline{w^2}$  were some four times as high as those in the oncoming unswirled flow. Redistribution to the other components is affected by the pressure-strain mechanism: four boundary-layer thicknesses downstream  $\overline{u^2}$  had roughly doubled and remained at approximately the same level further downstream, while the response in  $\overline{v^2}$  was appreciably slower, showing a steady increase to about twice the upstream levels after a distance  $x$  of twenty

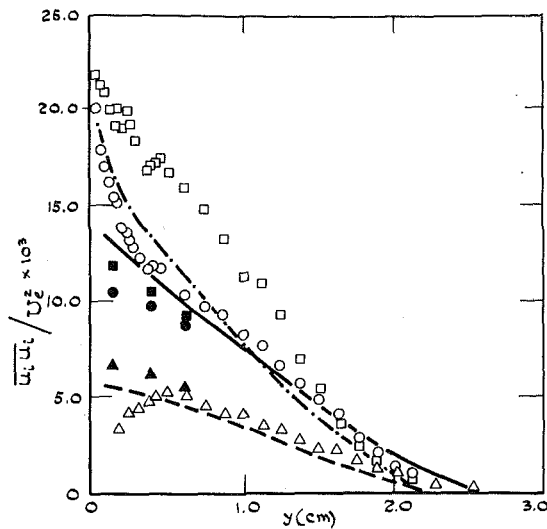


Fig. 11 Measured and calculated profiles of the normal stresses. Data of Lohmann,  $x = 40.6$  cm.  $u^2/U_e^2$ :  $\circ$  (measured), \_\_\_\_\_ (calculated);  $v^2/U_e^2$ :  $\Delta$ , \_\_\_\_\_;  $w^2/U_e^2$ :  $\square$ , \_\_\_\_\_ Filled symbols are Wilcox and Rubesin model predictions from reference [20]

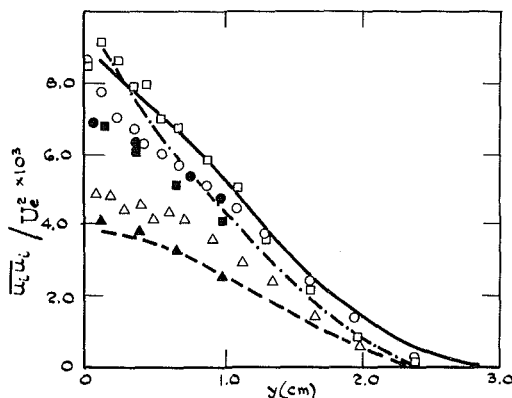


Fig. 12 Measured and calculated profiles of the normal stresses. Data of Bissonnette and Mellor,  $x = 58.4$  cm. Notation as in Fig. 11.

boundary-layer thicknesses. The Bissonnette and Mellor data reveal similar general trends with a relatively slower rate of increase in  $u^2$ . These trends are fairly well recovered in the calculations [14] though for brevity we show in Figs. 11 and 12 only the profiles at the last station in each flow. The results compare favourably with those of Higuchi and Rubesin [20] which at the last stations are considerably below the measured values. The difference here is greater than it was for the shear stresses because the present model contains a mean-strain component of the pressure strain and wall-proximity terms that are needed to represent correctly the anisotropy in simple two-dimensional wall flow.

Inspection of the stress transport equations [8, 9] shows why the present changes in the model constants do not significantly alter the results for this type of flow. Substitution of the pressure-strain model (1) reveals that the modification of  $\partial W/\partial r$  production is almost unaffected as long as the ratio  $(1 - C_2)/C_1$  is unaltered, as it is here. It is when the terms in  $W/r$  become significantly large that the two sets of model constants give different results. In the case of the free swirling jet  $W/r$  is of the same order as the main gradient-production terms in the inner region, and the new constants give much better results than the old ones. The boundary layer on the spinning cylinder is similar to the outer region of the jet where  $W/r$  is relatively small, and its modelled effects on the generation and redistribution of turbulent energy are much weaker. As a consequence the values of turbulence correlations

predicted from the two sets of model constants differ by less than five percent.

### 3 Closure

The response of a developed boundary layer to the sudden imposition of a transverse strain, and the subsequent development of the flow on a spinning cylinder in an axial stream, are predicted with reasonable accuracy by a revised Reynolds-stress closure. The main findings are:

- the shear-stress distributions in the sublayers and at the wall may be obtained from a three-dimensional form of the law of the wall
- turbulence anisotropy near the surface of the cylinders is adequately represented by a recalibrated wall-proximity term in the pressure-strain model
- changes in the main pressure-strain model constants that are needed for the calculation of free swirling jets do not significantly affect the present predictions because the ratio  $(1 - C_2)/C_1$  is unchanged and the terms in  $W/r$  are relatively unimportant away from the swirl axis.

In both the experiments referred to it was found that the turbulence responded quickly to the sudden imposition of an additional strain rate and that the adjustment time of the mean field was slower. This behavior is entirely consistent with our studies of the response of plane boundary layers to a sudden change in surface curvature. In both instances the Reynolds-stress method appears to account for the adjustment, particularly in respect of energy redistribution through the pressure-strain mechanism. Although the present approach improves the prediction of anisotropy near the surface the other results for the mean motion and shear stresses are not significantly different to those obtained previously [20], suggesting that the normal stresses may not be very important in an attached, shear-driven boundary layer. The main weakness is in the prediction of  $uw$  in swirling flows.

### References

- 1 Launder, B. E., Reece, G. J., and Rodi, W., *J. Fluid Mech.*, Vol. 68, 1975, p. 537.
- 2 Rotta, J. C., *Z. Phys.*, Vol. 129, 1951, p. 547.
- 3 Gibson, M. M., and Launder, B. E., *J. Fluid Mech.*, Vol. 86, 1978, p. 491.
- 4 Rodi, W., *Turbulence Models and their Application in Hydraulics*, I.A.H.R. Delft, 1980.
- 5 Gibson, M. M., Jones, W. P., and Younis, B. A., *Phys. Fluids*, Vol. 24, 1981, p. 386.
- 6 Champagne, F. H., Harris, V. G., and Corrsin, S., *J. Fluid Mech.*, Vol. 41, 1970, p. 81.
- 7 Uberoi, M. S., *J. App. Phys.*, Vol. 28, 1957, p. 1165.
- 8 Launder, B. E., and Morse, A. P., *Turbulent Shear Flows 1*, Springer, Berlin, 1979, p. 279.
- 9 Gibson, M. M., and Younis, B. A., *Phys. Fluids*, Vol. 29, 1986, p. 38.
- 10 Maxey, M. R., *J. Fluid Mech.*, Vol. 124, 1982, p. 261.
- 11 Newley, T. M. J., Ph.D. thesis, Cambridge, 1986.
- 12 Lumley, J. L., *Adv. App. Mech.*, Vol. 18, 1978, p. 123.
- 13 Hanjalic, K., and Launder, B. E., *J. Fluid Mech.*, Vol. 74, 1976, p. 593.
- 14 Younis, B. A., Ph.D. thesis, London, 1984.
- 15 Bissonnette, L. R., and Mellor, G. L., *J. Fluid Mech.*, Vol. 63, 1974, p. 369.
- 16 Lohmann, R. P., *ASME JOURNAL OF FLUIDS ENGINEERING*, Vol. 98, 1976, p. 354.
- 17 Driver, D. M., and Hebbbar, S. K., AIAA paper 85-1610, 1985.
- 18 Horlock, J. H., Norbury, J. F., and Cooke, J. C., *J. Fluid Mech.*, Vol. 27, 1967, p. 369.
- 19 Humphreys, D. A., and Van den Berg, B., Workshop on Three-Dimensional Boundary Layer Calculation, Berlin, Apr. 1982 (to be published).
- 20 Higuchi, H., and Rubesin, M. W., *AIAA J.*, Vol. 17, No. 9, 1979, p. 931.
- 21 Rastogi, A. K., and Rodi, W., in *Turbulent Boundary Layers*, ASME, New York, 1979, p. 27.
- 22 Van den Berg, B., *J. Fluid Mech.*, Vol. 70, 1975, p. 149.
- 23 Johnston, J. P., Stanford University Thermosciences Division Rep. No. MD-34, 1976.
- 24 Patankar, S. V., and Spalding, D. B., *Heat and Mass Transfer in Boundary Layers*, 2nd ed., Intertext, London, 1970.

**D. K. Das**

Assistant Professor of Mechanical  
Engineering,  
University of Alaska-Fairbanks,  
Fairbanks, AK 99775-0660  
Mem. ASME

**F. M. White**

Professor of Mechanical Engineering,  
University of Rhode Island,  
Kingston, RI 02881-0805  
Mem. ASME

# Integral Skin Friction Prediction for Turbulent Separated Flows

*An integral method is presented for computing incompressible two-dimensional turbulent skin friction for separated flows based on the inner-variable theory. Using a velocity profile in the form of the logarithmic law and wake, continuity and momentum equations are integrated across the boundary layer in terms of inner-variables  $u^+$  and  $y^+$ . With the aid of correlations relating the wake parameter to the pressure gradient parameter, derived from experimental results of several near-separating and separated flows, the governing equations are reduced to a single differential equation in skin friction. Predictions by the theory for several separated flows show satisfactory agreement with experimental data.*

## Introduction

Viscous flow separation occurs in many practical engineering applications such as the trailing edge of airfoils and turbine blades, and on boattailed afterbodies of missiles and jet engines. The stall phenomenon in diffusers is another example of flow separation. In recent years, there have been increased efforts to develop theories for calculating separated flows. Two approaches are available for solving separated flow problems; one uses the full Navier-Stokes equation, the second uses the boundary layer equations. Due to the complexity of solving the full Navier-Stokes equation with an appropriate model for turbulence terms, only limited work has appeared in the literature, notably by Cebeci et al. [1], Cline and Wilmoth [2], and Hasen [3]. These solutions require considerable effort in turbulence modeling, computer memory and processing time, so they remain as research methods.

On the other hand, a great deal of work [4-11] has appeared that employs the boundary layer approach to solve the separated flow problem. These studies demonstrate that the boundary layer equations can yield solutions of acceptable engineering accuracy. Under the boundary layer scheme, both integral and differential methods are available. References [1, 4, and 5] present the differential approach for solving the boundary layer equations. Cebeci et al. [1] have compared their Navier-Stokes solution, mentioned earlier, with an inverse boundary layer solution for the separated flow of Simpson et al. [12], using the experimental distribution of the displacement thickness. Pletcher [4] presents an inverse finite difference method that compares five different turbulence models in predicting separated flows. The method of Kwon and Pletcher [5] features a viscous-inviscid finite difference interaction theory for predicting laminar separation and turbulent reattachment.

Various integral methods dealing with turbulent separation

are presented in references [6 through 11]. Gerhart's theory [6] uses the momentum and the moment of momentum integral equations that proceeds in the strong interaction mode using the flow angle distribution near separation. Four differential equations are solved simultaneously that makes the method fairly complex. Assassa and Papailiou [7] present a direct boundary layer method that employs the momentum and the kinetic energy integral equations retaining the normal stress terms. These terms and the dissipation integral are expressed through correlations involving displacement, momentum, and energy thicknesses, and the integral equations are transformed to a new set in terms of Le Foll's coordinates for final calculation. The development of the theory does not contain adequate information: so it is difficult to replicate or to implement it for calculating other flows.

Moses et al. [8] present a procedure where the boundary layer region is solved simultaneously with the inviscid flow field. The momentum and the kinetic energy integral equations are used in the boundary layer region. The simultaneous solution requires a finite difference procedure. Comparisons with experimental data are only shown for pressure coefficient and momentum thickness in a diffuser. The method due to Whitfield et al. [9] uses an Euler equation code and the momentum and the kinetic energy integral equations. An accurate analytical expression for their velocity profile is presented, but it requires nine steps to compute the profile. With a shape factor correlation and a skin friction correlation the integral equations are solved in the inverse mode. Ghose and Kline [10] apply the momentum integral equation and the entrainment-lag equation with a one-dimensional potential flow model for calculating diffuser flows in the unstalled and the incipient stall regimes. This method is further refined to fully developed stall regime by Bardina et al. [11] by adding an improved correlation for flow detachment, and recasting the integral equations in terms of new dimensionless variables.

In this paper, we present a simple theory that requires the solution of a single differential equation as opposed to two or more for the other methods discussed in the preceding sections. Based on the observation from experimental data that the wake parameter is related to the pressure gradient

Contributed by the Fluids Engineering Division and presented at the AIAA/ASME Fluid Mechanics, Plasma Dynamics, and Laser Conference, Atlanta, Ga., May 11-14, 1986 of THE AMERICAN SOCIETY OF MECHANICAL ENGINEERS. Manuscript received by the Fluids Engineering Conference, August 26, 1985.

parameter, the development of this method is conceptually simple and the solution requires very modest computational effort. The approach follows the inner-variable theory of White [13, 14] developed for unseparated turbulent boundary layers. In the present work the theory is extended to encompass separated flows. Before applying this theory to separated flows, it was tested against several unseparated flows including flat-plate, accelerating and decelerating flows from the Proceedings of the Stanford Conference [17]. In all these cases good agreement was obtained with the experimental data [16, 22].

### Derivation of the Final Equations

For steady, incompressible, two-dimensional turbulent flows, the boundary layer equations are

$$\frac{\partial u}{\partial x} + \frac{\partial v}{\partial y} = 0 \quad (1)$$

$$u \frac{\partial u}{\partial x} + v \frac{\partial u}{\partial y} = U_e \frac{dU_e}{dx} + \frac{1}{\rho} \frac{\partial \tau}{\partial y} \quad (2)$$

The velocity profile chosen here is in the form of the law-of-the-wall and wake proposed by Coles [17]. Ghose and Kline [10] show that the wall-wake law is able to represent both attached and detached boundary layers. The velocity profile is expressed as

$$u(x, y) = v^* \left( \frac{1}{\kappa} \ln y^+ + B \right) + \frac{\Pi |v^*|}{\kappa} \omega \left( \frac{y^+}{\delta^+} \right) \quad (3)$$

where

$$y^+ = \frac{y |v^*|}{\nu}, \quad \delta^+ = \frac{\delta |v^*|}{\nu}, \quad v^* = (\text{sign } \tau_w) \sqrt{\frac{|\tau_w|}{\rho}}$$

The wake shape  $\omega$  proposed by Coles is a sine function, and subsequently Moses [15] proposed a polynomial approximation in the form

$$\omega(z) = 6z^2 - 4z^3, \quad z = y^+ / \delta^+ \quad (4)$$

In the present study, we have used equation (4) since it is possible to evaluate all integrals across the boundary layer analytically.

With  $u(x, y)$  known from the velocity profile assumption, the  $v(x, y)$  component follows from the integration of the continuity equation (1). Substituting  $u$  and  $v$  into the momentum equation (2) and integrating it from the wall ( $y^+ = 0, \tau =$

$\tau_w$ ) to the edge of the boundary layer ( $y^+ = \delta^+, \tau = 0$ ) yields the momentum integral equation.

$$A_1 \frac{dv^*}{dx} + A_2 \frac{d|v^*|}{dx} + A_3 \frac{d\Pi}{dx} + A_4 \frac{d\delta^+}{dx} = \delta^+ U_e \frac{dU_e}{dx} - \frac{|v^*| \tau_w}{\mu} \quad (5)$$

All integrals were evaluated analytically. The coefficients,  $A_1$  through  $A_4$ , are algebraic functions of  $v^*$ ,  $\Pi$ , and  $\delta^+$ . They are intermediate results in the derivation of the final equation, and are presented in [16]. The coefficients of the final working equation (equation (14)) that are necessary for the present method are listed in the Appendix.

Equation (5) contains four variables:  $v^*$ ,  $\Pi$ ,  $\delta^+$ , and  $U_e$ . The actual velocity distribution  $U_e(x)$  is presumed known either from a viscous-inviscid interaction calculation or from measurements of a separated boundary layer. Therefore, we must seek two additional equations to solve for the three unknowns,  $v^*$ ,  $\Pi$ , and  $\delta^+$ . One such relation can be obtained from the wall-wake law by applying the boundary condition  $u(x, y) = U_e(x)$  at  $y^+ = \delta^+$  and then differentiating it with respect to the streamwise distance  $x$  with the result

$$\frac{d\delta^+}{dx} = \frac{\kappa \delta^+}{v^*} \frac{dU_e}{dx} - \frac{\delta^+}{v^*} (\ln \delta^+ + \kappa B) \frac{dv^*}{dx} - \frac{2\delta^+}{v^*} \left[ |v^*| \frac{d\Pi}{dx} + \Pi \frac{d|v^*|}{dx} \right] \quad (6)$$

The second equation is obtained from an empirical correlation between Coles' wake parameter  $\Pi$  and Clauser's pressure gradient parameter  $\beta$ . This correlation and the development of the final differential equation is presented in the next section.

### Relation Between Wake and Pressure Gradient Parameters

Flow separation occurs under the influence of a continuous adverse pressure gradient. When velocity profiles for strong adverse pressure gradient flows are examined, they exhibit considerable upward deviations from the logarithmic law indicating that the outer layer is strongly dependent upon the strength of the pressure gradient. Based on these observations, several correlations relating the outer or wake layer parameter to the pressure gradient parameter have been presented in the literature. Nash [24] proposed a correlation relating Clauser's outer layer shape parameter  $G$  to the pressure gradient

### Nomenclature

$A_1$  thru  $A_4$  = coefficients in equation (5)  
 $B$  = constant in the law-of-the-wall = 5.5 [14]  
 $B_1$  thru  $B_4$  = coefficients in equation (13)  
 $c_f$  = skin friction coefficient  
DEN = denominator function in equation (14)  
 $G$  = Clauser outer layer shape factor  
 $L$  = reference length  
NUM = numerator function in equation (14)  
 $p$  = pressure  
 $R_L$  = nominal Reynolds number  
 $R^*$  = stretched Reynolds number in equation (16)

$T_1$  thru  $T_9$  = dimensionless terms in equation (14)  
 $u, v$  = velocity components parallel and normal to the wall  
 $u^+, y^+$  = dimensionless law-of-the-wall variables  
 $U_e$  = velocity at the edge of the boundary layer  
 $U_0$  = reference velocity  
 $v^*$  = shear velocity  
 $v_\beta$  = wake velocity  
 $V$  = dimensionless velocity  
 $x, y$  = coordinates parallel and normal to the wall  
 $x^*$  = dimensionless surface distance  
 $\beta$  = Clauser's pressure gradient parameter

$\delta$  = boundary layer thickness  
 $\delta^+$  = value of  $y^+$  at the edge of the boundary layer  
 $\delta^*$  = displacement thickness  
 $\zeta$  = dimensionless shear velocity  
 $\theta$  = momentum thickness  
 $\kappa$  = Von Karman's constant in the law-of-the-wall = 0.4 [14]  
 $\mu$  = absolute viscosity  
 $\nu$  = kinematic viscosity  
 $\Pi$  = Coles' wake parameter in the law-of-the-wall and wake  
 $\rho$  = density  
 $\tau$  = shear stress  
 $\tau_w$  = shear stress at the wall

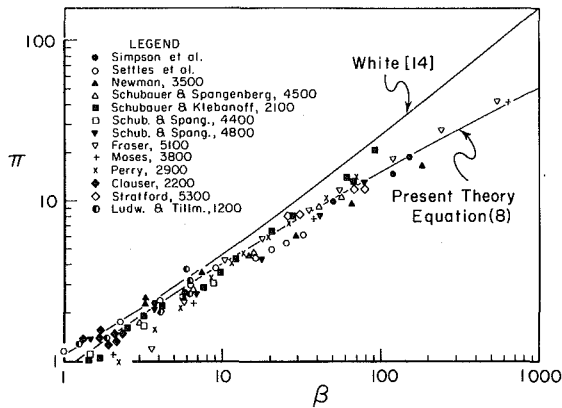


Fig. 1  $\Pi$ - $\beta$  correlation in the unseparated zone. All data points except that of Simpson et al. [12] and Settles et al. [18] are from reference [17]

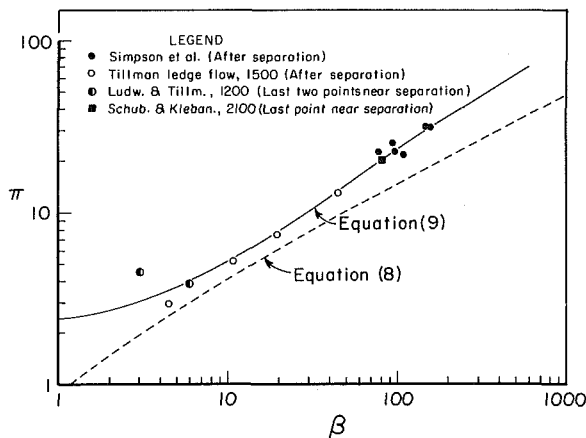


Fig. 2  $\Pi$ - $\beta$  correlation in the separated zone. All data points except that of Simpson et al. [12] are from reference [17]

parameter  $\beta$ . Alber [15] concluded that  $G$  is uniquely related to the wake parameter  $\Pi$  and presented two correlations, one for adverse pressure gradient flows and the other for favorable pressure gradient flows. White [14] suggested a power-law expression

$$\beta = (1.25\Pi)^{4/3} - 0.5 \quad (7)$$

All the correlations mentioned above were for unseparated flows.

In the present study we have compiled a large amount of experimental data from several adverse gradient flows including near-separating and separated flows, and favorable gradient flows. Examination of these data shows that there is an approximate correlation that is best broken into three regions: (a) adverse gradient unseparated flow; (b) adverse gradient separated flow; and (c) favorable gradient flow. The appropriate equations applicable in these regions are

$$\beta = 0.76\Pi + 0.42\Pi^2 \quad (8)$$

$$\beta = -5.5 + 2.5\Pi + 0.09\Pi^2 \quad (9)$$

$$\beta = 0.6\Pi - 0.33 \quad (10)$$

Figure 1 shows the data points and the correlation for adverse gradient flows in the unseparated region. As a comparison, the correlation proposed by White is also shown on this plot. The correlation for the separated region, equation (9), is shown in Fig. 2, and equation (8) is superposed here for comparison. From the plot presented in [16] for favorable gradient flows, equation (10) is obtained.

With  $\beta$  expressed in terms of  $\Pi$  from these proposed correlations, the third equation containing  $d\Pi/dx$  is derived

which provides closure to the problem in conjunction with equations (5) and (6). To accomplish this, we first obtain an expression for the displacement thickness  $\delta^*$  given by the following equation upon integrating the velocity profile defined by equations (3) and (4).

$$\frac{\delta^*}{\delta} = \frac{\Pi |v^*| + v^*}{\kappa U_e} \quad (11)$$

Clauser's pressure gradient parameter  $\beta$  by definition is

$$\beta = \frac{\delta^*}{|\tau_w|} \frac{dp}{dx} = \frac{\delta^*}{|v^*| |v^*|} \left( -U_e \frac{dU_e}{dx} \right) \quad (12)$$

The sign of  $\beta$  depends on the sign of the pressure or velocity gradient. Therefore, absolute values of  $\tau_w$  and  $v^*$  are used on the right-hand side of the foregoing equation so that it does not affect the sign of  $\beta$  when separation occurs and  $\tau_w$  and  $v^*$  change sign. We eliminate  $\delta^*$  from equation (12) via equation (11) and substitute  $\beta = \beta(\Pi)$  from equations (8) through (10). Differentiating this result with respect to  $x$  yields

$$\frac{d\Pi}{dx} = B_1 \frac{dv^*}{dx} + B_2 \frac{d|v^*|}{dx} + B_3 \left( \frac{dU_e}{dx} \right)^2 + B_4 \left| \frac{d^2 U_e}{dx^2} \right| \quad (13)$$

where the coefficients  $B_1$  through  $B_4$  are functions of  $\Pi$ ,  $\delta^+$ , and  $v^*$  given in [16]. The absolute value term used in equation (13) becomes important very near separation and is consistent with the observation of Hinze [19] that the wake parameter  $\Pi$  increases monotonically as separation is approached. Using equations (6) and (13),  $d\Pi/dx$  and  $d\delta^+/dx$  can be eliminated from equation (5) that results in a differential equation in  $v^*$ . This equation is subsequently nondimensionalized for convenience, by using the following dimensionless variables.

$$x^* = \frac{x}{L}, \quad V = \frac{U_e}{U_0}, \quad \zeta = \frac{v^*}{U_e}$$

Here  $U_0$  and  $L$  are characteristic velocity and length, respectively.

In terms of these variables, the differential equation then becomes

$$\frac{d\zeta}{dx^*} = -\frac{\zeta}{V} \frac{dV}{dx^*} + \frac{1}{V} \left( \frac{\text{NUM}}{\text{DEN}} \right) \quad (14)$$

where the numerator function

$$\text{NUM} = T_1 - T_2 + R_L (T_3) [T_4 - R_L (T_5)]$$

and the denominator function

$$\text{DEN} = R_L (T_3) (T_6 \pm T_7) + (T_8 \pm T_9)$$

and  $R_L = U_0 L / \nu$  is the nominal Reynolds number. More details on the derivation may be obtained from [16, 23]. Equation (14) is the final result of the present study. One only needs the expressions for the dimensionless terms,  $T_1$  through  $T_9$ , to program this method, that we have listed in the Appendix. This final working equation is a first order, nonlinear ordinary differential equation in dimensionless shear velocity  $\zeta(x^*)$  which is solved numerically from a given initial condition  $\zeta_0$  at  $x_0^*$ . The skin friction  $c_f$  is, then, obtained from the relation  $c_f = 2(\text{sign } \zeta)\zeta^2$ . The other two variables  $\Pi$  and  $\delta^+$  are calculated at each streamwise position from two algebraic equations obtained from the wall-wake law and the  $\Pi - \beta$  correlations. The dimensionless forms of these two equations are

$$1.0 = \zeta \left( \frac{1}{\kappa} \ln \delta^+ + B \right) + \frac{2\Pi}{\kappa} |\zeta| \quad (15)$$

and

$$\frac{\beta}{\Pi + \frac{\zeta}{|\zeta|}} = \frac{\delta^+}{\kappa |\zeta| |\zeta| R^*} \quad (16)$$



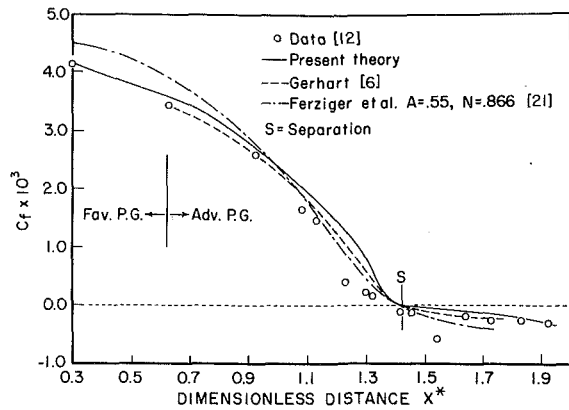


Fig. 3 Comparison with the experiment of Simpson et al. [12]

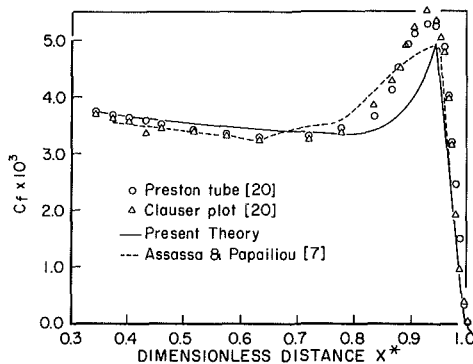


Fig. 4 Comparison with the experiment of Chu and Young, Series I [20]

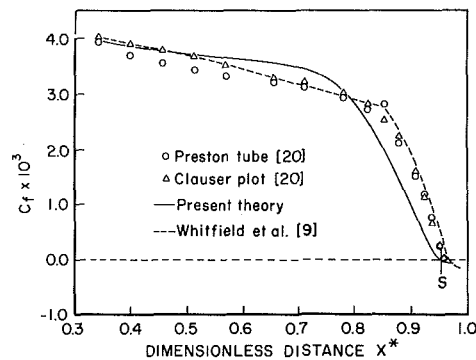


Fig. 5 Comparison with the experiment of Chu and Young, Series II [20]

where  $R^* = R_L/[d(1/V)/dx^*]$  is the stretched Reynolds number [13].

The knowledge of  $\zeta$ ,  $\Pi$ , and  $\delta^+$  from equations (14), (15), and (16) can provide values of integral thicknesses. The algebraic relations for them are obtained by integrating the wall-wake law defined in equations (3) and (4). Upon non-dimensionalization they yield

$$\delta^* = \left( \frac{\delta^+ \nu}{|\zeta| V U_{0\kappa}} \right) (\Pi |\zeta| + \zeta) \quad (17)$$

and

$$\theta = \left( \frac{\delta^+ \nu}{|\zeta| V U_{0\kappa}} \right) [(\Pi |\zeta| + \zeta) - \frac{1}{\kappa} (2\zeta^2 + 3.1667\Pi\zeta|\zeta| + 1.4857\Pi^2\zeta^2)] \quad (18)$$

We have used these thickness formulas with good results for a wide variety of unseparated flows [22]. But they do not give

satisfactory results in the separated region and are, therefore, not used in the present calculations. As shown in [16], additional study is needed to devise accurate formulas for boundary layer thickness and shape parameters to accompany the skin friction values.

### Comparison With Experiments

To test the present theory against experimental data, we selected the following separated flow experiments.

Table 1 List of experiments

Title and reference	Description
1. Simpson et al. [12]	Pressure gradient initially favorable, then adverse with separation.
2. Chu and Young, Series-I [20]	An initial region of favorable pressure gradient followed by a strong adverse pressure gradient provoking separation in a short distance.
3. Chu and Young, Series-II [20]	Monotonic adverse pressure gradient leading to flow separation.
4. Moses, 3800 [17]	Boundary layer on a cylinder under strong pressure gradient with separation.
5. Newman, 3500 [17]	Airfoil boundary layer flow proceeding toward separation.

Figure 3 presents the prediction for the flow of Simpson et al. [12]. The initial region of this flow is under favorable pressure gradient which is followed by an adverse pressure gradient until separation occurs. Satisfactory agreement with the experimental data is observed. Interpolation of Simpson's data establishes the steady separation point at  $x^* = 1.377$ . The present theory predicts separation slightly behind at  $x^* = 1.424$ . Predictions by Gerhart [6] and Ferziger et al. [21] are also presented in this figure for comparison. Gerhart's computation starts from the adverse region in a direct mode using the velocity distribution and then switches over to the inverse mode where the measured flow angle distribution is used. Ferziger et al. [21] have presented three curves that correspond to three sets of curve-fit constants for their skin friction correlation. The one shown here represents the result of their linear regression approximation. The separation points predicted by all three methods coincide with each other within the plotting accuracy.

Figure 4 shows the prediction for the flow of Chu and Young [20] designated as Series-I. This flow begins with a very mild favorable pressure gradient that prevails over 80% of the test section. Then the favorable gradient is increased to an extremely high value followed by an equally severe adverse gradient that leads to separation in a very short distance. The skin friction prediction agrees well except in the highly accelerated region of the flow field. The disagreement is due to the highly nonequilibrium effect present in this region. The results of Assasa and Papailiou's [7] prediction shown in this figure also displays similar effect in this region. The separation point prediction is quite satisfactory. Predictions for the flow of Chu and Young, Series-II, is shown in Fig. 5. This experiment is for a monotonic adverse pressure gradient flow. Skin friction is slightly overpredicted in the forward region and underpredicted over the rear section. But the calculations follow the experimental trend and the location of the separation point is predicted quite well. The results of Whitfield et al. [9] are also presented in this figure, which show better agreement than the present prediction.

The fourth test case is the flow over a cylinder as presented by Moses [17]. Overall agreement with the data in Fig. 6 is

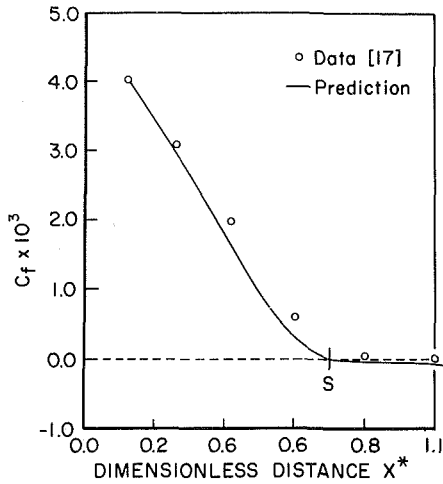


Fig. 6 Comparison with the experiment of Moses, 3800 [17]

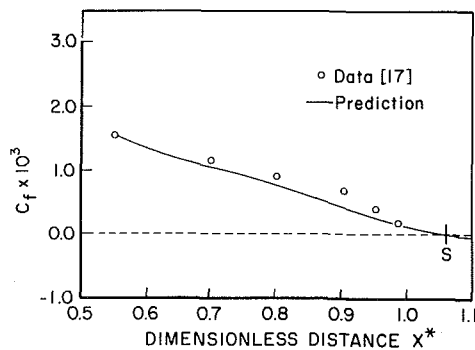


Fig. 7 Comparison with the experiment of Newman, 3500 [17]

seen to be satisfactory but the separation is predicted ahead of the experimental point. Figure 7 presents the prediction for the flow over an airfoil measured by Newman [17]. Overall, the calculations show reasonably good agreement with the measurements; but the separation is predicted somewhat farther than the actual location.

**Effect of the Singularity at Separation.** Boundary layer solutions are affected by the separation point singularity [6-8] when the skin friction  $c_f$  approaches zero. Therefore, we studied its effects on the final differential equation (14) and the parameters  $\delta^+$  and  $\Pi$  used in this theory. Using the data from Simpson's experiment it was shown in [23] that for  $c_f = \pm 10^{-6}$  the values of  $\delta^+$  and  $\Pi$  were of the order of 100 and 300, respectively. So, although  $\delta^+$  approaches zero and  $\Pi$  approaches infinity at the separation point theoretically, they have finite values very close to separation. In a numerical run, it is unlikely that  $\delta^+$  will ever approach zero or  $\Pi$  infinity.

It was shown in [16], by applying L'Hospital's rule to the dimensionless terms of our basic skin friction equation (14), that the skin friction variation  $d\zeta/dx^*$  remains finite in the limit of  $\zeta \rightarrow 0$ . This has been confirmed by extensive numerical calculations which show that  $c_f$  can be reduced to a value of about  $\pm 10^{-6}$  without having any notable effect on numerical computations. In this narrow region of  $10^{-6} < c_f < -10^{-6}$ , computations are carried out by maintaining the same values of the DEN and NUM functions of equation (14), which are obtained at the previous interval in  $x^*$ . For engineering calculations, this assumption in a narrow range of  $c_f$  is not a bad approximation.

Figure 7 shows the behaviors of NUM and DEN functions for the flow of Simpson et al. [12]. They exhibit smooth variation in the neighborhood of the separation point indicating that calculations can proceed smoothly through the separation

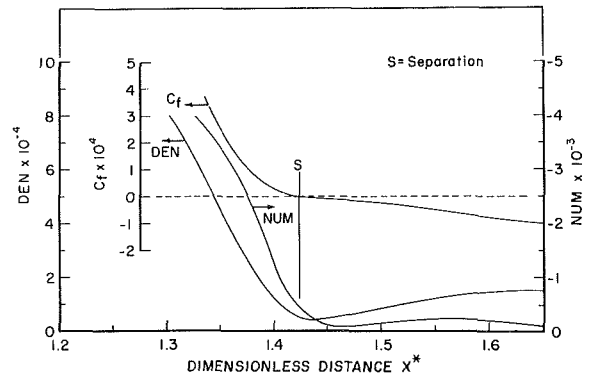


Fig. 8 Behavior of the numerator and denominator functions in the vicinity of separation for the flow of Simpson et al. [12]

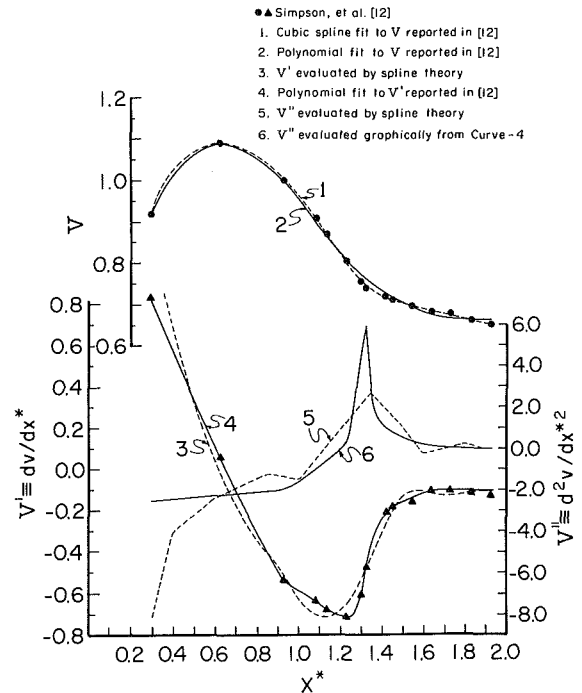


Fig. 9 Distributions of velocity and its derivatives by separate schemes

point into the reverse flow region without any numerical instability. We also conducted further tests by starting from the separated region and integrating with a backward Runge-Kutta scheme. No numerical difficulty is experienced and the results of the forward and backward solutions are identical. The methods of Gerhart [6], and Assassa and Papailiou [7] also present similar observations regarding the weak nature of the separation singularity.

**Sensitivity Analysis.** To assess the sensitivity of the method to the distributions of  $V$ ,  $V'$ , and  $V''$  several runs were made in [16] by prescribing these values with different schemes. Two such schemes are displayed in Fig 9. In this figure lines 2, 4, and 6 represent piecewise polynomial fit to these distributions. Lines 2 and 4 were fitted to the results reported by Simpson et al. [12] and line 6 was obtained by measuring slopes of line 4 from an enlarged plot. Line 1 is obtained by fitting the velocity data to cubic splines, and lines 3 and 5 are the derivatives evaluated from this spline fit. The velocity and its first derivative are in good agreement using both schemes. But the second derivative shows large differences, indicating that there are uncertainties in its values. These uncertainties are difficult to avoid, since numerical differentiation is a rather inaccurate process.

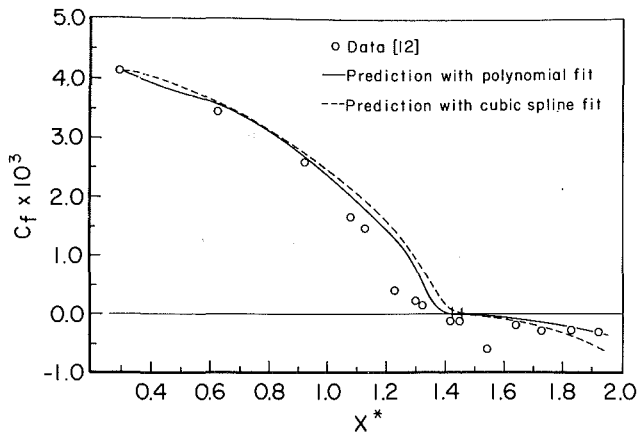


Fig. 10 Skin friction prediction using the distributions of Fig. 9

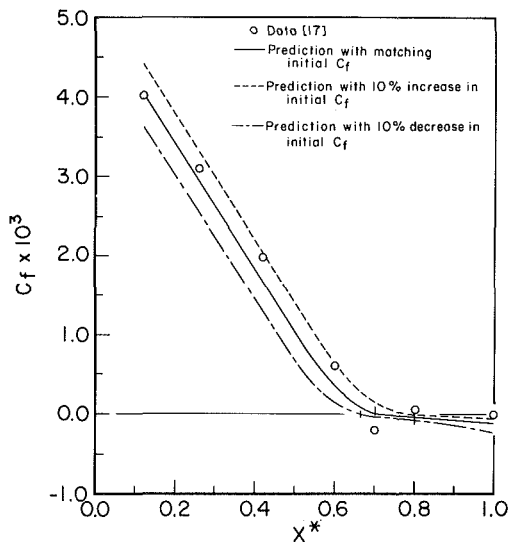


Fig. 11 Sensitivity of the method to the initial condition

The effect of these two schemes on skin friction is shown in Fig. 10. The differences are small in the region upstream of separation, where the numerator and denominator terms of Fig. 8 (which are functions of the derivatives) have large values. In the separated region, the magnitudes of these terms are small, so small variations in the input distributions cause large percentage changes in skin friction values.

Figure 11 shows the sensitivity of the method to the specification of the initial condition. Two predictions are shown for one of the test cases (presented earlier in Fig. 6) by changing the initial condition by  $\pm 10$  percent. The effect is a change of approximately 10 percent in the calculated values of skin friction.

## Conclusions

An inner-variable method is presented in this paper for calculating the skin friction in separated turbulent flows. New empirical correlations between  $\Pi$  and  $\beta$  have been derived from a large amount of experimental data. The method is simple, and requires a very modest amount of computational effort. The results show satisfactory agreement in predicting the skin friction and the separation point. The method shows stable numerical behavior in the vicinity of separation.

The following deficiencies of the method may also be noted. It requires the second derivative of the velocity distribution. As we see from the sensitivity analysis, the numerical differentiation introduces some uncertainty in specifying this distribu-

tion. Detailed measurements in separated regions are quite limited and the  $\Pi$ - $\beta$  correlation in this region can be improved as more data become available.

Various refinements to overcome the deficiencies are possible. One modification is the use of wake velocity  $v_\beta = \Pi |v^*|$  as a variable in place of  $\Pi$ . As Ghosh and Kline [10] show, although  $\Pi$  approaches infinity at separation  $v_\beta$  remains finite with smooth transition from the attached to reversed flow region. Another possible refinement is to recast the inner-variable integral equations in the inverse form. A set of equations has been derived in [16] that could be solved with a prescribed  $\delta^*$  distribution. This formulation does not require the second derivative of the velocity and solves a set of differential equations which should bring about improvement in predicting thickness and shape factor.

## References

- 1 Cebeci, T., Khalil, E. E., and Whitelaw, J. H., "Calculation of Separated Boundary-Layer Flows," *AIAA Journal*, Vol. 17, No. 12, Dec. 1979, pp. 1291-1292.
- 2 Cline, M. C., and Wilmoth, R. G., "Computation of High Reynolds Number Internal/External Flows," *AIAA Journal*, Vol. 21, No. 2, Feb. 1983, pp. 172-173.
- 3 Hasen, G. A., "Navier-Stokes Solutions for an Axisymmetric Nozzle," *AIAA Journal*, Vol. 20, No. 9, Sept. 1982, pp. 1219-1227.
- 4 Pletcher, R. H., "Prediction of Incompressible Turbulent Separating Flows," *ASME JOURNAL OF FLUIDS ENGINEERING*, Vol. 100, Dec. 1978, pp. 427-433.
- 5 Kwon, O. K., and Pletcher, R. H., "Predictions of Incompressible Separated Boundary Layers Including Viscous-Inviscid Interaction," *Turbulent Boundary Layers*, H. E. Weber (ed.), ASME Fluids Engineering Conference, Niagara Falls, June 1979, pp. 75-84.
- 6 Gerhart, P. M., "An Integral Method for Predicting Subsonic Turbulent Separating Boundary Layers with Specified Free Stream Input," *Turbulent Boundary Layers*, H. E. Weber (ed.), ASME Fluids Engineering Conference, Niagara Falls, June 1979, pp. 69-78.
- 7 Assassa, G. M., and Papailiou, K. D., "An Integral Method for Calculating Turbulent Boundary Layer With Separation," *ASME JOURNAL OF FLUIDS ENGINEERING*, Vol. 101, Mar. 1979, pp. 110-116.
- 8 Moses, H. L., Jones, III, R. R., and Sparks, J. F., "An Integral Method for the Turbulent Boundary Layer with Separated Flows," *Turbulent Boundary Layers*, H. E. Weber (ed.), ASME Fluids Engineering Conference, Niagara Falls, June 1979, pp. 69-73.
- 9 Whitfield, D. L., Swafford, T. W., and Jacocks, J. L., "Calculation of Turbulent Boundary Layers with Separation and Viscous-Inviscid Interaction," *AIAA Journal*, Vol. 19, No. 10, Oct. 1981, pp. 1315-1322.
- 10 Ghose, S., and Kline, S. J., "The Computation of Optimum Pressure Recovery in Two-Dimensional Diffusers," *ASME JOURNAL OF FLUIDS ENGINEERING*, Vol. 100, Dec. 1978, pp. 419-426.
- 11 Bardina, J., Lyrio, A., Kline, S. J., Ferziger, J. H., and Johnston, J. P., "A Prediction Method for Planar Diffuser Flows," *ASME JOURNAL OF FLUIDS ENGINEERING*, Vol. 103, June 1981, pp. 315-321.
- 12 Simpson, R. L., Strickland, J. H., and Barr, P. W., "Features of a Separating Turbulent Boundary Layer in the Vicinity of Separation," *J. Fluid Mechanics*, Vol. 79, Mar. 1977, pp. 553-594.
- 13 White, F. M., "A New Integral Method for Analyzing the Turbulent Boundary Layer with Arbitrary Pressure Gradient," *ASME Journal of Basic Engineering*, Vol. 91, Sept. 1969, pp. 371-378.
- 14 White, F. M., *Viscous Fluid Flow*, McGraw-Hill, New York, 1974, pp. 550-657 and pp. 481-482.
- 15 Kline, S. J., Cockrell, D. G., Morkovin, M. V., and Sovran, G. (eds.), *Proceedings, Computation of Turbulent Boundary Layers—1968, AFOSR-IFP-Stanford Conference*, Vol. I, Stanford University, 1968.
- 16 Das, D. K., "An Integral Method for Analyzing Incompressible Two-Dimensional Turbulent Boundary Layers with Separation," Ph.D. thesis, University of Rhode Island, 1983.
- 17 Coles, D. E., and Hirst, E. A. (eds.), *Proceedings, Computation of Turbulent Boundary Layers—1968, AFOSR-IFP-Stanford Conference*, Vol. II, Stanford University, 1968.
- 18 Settles, G. S., Williams, D. R., Bac, B. K., and Bogdonoff, S. J., "Reattachment of a Compressible Turbulent Free Shear Layer," *AIAA Journal*, Vol. 20, No. 1, Jan. 1982, pp. 60-67.
- 19 Hinze, J. O., *Turbulence*, Second Edition, McGraw-Hill, New York, 1975, pp. 696-698.
- 20 Chu, J., and Young, A. D., "Measurements in Separating Two-dimensional Turbulent Boundary Layers," *AGARD Conference Proceedings No. 168 on Flow Separation*, Paper 13, Nov. 1975, pp. 13-1 to 13-12.
- 21 Ferziger, J. H., Lyrio, A. A., and Bardina, J. G., "New Skin Friction and Entrainment Correlations for Turbulent Boundary Layers," *ASME JOURNAL OF FLUIDS ENGINEERING*, Vol. 104, Dec. 1982, pp. 537-540.

22 Das, D. K., "Application of Pressure Gradient-Wake Correlations to Inner Variable Theory for Turbulent Boundary Layer Calculations," *Proceedings Southeastern Conference on Theoretical and Applied Mechanics*, Vol. 1, Ranson, W. F., and Biedenback, J. M. (eds.), University of South Carolina, Apr. 1986, pp. 288-295.

23 Das, D. K., and White, F. M., "An Integral Method for Calculating Turbulent Skin Friction in Two-Dimensional Incompressible Separated Flows," AIAA Paper No. 86-1068, AIAA/ASME 4th Fluid Mechanics, Plasma Dynamics and Lasers Conference, Atlanta, May 1986.

24 Nash, J. F., "Turbulent Boundary Layer Behaviour and the Auxiliary Equation," NPL Aero Rep. 1137, see also *AGARDograph 97, part 1*, 1965, pp. 245-279.

## APPENDIX

The dimensionless terms of the final working equation, equation (14), are presented here.

$$T_1 = \delta^+ [F_1] \left[ \frac{1}{V} \left( \frac{dV}{dx^*} \right)^2 \right]$$

where

$$F_1 = \zeta(6.25 \ln \delta^+ + 8.54 + 6.42\Pi^2) + |\zeta|\Pi(12.5 \ln \delta^+ + 18.97)$$

$$T_2 = 2.5 \delta^+ \zeta [F_1] \left| \frac{d^2V}{dx^{*2}} \right| \text{ for adverse gradient.}$$

Replace the absolute value term by  $(-d^2V/dx^{*2})$  for favorable gradient.

$$T_3 = \frac{[F_2] \zeta |\zeta|}{(1 + \Pi)^2} - \frac{5 \delta^+}{R_L V^2} \left( \frac{dV}{dx^*} \right)$$

where

$$F_2 = 0.76 + 0.84\Pi + 0.42\Pi^2 \text{ in adverse gradient unseparated region.}$$

$$= 8.0 + 0.18\Pi + 0.09\Pi^2 \text{ in adverse gradient separated region.}$$

$$= 0.93 \text{ in favorable gradient region.}$$

$$T_4 = [\zeta(1.28 \Pi^2) + |\zeta|\Pi(2.5 \ln \delta^+ + 2.58) + 1] \left[ V \frac{dV}{dx^*} \right]$$

$$T_5 = \zeta^3 V^3 / \delta^+$$

$$T_6 = [\zeta(6.25 \ln^2 \delta^+ + 8.75 \ln \delta^+ + 14.0)$$

$$+ \zeta\Pi^2(3.21 \ln \delta^+ + 7.06)$$

$$+ |\zeta|\Pi(6.25 \ln^2 \delta^+ + 20.2 \ln \delta^+ + 21.48)]V$$

$$T_7 = [\zeta\Pi(12.5 \ln \delta^+ + 63.12 + 6.42 \Pi^2)$$

$$+ |\zeta|(6.25 \ln \delta^+ + 1.25) + |\zeta|\Pi^2(12.5 \ln \delta^+ + 22.18)]V$$

$$T_8 = \delta^+ (2.5 \ln \delta^+ + 5.5) [F_1] \left[ \frac{1}{V} \frac{dV}{dx^*} \right]$$

$$T_9 = 5 \delta^+ (\Pi + |\zeta|/\zeta) [F_1] \left[ \frac{1}{V} \frac{dV}{dx^*} \right]$$

## Some Remarks on the Helical-Cartesian Coordinate System and Its Applications

Zhong-Guang Xu<sup>1</sup> and Dah-Nien Fan<sup>2</sup>

### Nomenclature

- $C_p$  = constant-pressure specific heat  
 $e$  = specific internal energy  
 $\mathbf{e}$  = base vector  
 $\mathbf{F}$  = body force per unit mass  
 $\mathbf{i}, \mathbf{j}, \mathbf{k}$  = Cartesian unit vectors along  $\bar{x}, \bar{y},$  and  $\bar{z}$ -axes, respectively  
 $h$  = specific enthalpy  
 $m$  = distance between two plates in twisted Couette flow  
 $\mathbf{n}$  = unit normal  
 $p$  = pressure  
 $T$  = temperature  
 $t$  = time  
 $u$  = flow speed  
 $v_{(\cdot)}$  = flow velocity component with respect to base indicated by subscripts  
 $x, y, z$  = helical-Cartesian coordinates  
 $\bar{x}, \bar{y}, \bar{z}$  = Cartesian coordinates  
 $\eta$  = the second coefficient of viscosity  
 $\theta$  = angle of twist, a function of  $z$   
 $\kappa$  = thermal conductivity  
 $\mu$  = the coefficient of viscosity  
 $\rho$  = fluid density  
 $T_{(\cdot)}$  = component of viscous stress tensor  
 $\Phi$  = viscous dissipation function

$$\frac{\delta}{\delta z} \equiv \theta' \left( y \frac{\partial}{\partial x} - x \frac{\partial}{\partial y} \right) + \frac{\partial}{\partial z}$$

$$\nabla \cdot \mathbf{V} = \frac{\partial V_x}{\partial x} + \frac{\partial V_y}{\partial y} + \frac{\partial V_z}{\partial z}$$

$$\nabla^2 \equiv \left( \frac{\partial^2}{\partial x^2} + \frac{\partial^2}{\partial y^2} + \frac{\delta^2}{\delta z^2} \right)$$

### Subscripts

- $0$  = at plate  $z=0$   
 $m$  = at plate  $z=m$   
 $x, y, z$  = components with respect to the respective physical base

<sup>1</sup>Visiting Scholar, Department of Mechanical Engineering, Howard University, Washington, D.C. 20059; Also, Professor, Department of Mechanical Engineering, Hangzhou Institute of Electronic Engineering, Hangzhou, Zhejiang Province, People's Republic of China.

<sup>2</sup>Professor, Department of Mechanical Engineering, Howard University, Washington, D.C. 20059.

Contributed by the Fluids Engineering Division of THE AMERICAN SOCIETY OF MECHANICAL ENGINEERS. Manuscript received by the Fluids Engineering Division, May 10, 1983.

$(x), (y), (z)$  = components with respect to the respective natural base

### Superscripts

$\bar{\quad}$  = with respect to Cartesian coordinates

$'$  = indicating  $\frac{d}{dz}$

### Introduction

The objectives of this note are: to present the complete compressible viscous flow equations including expressions for the viscous stress components and the viscous dissipation function in a general curvilinear coordinate system which is helical with an arbitrary inhomogeneous pitch; to comment on some of the results on steady incompressible laminar flow in twisted square tubes [1] and to resolve an apparent discrepancy in the viscous dissipation function given therein. In the limit of constant-density and constant-property flow the continuity and momentum equations presented below reduce to those given by Todd [2].

### Governing Differential Equations and Analysis

*Coordinates System and Bases.* The general curvilinear coordinates  $(x, y, z)$  are defined in terms of a set of inertial Cartesian coordinates  $(\bar{x}, \bar{y}, \bar{z})$  as follows

$$\begin{pmatrix} x \\ y \\ z \end{pmatrix} = \begin{pmatrix} \cos \theta & \sin \theta & 0 \\ -\sin \theta & \cos \theta & 0 \\ 0 & 0 & 1 \end{pmatrix} \begin{pmatrix} \bar{x} \\ \bar{y} \\ \bar{z} \end{pmatrix} \quad (1)$$

where  $\theta$  is a monotonically increasing function of  $z$  and is twice differentiable. Since  $\theta$  is independent of time  $t$ , the  $(x, y, z)$  system so defined remains inertial. Thus we shall refrain from calling the  $(x, y, z)$  system as a rotating one as in [1], and instead identify it as a helical-Cartesian one with an inhomogeneous pitch. Note that the  $z$ -coordinate curve is in general nonorthogonal to the  $x$ - $y$  plane.

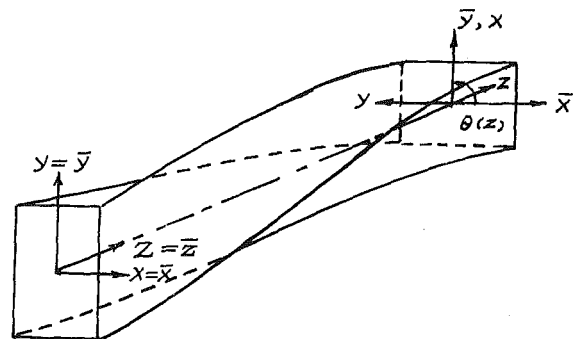


Fig. 1 Helical-Cartesian coordinate system

The natural-base vectors are therefore

$$\begin{pmatrix} \mathbf{e}_{(x)} \\ \mathbf{e}_{(y)} \\ \mathbf{e}_{(z)} \end{pmatrix} = \begin{pmatrix} \cos \theta \sin \theta & 0 \\ -\sin \theta \cos \theta & 0 \\ -y\theta' & x\theta' & 1 \end{pmatrix} \begin{pmatrix} \mathbf{i} \\ \mathbf{j} \\ \mathbf{k} \end{pmatrix} \quad (2)$$

Following Todd [2] the physical-base vectors with respect to which, say, the velocity is decomposed into components are chosen as

$$\begin{pmatrix} \mathbf{e}_x \\ \mathbf{e}_y \\ \mathbf{e}_z \end{pmatrix} = \begin{pmatrix} \mathbf{e}_{(x)} \\ \mathbf{e}_{(y)} \\ \mathbf{k} \end{pmatrix} \quad (3)$$

The velocity vector is equal to

$$[V_x, V_y, V_z] \begin{pmatrix} \mathbf{e}_x \\ \mathbf{e}_y \\ \mathbf{e}_z \end{pmatrix} \quad (4)$$

Thus the physical base is orthonormal and is indistinguishable to its dual or reciprocal base. In the spirit of choices made in equations (2) and (3), we shall take the base dyads to be the outer product of the two sets of base vectors  $\{\mathbf{e}_x, \mathbf{e}_y, \mathbf{e}_z\}$  and  $\{\mathbf{e}_{(x)}, \mathbf{e}_{(y)}, \mathbf{e}_{(z)}\}$ . Hence the viscous stress dyad or tensor can be expressed as

$$[\mathbf{e}_x, \mathbf{e}_y, \mathbf{e}_z] \begin{pmatrix} T_{x(x)} & T_{x(y)} & T_{x(z)} \\ T_{y(x)} & T_{y(y)} & T_{y(z)} \\ T_{z(x)} & T_{z(y)} & T_{z(z)} \end{pmatrix} \begin{pmatrix} \mathbf{e}_{(x)} \\ \mathbf{e}_{(y)} \\ \mathbf{e}_{(z)} \end{pmatrix} \quad (5)$$

It should be remarked that  $T_{x(y)}$  is not necessarily equal to  $T_{y(x)}$  because of the choice of base dyads. Similar conclusions hold for  $T_{y(z)}$  and  $T_{z(y)}$ .

**Compressible Viscous Flow Equations.** Employing a generalized matrix method procedure developed by the authors [3-4] based upon tensor analysis, the governing partial differential equations of compressible viscous flows can be systematically generated for the general curvilinear coordinate system and bases with equations (1-3) as inputs.

The continuity equation is

$$\frac{\partial \rho}{\partial t} + V_x \frac{\partial \rho}{\partial x} + V_y \frac{\partial \rho}{\partial y} + V_z \frac{\partial \rho}{\partial z} + \rho \left( \frac{\partial V_x}{\partial x} + \frac{\partial V_y}{\partial y} + \frac{\delta V_z}{\delta z} \right) = 0 \quad (6)$$

The three components of the Navier-Stokes equation are, respectively,

$$\begin{aligned} \rho \left[ \frac{\partial V_x}{\partial t} + V_x \frac{\partial V_x}{\partial x} + V_y \frac{\partial V_x}{\partial y} + V_z \left( \frac{\delta V_x}{\delta z} - \theta' V_y \right) \right] \\ = -\frac{\partial p}{\partial x} + \rho F_x + 2 \frac{\partial V_x}{\partial x} \frac{\partial \mu}{\partial x} + \left( \frac{\partial V_x}{\partial y} + \frac{\partial V_y}{\partial x} \right) \frac{\partial \mu}{\partial y} \\ + \left( \frac{\delta V_x}{\delta z} + \frac{\partial V_z}{\partial x} - \theta' V_y \right) \frac{\delta \mu}{\delta z} \\ + \left( \frac{\partial V_x}{\partial x} + \frac{\partial V_y}{\partial y} + \frac{\delta V_z}{\delta z} \right) \frac{\partial}{\partial x} \left( \eta - \frac{2}{3} \mu \right) \\ + \mu \left( \nabla^2 V_x - 2\theta' \frac{\delta V_y}{\delta z} - \theta'^2 V_x - \theta'' V_y \right) \\ + \left( \eta + \frac{\mu}{3} \right) \frac{\partial}{\partial x} \left( \frac{\partial V_x}{\partial x} + \frac{\partial V_y}{\partial y} + \frac{\delta V_z}{\delta z} \right) \end{aligned} \quad (7)$$

$$\begin{aligned} \rho \left[ \frac{\partial V_y}{\partial t} + V_x \frac{\partial V_y}{\partial x} + V_y \frac{\partial V_y}{\partial y} + V_z \left( \frac{\delta V_y}{\delta z} + \theta' V_x \right) \right] \\ = -\frac{\partial p}{\partial y} + \rho F_y + \left( \frac{\partial V_x}{\partial y} + \frac{\partial V_y}{\partial x} \right) \frac{\partial \mu}{\partial x} + 2 \frac{\partial V_y}{\partial y} \frac{\partial \mu}{\partial y} \\ + \left( \frac{\delta V_y}{\delta z} + \frac{\partial V_z}{\partial y} + \theta' V_x \right) \frac{\delta \mu}{\delta z} \\ + \left( \frac{\partial V_x}{\partial x} + \frac{\partial V_y}{\partial y} + \frac{\delta V_z}{\delta z} \right) \frac{\partial}{\partial y} \left( \eta - \frac{2}{3} \mu \right) \\ + \mu \left( \nabla^2 V_y + 2\theta' \frac{\delta V_x}{\delta z} - \theta'^2 V_y + \theta'' V_x \right) \\ + \left( \eta + \frac{\mu}{3} \right) \frac{\partial}{\partial y} \left( \frac{\partial V_x}{\partial x} + \frac{\partial V_y}{\partial y} + \frac{\delta V_z}{\delta z} \right) \end{aligned} \quad (8)$$

$$\begin{aligned} \rho \left( \frac{\partial V_z}{\partial t} + V_x \frac{\partial V_z}{\partial x} + V_y \frac{\partial V_z}{\partial y} + V_z \frac{\delta V_z}{\delta z} \right) \\ = -\frac{\delta p}{\delta z} + \rho F_z + \left( \frac{\delta V_x}{\delta z} + \frac{\partial V_z}{\partial x} - \theta' V_y \right) \frac{\partial \mu}{\partial x} \\ + \left( \frac{\delta V_y}{\delta z} + \frac{\partial V_z}{\partial y} + \theta' V_x \right) \frac{\partial \mu}{\partial y} + 2 \frac{\delta V_z}{\delta z} \frac{\delta \mu}{\delta z} \\ + \left( \frac{\partial V_x}{\partial x} + \frac{\partial V_y}{\partial y} + \frac{\delta V_z}{\delta z} \right) \frac{\delta}{\delta z} \left( \eta - \frac{2}{3} \mu \right) \\ + \mu \nabla^2 V_z + \left( \eta + \frac{\mu}{3} \right) \frac{\delta}{\delta z} \left( \frac{\partial V_x}{\partial x} + \frac{\partial V_y}{\partial y} + \frac{\delta V_z}{\delta z} \right) \end{aligned} \quad (9)$$

The energy equation is

$$\begin{aligned} \rho \cdot \left( \frac{\partial h}{\partial t} + V_x \frac{\partial h}{\partial x} + V_y \frac{\partial h}{\partial y} + V_z \frac{\delta h}{\delta z} \right) \\ - \left( \frac{\partial p}{\partial t} + V_x \frac{\partial p}{\partial x} + V_y \frac{\partial p}{\partial y} + V_z \frac{\delta p}{\delta z} \right) \\ = \Phi + \left( \frac{\partial \kappa}{\partial x} + y\theta' \frac{\delta \kappa}{\delta z} \right) \frac{\partial T}{\partial x} + \left( \frac{\partial \kappa}{\partial y} - x\theta' \frac{\delta \kappa}{\delta z} \right) \frac{\partial T}{\partial y} \\ + \frac{\delta \kappa}{\delta z} \frac{\partial T}{\partial z} = \Phi + \frac{\partial \kappa}{\partial x} \frac{\partial T}{\partial x} + \frac{\partial \kappa}{\partial y} \frac{\partial T}{\partial y} + \frac{\delta \kappa}{\delta z} \frac{\delta T}{\delta z} \\ + \kappa \nabla^2 T \end{aligned} \quad (10)$$

where the viscous dissipation function  $\Phi$  is given by

$$\begin{aligned} \Phi = \mu \left[ 2 \left( \frac{\partial V_x}{\partial x} - \frac{1}{3} \nabla \cdot \mathbf{V} \right)^2 + 2 \left( \frac{\partial V_y}{\partial y} - \frac{1}{3} \nabla \cdot \mathbf{V} \right)^2 \right. \\ + 2 \left( \frac{\delta V_z}{\delta z} - \frac{1}{3} \nabla \cdot \mathbf{V} \right)^2 + \left( \frac{\partial V_x}{\partial y} + \frac{\partial V_y}{\partial x} \right)^2 + \left( \frac{\delta V_y}{\delta z} \right. \\ + \left. \frac{\partial V_z}{\partial y} + \theta' V_x \right)^2 + \left( \frac{\delta V_x}{\delta z} + \frac{\partial V_z}{\partial x} \right. \\ \left. - \theta' V_y \right)^2 \left. \right] + \eta (\nabla \cdot \mathbf{V})^2 \end{aligned} \quad (11)$$

The viscous stress dyad arranged as the  $3 \times 3$  matrix shown in (5) is equal to

$$\mu \begin{pmatrix} 2 \frac{\partial V_x}{\partial x} + y\theta' \left( \frac{\delta V_x}{\delta z} + \frac{\partial V_z}{\partial x} - \theta' V_y \right), & \frac{\partial V_y}{\partial x} + \frac{\partial V_x}{\partial y} - x\theta' \left( \frac{\delta V_x}{\delta z} + \frac{\partial V_z}{\partial x} - \theta' V_y \right) & \frac{\delta V_x}{\delta z} + \frac{\partial V_z}{\partial x} - \theta' V_y \\ \frac{\partial V_x}{\partial y} + \frac{\partial V_y}{\partial x} + y\theta' \left( \frac{\delta V_y}{\delta z} + \frac{\partial V_z}{\partial y} + \theta' V_x \right), & 2 \frac{\partial V_y}{\partial y} - x\theta' \left( \frac{\delta V_y}{\delta z} + \frac{\partial V_z}{\partial y} + \theta' V_x \right) & \frac{\delta V_y}{\delta z} + \frac{\partial V_z}{\partial y} + \theta' V_x \\ \frac{\delta V_x}{\delta z} + \frac{\partial V_z}{\partial x} - \theta' V_y + 2y\theta', & \frac{\delta V_y}{\delta z} + \frac{\partial V_z}{\partial y} + \theta' V_x - 2x\theta' & 2 \frac{\delta V_z}{\delta z} \end{pmatrix}$$

$$+ \left( \eta - \frac{2}{3} \mu \right) \nabla \cdot \mathbf{v} \begin{pmatrix} 1 & 0 & 0 \\ 0 & 1 & 0 \\ y\theta' & -x\theta' & 1 \end{pmatrix} \quad (12)$$

Note that the two matrices above are asymmetrical as remarked earlier.

In the limit of constant-density and constant-property flow the divergence of the velocity field and the gradients of properties vanish. The three components of the Navier-Stokes equation simplify to those given in [2]. The viscous dissipation function  $\Phi$  in the incompressible limit, however, is at variance with that given in [1] which contains neither the  $\theta' V_x$  nor the  $-\theta' V_y$  terms [5]. Their appearance in  $\Phi$  is not unexpected since the velocity components themselves as well as their derivatives appeared as viscous-force terms in equations (7) and (8). That these additional terms in  $\Phi$  are essential will be further elucidated later.

### Twisted Couette Flow

Solving the Couette flow in the helical coordinate system serves to illustrate some of its salient features and to elucidate at the mean time the essential roles played by the  $-\theta' V_y$  and  $\theta' V_x$  terms in the viscous dissipation function.

Consider the steady laminar flow of an incompressible viscous fluid between two infinite plates at  $z = 0$  and  $z = m$ , respectively. The lower plate at  $z = 0$  moves with a constant velocity  $\mathbf{u}_0$  and the upper plate with a constant velocity  $\mathbf{u}_m$ . Denote  $\theta_m$  to be the lesser angle between the directions of the two velocities. Assume further there are no body force acting;

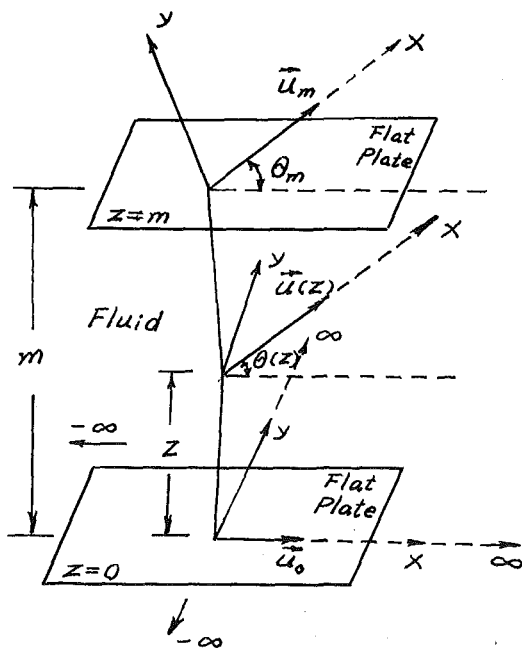


Fig. 2 Twisted Couette flow

the pressure between the plates is uniform; and  $\mu$  is constant. Thus it is feasible to look for solution of the type

$$\begin{aligned} V_x &= u(z) \\ V_y &= 0 \\ V_z &= 0 \end{aligned}$$

by a suitable definition of the helical coordinate system, i.e.,  $\theta(z)$  should be taken to be the angle which the flow velocity makes with a reference direction, say, that of  $\mathbf{u}_0$ . This is a case of an implicitly defined coordinate system in which the coordinate system is to be determined simultaneously with the flow field.

The differential equations governing  $u$  and  $\theta$  are, respectively, from equations (7) and (8)

$$0 = u'' - \theta'^2 u \quad (13)$$

$$0 = 2\theta' u' + \theta'' u \quad (14)$$

The boundary conditions to be satisfied are

$$\begin{aligned} u(0) &= u_0, & u(m) &= u_m \\ \theta(0) &= 0, & \theta(m) &= \theta_m \end{aligned} \quad (15)$$

Equation (14) admits an integral of the form

$$\theta' u^2 = a \quad (16)$$

The constant  $a$  is taken to be nonzero. In term of the new dependent variable  $f \equiv (\theta')^{-1}$  equations (13) and (16) combine to give the differential equation

$$2ff'' - f'^2 - 4 = 0 \quad (17)$$

Equation (17) again has an integral

$$\left( \frac{f'}{2} \right)^2 - bf + 1 = 0 \quad (18)$$

which can be solved by separating variables. The general solutions for  $u$  and  $\theta$  are thus

$$\begin{aligned} u &= \left\{ \frac{a}{b} [1 + (bz + c)^2] \right\}^{1/2} \\ \theta &= \tan^{-1}(bz + c) - d \end{aligned} \quad (19)$$

The constants of integration as determined by the boundary conditions are

$$\begin{aligned} a &= \frac{u_0 u_m \sin \theta_m}{m} \\ b &= \frac{u_0^2 - 2u_m u_0 \cos \theta_m + u_m^2}{m u_0 u_m \sin \theta_m} \\ c &= \frac{u_m \cos \theta_m - u_0}{u_m \sin \theta_m} \\ d &= \tan^{-1} \left( \frac{u_m \cos \theta_m - u_0}{u_m \sin \theta_m} \right) \end{aligned}$$

Thus the solutions can be written as

$$u = \left\{ \left[ u_0 + (u_m \cos \theta_m - u_0) \frac{z}{m} \right]^2 + \left( u_m \sin \theta_m \frac{z}{m} \right)^2 \right\}^{1/2}$$

$$\theta = \tan^{-1} \frac{z u_m \sin \theta_m}{u_0 m + (u_m \cos \theta_m - u_0) z}$$
(20)

The viscous-dissipation function for the twisted Couette flow according to equations (11) and (20) is simply

$$\begin{aligned} \Phi &= \mu[(\theta' u)^2 + u'^2] \\ &= \mu ab \\ &= \mu \frac{|u_m - u_0|^2}{m^2} \end{aligned}$$
(21)

Equation (21) is clearly correct as can be seen by an observer moving at the velocity of the lower plate. In this particular frame of reference  $\theta$  is a constant independent of  $z$ . The coordinate system becomes Cartesian and the nonlinear equations (13) and (14) become linear.

### Concluding Remarks

It is straightforward, though lengthy, to derive the compressible viscous flow equations with respect to any physical base or to a different, for examples, helical-paraboloidal coordinate system and surface-oriented coordinates [6].

### References

- Masliyah, J. H., and Nandakumar, K., "Steady Laminar Flow through Twisted Pipes: Fluid Flow in Square Tubes," *ASME Journal of Heat Transfer*, Vol. 103, Nov. 1981, pp. 785-790.
- Todd, L., "Some Comments on Steady, Laminar Flow through Twisted Pipes," *Journal of Engineering Mathematics*, Vol. 11, 1977, pp. 29-48.
- Fan, Dah-Nien, and Xu, Zhong-Guang, *Tensorial Fluid Mechanics—A Work Book*, Space Graphic, Inc., Washington, D.C., 1983.
- Fan, Dah-Nien, and Xu, Zhong-Guang, *Tensorial Fluid Mechanics*, The Water Resources and Power Press, Beijing, 1985.
- Xu, Zhong-Guang, and Fan, Dah-Nien, "Discussion—Steady Laminar Flow through Twisted Pipes: Fluid Flow in Square Tubes and Steady Laminar Flow through Twisted Pipes: Heat Transfer in Square Tubes," *ASME Journal of Heat Transfer*, Vol. 106, May 1984, p. 480.
- Hirschel, E. H., and Kordulla, W., "Shear Flow in Surface Oriented Coordinate," Friedr. Vieweg and Sohn, Draunschweig/Wiesbaden, 1981.

## Modeling of Wall Friction for Multispecies Solid-Gas Flows

E. D. Doss<sup>1</sup> and M. G. Srinivasan<sup>1</sup>

*The empirical expressions for the equivalent friction factor to simulate the effect of particle-wall interaction with a single solid species have been extended to model the wall shear stress for multispecies solid-gas flows. Expressions representing the equivalent shear stress for solid-gas flows obtained from these wall friction models are included in the one-dimensional two-phase flow model and it can be used to study the effect of particle-wall interaction on the flow characteristics.*

### Introduction

Understanding the flow characteristics of multiphase solid-gas flows is very important for the design and development of

many industrial processes and components for advanced fossil-energy systems. Accurate predictions of the flow parameters for solid-gas mixtures is also essential for the proper development, design and interpretation and/or calibration of nonintrusive flow instruments.

Recently, we have developed [1] a one-dimensional, two-phase, multiparticle computational model that includes particle-particle interaction and particle-wall interaction for solid-gas flows in a horizontal duct of variable area. Furthermore, relatively simple expressions were derived [2] to account for momentum transfer due to collision between particles.

The objective of the work reported here is to develop expressions for the shear stress term representing the effect of wall friction in the momentum equations for each particle species as well as for the overall solid-gas mixture for flows with solids of different particle sizes. To achieve this, we investigate first some available empirical relationships for the friction factor that were based on gas-solid flow with single species (i.e., size) of particles, adapted them to the present model, and extended them to the model for flow of a mixture of multiple species of solid particles and a gas.

### Approach

Investigators have so far followed two distinct approaches to correlate the pressure drop for pipe flow with suspensions with the solid-to-gas loading ratio and other flow, particle, and wall physical characteristics. The first approach is basically a Monte Carlo approach that takes into account the mechanics of particle bounce (see [3-7]). The results of such an approach depend on the geometry of the particle, wall roughness, boundary conditions, wall coefficient of static friction, and coefficient of restitution. As this approach involves many assumptions and requires knowledge of difficult-to-obtain parameters, besides requiring a more complex two-dimensional model, it is not pursued in our analysis.

The second approach, followed in this work, may be referred to as a classical approach, in which the effect of particle-wall interaction is expressed in a manner similar to that for gas-wall friction. This approach has been adopted by many investigators (see, for example, references [8-12]).

The equation of conservation of momentum for a particle of each species and that for the gas-solid mixture for one-dimensional flow along a horizontal axis,  $x$ , is written, respectively, as:

$$\rho_p u p_i \frac{d u p_i}{d x} = \rho_p F_i (u_g - u_{p_i}) + \rho_p \sum_j F_{ij} (u_{p_j} - u_{p_i}) - \frac{4 \tau_{w-p_i}}{D}$$
(1)

$$\phi_g \rho_g u_g \frac{d u_g}{d x} + \rho_p \sum_i \phi_{p_i} u_{p_i} \frac{d u p_i}{d x} = - \frac{d p}{d x} - \frac{4 \tau_{w-pg}}{D}$$
(2)

with  $i = 1, 2, \dots, n$ .

The quantities  $\rho$ ,  $u$ ,  $\phi$ , and  $p$  are material density, velocity, volume fraction and pressure respectively, the subscripts  $p$  and  $g$  denote the solid and gas respectively, the subscript  $p_i$  denotes particles of the  $i$ th species and  $n$  is the number of species of particles. The first and second terms on the right side of equation (1) represent the drag force of gas and the resultant force due to collision of other species of particles, respectively, on a particle of the  $i$ th species.

The last terms on the right side of equations (1) and (2) represent the drag force due to wall friction with  $\tau$  being the shear stress and  $D$ , the hydraulic radius of the duct. The subscript  $w-p_i$  denotes the friction between wall and particle species  $i$ , and the subscript  $w-pg$  denotes the friction between

<sup>1</sup>Mechanical Engineers, Argonne National Laboratory, Argonne, Ill. 60439. Contributed by the Fluids Engineering Division of THE AMERICAN SOCIETY OF MECHANICAL ENGINEERS. Manuscript received by the Fluids Engineering Division June 5, 1985.



Thus the solutions can be written as

$$u = \left\{ \left[ u_0 + (u_m \cos \theta_m - u_0) \frac{z}{m} \right]^2 + \left( u_m \sin \theta_m \frac{z}{m} \right)^2 \right\}^{1/2}$$

$$\theta = \tan^{-1} \frac{z u_m \sin \theta_m}{u_0 m + (u_m \cos \theta_m - u_0) z}$$
(20)

The viscous-dissipation function for the twisted Couette flow according to equations (11) and (20) is simply

$$\begin{aligned} \Phi &= \mu[(\theta' u)^2 + u'^2] \\ &= \mu ab \\ &= \mu \frac{|u_m - u_0|^2}{m^2} \end{aligned}$$
(21)

Equation (21) is clearly correct as can be seen by an observer moving at the velocity of the lower plate. In this particular frame of reference  $\theta$  is a constant independent of  $z$ . The coordinate system becomes Cartesian and the nonlinear equations (13) and (14) become linear.

### Concluding Remarks

It is straightforward, though lengthy, to derive the compressible viscous flow equations with respect to any physical base or to a different, for examples, helical-paraboloidal coordinate system and surface-oriented coordinates [6].

### References

- Masliyah, J. H., and Nandakumar, K., "Steady Laminar Flow through Twisted Pipes: Fluid Flow in Square Tubes," *ASME Journal of Heat Transfer*, Vol. 103, Nov. 1981, pp. 785-790.
- Todd, L., "Some Comments on Steady, Laminar Flow through Twisted Pipes," *Journal of Engineering Mathematics*, Vol. 11, 1977, pp. 29-48.
- Fan, Dah-Nien, and Xu, Zhong-Guang, *Tensorial Fluid Mechanics—A Work Book*, Space Graphic, Inc., Washington, D.C., 1983.
- Fan, Dah-Nien, and Xu, Zhong-Guang, *Tensorial Fluid Mechanics*, The Water Resources and Power Press, Beijing, 1985.
- Xu, Zhong-Guang, and Fan, Dah-Nien, "Discussion—Steady Laminar Flow through Twisted Pipes: Fluid Flow in Square Tubes and Steady Laminar Flow through Twisted Pipes: Heat Transfer in Square Tubes," *ASME Journal of Heat Transfer*, Vol. 106, May 1984, p. 480.
- Hirschel, E. H., and Kordulla, W., "Shear Flow in Surface Oriented Coordinate," Friedr. Vieweg and Sohn, Draunschweig/Wiesbaden, 1981.

## Modeling of Wall Friction for Multispecies Solid-Gas Flows

E. D. Doss<sup>1</sup> and M. G. Srinivasan<sup>1</sup>

*The empirical expressions for the equivalent friction factor to simulate the effect of particle-wall interaction with a single solid species have been extended to model the wall shear stress for multispecies solid-gas flows. Expressions representing the equivalent shear stress for solid-gas flows obtained from these wall friction models are included in the one-dimensional two-phase flow model and it can be used to study the effect of particle-wall interaction on the flow characteristics.*

### Introduction

Understanding the flow characteristics of multiphase solid-gas flows is very important for the design and development of

many industrial processes and components for advanced fossil-energy systems. Accurate predictions of the flow parameters for solid-gas mixtures is also essential for the proper development, design and interpretation and/or calibration of nonintrusive flow instruments.

Recently, we have developed [1] a one-dimensional, two-phase, multiparticle computational model that includes particle-particle interaction and particle-wall interaction for solid-gas flows in a horizontal duct of variable area. Furthermore, relatively simple expressions were derived [2] to account for momentum transfer due to collision between particles.

The objective of the work reported here is to develop expressions for the shear stress term representing the effect of wall friction in the momentum equations for each particle species as well as for the overall solid-gas mixture for flows with solids of different particle sizes. To achieve this, we investigate first some available empirical relationships for the friction factor that were based on gas-solid flow with single species (i.e., size) of particles, adapted them to the present model, and extended them to the model for flow of a mixture of multiple species of solid particles and a gas.

### Approach

Investigators have so far followed two distinct approaches to correlate the pressure drop for pipe flow with suspensions with the solid-to-gas loading ratio and other flow, particle, and wall physical characteristics. The first approach is basically a Monte Carlo approach that takes into account the mechanics of particle bounce (see [3-7]). The results of such an approach depend on the geometry of the particle, wall roughness, boundary conditions, wall coefficient of static friction, and coefficient of restitution. As this approach involves many assumptions and requires knowledge of difficult-to-obtain parameters, besides requiring a more complex two-dimensional model, it is not pursued in our analysis.

The second approach, followed in this work, may be referred to as a classical approach, in which the effect of particle-wall interaction is expressed in a manner similar to that for gas-wall friction. This approach has been adopted by many investigators (see, for example, references [8-12]).

The equation of conservation of momentum for a particle of each species and that for the gas-solid mixture for one-dimensional flow along a horizontal axis,  $x$ , is written, respectively, as:

$$\rho_p u p_i \frac{d u p_i}{d x} = \rho_p F_i (u_g - u_{p_i}) + \rho_p \sum_j F_{ij} (u_{p_j} - u_{p_i}) - \frac{4 \tau_{w-p_i}}{D}$$
(1)

$$\phi_g \rho_g u_g \frac{d u_g}{d x} + \rho_p \sum_i \phi_{p_i} u_{p_i} \frac{d u p_i}{d x} = - \frac{d p}{d x} - \frac{4 \tau_{w-pg}}{D}$$
(2)

with  $i = 1, 2, \dots, n$ .

The quantities  $\rho$ ,  $u$ ,  $\phi$ , and  $p$  are material density, velocity, volume fraction and pressure respectively, the subscripts  $p$  and  $g$  denote the solid and gas respectively, the subscript  $p_i$  denotes particles of the  $i$ th species and  $n$  is the number of species of particles. The first and second terms on the right side of equation (1) represent the drag force of gas and the resultant force due to collision of other species of particles, respectively, on a particle of the  $i$ th species.

The last terms on the right side of equations (1) and (2) represent the drag force due to wall friction with  $\tau$  being the shear stress and  $D$ , the hydraulic radius of the duct. The subscript  $w-p_i$  denotes the friction between wall and particle species  $i$ , and the subscript  $w-pg$  denotes the friction between

<sup>1</sup>Mechanical Engineers, Argonne National Laboratory, Argonne, Ill. 60439. Contributed by the Fluids Engineering Division of THE AMERICAN SOCIETY OF MECHANICAL ENGINEERS. Manuscript received by the Fluids Engineering Division June 5, 1985.

wall and the solid-gas mixture. The remainder of the paper focuses on the expression of these two terms. The shear stress,  $\tau_{w-pg}$ , for a solid-gas mixture with a single species of particles is expressed as [12]

$$\tau_{w-pg} = \phi_p \tau_{w-p} + \phi_g \tau_{w-g} \quad (3)$$

where,

$$\tau_{w-g} = 1/2 f_g \rho_g u_g^2 \quad (4)$$

$$\tau_{w-p} = 1/2 f_p \rho_p u_p^2, \quad (5)$$

and

$$\tau_{w-pg} = 1/2 f_{pg} \rho_g u_g^2 \quad (6)$$

where  $f$  is the friction factor. The parameter  $f_{pg}$  is an equivalent friction factor that would yield the shear stress  $\tau_{w-pg}$  for the solid-gas mixture when multiplied by the kinetic energy of the gas alone. In this approach, the friction factor for gas flow without solids,  $f_g$ , is assumed to remain the same when solid particles are suspended in the flow, even though we are aware that the turbulence structure most likely changes, particularly near the wall. However, this change is accounted for by the particle-wall shear stress term.

Three different models dealing with the representation of the equivalent friction factor,  $f_{pg}$ , have been developed by previous investigation. They are discussed here briefly for the sake of background.

**Eddy Viscosity Approach.** Julian and Dukler [13] suggested that for dilute-phase transport, the presence of the solids is shown primarily by modification of the local turbulence in the gas phase, increase in turbulent fluctuations, mixing length, and eddy viscosity, and thus frictional pressure drop.

Following the discussion given in reference [13], Julian and Dukler found the following simple relationship.

$$\frac{f_{pg}}{f_g} = (1 + Z)^{0.3}. \quad (7)$$

This relationship for the ratio of friction factor of suspension to friction factor of gas is a function of loading ratio,  $Z$ , only.

More recently, Michaelides [14] presented a two-dimensional analytical approach for solid-gas flow based on a turbulence model. He extended the work of Julian and Dukler, but he considered the eddy viscosity that models the Reynolds stress for turbulent flow to change not only with the velocity gradient but also with the density gradient. The Reynolds stress is then calculated according to the mixing-length hypothesis. The results of the Michaelides model agree well with the considered experimental data.

**Reynolds Analogy Approach.** The Reynolds analogy is of historical importance as the first recognition of analogous behavior of momentum- and heat-transfer rates. The analogy can be applied to solid-gas suspensions if the suspension is assumed to behave as a homogeneous fluid and if an accurate relation for heat transfer coefficient of suspensions is available.

Following the discussion given in [9], Pfeffer et al. obtained the following simple relationship

$$\frac{f_{pg}}{f_g} = 1 + 4.0 R_N^{-0.32} Z. \quad (8)$$

This relationship shows a linear dependence between the ratio of friction factor of suspension to friction factor of gas and the solid-to-gas loading ratio. It also shows a weaker dependence on the gas Reynolds number, whereas the eddy viscosity model shows no such dependence.

**Dimensional Analysis Approach.** Although the two previously reported expressions for wall friction due to solid-gas suspension are simple, the phenomena that occur in pneumatic conveying of solids by gas are too varied and too

complex to be expressed in an equation of general form. Rose et al. [15] indicated that the friction factor could be a function of some nondimensional groups.

They investigated experimentally the effect of these nondimensional parameters. For a fixed pipe geometry and solid particle size and shape, the dependence of the equivalent friction factor was then reduced to three nondimensional parameters, namely, the gas Reynolds number, the solid-to-gas loading ratio and the solid-to-gas density ratio. An empirical relationship was developed using their experimental data which took the form:

$$f_{pg} = f_g + \beta Z, \quad (9)$$

where

$$\beta = \frac{\pi}{8} \left( \frac{\rho_p}{\rho_g} \right)^{1/2} \psi \quad (10)$$

The parameter  $\psi$  was given as a function of Reynolds number. The advantage of the above empirical relationship is its additional dependence on solid-to-gas density ratio. However, the disparity between the different investigators on the value of  $\psi$  is a drawback, and therefore, it is subject to further experimental verification.

### Particle-Wall Interaction for Multiple Species of Solids

The momentum conservation equation for each species of particles, equation (1), requires the expression of  $\tau_{w-p_i}$ , the wall shear stress of particles of species  $i$  in terms of a friction factor. If the solids consist of only one size, i.e., one species, then  $\tau_{w-p_i}$  is just replaced by  $\tau_{w-p}$  the expression for which is given by equation (12) below. In the general case in which more than one species is present, it becomes necessary to express the term  $\tau_{w-p_i}$ . In the absence of any previous analytical or empirical method for doing this, we propose the following procedure.

From equation (3), we can write the total wall shear stress on all species of particles as

$$\tau_{w-p} = (\tau_{w-pg} - \phi_g \tau_{w-g}) / \phi_p, \quad (11)$$

which becomes, when we use equations (4) and (5) and recall,  $\phi_p = 1 - \phi_g$ ,

$$\tau_{w-p} = \frac{1}{2} f_g \rho_g u_g^2 \left( \frac{f_{pg}}{f_g} - \phi_g \right) / \phi_p. \quad (12)$$

Since the expression for  $f_{pg}/f_g$  is different in the three approaches discussed in the previous section, different assumptions are made for expressing  $\tau_{w-p_i}$ .

**Eddy-Viscosity Approach.** The wall shear stress in this approach does not depend on particle size. Therefore, we can assume that

$$\tau_{w-p_i} = \tau_{w-p}. \quad (13)$$

Substituting equation (12) into equation (13) and expressing  $f_{pg}/f_g$  of equation (7), we obtain

$$\tau_{w-p_i} = \frac{1}{2} f_g \rho_g u_g^2 \{ (1 + Z)^{0.3} - \phi_g \} / \phi_p \quad (14)$$

from which we can write

$$\phi_{p_i} \tau_{w-p_i} = \frac{1}{2} \left( \frac{\phi_{p_i}}{\phi_p} \right) f_g \rho_g u_g^2 \{ (1 + Z)^{0.3} - \phi_g \}. \quad (15)$$

**Reynolds Analogy Approach.** Substituting equation (8) into equation (12), we obtain

$$\tau_{w-p} = \frac{1}{2} f_g \rho_g u_g^2 (1 + 4 R_N^{-0.32} Z - \phi_g) / \phi_p. \quad (16)$$

Replacing  $1 - \phi_g$  with  $\phi_p$  and simplifying, we obtain

$$\tau_{w-p} = \frac{1}{2} f_g \rho_g u_g^2 \left( 4R_N^{-0.32} \frac{Z}{\phi_p} + 1 \right). \quad (17)$$

If only one species is present,

$$\frac{Z}{\phi_p} = \frac{\rho_p u_p}{\rho_g u_g \phi_g}, \quad (18)$$

and equation (17) then seems to suggest that  $\tau_{w-p}$  is proportional to  $u_p$ . On this basis, we assume  $\tau_{w-p_i}$  is proportional to  $u_{p_i}$ , i.e.,

$$\tau_{w-p_i} = \frac{1}{2} f_g \rho_g u_g^2 \left( 4R_N^{-0.32} \frac{\rho_p u_{p_i}}{\rho_g u_g \phi_g} + 1 \right) \quad (19)$$

or

$$\phi_{p_i} \tau_{w-p_i} = \frac{1}{2} f_g \rho_g u_g^2 \left( 4R_N^{-0.32} Z_i + \phi_{p_i} \right), \quad (20)$$

where

$$Z_i = \frac{\rho_p u_{p_i} \phi_{p_i}}{\rho_g u_g \phi_g} = \frac{\dot{m}_{p_i}}{\dot{m}_g},$$

$\dot{m}_{p_i}$  and  $\dot{m}_g$  being the mass flowrates of particles of species  $i$  and the gas.

**Dimensional Analysis Approach.** Comparing equations (8) and (9), we note that they are similar and the difference between them lies only in the coefficient of  $Z$ . Thus the equivalent equations for equations (19) and (20) become, by analogy

$$\tau_{w-p_i} = \frac{1}{2} f_g \rho_g u_g^2 \left( \frac{\beta}{f_g} \frac{\rho_p u_{p_i}}{\rho_g u_g \phi_g} + 1 \right) \quad (21)$$

and

$$\phi_{p_i} \tau_{w-p_i} = \frac{1}{2} f_g \rho_g u_g^2 \left( \frac{\beta Z_i}{f_g} + 1 \right) \quad (22)$$

with  $\beta$  being given by equation (10).

It may be noted that the different expressions for  $\phi_{p_i} \tau_{w-p_i}$ , given by equations (15), (20), and (22), all satisfy the requirement that

$$\sum_i \phi_{p_i} \tau_{w-p_i} = \phi_p \tau_{w-p}. \quad (23)$$

In conclusion, it is fair to mention that the validity of any of the approaches considered should be determined on the basis of how well it agrees with experimental data. We are planning a series of tests with solid-gas flow in which irradiated particles will be injected into the flow stream along a long horizontal pipe. The particle velocity will be experimentally obtained by measuring the time of flight of the irradiated par-

ticles as observed by gamma detectors installed at different locations along the pipe. The pressure drop will be also measured along several locations. It is expected that these two kind of measurements, the particle velocity and pressure drop, will give us enough information to make it possible to select the best of the three models for the solid-gas flow equivalent friction factor.

#### Acknowledgment

The authors thank Dr. A. C. Raptis of Argonne National Laboratory for providing support and program direction.

#### References

- 1 Doss, E. D., "Analysis and Application for Solid-Gas Flow Inside a Venturi with Particle Interaction," *Int. J. Multiphase Flow*, Vol. 11, No. 4, 1985, pp. 445-458.
- 2 Srinivasan, M. G., and Doss, E. D., "Momentum Transfer Due to Particle-Particle Interaction in Dilute-Gas Solid Flows," *Chemical Engineering Science*, Vol. 40, No. 9, 1985, pp. 1791-1792.
- 3 Ranz, W. E., Tulandis, G. R., and Gutterman, Bernard, "Mechanics of Particle Bounce," *AIChE Journal*, Vol. 6, No. 1, Mar. 1960, pp. 114-127.
- 4 Konne, H., and Saito, S., "Pneumatic Conveying of Solids through Straight Pipes," *J. Chem. Eng. of Japan*, Vol. 2, No. 2, 1969, pp. 211-216.
- 5 Matsumoto, S., and Saito, S., "On the Mechanism of Suspension of Particles in Horizontal Pneumatic Conveying: Monte Carlo Simulation Based on Irregular Bouncing Model," *J. Chem. Eng. of Japan*, Vol. 3, No. 1, 1970, pp. 83-92.
- 6 Matsumoto, S., and Saito, S., "Monte Carlo Simulation of Horizontal Pneumatic Conveying Based on the Rough Wall Model," *J. Chem. Eng. of Japan*, Vol. 3, No. 2, 1970, pp. 223-230.
- 7 Matsumoto, S., Saito, S., and Maeda, S., "Simulation of Gas-Solid Two-Phase Flow in Horizontal Pipe," *J. Chem. Eng. of Japan*, Vol. 9, Vol. 1, 1976, pp. 23-28.
- 8 "Handbook of Multiphase Systems," Hetsroni, G., ed., McGraw-Hill, New York, 1981, (Chapter 7, Pneumatic Conveying, by S. L. Soo).
- 9 Pfeffer, R., Rossetti, S., and Lieblein, S., "Analysis and Correlation of Heat Transfer Coefficients and Friction Factor Data for Dilute Gas-Solid Suspension," NASA TN D-3603, Sept. 1966.
- 10 Mehta, N. C., Smith, J. M., and Comings, E. W., "Pressure Drop in Air-Solid Flow Systems," *Ind. & Eng. Chemistry*, Vol. 49, No. 9, June 1957, pp. 986-992.
- 11 Wen, C., and Simons, H. P., "Flow Characteristics in Horizontal Fluidized Solids Transport," *AIChE Journal*, Vol. 5, No. 2, June 1959, pp. 263-267.
- 12 Fortier, A., and Pen, C. C., "Turbulent Two-Phase Air-Solid Flow in Duct of Circular Cross Section at High Solid Concentrations" (In French), *J. de Mécanique*, Vol. 15, No. 1, 1976, pp. 155-182.
- 13 Julian, F. M., and Dukler, A. E., "An Eddy Viscosity Model for Friction in Gas-Solids Flow," *AIChE Journal*, Vol. 11, No. 5, Sept. 1965, pp. 853-858.
- 14 Michaelides, E. E., "A Model for the Flow of Solid Particles in Gases," *Int. J. Multiphase Flow*, Vol. 10, No. 1, 1984, pp. 61-77.
- 15 Rose, H. E., and Barnach, E., "Flow of Suspensions of Non-Cohesive Spherical Particles in Pipes," *Engineer*, June 14, pp. 880-901; June 21, pp. 939-941, 1957.
- 16 Rose H. E., and Duckworth, R. A., "Transport of Solid Particles in Liquid and Gases," *Engineer*, March 14, pp. 392-396; March 21, pp. 430-433; March 28, pp. 478-483, 1969.

## Unsteady Flow in a Porous Medium Between Two Infinite Parallel Plates in Relative Motion.<sup>1</sup>

**Mario Letelier.**<sup>2</sup> The authors, according to their introductory statements, consider the problem of predicting the effect of boundary oscillation on the flow through a porous medium bounded by two parallel plates, one of which is stationary and the other displaces and oscillates in its own plane. Their linear equation of motion (eq. (2)) contains a pressure gradient term, which in general can be either a constant or an arbitrary function of time independent of boundary conditions. Therefore, it should be expected that the ensuing flow depend both on the pressure gradient and on the boundary conditions. However, in their next step they substitute the pressure gradient in terms of the moving wall velocity  $U$ , viz.

$$-\frac{\partial p}{\partial x} = \rho \frac{\partial U'}{\partial t'} + \frac{\mu}{k} U'$$

This relation implies that for steady motion of the wall, and infinite permeability (i.e., a free duct),  $-\partial p/\partial x = 0$ , which is a

<sup>1</sup>By V. M. Soundalgekar, H. S. Takhar, and M. Singh, published in the December 1985 issue of the JOURNAL OF FLUIDS ENGINEERING, Vol. 107, No. 4, pp. 534-535.

<sup>2</sup>Department of Mechanical Engineering, University of Santiago, casilla 10233, Santiago, Chile.

very particular and restricted flow condition. It seems that the authors have rather addressed the problem of unsteady flow through a porous medium bounded by two parallel plates where the pressure gradient, in their dimensionless nomenclature, is given by

$$-\frac{\partial p}{\partial x} = \sigma^2 + \epsilon(\sigma^2 \cos \omega t - \omega \sin \omega t) \left( = \frac{\partial U}{\partial t} + \sigma^2 U \right)$$

and in which the lower wall is stationary, while the upper one moves with velocity  $U = 1 + \epsilon \cos \omega t$ .

My contention is that the authors have attacked an interesting problem whose analytical restrictions are greater than would appear from their presentation.

They further state that the flow resistance decreases with decreasing permeability, which is contrary to theory and fact. Such statement introduces some confusion into their conclusions.

### Authors' Closure

We would like to thank Professor Letelier for finding our problem interesting. However, we have to have analytical restrictions in the beginning. Gradually, these restrictions will be removed.

Our statement is correct. When the permeability decreases, the medium becomes less porous and hence the flow resistance decreases which is true also physically.